

Modification and degradation of Ni-rich cathode-based Li-ion batteries

Citation for published version (APA):

Jiang, M. (2022). *Modification and degradation of Ni-rich cathode-based Li-ion batteries*. [Phd Thesis 1 (Research TU/e / Graduation TU/e), Electrical Engineering]. Eindhoven University of Technology.

Document status and date:

Published: 07/04/2022

Document Version:

Publisher's PDF, also known as Version of Record (includes final page, issue and volume numbers)

Please check the document version of this publication:

- A submitted manuscript is the version of the article upon submission and before peer-review. There can be important differences between the submitted version and the official published version of record. People interested in the research are advised to contact the author for the final version of the publication, or visit the DOI to the publisher's website.
- The final author version and the galley proof are versions of the publication after peer review.
- The final published version features the final layout of the paper including the volume, issue and page numbers.

[Link to publication](#)

General rights

Copyright and moral rights for the publications made accessible in the public portal are retained by the authors and/or other copyright owners and it is a condition of accessing publications that users recognise and abide by the legal requirements associated with these rights.

- Users may download and print one copy of any publication from the public portal for the purpose of private study or research.
- You may not further distribute the material or use it for any profit-making activity or commercial gain
- You may freely distribute the URL identifying the publication in the public portal.

If the publication is distributed under the terms of Article 25fa of the Dutch Copyright Act, indicated by the "Taverne" license above, please follow below link for the End User Agreement:

www.tue.nl/taverne

Take down policy

If you believe that this document breaches copyright please contact us at:

openaccess@tue.nl

providing details and we will investigate your claim.

Modification and degradation of Ni-rich cathode-based Li-ion batteries

PROEFSCHRIFT

ter verkrijging van de graad van doctor aan de Technische Universiteit Eindhoven, op gezag van de rector magnificus prof.dr.ir. F.P.T. Baaijens, voor een commissie aangewezen door het College voor Promoties, in het openbaar te verdedigen op donderdag 7 april 2022 om 11:00 uur

door

Ming Jiang

geboren te Tianjin, China

Dit proefschrift is goedgekeurd door de promotoren en de samenstelling van de promotiecommissie is als volgt:

voorzitter	Prof.dr.ir. P. de With
1 ^e promotor	Prof.dr. P.H.L. Notten
2 ^e promotor	Prof.dr.rer.nat.habi R.-A. Eichel (RWTH Aachen)
Co-promotor	Dr. D.L. Danilov
Promotiecommissieleden	Prof.dr.rer.nat. F. Hausen (RWTH Aachen) Prof.dr.ir. M. Huijben (Universiteit Twente) Prof.dr.ir. H.J. Bergveld Prof.dr.ir. P.M.J. Van den Hof

Het onderzoek of ontwerp dat in dit proefschrift wordt beschreven is uitgevoerd in overeenstemming met de TU/e Gedragscode Wetenschapsbeoefening.

**Modification and degradation of Ni-rich
cathode-based Li-ion batteries**

Ming Jiang

The work represented in this dissertation has been carried out at Eindhoven University of Technology (the Netherlands) and Forschungszentrum Jülich (Germany). Financial support was from China Scholarship Council (CSC).

Copyright © 2022 by Ming Jiang

All rights are reserved. No part of this dissertation is allowed to be reproduced, stored in a retrieval system or transmitted in any form or by any means, electronic, mechanical, photocopying, recording, scanning or otherwise without the prior written permission of the Author.

Wisdom comes out of dialogue. You have to develop a capacity to expose your own ignorance so that they may discover their own wisdom.

– John B. Goodenough, 2019 Noble Lecture in Chemistry

Table of Contents

Chapter 1 Introduction	1
1.1 Overview of Battery Systems.....	2
1.2 Basics of Li-ion Batteries.....	3
1.3 Battery Materials.....	5
1.4 Fundamentals of Ni-rich Cathode Materials	7
1.4.1 Crystal Structure	8
1.4.2 Electrochemical Characteristics.....	9
1.5 Scope of this Thesis	11
References.....	13
Chapter 2 Degradation and Improvement Strategies for Ni-rich Cathode-based Batteries	2
2.1 Degradation Mechanisms.....	3
2.1.1 Cathode.....	4
2.1.1.1 Residual lithium compounds	4
2.1.1.2 Cation disorder	7
2.1.1.3 Surface reconstruction	13
2.1.1.4 Gas release.....	17
2.1.1.5 Transition-metal dissolution.....	21
2.1.1.6 Intragranular and intergranular cracks.....	25
2.1.1.7 Thermal stability.....	29
2.1.2 Anode.....	33
2.1.2.1 Graphite anode.....	33
2.1.2.2 Li-metal anode.....	36
2.1.3 Electrolyte.....	39
2.1.3.1 Decomposition.....	39
2.1.3.2 CEI formation.....	41
2.2 Improvement Strategies	43

2.2.1	Cathode	44
2.2.1.1	Novel synthesis methods	44
2.2.1.2	Single-crystal fabrication.....	47
2.2.1.3	Microstructural modification.....	51
2.2.1.4	Doping.....	54
2.2.1.5	Protective layer coatings.....	58
2.2.1.6	Concentration gradient	61
2.2.2	Anode.....	65
2.2.2.1	Graphite anode.....	65
2.2.2.2	Li-metal anode.....	68
2.2.3	Electrolyte.....	71
2.2.3.1	Multifunctional electrolyte additives.....	71
2.3	Summary	73
	References.....	76
	Chapter 3 Experimental.....	86
3.1	Materials Preparation Methods	87
3.1.1	Hydrothermal Synthesis.....	87
3.1.2	Sputter Deposition	88
3.2	Characterization Techniques	89
3.2.1	X-ray Diffraction	89
3.2.2	Scanning Electron Microscopy.....	90
3.2.3	Transmission Electron Microscopy	91
3.2.4	X-ray Photoelectron Spectroscopy	93
3.2.5	Inductively Coupled Plasma-Mass Spectrometry.....	94
3.3	Electrode Preparation.....	95
3.3.1	Electrode Slurry Preparation.....	95
3.3.2	Cell Assembly.....	95
3.4	Electrochemical Measurements.....	96
	References.....	97

Chapter 4 LiNi_{0.6}Co_{0.2}Mn_{0.2}O₂ Nanomaterials with Enhanced Li-ion Diffusion Pathways	98
4.1 Introduction	99
4.2 Materials Preparation	101
4.3 Results and Discussion.....	102
4.3.1 Characterization Analysis	102
4.3.2 Electrochemical Analysis	109
4.3.3 Post-Mortem Analysis	116
4.4 Conclusions.....	117
References.....	118
Chapter 5 Interfacial Characterization of LiNi_{0.6}Co_{0.2}Mn_{0.2}O₂ Thin Film Cathodes	122
5.1 Introduction	123
5.2 Materials Preparation	124
5.3 Results and Discussion.....	125
5.3.1 Characterization Analysis	125
5.3.2 Electrochemical Analysis	135
5.3.3 Post-Mortem Analysis	137
5.4 Conclusions.....	148
References.....	149
Chapter 6 Stabilized Li-metal Anodes for LiNi_{0.6}Co_{0.2}Mn_{0.2}O₂/Li Batteries	154
6.1 Introduction	155
6.2 Materials Preparation	157
6.3 Results and Discussion.....	158
6.3.1 Characterization Analysis	158
6.3.2 Electrochemical Analysis.....	160
6.3.3 Post-Mortem Analysis	167
6.4 Conclusions.....	177
References.....	178

Chapter 7 Summary and Outlook	182
List of Abbreviations	188
List of Symbols	191
List of Publications	192
Curriculum Vitae	194
Acknowledgements	195

Chapter 1

Introduction

Abstract

The growing demand for sustainable energy storage devices intensively requires rechargeable lithium-ion batteries (LIBs) with higher specific capacity and stricter safety standards. In particular, Ni-rich layered transition-metal oxides outperform other cathode materials and attract much attention in academia and industry. This chapter starts with an introduction to existing LIBs and well-established electrode materials. It is followed by a general introduction of the fundamentals of Ni-rich cathode materials. In the final section, the scope of this thesis is described.

1.1 Overview of Battery Systems

Nowadays, the world's energy shortage and the danger of climate change place serious threats to social and economic development. The necessity of reducing greenhouse gases emission and the transition from fossil fuels to sustainable clean energy sources have become a global priority. Motivated by the urgent demands for energy upgrades, various clean energy systems have been announced and intensively developed. Rechargeable battery systems, as one of the most important sources of sustainable energy, have been implemented dominantly in numerous applications, particularly for portable electronic devices (PEDs) and electronic vehicles (EVs).^[1]

The evolution of rechargeable battery systems has gone through several stages, including lead-acid, nickel-cadmium (Ni-Cd), nickel-metal-hybrid (Ni-MH), sodium-nickel (Na/NiCl), lithium-metal polymer (LiM-Polymer), and LIBs. Figure 1.1 illustrates the energy storage properties of commonly used battery systems. It can be seen that LIBs outperform others in terms of both specific power and specific energy.^[2] Therefore, since the first commercialization by Sony in 1991, LIBs have received tremendous academic and industrial attention.^[3] Stimulated by the constant renovation of battery technology and government subsidies, the thriving markets of EVs and other electrical devices powered by LIBs have achieved considerable progress.^[4]

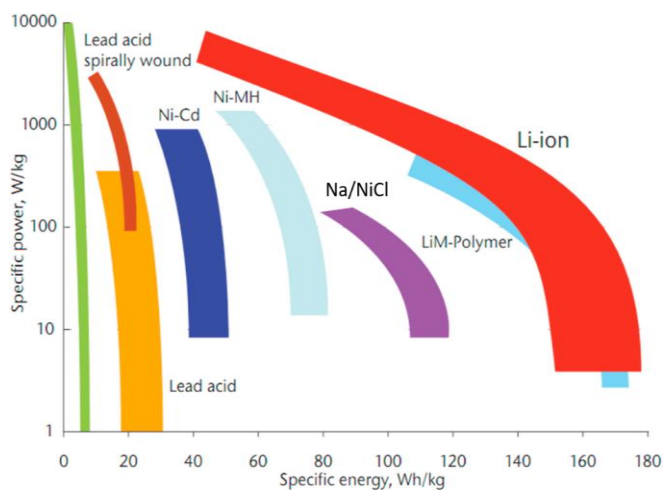


Figure 1.1 Summary of various battery systems on the performance of specific power vs. specific energy.^[2]

The first generation LIB comprises graphite as an anode and LiCoO_2 as a cathode. It delivers specific energy of approximately 160 Wh kg^{-1} , as shown in Figure 1.1. To meet the growing demands for a higher-energy storage system with an extended lifetime, researchers continuously devote efforts to designing novel electrode materials and promoting battery technology.

1.2 Basics of Li-ion Batteries

The basic operation of LIBs is that Li-ions are transported from one electrode to the other via the electrolyte and are safely (de)intercalated in both electrodes.^[5] A non-aqueous liquid with ideally high ionic conductivity and chemical inertness acts as an electrolyte. A flexible porous separator is placed in between to prevent direct contact of two electrodes.

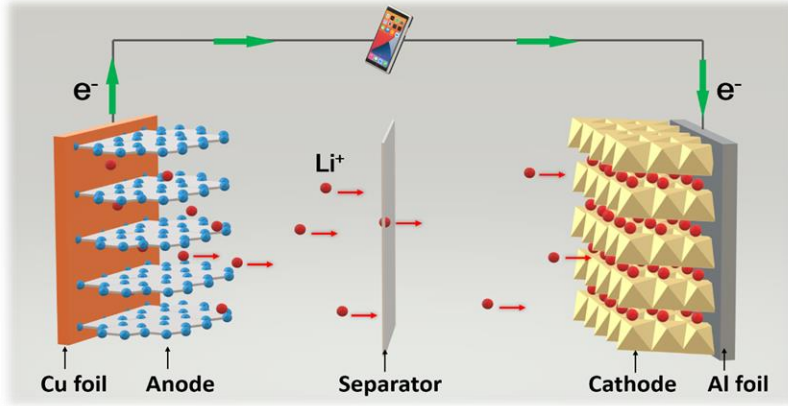
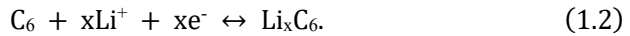
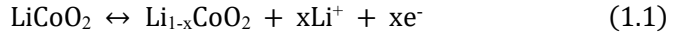


Figure 1.2 Schematic illustration of a rechargeable Li-ion battery with graphite anode and LiCoO₂ cathode during discharging.

Figure 1.2 gives a schematic illustration of a commercialized C₆/LiCoO₂ cell in the discharge process. During discharging, Li-ions leave from the graphite anode, are transported through the separator, and intercalate into the LiCoO₂ cathode. Simultaneously, electrons are transported through the external circuit, powering the electrical devices. The electrochemical reactions of this cell can be described as



The specific energy (volumetrically or gravimetrically) of LIBs is determined by the charge capacity Q_{cell} and the cell voltage V_{cell} , according to

$$E = Q_{cell} \times V_{cell}, \quad (1.3)$$

where V_{cell} is determined by the difference between the chemical potentials of cathode and anode

$$V_{cell} = \frac{\mu_{cathode}^{Li} - \mu_{anode}^{Li}}{F}, \quad (1.4)$$

where F is the Faraday constant. Eq. (1.4) shows that choosing electrode materials with high intrinsic storage capacity and operating voltage is essential to increase the energy density of batteries.^[6]

1.3 Battery Materials

During the intensive exploration of the LIB technology for several decades, numerous electrode materials have been developed. Figure 1.3 lists the state-of-art cathode and anode materials, as well as their performance characteristics. It can be seen that the specific capacities of the cathode and anode are not matching. The anode materials show an overall much higher specific capacity than that of the cathodes. Therefore, the development of cathode materials has proven a crucial bottleneck regarding performance improvement from a full-cell perspective.

LiFePO₄ (LFP) is a cathode material with the highest safety and stability. Yet, the operating voltage range and specific capacity are both quite low (see Figure 1.3).^[7] LiNi_{0.5}Mn_{1.5}O₄ (LNMO) is a high-voltage cathode material with an operating voltage up to 4.8 V (*vs.* Li⁺/Li). However, the specific capacity of this material is unfortunately rather low (~100 mAh g⁻¹), hindering the further development of LNMO-based LIBs.^[8] With regard to Li-rich metal oxides ($x\text{Li}_2\text{MnO}_3 \cdot [1-x]\text{LiTMO}_2$ [TM = Ni, Co, Mn]) (HE-NCM), the specific capacity is exceptionally high, approaching 300 mAh g⁻¹. At the same time, its discharge voltage plateau is slightly lower (at around 3.4 V).^[9] On the other hand, Ni-based transition-metal oxides, LiNi_{*x*}Co_{*y*}Mn_{1-*x-y*}O₂ (NCM)/LiNi_{*x*}Co_{*y*}Al_{1-*x-y*}O₂ (NCA)-based LIBs can deliver specific capacities beyond 200 mAh g⁻¹ with no compromising operating voltage, exhibiting a dominant position in choosing cathode materials.^[10]

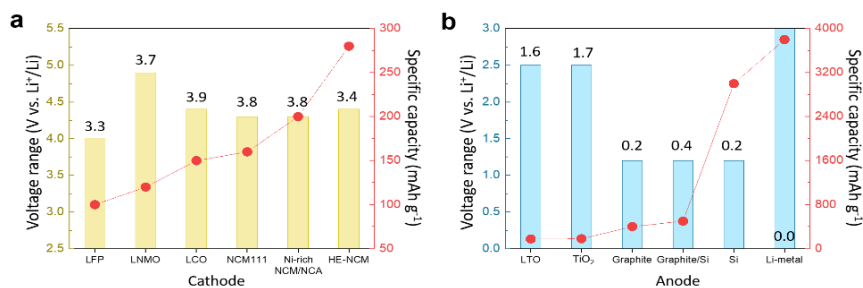


Figure 1.3 Summary of specific capacity and operating voltage for various cathode (a) and anode (b) electrode materials. The columns indicate the operating voltage range at the left-hand axes; the values above the columns indicate the position of discharge voltage plateau. The red dots indicate the specific capacity at the right-hand axes. The specific capacities refer to electrodes capacities combined with a Li metal anode discharged at 0.1 C-rate. Cathodes are defined as LFP (LiFePO₄),^[7] LNMO (LiNi_{0.5}Mn_{1.5}O₄),^[8] LCO (LiCoO₂),^[11] NCM111 (LiNi_{1/3}Co_{1/3}Mn_{1/3}O₂),^[12] Ni-rich NCM (LiNi_{0.8}Co_{0.1}Mn_{0.1}O₂),^[10] Ni-rich NCA (LiNi_{0.8}Co_{0.15}Al_{0.05}O₂),^[13] and HE-NCM (Li-rich NCM).^[9] Anodes are defined as LTO (Li₄Ti₅O₁₂),^[14] TiO₂,^[15] Graphite,^[16] Graphite/Si,^[17] Si,^[18] and Li metal.^[19]

In 2012 all early EV models used LiNi_{1/3}Co_{1/3}Mn_{1/3}O₂ (NCM111) cathode-based LIBs. However, NCM111 cannot fulfill the growing demand for higher specific energy of 350 Wh kg⁻¹ at a cell level by 2025.^[20] To increase the energy density, layered transition-metal oxides with higher Ni-content have been developed, denoted as Ni-rich cathodes. Two major advantages of Ni-rich cathodes are their high specific energy capacity of 200 ~ 250 mAh g⁻¹ and the relatively high operating voltage of about 4.4 V, which is more promising in applications than other cathode materials.^[21]

The superiority of Ni-rich cathodes in storage capacity also brings the tradeoff with electrochemical stability. It is confirmed that the crystal structure of Ni-rich cathode materials is prone to irreversibly transform during the (de)lithiation process, resulting in rapid performance fading.^[22] The degree of

degradation depends on the particular elemental composition in the cathode material. However, all Ni-rich cathodes undergo similar electronic and structural changes. Apart from cathode materials, the degradation of both the anode and electrolyte should also be considered from a full-cell perspective.^[23]

Graphite is the commercially most successful anode material in the market. It is commonly employed together with Ni-rich cathodes in modern batteries.^[24] Li-metal is considered an ideal anode material because of its lowest negative electrochemical electrode potential. Coupled with a Ni-rich cathode, it will significantly boost the battery capacity.^[25] However, both anode materials suffer from serious problems, such as solid-electrolyte-interphase (SEI) formation, dendrite growth, *etc.* Such detrimental issues severely hinder the large-scale commercialization of the Ni-rich based-LIBs as next-generation batteries.^[26]

1.4 Fundamentals of Ni-rich Cathode Materials

Ni-rich cathode materials are derived from layered LiNiO_2 , which was first discovered by Dyer *et al.* in the 1950s.^[27] LiNiO_2 was one of the candidates as electrode material with a strong commercialization perspective. However, the structural degradation of LiNiO_2 is extreme, hindering its further development. Other elements, such as Co, Mn, Al, Zr, *etc.*, were introduced into the LiNiO_2 and partially substituted Ni to overcome this deficiency. Among all elements, Co, Mn, and Al substitutions are most relevant for improving Ni-rich cathode materials' performance.^[28] Co contributes to the rate capacity enhancement and cation-mixing mitigation. Substitution of Co by Mn is beneficial for the structural stability of LiNiO_2 .

Furthermore, partial substitution of Ni by Al ions is also advantageous and cost-effective due to the low cost and light atomic weight of Al. Consequently, the excellent synergy between Ni, Co, Mn, and Ni, Co, Al ensures Ni-rich NCM ($\text{LiNi}_x\text{Co}_y\text{Mn}_{1-x-y}\text{O}_2$, $x > 0.5$) and NCA ($\text{LiNi}_x\text{Co}_y\text{Al}_{1-x-y}\text{O}_2$, $x > 0.5$) materials are

the most promising materials to improve LIBs further.^[20] Up to now, Ni-rich cathodes of various compositions have been proposed and comprehensively investigated, leading to a better understanding of the degradation mechanisms and improvement in performance.^[29]

1.4.1 Crystal Structure

The structure of layered LiTMO_2 (TM=transition-metals, Ni, Co, Mn, Al, *etc.*) is isostructural with $\alpha\text{-NaFeO}_2$, where the rhombohedral crystal with $R\bar{3}m$ space group, formed by a cubic close-packed (ccp) lattice, is surrounded by oxygen atoms (Figure 1.4).^[30] Considering that the octahedral sites in the LiTMO_2 crystal are occupied by lithium or transition-metals, the layer structure in LiTMO_2 can be divided into Li slabs and transition-metal-oxide slabs. Such slabs alternate each other in the crystal.

The layered structure has two-dimension channels for Li-ion diffusion. Apart from that, two kinds of Li-ion diffusion routes proceed in the crystal.^[30] Li^+ ions will either move from one octahedral site to the following site through the intermediate tetrahedral sites (route I) or hop via the oxygen dumbbells (route II). At the early stage of delithiation, the oxygen dumbbell diffusion is most dominant. When about 1/3 of lithium is extracted, the tetrahedral site pathway becomes prevailing.

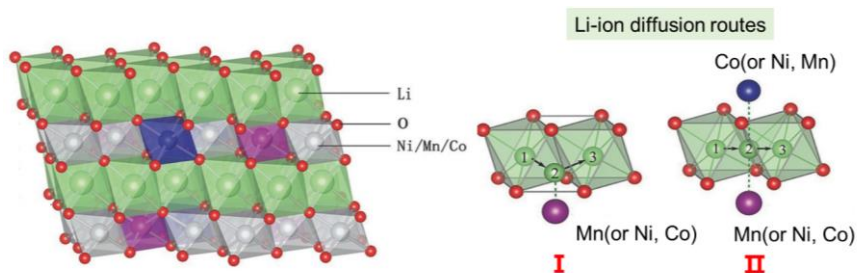


Figure 1.4 Lattice of an NMC layered structure, tetrahedral site pathway (route I), and oxygen dumbbell pathway (route II) for Li-ion diffusion.^[30]

1.4.2 Electrochemical Characteristics

The Ni-content in NCM materials mainly determines the electrochemical performance and structural stability. Nowadays, many studies confirmed a concomitant increase in storage capacity and decreased electrode stability with increasing Ni-content.^[31] Figure 1.5a gives the typical charge and discharge voltage profiles of NCMs with various Ni-content. The experimental results indicate the improved specific capacity with the increase of Ni-content in NCMs. Based on the calculation, the theoretical capacity of NCM material is 275 mAh g^{-1} , suggesting the considerable potential for further growth. An increasing Ni content is therefore essential for further developments. However, the studies have experimentally confirmed that NCMs with higher Ni fractions reveal lower capacity retention upon cycling. When the composition reaches LiNiO_2 , the capacity retention drops dramatically after 100 cycles, making it unsuitable for practical applications.^[32]

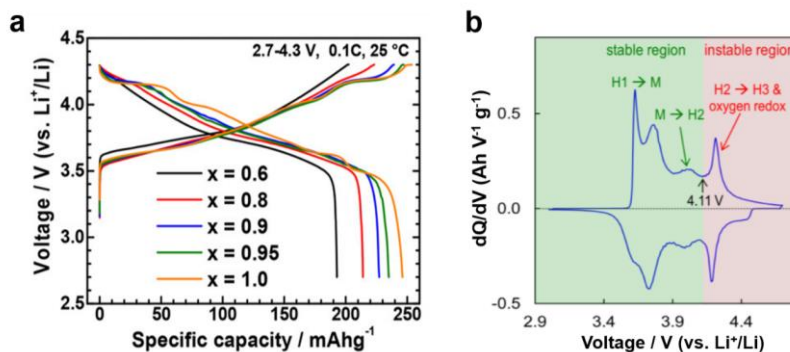


Figure 1.5 (a) Initial charge and discharge voltage curves for $\text{LiNi}_x\text{Co}_y\text{Mn}_{1-x-y}\text{O}_2$ ($x = 0.6, 0.8, 0.9, 0.95, 1$).^[32] (b) Typical dQ/dV curves for Ni-rich NCM/Li cells.^[33]

The characteristic phase evolution of the Ni-rich cathode can be identified in the differential capacity plot as a function of electrode voltage (dQ/dV). As illustrated in Figure 1.5b, three-phase transition areas are detected, starting from hexagonal-1 (denoted as H1) to monoclinic (denoted as M), then from M to hexagonal-2 (denoted as H2), and finally from H2 to hexagonal-3 (H3). The definitions of three hexagonal phases are determined by the evolution of lattice parameters in $\text{Li}_{1-x}\text{NiO}_2$.^[34] Three phase-coexistence regions are located at around 3.7 (H1+M), 4.0 (M+H2), and 4.2 V (H2+H3).

The dQ/dV full profile can be split into stable (green) and unstable (red) regions depending on the cut-off voltage. When the voltage is above 4.11 V, the electrode undergoes the H2-H3 transition, accompanied by lattice oxygen reduction. The transition from H2 to H3 under a high voltage regime is mainly attributed to the abrupt shrinkage on the c-axis in the unit cell, resulting in detrimental anisotropic lattice volume changes. Based on theoretical and experimental studies, the lattice collapse induced by H2-H3 transition is considered harmful for maintaining the reversible storage capacity.^[35] Such lattice collapse will trigger a series of problems, such as cations disorder, surface reconstruction, gas release, *etc.* The problems become severe with the increase of

Ni-content, operation temperature, and state-of-charge (SOC). In Chapter 2, the discussion on corresponding degradation mechanisms will be presented in detail.

1.5 Scope of this Thesis

Ni-rich layered metal oxides have drawn a lot of attention in investigating high energy density, low cost, and reduced-Co-content cathode materials. Pouch cells, equipped with Ni-rich cathodes with Li metal anodes, can meet the goal of a high energy density of up to 890 Wh l^{-1} . However, despite the above merits, Ni-rich LIBs still suffer from several drawbacks, such as cation disorder, transition-metal dissolution, surface passive layer formation, Li dendrite growth, *etc.* Therefore, further improvements and optimizations are essential for Ni-rich LIBs. This thesis investigates degradation mechanisms and explores modification strategies for Ni-rich NCM and Li metal anode, aiming to fabricate Ni-rich LIBs with enhanced performance.

In **Chapter 2**, various degradations processes occurring in Ni-rich cathode-based LIBs and corresponding remedying strategies are overviewed. The battery degradation is systematically discussed from a full-cell perspective, comprising the degradation occurring on cathode, anode, and electrolyte. Many mitigation methods have been proposed to address these problems. Six approaches are offered for the cathode, including synthesis upgrading, single-crystal fabrication, microstructural manipulation, elemental doping, protective layer coating, and concentration gradient designing. For the anode, chemical treatment, surface coating, and approaches for uniform Li deposition are discussed. Regarding the electrolyte, multifunctional additives are noteworthy for mitigating the degradations on cathode and anode simultaneously. Finally, several directions for further progress have been briefly prospected.

In **Chapter 3**, the detailed experimental methods and parameters that are used in this thesis are given. Material preparation methods, characterization

techniques, electrode preparation process, and electrochemical measurements will be presented in detail.

In **Chapter 4**, the development of $\text{LiNi}_{0.6}\text{Co}_{0.2}\text{Mn}_{0.2}\text{O}_2$ materials with a nanostructured morphology will be described. A facile surfactant-assisted hydrothermal method followed by the solid-state reaction is employed as the synthesis method. Corresponding characterizations validate that the as-prepared NCM sample possesses a highly ordered crystal facet orientation in the particles, facilitating the presence of Li-ion diffusion tunnels and improving Li-ion diffusivity. Benefited from the structural advantage, the nanostructured $\text{LiNi}_{0.6}\text{Co}_{0.2}\text{Mn}_{0.2}\text{O}_2$ cathode demonstrates a more favorable Li-ion (de)intercalation reaction kinetics, promising discharge rate capability, and stable cycling performances compared with commercially produced cathode materials. Additionally, faster reaction kinetics also confers the electrode materials the ability of the fast charging, showing a high potential for practical applications in Li-ion batteries.

In **Chapter 5**, $\text{LiNi}_{0.6}\text{Co}_{0.2}\text{Mn}_{0.2}\text{O}_2$ thin-film electrodes are prepared to investigate the degradation mechanisms in more detail. LiNbO_3 , as a promising solid electrolyte with high ionic conductivity, is introduced as the protective layer on the Ni-rich cathodes to alleviate parasitic reactions at the electrode surface. Electrochemical investigations show that a LiNbO_3 -coated $\text{LiNi}_{0.6}\text{Co}_{0.2}\text{Mn}_{0.2}\text{O}_2$ electrode enhances stability and mitigates the impedance increase upon cycling compared to a bare $\text{LiNi}_{0.6}\text{Co}_{0.2}\text{Mn}_{0.2}\text{O}_2$ electrode. The interaction between LiNbO_3 and $\text{LiNi}_{0.6}\text{Co}_{0.2}\text{Mn}_{0.2}\text{O}_2$ layers is probed by X-ray photoelectron spectroscopy (XPS) depth profiling. The formation of a favorable Ni-ions diffusion interface is successfully detected. Post-mortem characterizations show various surface components and cathode-electrolyte interphase (CEI) film formation, revealing the degradation of Ni-rich NCM cathodes in more detail.

In **Chapter 6**, a robust LiNbO₃-modified Li metal anode with high stability will be presented. The modified Li metal electrodes show restrained Li dendrite growth and neglectable transition-metal reduction at the anode surface. LIBs assembled with Ni-rich LiNi_{0.6}Co_{0.2}Mn_{0.2}O₂ cathodes and modified-Li metal anodes significantly improved electrochemical performance with prolonged cycle life. The mechanisms on SEI formations of Li metal anodes are also investigated, presenting new insights for material design and mechanisms analyses of stable Ni-rich NCM-based LIBs.

At the end of this thesis, the summary of conclusions and an overall outlook will be given in **Chapter 7**.

References

- 1 Y. Liang, C. Z. Zhao, H. Yuan, Y. Chen, W. Zhang, J. Q. Huang, D. Yu, Y. Liu, M. M. Titirici, Y. L. Chueh, H. Yu, Q. Zhang, *InfoMat* **1** (2019) 6.
- 2 Y. Li, J. Yang, J. Song, *Renewable and Sustainable Energy Reviews* **74** (2017) 19.
- 3 R. Schmich, R. Wagner, G. Hörpel, T. Placke, M. Winter, *Nature Energy* **3** (2018) 267.
- 4 A. Manthiram, *Nature Communication* **11** (2020) 1550.
- 5 M. R. Palacin, *Chemical Society Reviews* **47** (2018) 4924.
- 6 A. Kraytsberg, Y. Ein-Eli, *Advanced Energy Materials* **2** (2012) 922.
- 7 H. Liu, Q. Cao, L. J. Fu, C. Li, Y. P. Wu, H. Q. Wu, *Electrochemistry Communications* **8** (2006) 1553.
- 8 M.-H. Liu, H.-T. Huang, C.-M. Lin, J.-M. Chen, S.-C. Liao, *Electrochimica Acta* **120** (2014) 133.
- 9 P. Zhang, X. Zhai, H. Huang, J. Zhou, X. Wang, B. Chen, Z. Guo, Y. He, *Journal of Power Sources* **499** (2021)
- 10 X. Xu, H. Huo, J. Jian, L. Wang, H. Zhu, S. Xu, X. He, G. Yin, C. Du, X. Sun, *Advanced Energy Materials* **9** (2019) 1803963.

- 11 J. Cho, J.-G. Lee, B. Kim, B. Park, *Chemistry of Materials* **15** (2003) 3190.
- 12 F. Fu, G.-L. Xu, Q. Wang, Y.-P. Deng, X. Li, J.-T. Li, L. Huang, S.-G. Sun, *Journal of Materials Chemistry A* **1** (2013) 3860.
- 13 P. Hou, H. Zhang, X. Deng, X. Xu, L. Zhang, *ACS Applied Materials & Interfaces* **9** (2017) 29643.
- 14 Y.-B. He, M. Liu, Z.-D. Huang, B. Zhang, Y. Yu, B. Li, F. Kang, J.-K. Kim, *Journal of Power Sources* **239** (2013) 269.
- 15 H. Han, T. Song, E.-K. Lee, A. Devadoss, Y. Jeon, J. Ha, Y.-C. Chung, Y.-M. Choi, Y.-G. Jung, U. Paik, *ACS Nano* **6** (2012) 8308.
- 16 J. Shim, K. A. Striebel, *Journal of Power Sources* **130** (2004) 247.
- 17 Y. N. Jo, Y. Kim, J. S. Kim, J. H. Song, K. J. Kim, C. Y. Kwag, D. J. Lee, C. W. Park, Y. J. Kim, *Journal of Power Sources* **195** (2010) 6031.
- 18 J. Cho, *Journal of Materials Chemistry* **20** (2010) 4009.
- 19 X. Fan, L. Chen, O. Borodin, X. Ji, J. Chen, S. Hou, T. Deng, J. Zheng, C. Yang, S. C. Liou, K. Amine, K. Xu, C. Wang, *Nature Nanotechnology* **13** (2018) 715.
- 20 W. Li, E. M. Erickson, A. Manthiram, *Nature Energy* **5** (2020) 26.
- 21 A. Manthiram, B. Song, W. Li, *Energy Storage Materials* **6** (2017) 125.
- 22 L. de Biasi, B. Schwarz, T. Brezesinski, P. Hartmann, J. Janek, H. Ehrenberg, *Advanced Materials* **31** (2019) e1900985.
- 23 J. P. Pender, G. Jha, D. H. Youn, J. M. Ziegler, I. Andoni, E. J. Choi, A. Heller, B. S. Dunn, P. S. Weiss, R. M. Penner, C. B. Mullins, *ACS Nano* **14** (2020) 1243.
- 24 V. Gopalakrishnan, A. Sundararajan, P. Omprakash, D. Bhat Panemangalore, *Journal of The Electrochemical Society* **168** (2021) 040541.
- 25 D. Lin, Y. Liu, Y. Cui, *Nature Nanotechnology* **12** (2017) 194.
- 26 T. Li, X.-Z. Yuan, L. Zhang, D. Song, K. Shi, C. Bock, *Electrochemical Energy Reviews* **3** (2019) 43.

- 27 L. D. Dyer, B. S. Borie Jr, G. P. Smith, *Journal of the American Chemical Society* **76** (1954) 1499.
- 28 J. U. Choi, N. Voronina, Y. K. Sun, S. T. Myung, *Advanced Energy Materials* (2020) 2002027.
- 29 P. Teichert, G. G. Eshetu, H. Jahnke, E. Figgemeier, *Batteries* **6** (2020) 8.
- 30 S. Cui, Y. Wei, T. Liu, W. Deng, Z. Hu, Y. Su, H. Li, M. Li, H. Guo, Y. Duan, W. Wang, M. Rao, J. Zheng, X. Wang, F. Pan, *Advanced Energy Materials* **6** (2016) 1501309.
- 31 H.-H. Ryu, K.-J. Park, C. S. Yoon, Y.-K. Sun, *Chemistry of Materials* **30** (2018) 1155.
- 32 X. Wang, Y. L. Ding, Y. P. Deng, Z. Chen, *Advanced Energy Materials* **10** (2020) 1903864.
- 33 S. S. Zhang, *Journal of Energy Chemistry* **41** (2020) 135.
- 34 C. Xu, P. J. Reeves, Q. Jacquet, C. P. Grey, *Advanced Energy Materials* (2020) 2003404.
- 35 S. S. Zhang, *Energy Storage Materials* **24** (2020) 247.

Chapter 2

Degradation and Improvement

Strategies for Ni-rich Cathode-based Batteries

Abstract

Lithium-ion batteries composed of Ni-rich layered cathodes and graphite anode (or Li-metal anode) are suitable for meeting the energy requirements of next-generation batteries. However, the instability of Ni-rich cathode-based LIBs poses challenges to large-scale commercialization. This chapter presents various degradation processes occurring at cathodes, anodes, and electrolytes in Ni-rich LIBs. Considering the underlying degradation in Ni-rich cathode-based LIBs, numerous efforts have been devoted to the battery performance improvements. Therefore, the state-of-the-art mitigation solutions proposed over the past few years are summarized in this chapter.

2.1 Degradation Mechanisms

Despite the growing expectations towards Ni-rich cathode-based LIBs, their practical application is still restricted due to the rapid performance degradation and safety hazard issues. Generally, for a Ni-rich cathode-based LIB, the degradation problem can originate from different parts in the battery system: cathode, electrolyte, and anode. The current problems and challenges that Ni-rich cathodes are still facing can be summarized as follows: (1) Residual lithium compounds that are inevitably formed during the material preparation process; (2) Cation disorder (or Li/TM lattice mixing) triggered by the material synthesis and battery cycling; (3) Structural reconstruction occurring at the electrode surface during electrochemical operation, induced by the layered-spinel-rocksalt phase transition combined with the formation of lattice oxygen vacancies; (4) O₂ and CO₂ gas release at the electrode material surface, which is closely related to surface reconstruction and side-reactions with the electrolyte; (5) Transition-metal dissolution as the consequence of HF attack; (6) Intragranular and intergranular cracks formed at high SOC and intensive cycling, and (7) The fragile thermal stability, which may lead to thermal runaway, leading to serious safety concerns.

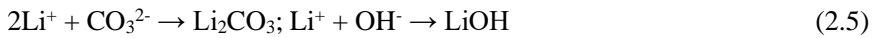
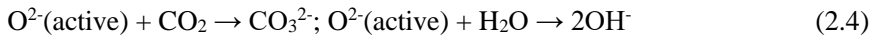
Apart from the various degradation mechanisms at the cathode side, detrimental reactions in the anode and the electrolyte could also cause further battery performance decay. On the one hand, the graphite anode suffers from severe volume expansion and graphite layer collapse. In contrast, the Li-metal anode suffers from dendrite growth and the formation of "death lithium" spots. On the other hand, electrolyte decomposition will spontaneously engage in the solid-electrolyte-interphase formation at both the cathode and anode, forming passivating layers at both electrodes. All the above challenges are generally interlinked in the battery operation. Therefore, a comprehensive and in-depth study of these problems is essential for developing LIBs with a prolonged life span

and improved stability. The degradation mechanisms associated with Ni-rich cathodes, anodes, and electrolytes will be presented in subsequent sections.

2.1.1 Cathode

2.1.1.1 Residual lithium compounds

Residual lithium compounds (RLCs) are inevitably formed in Ni-rich cathodes and mainly consist of LiOH, Li₂CO₃, Li₂O, Li₂O₂, and LiHCO₃.^[1] Most of these compounds will eventually convert into LiOH and Li₂CO₃ during storage. The formation of RLCs stems from two processes. During the synthesis process, an excess amount of lithium salts (typically 5 mol% higher) is added as transition-metal precursor(s) to compensate for the lithium loss during calcination because of the volatilization of lithium at high temperatures. On the one hand, a higher amount of lithium salt can inhibit Li/TM mixing. On the other hand, the excessive lithium content will remain at the particle surface and simultaneously react with H₂O, O₂, and CO₂ in the air.^[2] With an increasing Ni-content in Ni-rich cathodes, a lower calcination temperature and higher oxygen purity will be needed during preparation. That will likely lead to the formation of undesirable RLCs layers.^[3] The highly active Ni³⁺ ions in the cathode material can contribute to the RLCs formation as well. The spontaneous reduction of Ni³⁺ to Ni²⁺ at the surface will give rise to lattice oxygen O²⁻ oxidation and the consequent reaction with Li⁺. It can be described by the following equations^[4]



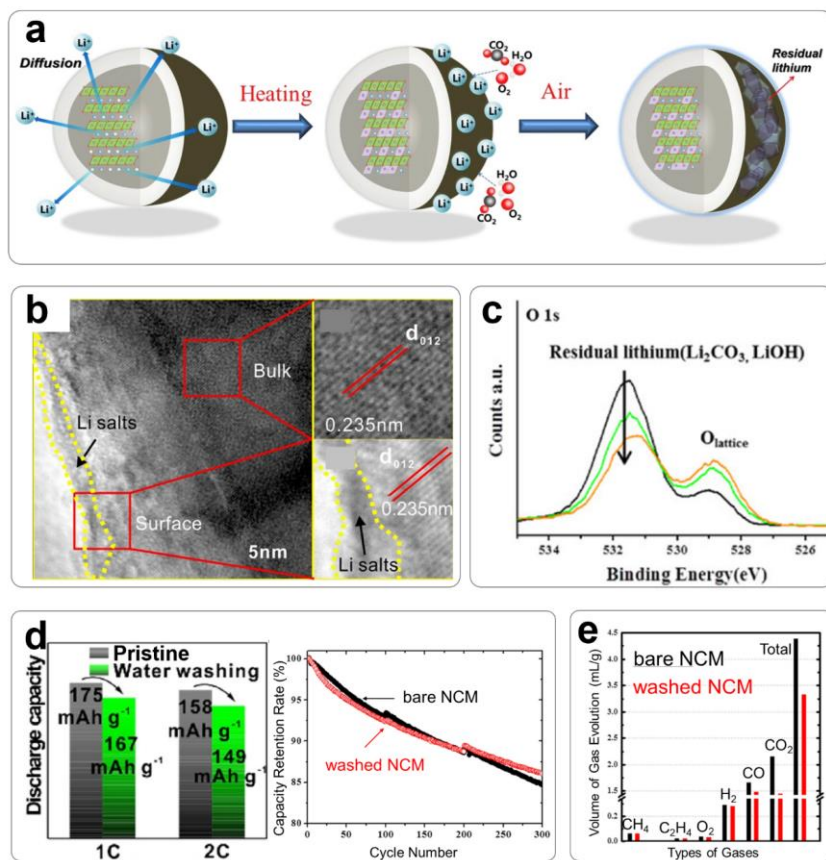


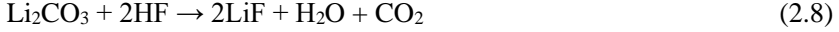
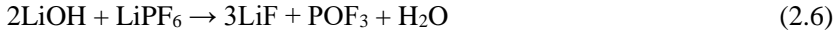
Figure 2.1 (a) Schematic representation of the formation process of LiOH and Li_2CO_3 at a $\text{LiNi}_{0.7}\text{Mn}_{0.3}\text{O}_2$ cathode surface.^[5] (b) TEM images of a pristine NCM811 cathode surface.^[6] (c) XPS depth spectra of O 1s at the surface of bare $\text{LiNi}_{0.80}\text{Co}_{0.15}\text{Mn}_{0.05}\text{O}_2$.^[7] (d) The discharge capacity of an NCM811/Li cell before and after washing with water and discharge stability of a $\text{LiNi}_{0.80}\text{Co}_{0.15}\text{Mn}_{0.05}\text{O}_2/\text{graphite}$ cell.^[6] (e) Gas evolution after cycling 300 times for a bare $\text{LiNi}_{0.80}\text{Co}_{0.15}\text{Mn}_{0.05}\text{O}_2$ cathode and a washed one.^[7]

Figure 2.1a shows a schematic representation of RLCs growth at a Ni-rich cathode surface.^[5] The actual composition and amount of surface impurities vary with the synthesis parameters and storage conditions, such as temperature and air

humidity. This Li-salt layer can be detected by transmission electron microscopy (TEM), as shown in Figure 2.1b. The lattice spacing of 2.35 Å is assigned to the (012) plane of the layered NCM811 material. An inhomogeneous Li-salt layer can be observed at the surface with a thickness around 3 nm. X-ray photoelectron spectroscopy (XPS) depth profile was also employed on a pristine $\text{LiNi}_{0.80}\text{Co}_{0.15}\text{Mn}_{0.05}\text{O}_2$ material (Figure 2.1c). In the O 1s spectra, the peak located at 531 eV is attributed to Li_2CO_3 (or LiOH), and the peak at 528.8 eV is the binding energy of TM-O in NCM. The peak intensities expose the amount and distribution of RLCs with sputtering depth, revealing the enrichment of the impurities at the NCM surface.

Many studies have confirmed that the generation of RLCs surface layers is detrimental to the performance of Ni-rich cathodes. The most efficient and feasible way to remove RLCs from the surface is by the water washing method. However, the washing will lead to capacity losses (Figure 2.1d), as water tends to react with the active electrode material at the subsurface and partially destroy the material's crystalline structure, which is a kind of tradeoff.^[6] Moreover, the water washing process also increases the sensitivity of Ni-rich cathodes to air, so careful control of washing parameters is required. Though the washing treatment leads to a reduced storage capacity, it offers enhanced electrode stability and moderate gas evolution compared in comparison to untreated electrode materials.

The study of Park *et al.* demonstrates that the total amount of gas evolution was reduced by 25% for treated samples after 300 cycles in a $\text{LiNi}_{0.80}\text{Co}_{0.15}\text{Mn}_{0.05}\text{O}_2/\text{graphite}$ cell (Figure 2.1e).^[7] The accumulation of gas in a battery places a considerable safety hazard. The gas generation in the battery predominantly arises from the reaction between RLCs and the electrolyte as well as phase transitions inside the electrode material. The latter factor will be illustrated in details in the following section, while the mechanism of RLCs reacting with electrolyte during cycling has been described reaction sequence^[7]



2.1.1.2 Cation disorder

Cation disorder is a phenomenon also known as Li/TM ions mixing in Ni-rich layered cathodes. Among the basic cations in Ni-rich cathodes, such as Ni^{2+} , Co^{3+} , Mn^{3+} , Al^{3+} , *etc.*, Ni^{2+} ions show a high propensity to mix with Li^+ ions due to the similar ionic radii of Ni^{2+} (0.69 Å) and Li^+ (0.76 Å) cations. Such mixing leads to crystal structure transformation from a pristine layer via a spinel phase to the final rock-salt phase. The Li-ion mobility will be hindered due to this cation disordering, thus reducing the rate capability of Ni-rich cathodes. It is worth noticing that cation disorder is observed during the synthesis process and exits throughout the whole battery life. This Li/Ni mixing tendency becomes much more frequent with increasing Ni-ratio, operation temperature, cut-off voltage during charging, and SOC.

Finding a suitable reactant ratio between the TM-precursor and lithium salt is the starting point for restraining TM migration during calcination. Chu *et al.* recently investigated the influence of the Li-excess during calcination on the Li/TM mixing.^[8] The schematic diagram shown in Figure 2.2a shows that the samples prepared with Li/TM ratios of 1.00, 1.06, and 1.12 are denoted by E00, E06, and E12, respectively. It is found that the Li slab in the lattice will experience shrinkage under both Li-loss (E00) and Li-excess (E12) conditions. For the E00 Li-loss sample, lithium volatilization during calcination will cause unoccupied defects in the sample. A large number of defects in the lattice leads to contraction of the Li slab and eventually creates severe Li/TM disorder. For the E12 Li-excess sample, the extra Li will partially occupy TM (3b) sites. The introduction of slightly larger Li^+ ions leads to larger TMO_6 octahedrons, expanding the distance

between TM slabs and contracting the Li slab resulting in Li/TM disorder. Only the sample with the most optimal Li/TM ratio (E06) shows a broader Li slab. The expansion of the Li slab and shrinkage of TMO_6 will guarantee better Li-ion diffusion.

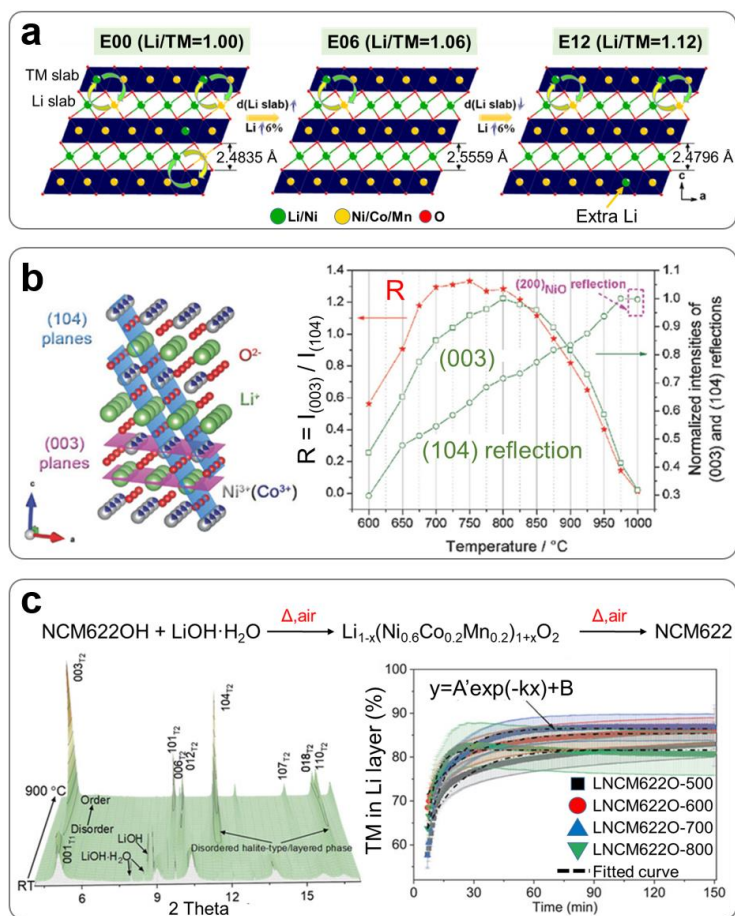


Figure 2.2 (a) Schematic diagram of NCM materials with different Li/TM ratios of 1.00 (E00), 1.06 (E06), and 1.12 (E12) in LiMO_2 .^[8] (b) Illustration of the atomic configuration and evolution of the intensity of the (003) and (104) reflections during synthesis of $\text{LiNi}_{0.8}\text{Co}_{0.2}\text{O}_2$.^[9] (c) *In situ* HTSRD pattern evolution during NCM622 synthesis and the evolution of cation disordering as a function of reaction time.^[10]

In situ XRD is a proper method to diagnose cation disorder and can even provide quantitative analyses.^[9] The relative intensity ratio between the (003) and (104) plane reflection ($R=I_{(003)}/I_{(104)}$) reveals the degree of cation disorder in the bulk of the material. Figure 2.2b illustrates the positions of the (003) and (104) planes in the lattice, where TM ions, Li⁺ ions, and O ions are evenly distributed in the (104) planes, making the reflection of (104) independent of the ordering. In contrast, the reflection of the (003) plane is highly sensitive to cationic ordering. When Li/Ni mixing occurs in the crystal, the X-ray reflection intensity of the (003) plane will reduce, leading to a decrease of the R-value. Thus, a preliminary determination on the degree of cation disorder can be obtained from the XRD result through the peak intensity ratio between the (003) and (104) plane. Wang *et al.* applied *in situ* XRD to study the structural ordering evolution of LiNiO₂ and LiNi_{0.8}Co_{0.2}O₂ during calcination.^[9] Their results highlight Co substitution's significance in facilitating the initial nucleation of a Li-deficient layered structure at low temperatures and restraining the cation disorder at high temperatures.

The cation disorder is also detectable during the high-temperature lithiation reaction of the calcination process. Liu *et al.* employed *in situ* high-temperature synchrotron radiation diffraction (HTSRD) to systematically investigate the nonequilibrium formation of layered NCM622 (Figure 2.2c).^[10] The starting reactants are the TM-hydroxide Ni_{0.6}Co_{0.2}Mn_{0.2}(OH)₂ (NCM622OH) precursor with trigonal layered structure ($P\bar{3}m1$, T1 phase), and lithium source LiOH·H₂O. The *in situ* HTSRD pattern shows that the characterized reflections of NCM622OH gradually disappear when the temperature increases to 300°C. Furthermore, a metastable layered Li_{1-x}(Ni_{0.6}Co_{0.2}Mn_{0.2})_{1+x}O₂ with a higher degree of Li/TM exchange of about 30% is detected at around 500°C. The Li/TM exchange ratio can be obtained from the c/a ratio calculation, as presented in the previous paragraph. With further increasing the temperature up to 900°C, a well-defined trigonal layered phase NCM622 can be indexed. Based on this investigation, it has been identified that complex reactions occur between the TM-

precursor and lithium sources during the thermal treatment in the air. Three dominant components (NCM622OH, $\text{Li}_{1-x}(\text{Ni}_{0.6}\text{Co}_{0.2}\text{Mn}_{0.2})_{1+x}\text{O}_2$, NCM622) have been identified throughout the process. Additionally, it is shown that a longer thermal treatment time should be considered at lower heating temperatures to stabilize the final structure. Therefore, it is important to carefully control the heating temperature and duration time to mitigate the cation disorder degree of Ni-rich cathodes. Noteworthy, the synthesis of different Ni-rich cathodes may require a different set of heating parameters.

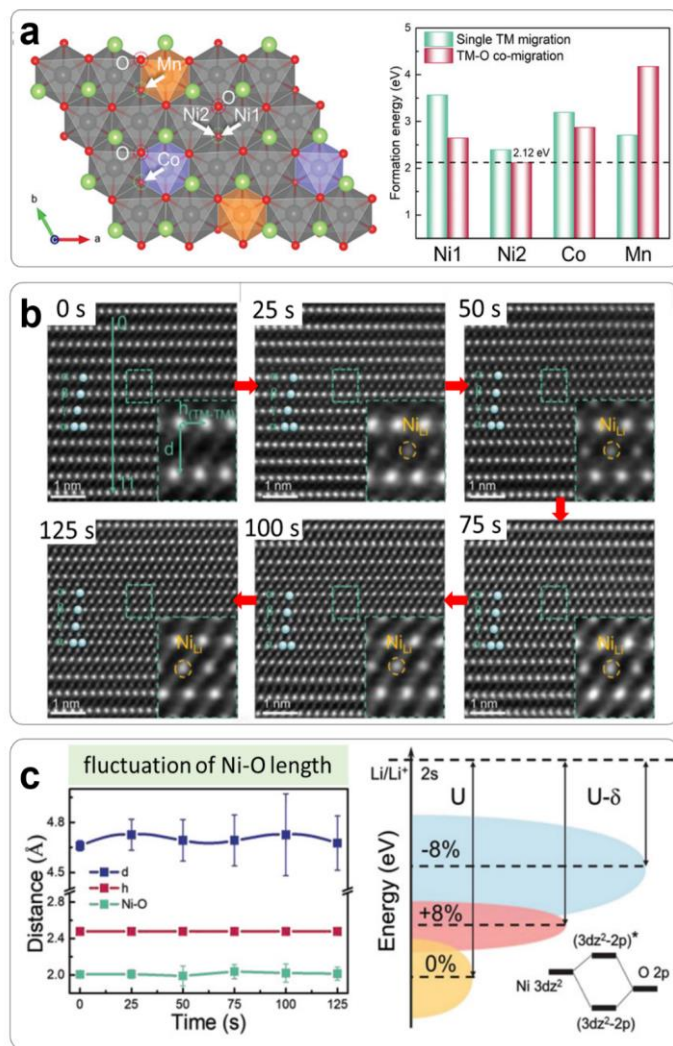


Figure 2.3 (a) Schematic representation of the outward migration paths of TM and O ions along the out-of-plane direction and the formation energy of “single TM migration” and “TM-O co-migration”.^[11] (b) Evolution of atomic arrangements during TM migration viewed along the [110] orientation.^[12] (c) Evolution of the average interlayer distance between TM slabs (d), spacing distance between two TM ions (h), and Ni-O length during TM migration. Schematic diagram of e_g^* antibonding orbitals hybridized by Ni $3d_z^2$ and O $2p$ orbitals in NiO_6 octahedron with different Ni-O bonds.^[12]

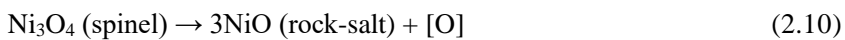
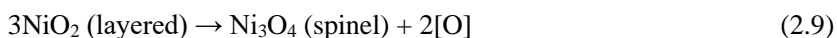
The visualization of Li/TM migration at an atomic scale has been realized by applying scanning transmission electron microscopy (STEM). Based on the STEM measurements, Zhang *et al.* proposed two possible TM ions migration pathways, as illustrated in Figure 2.3a.^[11] The first process is "single TM migration", where one single TM ion migrates to the nearest surface vacancy of the Li site (V_{Li}). The second process is "TM-O co-migration", when a single TM ion migrates to the nearest surface V_{Li} , and the nearest O ion migrates to the outermost layer simultaneously. Among all TM-O co-migrations, the Ni₂-O migration was accompanied by the lowest formation energy, implying the higher tendency for Ni ions to migrate with O ions. In addition, Zhang *et al.* further divided the second process into three different trajectories: (1) single Ni-migration, (2) Ni-O co-migration, and (3) O migration followed by Ni migration. Another enlightened work of the same group is the *in-operando* observation of cation disorder, elaborating its impact on battery voltage decay.^[12]

The high-angle annular dark-field STEM (HAADF-STEM) images of Figure 2.3b show the atomic arrangement as a function of measurement time, revealing the gradually increasing number of Ni_{Li} (migrated Ni ion) in Li sites during cation migration. Moreover, the authors observed that the TM migration gives rise to some fluctuation of Ni-O bond length (Figure 2.3c). The length of Ni-O changes in the range of 1.804 - 2.184 Å, corresponding to the rate of -10.2 - 8.6% in comparison to the pristine Ni-O length (2.010 Å). They further performed calculations of the energy bands of LiNiO₂ with the pristine Ni-O bond length, increased Ni-O bond length (+8%), and decreased Ni-O bond length (-8%). The 0% pristine length is defined by the primitive LiNiO₂ cell, taken from the DFT simulation package. The calculation results reveal that the changes of Ni-O bond length (+8% and -8%) will both ultimately lift the energy density of e_g^* antibonding orbitals ($3d_z^2-2p$)* in the NiO₆ octahedrons. Given the fact that the thermodynamic equilibrium voltage of a full-cell is determined by the energy gap between Li 2s and the highest occupied molecular orbital (HOMO) energy level

$((3d_z^2-2p)^*$ in NiO_6), lifting the HOMO level will ultimately result in a cell voltage decline.

2.1.1.3 Surface reconstruction

Surface reconstruction in Ni-rich cathodes is related to a phase transition process, mostly at the material's surface. During this phase transition, the original crystal structure changes from layered-structured to spinel and eventually to rock-salt. Typical differential capacity profiles can be observed at the highly delithiated state, as previously shown in Figure 1.5b, suggesting that the H2-to-H3 transition is responsible for this process.^[13] This transformation is the combined impact of cation disorder and lattice oxygen loss and is accelerated at high Ni-content, high SOC, and high temperatures. The following equations describe this transition^[14]



The formed rock-salt phase has poor Li transportation kinetics, resulting in blocking Li-ion diffusion paths and reducing ionic conductivity. The NiO-like rock-salt phase in the surface reconstruction layer grows epitaxially on the edge of aged Ni-rich cathodes. Grey *et al.* proposed a surface reconstruction-driven degradation mechanism for NCM811 by applying *in situ* synchrotron-radiation powder X-ray diffraction (SR-PXRD).^[17] During the long-duration electrochemical cycling experiments, the phase fraction obtained for the aged NCM811 cathode reveals a growing proportion of fatigued phase. In contrast, the amount of electrochemically active phase is decreasing. In the fatigued phase, the layered structure in the bulk material will be pinned by the thick rock-salt surface layer due to the high interfacial lattice strain, as illustrated in Figure 2.4a. Thus, the Li slab is prevented from contracting further, making the active Li^+ trapped in the lattice, which is no longer available to participate in the delithiation process at the higher SOC. Their analysis indicates the lattice mismatch between the layered

and rock-salt phases developing after intensive cycling of Ni-rich cathodes, restricting the reversible SOC range to 75%. Attempts to reach higher SOC values by applying higher cut-off voltage lead to even larger lattice mismatches and even more rapid electrode degradation.

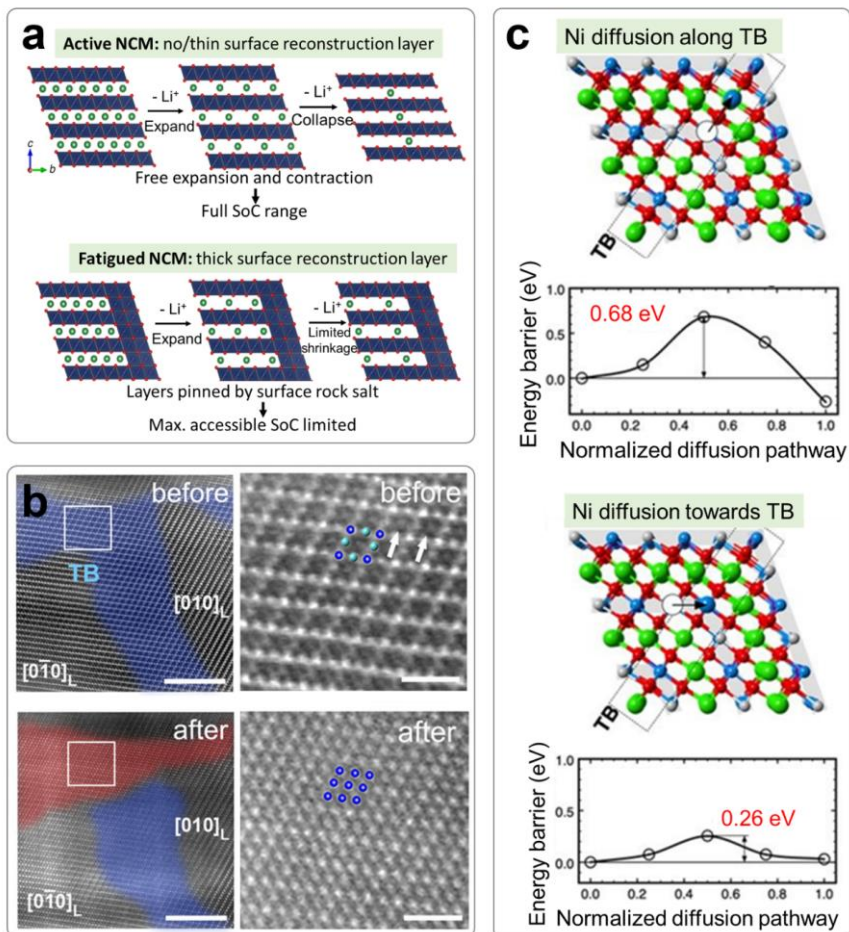


Figure 2.4 (a) Illustrations of the NCM811 structural evolution of the active and fatigued phase during delithiation.^[15] (b) HAADF-STEM images before and after delithiation of NCM76 surface.^[16] (c) The kinetics of a series of reaction steps required by the layered \rightarrow rock-salt phase transformation.^[16]

Some studies also demonstrate that phase transitions can already be detected before lithiation occurs at the material surface. Su *et al.* investigated the structural evolution close to the surface region at the atomic scale by *in situ* TEM.^[16] They confirmed that crystallographic defects in pristine materials could trigger the formation of additional phases and distinct boundaries between three phases (layered, spinel, rock-salt). These intrinsic defects enable the appearance of a broad area with a spinel phase even before lithiation. Subsequently, the rock-salt phase starts growing and keeps propagating after lithiation (Figure 2.4b). According to these observations, the structural changes tend to evolve along with planar defects. DFT calculations suggest that the existence of a coherent twin boundary (TB) in the crystal reduces the energy barrier of cation migration and provides a more feasible pathway for Li/TM diffusion (Figure 2.4c). This work reveals that intrinsic crystallographic defects in Ni-rich cathodes significantly influence the layer-spinel-rocksalt phase transformation. Additionally, Wang *et al.* observed that evolution of the rock-salt phase upon electrochemical cycling can also develop along the grain boundaries in $\text{LiNi}_{0.76}\text{Mn}_{0.14}\text{Co}_{0.10}\text{O}_2$ (NMC76) (Figure 2.5a).^[18] Apart from the crystallographic defects in the primary particles, structural reconstruction is also escalated by the direct contact with the liquid electrolyte and oxygen depletion in the crystal lattice.

Surface reconstruction is generally considered as an unfavorable consequence of electrochemical cycling in Ni-rich cathodes. Studies have shown that this layer is already formed during the synthesis process and found in freshly prepared samples. Interestingly, the formation of this surface reconstruction layer (SRL) is facet-dependent. Chen *et al.* reported that the surface layer was selectively constructed on the non-(001) surface at the pristine NCM622 particles. In contrast, no such layer is observed at the (001) surface.^[19] As shown in Figure 2.5b, Li loss occurs during the heating treatment at the non-(001) surface, leaving behind Li-vacancies in the lattice. The Li loss is accompanied by O losses. These vacant sites then become available for the development of defects for Li/Ni mixing.

At the same time, at the (001) surface, the TM-O-Li layers significantly hinder such evolution, resulting in a negligible formation of surface reconstruction layers (Figure 2.5c).

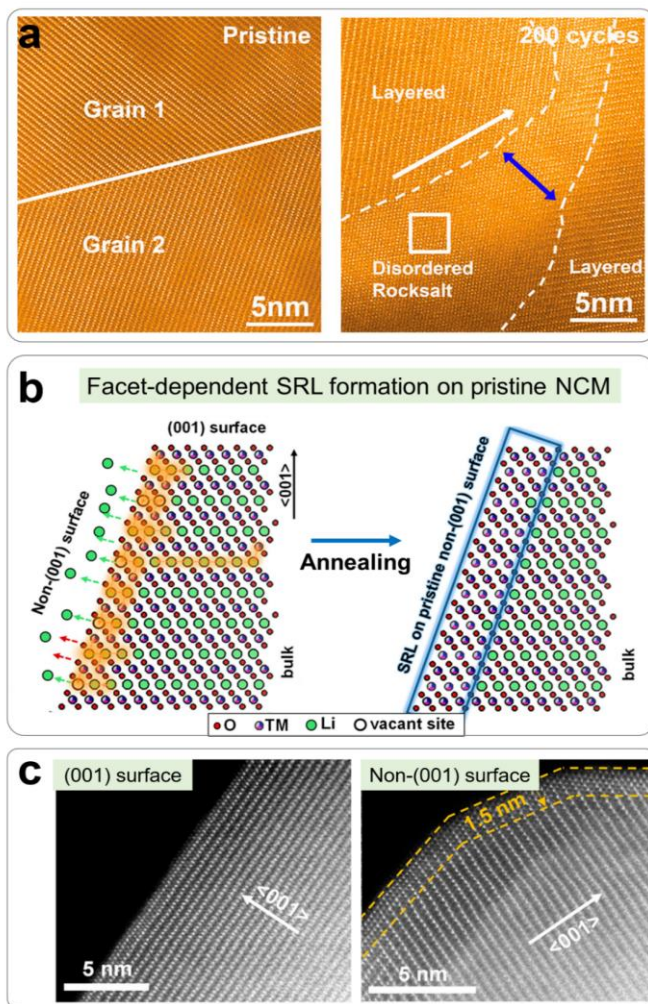


Figure 2.5 (a) HAADF-STEM images of a twin boundary in pristine and cycled NMC76.^[18] (b) Schematic representation of the annealing process, which leads to growth of the surface reconstruction layer (SRL) at the pristine NMC surface.^[19] (c) HRTEM images at the (001) surface and non-(001) surface.^[19]

2.1.1.4 Gas release

The gas releasing problem is the most hazardous safety issue in LIBs. The reactions involved in the gas release are typically exothermic, triggering a series of chain reactions and eventually leading to a severe risk of catastrophic self-combustion of the battery.^[20] The gaseous decomposition products are generally CO₂ and O₂. In Ni-rich cathodes, the origins of gas generation arise from three aspects, as schematically shown in Figure 2.6a: (1) Electrolyte/surface mixed reactivity, including lattice oxygen loss induced by the structural defects (cation disorder and surface reconstruction as discussed above), lithium hydroxides, and unreacted precursors at the surface; (2) Decomposition of Li₂CO₃ and reaction with the electrolyte; (3) Direct electrolyte oxidation.^[21]

High SOC will accelerate gas generation due to the presence of surface defects. A high delithiation state also stimulates electrolyte decomposition reactions. Washing has been frequently used to alleviate such side effects and reduce the amount of the gaseous products that stem from surface contaminations. Studies have confirmed that different solvents and procedures used in the washing process will result in various surface contamination compounds, leading to diverse gas evolution behavior. McCloskey *et al.* employed various washing treatments to study the impact of surface contamination on the gas evolution in delithiated NCM622 (Figure 2.6b).^[22] They prepared NCM622 samples with different treatments (¹⁸O-NCM622, ¹⁸O-MeOH, ¹⁸O-H₂O, ¹⁸O-soak, Li₂CO₃-¹⁸O, and H₂O-¹⁸O) and kept the cathodes at 4.8 V for a long time while monitoring the gas evolution. It turns out that the sample with H₂O soaking treatment (¹⁸O-soak) shows the smallest gas evolution and capacity loss. Their results indicated rather complex gas generation mechanisms depending on surface contaminants and defects. Thus, a proper surface pre-treatment is necessary for reducing overall gas formation.

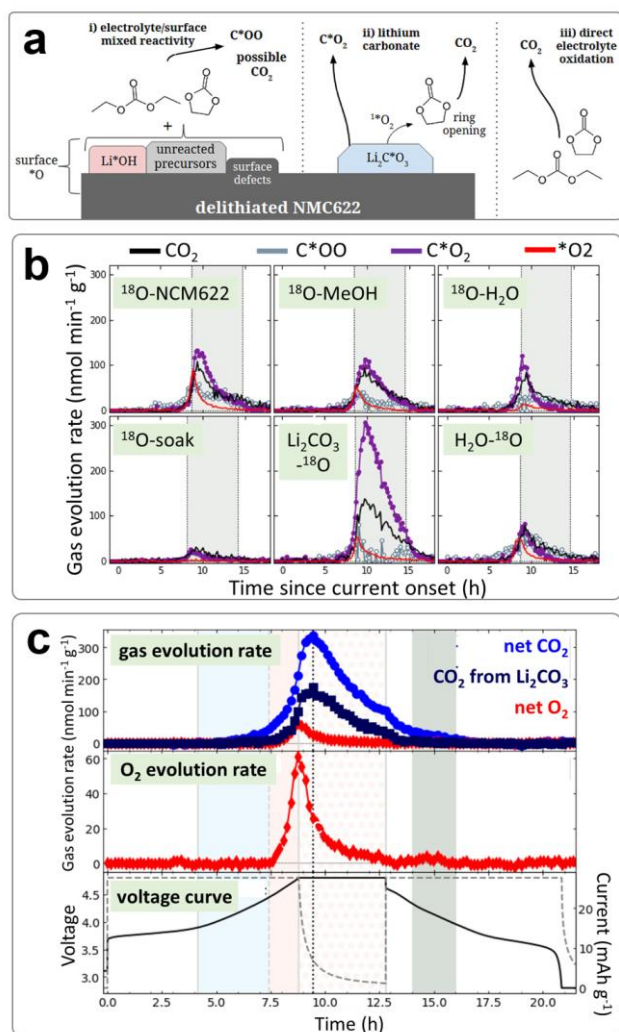


Figure 2.6 (a) Possible reaction routes for gas formation at the surface.^[21] (b) Rate of $^*\text{O}_2$ and carbon dioxide evolution for NMC622s under various treatments (^{18}O -NCM622: the baseline sample synthesized via conventional procedure; ^{18}O -MeOH: sample treated by methanol rinsing; ^{18}O -H $_2$ O: sample treated by H $_2$ O rinsing; ^{18}O -soak: sample treated by H $_2$ O soaking; Li_2CO_3 - ^{18}O : sample treated by Li_2CO_3 enriching; H_2O - ^{18}O : sample treated by H $_2$ O washing and ^{18}O enriching).^[21] (c) Gas evolution and corresponding voltage profiles for NMC622.^[22]

O₂ and CO₂ gas evolution in the battery system are significantly accelerated under high-voltage operation. As shown in Figure 2.6c, the gas formation at the NCM622 electrode was investigated by applying differential electrochemical mass spectrometry (DEMS) under potentiostatic control at 4.8 V.^[22] Interestingly, the CO₂ and O₂ evolution exhibit diverging behaviors. The O₂ evolution rate reached a maximum at the end of galvanostatic charging at 4.8 V and dropped during the potentiostatic period as the current fell. In contrast, the CO₂ evolution rate continues to rise at the beginning of the potentiostatic period. It starts to drop only after approximately 1 hour. This trend suggests that the amount of O₂ evolution is closely related to the lattice deflection at the outermost surface, influenced by the delithiation depth. The CO₂ evolution mostly depends on the decomposition of Li₂CO₃ (and electrolyte) at the cathode surface. This conclusion has been further confirmed by growing a surface carbonate layer and studying these materials as a function of various cut-off voltages. The surface carbonate layer has already been detected at 3.9 V, while the onset voltage of O₂ lattice loss was found at around 4.45 V. Most of the electrolyte degradation products will stem from the surface after discharge. On the contrary, the formation of the surface disorder layer is irreversible and can persist at the electrode surface.

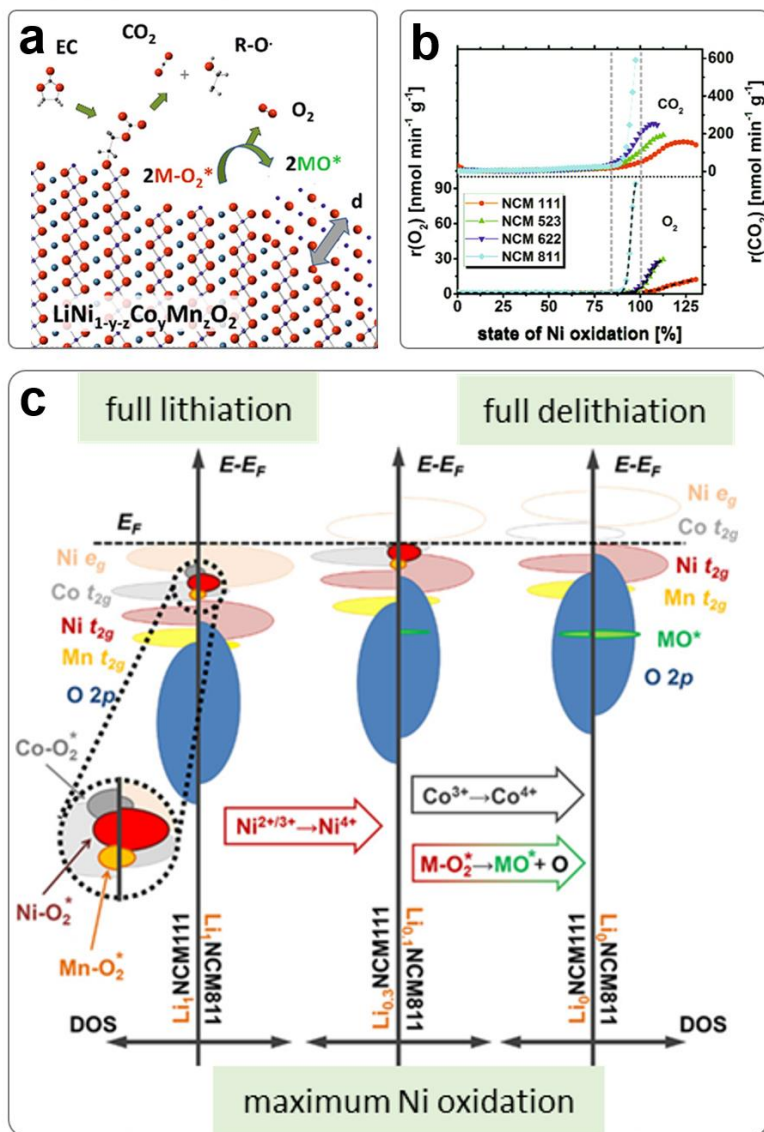


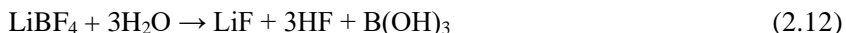
Figure 2.7 (a) Schematic representation of selected reactions resulting in gas formation.^[23] (b) The dependence of gas evolution on the state of Ni oxidation.^[23] (c) Qualitative DOS diagrams for NCM111 and NCM811 at full lithiation, maximum nickel oxidation, and complete delithiation.^[23]

It has been widely accepted that the complex interaction between surface reconstruction and interface reactivity results in gaseous decomposition products. Apart from the decomposition of surface impurity products, CO₂ generation could also originate from phase transformation at the electrode surface. Figure 2.7a schematically shows these reactions at the electrode surface, as found by Berg *et al.*^[23] On the one hand, partly oxidized surface oxygen reacts with organic carbonate electrolytes, such as EC, DMC, DEC, *etc.*, which results in CO₂ generation. On the other hand, lattice oxygen losses induced by structural transformations (LiMO₂→MO or M₃O₄) lead to O₂ evolution. Additionally, the evolving CO₂, O₂, and R-O intermediates generated from electrolyte decomposition are known to be strongly reactive towards electrolyte solvents, contributing to the formation of the surface inactive layer. Analysis based on the electrochemical mass spectroscopy (EMS) shows that the onset point of gas formation falls within a narrow range of Ni-oxidation state (85%-100%). Higher Ni-content facilitates gas formation (Figure 2.7b). The authors also presented electronic density of state (DOS) calculations for NCM111 and NCM811 at three different states, as illustrated in Figure 2.7c. They concluded that the rate of gas formation (CO₂ and O₂) is mainly determined by the rate of electron depletion from the Ni-O₂* surface state. To a smaller extent, it is affected by the competitive Co t_{2g} bulk oxidation and Co-O₂* surface states.

2.1.1.5 Transition-metal dissolution

The dissolution of transition-metal ions from the cathode into electrolyte is an inevitable process, resulting in capacity degradation because of the loss of Li-ion insertion sites in the host structure. It is mainly triggered by corrosion of electrolyte decomposition by-products, such as HF. It accelerates at elevated temperatures and high operating voltages. It is widely acknowledged that the electrolyte solvents might contain traces of water during manufacturing, which

react with lithium salts (LiPF_6 or LiBF_4), yielding acidic species. The related reactions can be described as follows^[24]



Alternatively, the generation of HF can arise from reactions between organic solvents and PF_6^- , such as the one-electron oxidation of EC- PF_6^- . Transition-metal dissolution might also occur due to the formation of low-valence ions caused by lattice oxygen loss during cycling. Metal ions with lower valence states are more soluble in the electrolyte than those with higher valence states.

Figure 2.8a presents evidence of transition-metal dissolution in secondary particles after battery cycling.^[25] The line-energy dispersive X-ray spectroscopy (EDX) results demonstrate severe deficiency of the metal ions at the particle surface, especially Ni ions. A similar trend can also be found by the corresponding sectionalized chemical composition maps of a single Ni-rich NCM particle in Figure 2.8b.^[26] Compared with the pristine state, the particles in cracked and especially in the broken states demonstrate increasing transition-metal deficiencies. Notably, the metal content decreases dramatically in the cracked and pulverized particles, suggesting that transition-metal ions prefer to be released from the broken sites. The fractured particles reveal a larger specific surface area than the intact particles, which allowed a severe acid attack and more drastic dissolution of transition-metals. Ion chromatograms of the electrolytes after zero (red), two (blue), and 500 cycles (purple) in Figure 2.8c imply that metal dissolution can be detected even at the beginning of battery cycling. Note that the black line is the standard chromatogram of the uncycled NCM powder.^[26] The concentration of Ni ions in the electrolyte is much higher than Co and Mn, which further confirms the extreme instability of Ni at the surface.

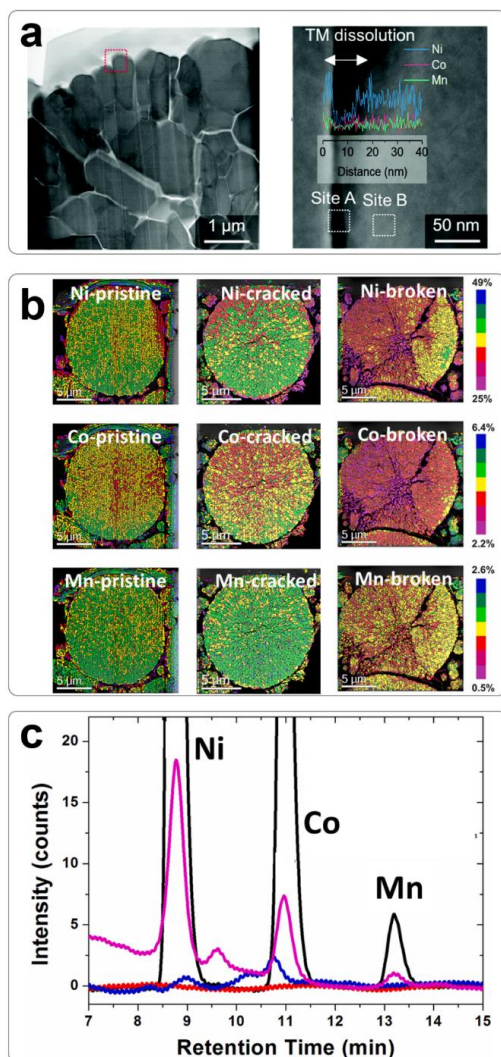


Figure 2.8 (a) HAADF-STEM image and line EDX of cycled NCM811.^[25] (b) Elemental mapping of Ni, Co, Mn in $\text{LiNi}_{0.87}\text{Co}_{0.09}\text{Mn}_{0.04}\text{O}_2$ particles at pristine, cracked, and broken states.^[26] (c) Ion chromatograms of the standard uncycled $\text{LiNi}_{0.87}\text{Co}_{0.09}\text{Mn}_{0.04}\text{O}_2$ cathode (black line) and the ion chromatograms of electrolytes obtained from the cells after zero (red line), two (blue line), and 500 (purple line) cycles.^[26]

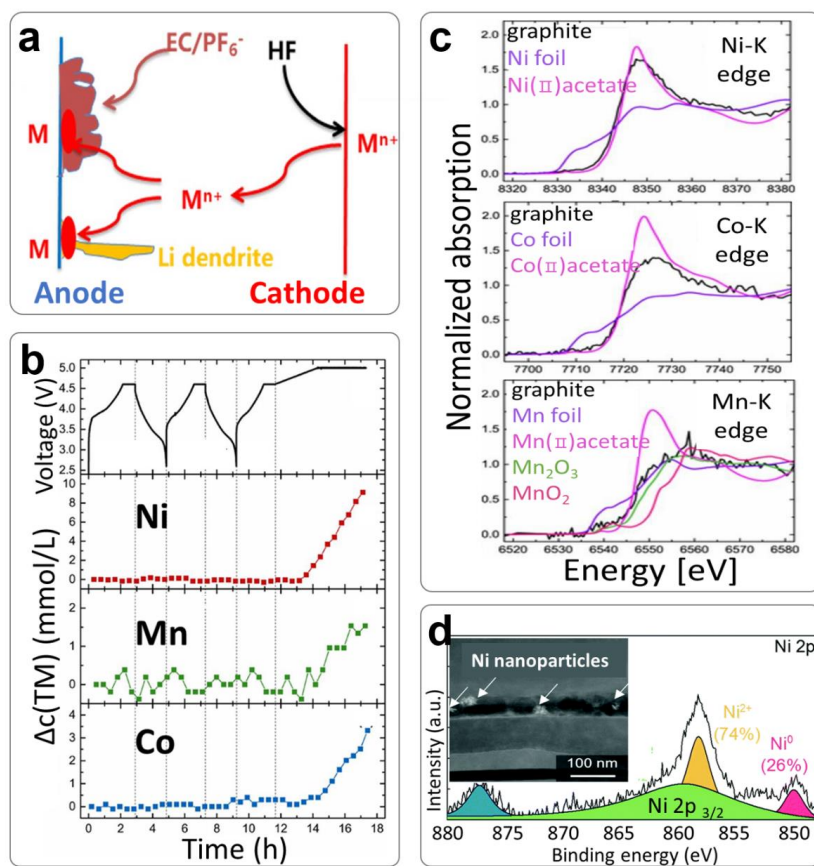


Figure 2.9 (a) Schematic of the dissolution and deposition of TM ions from the cathode.^[24] (b) Concentration changes of Ni, Mn, Co on the graphite anode with the cycling of NCM622/graphite cell.^[27] (c) XAS K-edge spectra of Ni, Co, Mn on the lithiated graphite anode.^[27] (d) XPS spectra and cross-section TEM image of graphite anode in cycled NCM811/graphite cell.^[25]

The negative impact of transition-metal dissolution is embodied both in the cathode and the anode side. As illustrated in Figure 2.9a, the dissolved metal ions can cross through the separator and deposit at the anode surface after a reduction during battery operation.^[24] Up to now, several studies have demonstrated that the deposited metal nanoparticles might participate in the SEI formation and serve as

catalysts for electrolyte reduction and lithium dendrite growth. Such side reactions will negatively influence the battery performance. Gasteiger *et al.* applied *in situ* X-ray absorption spectroscopy (XAS) measurements at NCM622-graphite cells to monitor the transition-metal deposition at the anode.^[27] The metal concentration evolutions at the graphite surface were recorded along with the charging and discharging process (Figure 2.9b). During the first two cycles up to 4.6 V, no significant increase of metal concentration can be detected at the graphite surface. That might be due to the detection limit of XAS measurements, considering that only a small amount of transition-metal ions will be made available in the electrolyte at the beginning of cycling. With the voltage ramping up to 4.8 V, the concentration of deposited metal on graphite elevates intensively. Subsequently, the K-edge spectra of Ni, Co, and Mn at the graphite surface reveal TM ions' elemental valence state (oxidation state) at the graphite surface, as shown in Figure 2.9c. Based on the analysis of the XAS spectra, Ni and Co K-edges match the edge position of the +2 oxidation state. In contrast, the edge position of Mn is located between +2 and +3 and is challenging to distinguish. Cho *et al.* employed XPS and TEM measurements on the cycled graphite surface to investigate Ni deposition at the anode side.^[25] The results reveal that Ni exists at graphite in the divalent and metallic states (Figure 2.9d). Interestingly, the metallic Ni nanoparticles can be observed to become part of the SEI film on the anode surface.

2.1.1.6 Intragranular and intergranular cracks

Mechanical failure of Ni-rich cathode particles, caused by the generation and development of cracks, has been widely considered a significant factor influencing battery degradation. The presence of particle cracks can be related to many reasons, such as lattice collapse, phase transformation, cation disorder, lattice oxygen loss, surface reconstruction, and heterogeneous lithiation/delithiation, *etc.*^[28] According to their positions, the cracks can be classified as intragranular or intergranular cracks, as illustrated in Figure 2.10a.^[29]

Intragranular cracks are commonly induced by Ni-Li anti-site defects and lattice disorder, as well as Coulombic repulsion between ions. The lattice deficiencies in the pristine particles keep growing during extended cycling and eventually develop into nanoscale cracks. In contrast, mechanical failure in intergranular cracks is initiated from the inner central particle area and spreads towards the surface. The generation of such cracks is mostly caused by the random crystal orientation of particles, which leads to anisotropic volume changes during cycling.

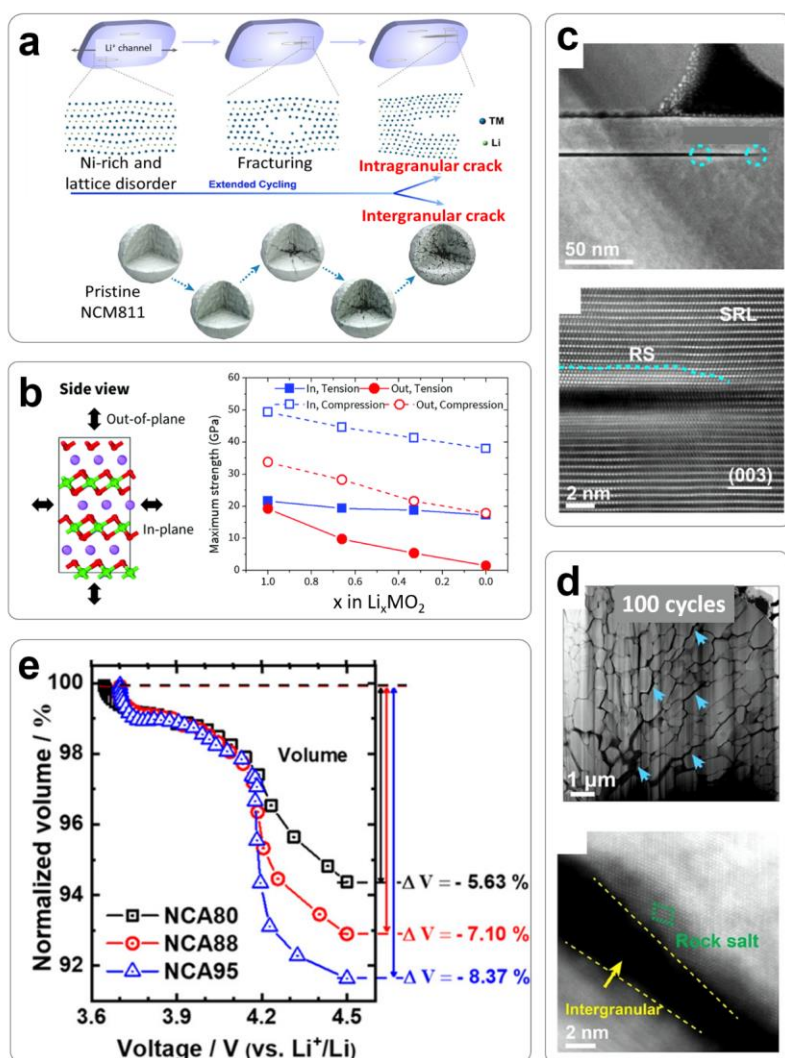


Figure 2.10 (a) Schematic representation of microstructural features of intragranular and intergranular cracks.^[29] (b) Illustration of the directions of tensile and compressive deformation and strength changes for NCM811 under the delithiation process.^[30] (c) STEM-HAADF images of an intragranular crack in cycled NMC811 (RS: rock-salt; SRL: structural reconstruction layer).^[29] (d) STEM-HAADF images of intergranular cracks in cycled NMC811.^[29] (e) Lattice parameter evolution of Ni-rich NCA electrodes during the first charging cycle.^[31]

Cho *et al.* performed first-principles calculations on NCM811 cathode material in the case of the formation of intragranular cracks and found an interesting mechanic anisotropy.^[30] Tensile and compressive stress calculations were performed to simulate the delithiation process in the layered structure. In-plane and out-of-plane mechanical deformations are initiated from two directions. Their results indicate that the maximum strength change in the material is not homogeneous. The out-of-plane stress is always weaker than those from the in-plane (Figure 2.10b). The subsequent accumulation of this strain unbalance during repeated lithiation and delithiation of the electrodes will lead to mechanical fatigue, finally resulting in intragranular cracks.

More detailed structural information about intragranular cracks can be obtained by atomic resolution techniques, such as shown in the HAADF-STEM images in Figure 2.10c.^[29] In the fracture region, a rock-salt phase has been found in the surface reconstruction layer located at the crack's edge. Such observation suggests that the cracks initiate and grow inside the rock-salt phase. Notably, with the increasing cycles, the length of the intragranular crack along the (003) plane can reach around 440 nm. Compared with intragranular cracks, intergranular cracks are more observable, especially for the intensively cycled particles. Figure 2.10d displays cross-section images of the particles obtained under various cycling conditions. After 200 cycles, large amounts of the anisotropic cracks are observed, demonstrating severe pulverization and mechanical failure of material particles. Besides, the structural reconstruction layer with the inactive rock-salt phase formed at the surface can also be detected at the edge of the intergranular crack. Such a reconstruction layer on the primary particle in the cracking area has an estimated thickness of around 30 nm.

The cracking phenomenon has been frequently discussed in the literature and represents a combined effect of intra- and intergranular cracking.^[32] The degree of cracking becomes considerable with higher Ni-content, increasing cycling number, and higher SOC. Sun *et al.* studied the cracking evolution of Ni-

rich NCMs with various Ni-content.^[33] They identified significant anisotropic shrinkage that occurs during the delithiation process in the compounds with a Ni-ratio above 0.8. Thus, high Ni content facilitates cracking in the particles and leads to the formation of many pores for electrolyte penetration. Consequently, all Ni-rich NCMs show increasing resistances as the function of cycling number in impedance measurements. The surface of exposed cracks is inactive rock-salt phase (Figure 2.10d), thus resulting in the slack kinetics. Compounds with higher Ni-content demonstrate higher overall resistances and higher rate of charge-transfer resistance increase during cycling.

The formation of intergranular cracks is also more prone to occur under inhomogeneous delithiation. Several studies have recently shown that lithium concentration in the primary particle is spatially inhomogeneous during cycling, especially at high C-rate conditions.^[34-36] The lithium-content inhomogeneity inside the particle leads to the coexistence of H2 and H3 phases, causing nonuniform stress and inducing lattice parameter changes and structural defects. In addition, a higher degree of delithiation can also give rise to accelerated cracks formation. When the material is highly delithiated, the H2-H3 phase transition occurs accompanied by severe lattice collapse along the c-direction, ultimately leading to unit volume shrinkage, as shown in Figure 2.10e.^[31] Consequently, cracks gradually propagate within the secondary particles, resulting in mechanical failure, local resistance increases, and capacity fading.

2.1.1.7 Thermal stability

Thermal stability is an important factor for the commercialization of Ni-rich cathode-based batteries. During battery operation, considerable heat will be generated in the system, initiating the risk of thermal runaway or even explosion under extreme circumstances.^[37] Numerous studies have proven that thermodynamic instability can develop at higher temperatures, also under storage conditions without cycling.^[38] As shown in Figure 2.11a, a capacity decay upon

storage is strongly temperature-dependent. In post-mortem analysis, it is noted that storage at high temperatures leads to a loss of electric contact between the electrodes and current collectors. It is concluded that high-temperature storage could give rise to more considerable capacity losses, escalated resistance, and even adhesive problems in pristine uncycled batteries.

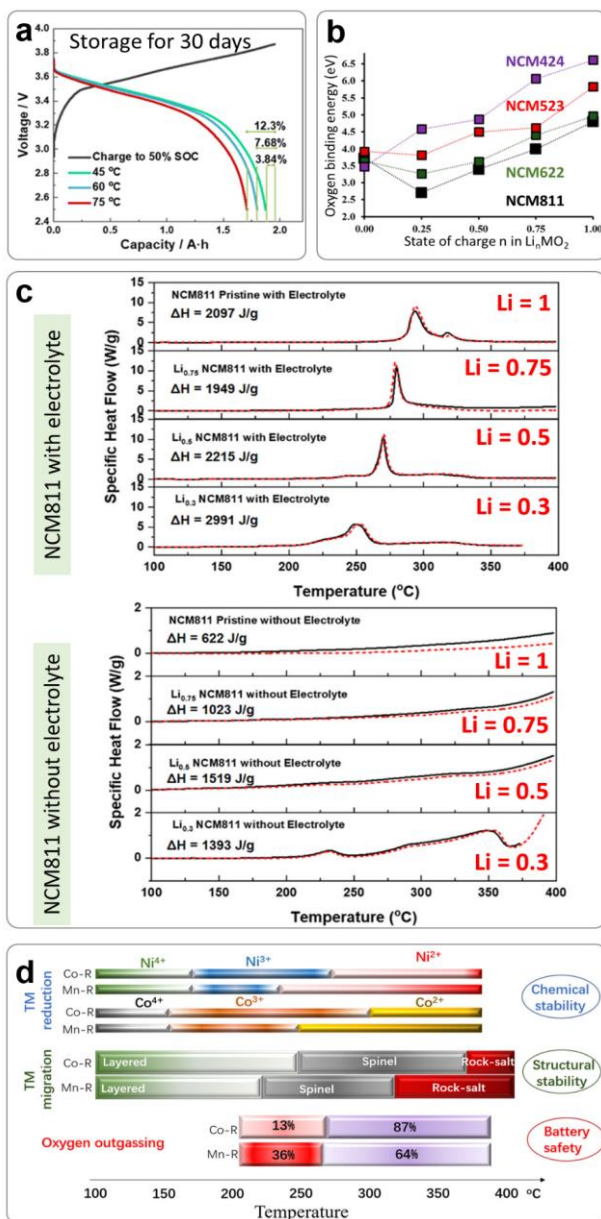


Figure 2.11 (a) Charge (before storage) and discharge (after storage for 30 days) voltage curves of 21700-type batteries at different temperatures.^[38] (b) Molecular oxygen binding energies for different NCMs as a function of SOC.^[39] (c) Specific

heat flow of an NMC811 electrode with and without the presence of an electrolyte.^[40]
(d) Illustration of chemical and structural stability during thermal degradation of a deep delithiated Ni-rich cathode.^[41]

The thermal instability of the Ni-rich cathode has also been attributed to the lower strength of M-O bonds in the delithiated state. Figure 2.11b shows the oxygen binding energy as a function of Li-content in various NCMs, indicating the strength of M-O bonds.^[39] It can be seen that the oxygen binding energy decreases with increasing Ni-content in NCMs and Li-deintercalation. Thus, oxygen is released under a highly delithiation state, leading to an exothermic reaction of Ni ions, reduced from a higher valence state. Recently, Yoon *et al.* proposed that the thermal expansion and oxygen vacancies are two new factors affecting the thermal stability of Ni-rich cathodes.^[42] X-ray absorption near edge structure (XANES) analysis of charged Ni-rich NCMs reveals that the most dramatic reduction of Ni⁴⁺ occurs in the materials at high temperatures. The reduction of Ni ions is accompanied by the formation of oxygen vacancies. Additionally, charged Ni-rich cathodes undergo a sizeable thermal expansion due to the lattice change. Both factors provide energetically favorable pathways for cation migration, accelerate thermal decomposition reactions, and finally lead to the thermal instability of Ni-rich cathodes.

The reactions between the active electrode material and electrolyte have also been investigated. The degree of heat-releasing of the electrode depends on the enthalpy of formation (ΔH). Figure 2.11c shows the heat generation of NCM811 cathodes filled with and without electrolytes at various delithiation states.^[40] Strong delithiation at low Li-content results in a shift of the onset exothermic peak towards lower temperatures. In comparison, the samples without electrolyte contact show only minor heat evolution in all cases. Additionally, the gas releasing process is also facilitated by the higher delithiation states of the NCM811 cathode in the electrolyte. This observation indicates that a high SOC in the presence of the electrolyte makes Ni-rich materials more susceptible to

thermal shock and produce more heat and gas during battery operation. This fact represents a serious safety hazard to LIBs.

Mn has been widely considered as a stabilizer for the NMC structure.^[43] However, Amine *et al.* recently demonstrated that the thermal stability of deeply delithiated Ni-rich NCMs might be dominated by Co.^[41] Based on their results, the presence of unstable Ni²⁺ and the onset point of phase transition in Mn-rich cathode occurs at a lower temperature compared with those of Co-rich cathode materials. Moreover, as illustrated in Figure 2.11d, Co-rich (Co-R) and Mn-rich (Mn-R) NCMs possess similar onset temperatures of two oxygen outgassing periods (red bar: first period, purple bar: second period), while Mn-R cathode outgasses 36% of its total oxygen in the first period, compared to the lower proportion for the Co-R cathode (13%). The earlier gas release brings a greater risk of thermal runaway, as the formed oxygen is highly reactive with electrolyte and lithiated anode. Thus, the Co/Mn concentration in Ni-rich cathodes has a considerable impact on battery safety. Extensive investigation of Ni-rich batteries with enhanced thermal stability is therefore of the highest priority.

2.1.2 Anode

2.1.2.1 Graphite anode

Graphite is an intercalation anode material widely applied in almost all commercial LIBs over the last two decades due to high specific capacity with a theoretical limit of 372 mAh g⁻¹, low costs, and low working potential between 50 to 250 mV vs. Li⁺/Li.^[44] The degradation of graphite anodes primarily results from three major causes. (1) Irreversible volume expansion and crack formation during cycling. Studies show the graphite-based cells can expand by 2-5% over their lifetime.^[37] (2) SEI formation induced by electrolyte decomposition and reduction of transition-metal cations dissolved from the cathode. (3) Li plating and dendrite growth.^[45-47]

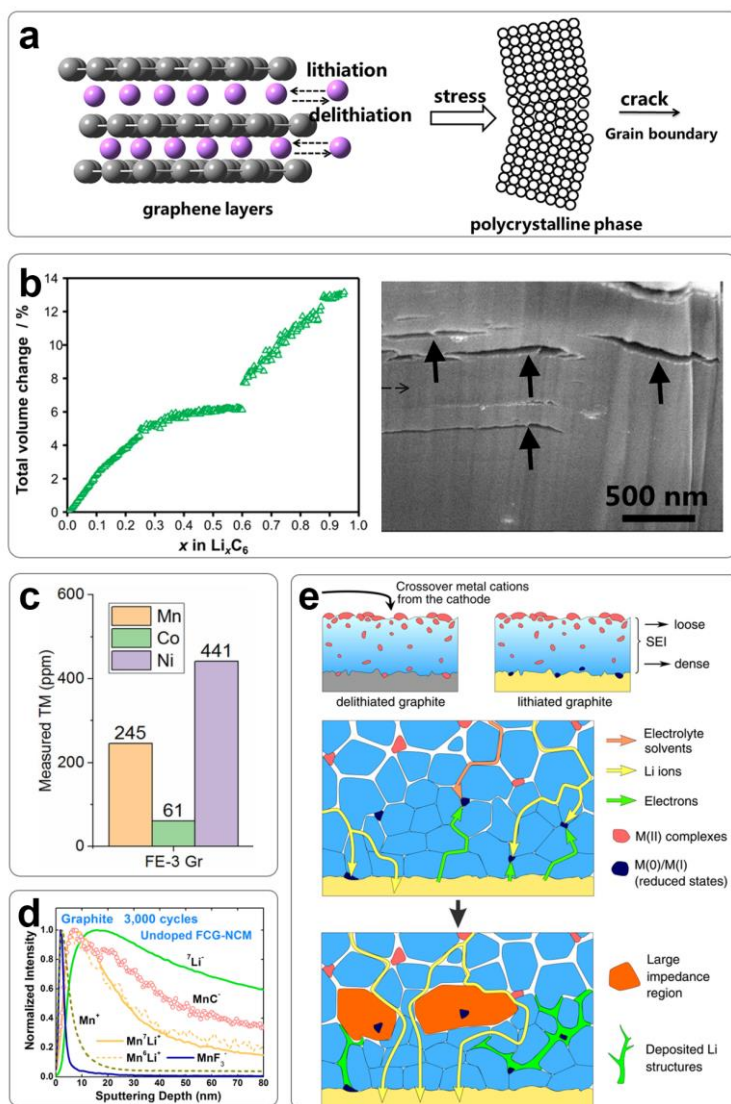


Figure 2.12 (a) Crack formation of graphite particles induced by cycling.^[48] (b) Volume change of a graphite electrode as a function of lithium content during lithiation and SEM image of cracks.^[49] (c) TM content obtained in a graphite anode after 120 cycles.^[50] (d) TOF-SIMS depth profiles of graphite anode after 3000 cycles.^[51] (e) Schematic representation of SEI film evolution at a graphite electrode during cycling under the influence of chemical crossover from the cathode.^[51]

Figure 2.12a shows that cracks in polycrystalline graphite originate from the stress along the grain boundaries during the Li-ion intercalation and deintercalation.^[48] Consequently, the propagated cracks result in an irreversible volume expansion of the graphite anode. Another study concluded that the total volume change of graphite unit cells could increase by 13.2% at the complete lithiation state (Figure 2.12b).^[49] The relationship between the unit cell volume change and lithium stoichiometric number shows two distinctive stages: the volume is increased by 6.1% at stage 1 ($0 \leq x(\text{Li}) \leq 0.50$) and by 13.2% at stage 2 ($0.50 \leq x(\text{Li}) \leq 0.95$). Notably, the volume change remains almost constant within the $0.25 \leq x(\text{Li}) \leq 0.50$ region. This behavior is attributed to the dominant intercalation mechanism, as Li accumulates in interlayers instead of occupying newly formed interlayers in the unit cell. These results demonstrate that occupation of only half of the intercalation sites can already lead to a significant crystallographic expansion of graphite. Figure 2.12b also shows an SEM image of cycled graphite, clearly revealing the formation of the parallel cracks inside the particles.^[48]

Dissolution of Ni from the surface of Ni-rich cathode with subsequent precipitation on the anode side creates unfavorable chemical crossover, causing intensive SEI formation and non-uniform Li insertion, leading to a decline in battery performance. Inductively coupled plasma mass spectroscopy (ICP-MS) analysis for cycled graphite in Figure 2.12c reveals a considerable amount of transition-metal deposited at the anode, especially Ni and Mn, attributed to the transition-metal ions dissolved from the Ni-rich cathode during cycling.^[50] Additionally, time-of-flight secondary-ion mass-spectrometry (TOF-SIMS) depth profiles of the cycled graphite confirm the migration of transition-metal ions.^[51] As shown in Figure 2.12d, a substantial amount of Mn ions (denoted by MnC^- , Mn^7Li^+ , Mn^6Li^+ , and MnF_3^-) penetrates inside the SEI film. The deposited transition-metal components and the electrolyte decomposition products are believed to mask significant portions of graphite. That can increase the local

current density and accelerate Li deposition and SEI growth. An overview of the parasitic reactions occurring and the formation of the SEI layer at the graphite surface can be seen in Figure 2.12e.^[51] The crossover of metal cations from the cathode through the outer loose SEI layer at the graphite electrode is suppressed by the inner SEI layer at the graphite surface. The reduced transition-metal ions subsequently serve as transport sites for electrons, facilitating electron transfer. When the SEI film grows, electrolyte decomposition and transition-metal reduction lead to an accumulation of high-impedance regions, hindering Li⁺ ions transportation. Simultaneously, the metallic Li will deposit at the graphite surface. Furthermore, the deposited Li structures will continuously develop into mosses and dendrite morphologies under extreme conditions, such as intensive cycling, rapid charging, high/low-temperature operation, *etc.*^[52] Hence, immobilized Li due to SEI formation and Li deposition will consume active Li⁺ ions from the battery system and accounts, in this way, for severe battery degradation.

Cross-over effects in LIBs can also be induced by gas. Cui *et al.* reported that LiH induced exothermic reactions at the anode and that H₂ gas migration to the cathode are the primary triggers for thermal runaway of LiNi_{0.5}Co_{0.2}Mn_{0.3}O₂/graphite pouch cells.^[53] Phase formations at the anode and O₂ release from the cathode have been considered the only accelerating factors.

2.1.2.2 Li-metal anode

Studies focusing on Li-metal anodes have become more frequent in recent years. Li-metal has a remarkably high specific capacity (3860 mAh g⁻¹), the lowest redox potential (0 V vs. Li⁺/Li), and low density (0.59 g cm⁻³).^[54] With these promising parameters, Li-metal anode has become essential for the next-generation LIBs in the market. Coupled with a Ni-rich cathode, pouch cells will be capable of meeting the goal with a high energy density of up to 890 Wh l⁻¹.^[55] However, Li-metal batteries face several critical challenges due to unstable dendrite growth and large volume expansion.^[56] These shortcomings pose a

significant risk of internal short-circuits in LIBs, resulting in big safety concerns, restraining the commercialization of Li-metal anodes.^[57]

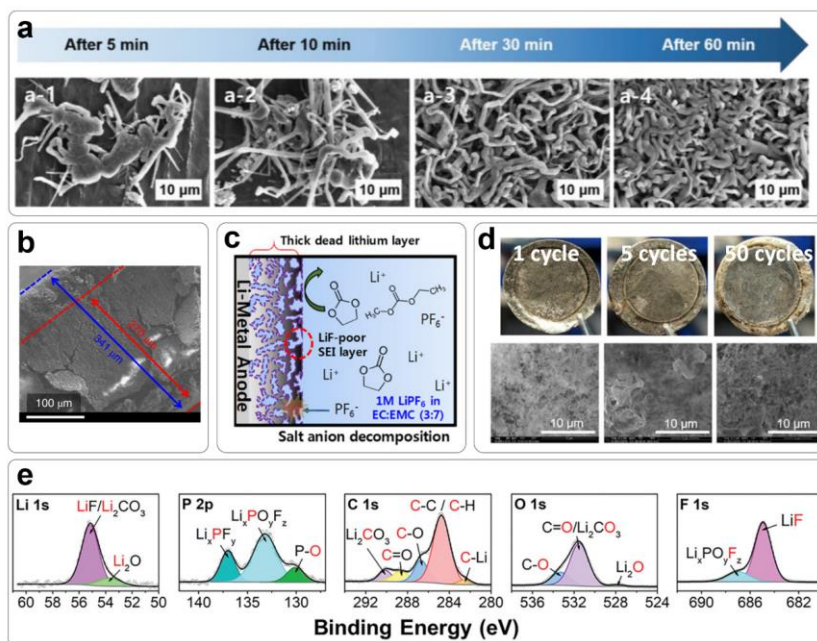


Figure 2.13 (a) SEM images of deposited Li on a Li-metal anode as a function of indicated deposit time.^[58] (b) SEM image of cycled Li-metal anode in 1 M LiPF₆ in a DMC/FEC (8:2) electrolyte.^[55] (c) Illustration of Li-metal anode degradation.^[59] (d) Optical and SEM images of cycled Li-metal anodes.^[60] (e) XPS spectra of a Li-metal anode after 50 cycles.^[60]

The electrodeposition of lithium on a Li-metal anode is a hazardous and rapid process. It has been confirmed that Li deposition is not homogeneous. Li will be deposited at primary nucleation sites into a Li-moss structure or needle-like microstructures. Figure 2.13a demonstrates the structural evolution of Li plating as the function of time at the current density of 1.8 mA cm⁻².^[58] It can be observed that Li is randomly deposited at the electrode surface already at the early stages (after 5 min) of charging and continuously aggregates into a porous

morphology with a loose structure. The high surface area of deposited Li is attributed to the enhanced electrolyte consumption and the accumulation of Li dendrite growth. After long-term cycling in the electrolyte (1 M LiPF₆ in EC/DMC), the thickness of the Li-metal electrode expanded dramatically. It increased from 250 μm for the pristine electrode up to 341 μm for the cycled electrode, as shown in the cross-section SEM image of Figure 2.13b.^[55] The red arrow reflects the highly porous and fragile Li layer, which shows poor resistance towards chemical degradation and suffers from side reactions between the electrolyte and Li-metal. Li dendrite growth and volume expansion of the Li-metal anode are illustrated in Figure 2.13c.^[59] The thick dead lithium layer is formed during combined electrolyte decomposition and Li plating/stripping cycling, which explains the low coulombic efficiency generally found for Li-metal anodes.

The crossover effect in batteries with a Ni-rich cathode and Li-metal anode (LiNi_{0.9}Mn_{0.05}Co_{0.05}O₂/Li) has been thoroughly investigated by Manthiram *et al.*^[60] Figure 2.13d shows optical and SEM images of cycled Li-metal anodes from disassembled cells. Gradually dark and rough surfaces with spatial inhomogeneities can clearly be observed with increasing cycle number, suggesting the formation of a brittle SEI film at the Li-metal anode. Further characterization of a cycled Li anode was performed by XPS to analyze the composition of the SEI layer, as shown in Figure 2.13e. The peaks can be assigned to the electrolyte decomposition products, including LiF, Li_xPF_y, Li_xPO_yF_z, Li₂O, ROCO₂Li, *etc.* In addition, the authors compared the cathode-electrolyte-interphase (CEI) formation in an NCM/Li cell with that in an NCM/graphite cell. They found that the decomposition products from anodes can be transported to the cathode side and eventually accelerate CEI formation and impedance growth at the cathode side also. Appropriate modifications should be applied to metallic Li-anodes to avoid the adverse effect of such a process on battery performance.

2.1.3 Electrolyte

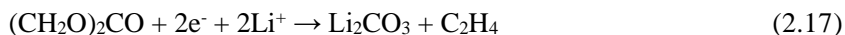
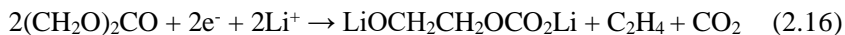
2.1.3.1 Decomposition

The electrolyte serves as an ionic bridge between the cathode and anode of batteries. The role of electrolytes in the performance and safety of LIBs is therefore immense. The electrolyte always consists of lithium salts and organic solvent(s). Both components are subject to side reactions. Figure 2.14a shows DFT molecular orbital calculations for PF₅ in solvents EC, DMC, DEC, which are the most conventional electrolyte components and have been widely used in the battery industry.^[61] PF₅ is the result of LiPF₆ decomposition. Owing to the relatively low LUMO energy, PF₅ is prone to gain electrons from other species in the electrolyte and initiate side reactions. The corresponding decomposition process of LiPF₆ has been described as follows^[62]



The decomposition process of solvents has been described by^[63-65]

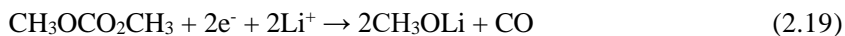
EC:



DEC:



DMC:



EMC:



PC:



The degradation of other electrolytes has also been intensively investigated, and various reaction pathways were proposed.^[67] The electrolyte decomposition has serious adverse effects on the battery performance, such as gas releasing and the consumption of Li^+ ions, leading to the loss of lithium inventory. Moreover, the decomposed products usually form passive layers at the electrode surface.

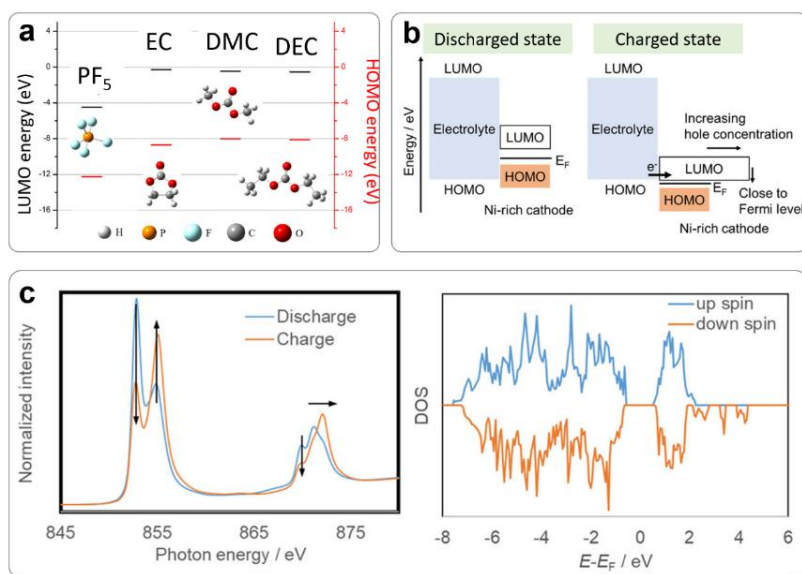


Figure 2.14 (a) DFT calculations of electrolyte components.^[61] (b) LUMO and HOMO energy levels of a Ni-rich cathode and electrolyte.^[66] (c) S-XAS spectra of Ni L-edge of a Ni-rich cathode and corresponding DOS at the fully charged (delithiated) state.^[66]

2.1.3.2 CEI formation

The electrolyte decomposition and CEI formation at the cathode are universal for all LIBs.^[68] Compared to other active materials, TM ions in Ni-rich cathodes have a lower LUMO energy level, accelerating electrolyte oxidation. During cycling, the CEI film is continuously growing through the reactions between the cathode and electrolyte. This process predominantly occurs during charging, particularly for the reduction of Ni⁴⁺, which attributes to the very low LUMO energy level of the antibonding orbital of e_g of Ni⁴⁺-O 2p in Ni-rich materials.^[66] According to previous DFT studies illustrated in Figure 2.14b, the Fermi level of NCM811 cathode materials approaches HOMO energy level of the electrolyte during charging. Thus, the hole concentration in the charged state increases dramatically, giving rise to electrolyte decomposition. In Figure 2.14c, the significant evolution of spectra can be detected in the Ni L-edge spectra measured in the charged and discharged states, suggesting a shift from Ni²⁺ - Ni³⁺ mixed-state to Ni⁴⁺ (peak located at 871.5 eV shifted to higher energy and intensity increased). The charged Ni⁴⁺ state has been confirmed to be highly nucleophilic to oxygen, which induces electrolyte oxidation. Additionally, DOS calculations of a discharged cathode show that an energy gap can be observed between the well-defined HOMO ($E-E_F < 0$ eV) and LUMO ($E-E_F > 0$ eV) energy levels. A high hole concentration (at $E-E_F = 0$ eV) is obtained for a fully charged NCM811 (Li₀Ni_{0.8}Co_{0.1}Mn_{0.1}O₂) electrode. That will induce electron transport from electrolyte molecules to the cathode, leading to electrolyte oxidation.

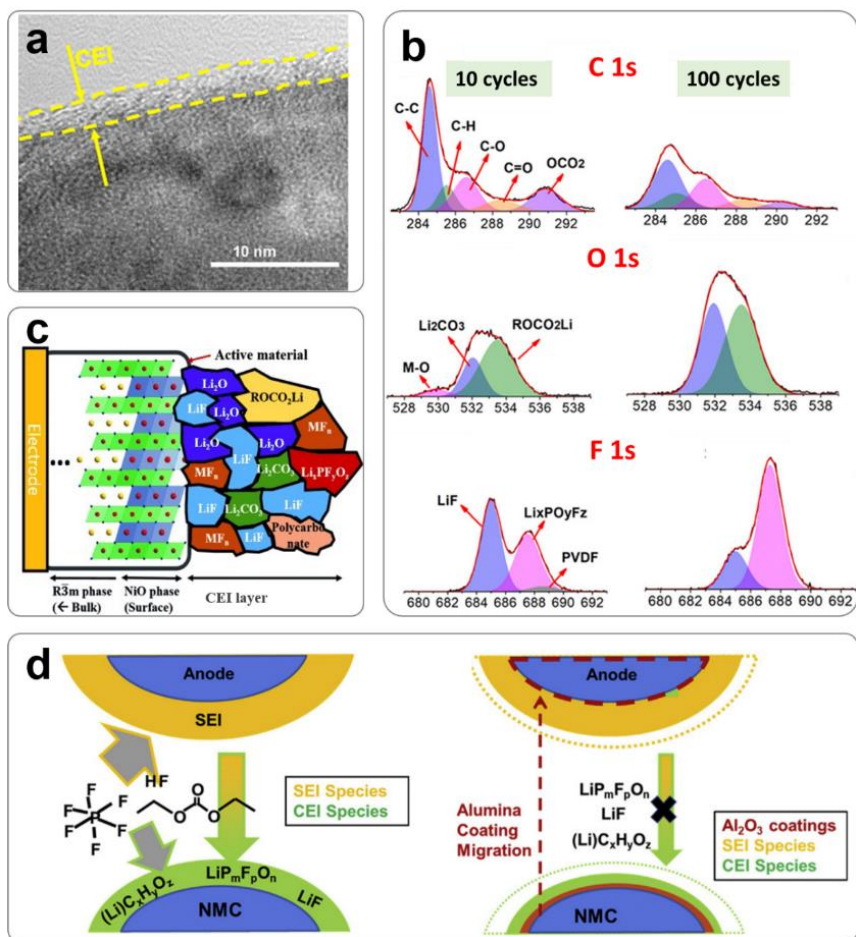


Figure 2.15 (a) SEM image of a CEI film on a cycled NCM811 electrode.^[69] (b) XPS spectra of NCM622 after 10 cycles and 100 cycles.^[61] (c) Illustration of CEI film formation on Ni-rich cathode surface.^[70] (d) Illustration of CEI formation via migration of SEI components.^[71]

Unlike SEI films on the anode surface, CEI films are extremely thin, making it difficult to make direct observations. A TEM image of a Ni-rich cathode surface after 10 cycles shows a CEI film thickness of approximately 3 nm (Figure 2.15a).^[69] The CEI film continuously grows during cycling and stabilizes at around 5 nm. The components of the CEI films have been investigated XPS, as

shown in Figure 2.15b^[61]. It has been concluded that the CEI film is composed of inorganic components, including metal fluorides (LiF, NiF, *etc.*), metal oxides (Li₂O, Li₂CO₃, *etc.*), and organic components such as ROCO₂Li and Li_xPO_yF_z. The inorganic components closely attach to the electrode surface and are considered as the “inner layer” of the CEI film, while the organic species are located at a larger distance from the electrode surface, defined as the outer CEI layer (Figure 2.15c).^[72] Both layers have relatively poor lithium-ion conductivities, resulting in increased local resistances and performance decay.

Moreover, a chemical crossover between cathode and anode has also been reported in the literature. Hamers *et al.* investigated the ionic migration in LiNi_{0.5}Co_{0.2}Mn_{0.3}O₂/graphite, LiNi_{0.5}Co_{0.2}Mn_{0.3}O₂/Li, and LiNi_{0.5}Co_{0.2}Mn_{0.3}O₂/Li₄Ti₅O₁₂ cells by quantitative XPS analysis.^[71] Their results show that the products of anodic decomposition can be detected in the CEI film at the cathode (Figure 2.15d). Subsequently, the migrated anodic species are reduced by the Al₂O₃ coating, protecting the cathode surface.

2.2 Improvement Strategies

Numerous efforts have been devoted to the performance improvement for Ni-rich cathode-based LIBs.^[73] The current strategies primarily focus on modifying the cathode, anode, and electrolyte. For cathode materials, the proposed strategies can be divided into the following categories: (1) Applying novel synthesis methods to avoid side-effects induced by conventional coprecipitation methods; (2) Fabricating single-crystallized primary particles in favor of mitigating inner stress during the (de)lithiation process; (3) Tailoring highly ordered morphologies to inhibit micro-cracks propagation within the electrode particles; (4) Introducing foreign ions (cations or anions) into the crystal lattice for structural stabilization of the host material; (5) Coating protective layers onto the cathode surface to prevent HF attack from the electrolyte; and (6) Synthesizing particles with elemental concentration gradient structure.

Concerning the anode modifications, structural changes and protective layer coatings are commonly employed for the graphite anode and Li-metal anode.^[74] Such strategies facilitate the stable mechanical properties of anode materials. Electrolyte decomposition and chemical crossover from the cathode can also be suppressed efficiently for the anodes. To optimize the electrolytes, many additives with various functional groups have been studied to restrain the decompositions of lithium salts and organic solvents in the electrolyte.^[75, 76] Some up-to-date and representative approaches for improving cathode, anode, and electrolyte in Ni-rich cathode-based LIBs will be discussed below.

2.2.1 Cathode

2.2.1.1 Novel synthesis methods

Coprecipitation combined with a solid-state reaction is the most mature and conventional method to prepare Ni-rich cathode materials. According to literature, the exact ratio between reactants and calcination parameters is essential for the quality of the final products.^[77] However, limited by the reaction conditions, such a procedure always results in intrinsic drawbacks, such as a considerable amount of RLCs at the powder surface, a high degree of cation disorder, and crystal defects inside the crystallographic structure. Appropriate water-washing or acid-washing processes can dramatically eliminate the side effects of RLCs.^[3] However, to fight cation disorder and crystallographic defects, more advanced synthesis methods have to be applied.

The high degree of cation disorder is attributed to the partial enrichment of Ni²⁺ at the cathode surface, inherited from Ni²⁺ in the transition-metal precursor during the coprecipitation process. One of the optimization procedures is based on the cathode pre-treatment via oxygen plasma and oxidants. Xie *et al.* reported an improvement in the cyclability of LiNi_{0.8}Co_{0.15}Al_{0.05}O₂ cathodes by a non-destructive plasma treatment, as demonstrated in Figure 2.16a.^[78] High-energy,

active groups (O , $\cdot OH$, O^3 , $O^{3\cdot}$) are obtained in the oxygen plasma, leading to $Ni^{2+} \rightarrow Ni^{3+}$ oxidation at the cathode surface. The formation of a NiOOH (nickeloxhydroxide) layer at the cathode surface has also been confirmed. The surface reconstruction layer is induced by lattice oxygen loss as presented in reactions (2.9) and (2.10) in Chapter 2.1.1.3. Thus, peroxidation of the cathode surface could reduce the following phase transformation in the synthesis. Hence, enhanced cycling stability and rate capability of Ni-rich cathode can be achieved.

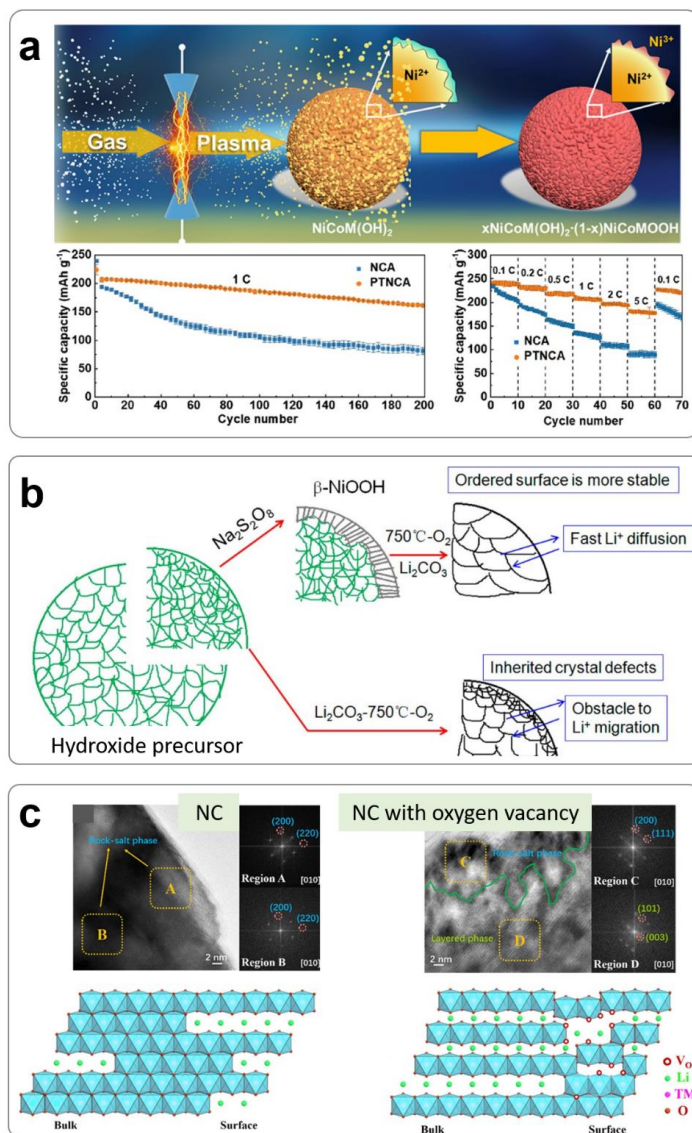


Figure 2.16 (a) Schematic representation of the plasma treatment process of NCA precursor and comparison of the electrochemical performance of pristine and plasma-treated NCA cathode.^[78] (b) Illustration of the reaction sequence of a $\text{Na}_2\text{S}_2\text{O}_8$ -treated NCA precursor.^[79] (c) HR-TEM images and structural model of $\text{LiNi}_{0.9}\text{Co}_{0.1}\text{O}_2$ (NC) and $\text{LiNi}_{0.9}\text{Co}_{0.1}\text{O}_2$ with oxygen vacancies (VO-NC-1) after cycling.^[80]

Another widely used surface-oxidation method based on wet chemistry is mixing oxidants, such as $\text{Na}_2\text{S}_2\text{O}_8$ and KMnO_4 , with the hydroxide precursor during synthesis.^[79] A representative study was carried out by Chen *et al.* with $\text{Na}_2\text{S}_2\text{O}_8$ peroxidization method (Figure 2.16b). Similarly, an ordered NiOOH layer is obtained after treatment, which guarantees the elimination of Li/Ni mixing and crystal defects at the cathode surface, eventually improving the cycling performance.

Apart from surface-oxidation, introducing oxygen vacancies at the cathode surface during the synthesis process is also a novel approach to avoid structural failure during cycling. Oxygen vacancies can serve as electron donors in the crystal host material. Massive oxygen vacancies are expected to form high-density dislocation layers at the grain surface. Wu *et al.* created oxygen vacancies by treating samples in an N_2 atmosphere.^[80] The obtained high-density dislocation layers originate from oxygen vacancies, preventing continuous propagation of intergranular cracks inside the particles during cycling. Figure 2.16c shows TEM analyses and crystal structures of untreated and treated cathodes after cycles. Restrained growth of the inactive rock-salt phase at the surface of the treated cathode can be clearly seen. In addition, approaches based on hydrothermal synthesis are also advantageous in forming Ni-rich cathode materials with enhanced structural stability and thus contributing to electrode performance improvement.^[81] Unfortunately, most of the proposed synthesis methods are quite complex for mass production, limiting their practical applications in large-scale battery production.

2.2.1.2 Single-crystal fabrication

The morphology of conventional Ni-rich cathodes has been described as a spherical secondary particle agglomerated with polycrystalline primary particles. The randomly aggregated primary particles result in strong grain boundary stress due to the anisotropy of Li-ion intercalation and deintercalation. In turn, the

increase of boundary stress will lead to the loss of electrical contact between primary particles and accelerated electrolyte attack. A direct strategy to reduce grain boundary stress is to fabricate single-crystal cathode particles.^[82] Advanced mechanical strength and more homogeneous electrochemical reactions can be achieved due to the high crystallinity and isotropy orientation of single-crystal cathode materials.

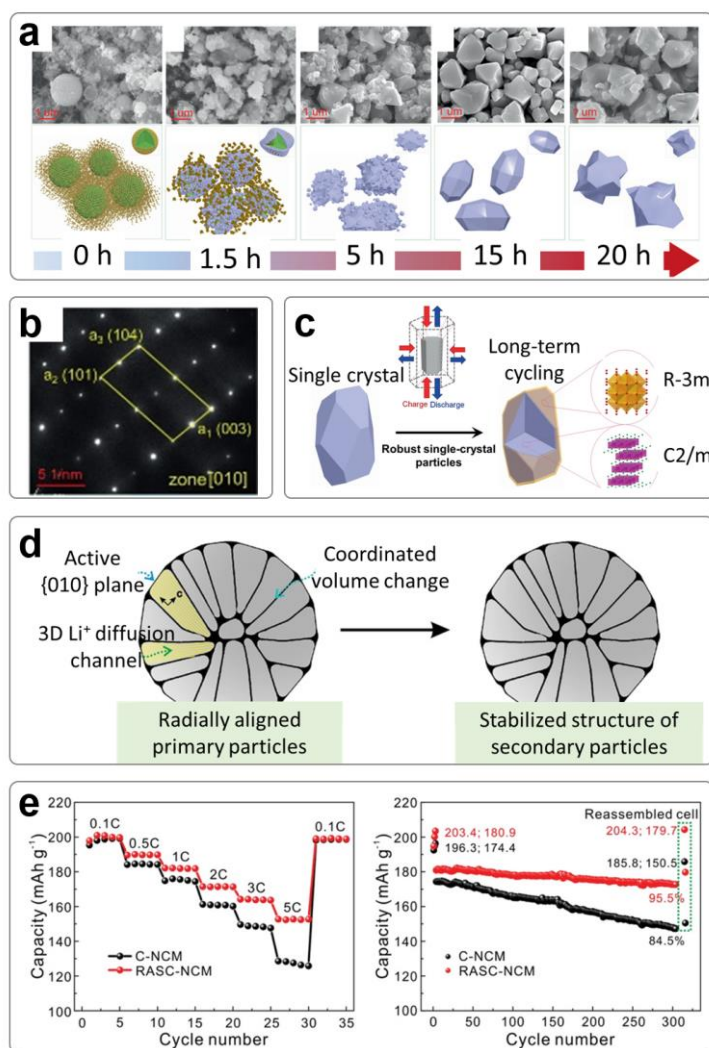


Figure 2.17 (a) Phase and morphological evolution during the sintering process of the single-crystal synthesis process.^[83] (b) SAED image of an as-prepared single-crystal NCA.^[83] (c) Schematic illustration of phase transformation in a single-crystal NCA particle upon cycling.^[83] (d) Schematic mechanism of the structural stability in a single-crystal NCM811 particle.^[84] (e) Performance comparison between commercial poly-crystal NCM 811 (C-NCM) and radially aligned single-crystal NCM811 (RASC-NCM).^[84]

One of the critical factors to produce single-crystal particles is the sintering temperature controlling the solid-state lithiation reactions. Wang *et al.* investigated the agglomeration degree of the final $\text{LiNi}_{0.8}\text{Co}_{0.15}\text{Al}_{0.05}\text{O}_2$ product with increasing sintering time, as shown in Figure 2.17a.^[83] Combining *in situ* XRD and *ex-situ* SEM measurements, the authors found that after 5 h sintering, single-crystal materials are formed with the most promising crystallinity. If the sintering time increases further, the grain size becomes much larger, suggesting a relatively high agglomeration. The diffraction spots in the selected area electron diffraction (SAED) image of a single-crystal particle are ideally aligned to the (104), (101), and (003) planes, confirming the well-defined hexagonal-layered crystal structure (Figure 2.17b). Compared with polycrystalline cathodes, single-crystal cathodes can adapt to volume changes, prevent intergranular microcracks, and shorten the Li-ion diffusion paths, ultimately improving the structural stability. However, the high dispersity of particles also facilitates the continuous growth of the surficial reconstruction layer (layered phase \rightarrow rock-salt phase), bringing a major challenge for this method. A surficial reconstruction layer is detected on the long-term cycled single-crystal cathode (Figure 2.17c).

Sun *et al.* proposed a smart modification based on a single-crystal NCM811 cathode to cope with the above disadvantageous.^[84] Single-crystal primary particles assemble into the secondary particles with radially aligned morphology, as illustrated in Figure 2.17d. Compatible lattice orientation exposing active crystal planes can provide open Li-ion diffusion channels from the surface to the center of these secondary particles. The compact aggregated primary particles with favorable crystal orientation can, on the one hand, mitigate intergranular stress by coordinated expansion/contraction. On the other hand, close contact between the primary particles prevents the growth of surface reconstruction layers. Only a minor surface reconstruction layer with 2-3 nm thickness can be observed at the cycled particles. Figure 2.17e shows that both the rate capability and cycle

stability are remarkably promoted in the single-crystal NCM811 cathode materials with compatible crystal orientation and facilitated Li⁺ diffusion.

It should be noted that although intergranular fractures can be avoided in single-crystal cathodes, the formation of intragranular fractures is still inevitable. That has also been considered as the primary degradation mechanism in single-crystal cathodes.^[85] However, unlike the uncontrolled growth of intragranular fractures in polycrystalline particles, the fracture along the (003) direction in single-crystal particles remains stable once it appears during cycling.^[86] The highly ordered orientation guarantees reversible planar gliding in the single-crystal lattice during cycling. Such self-limiting nature prevents continuous propagation of intragranular fracturing that eventually pulverizes the primary particles. The cycling performance is, therefore, significantly improved.

2.2.1.3 Microstructural modification

Another strategy related to structural optimization of Ni-rich cathodes is microstructural modification. Cathodes with specially designed heterostructures or unique morphologies have remarkably improved structural stability with respect to long-term cycling. Heterostructure cathodes are typically composed of two structurally partitioned regions, including a compact inner-core region and a more open outer-shell region with completely different structures.^[87]

As discussed in the previous section, conventional polycrystalline Ni-rich cathodes suffer from strong internal strain due to the anisotropic orientation. Thus, Ni-rich cathodes with a hierarchical structure could be a promising alternative. A pioneering work about hetero-structured Ni-rich cathodes was reported by Sun *et al.*^[88] They presented a multi-compositional NCM cathode material with polygonal shaped $\text{LiNi}_{0.94}\text{Co}_{0.038}\text{Mn}_{0.022}\text{O}_2$ in the particle core region, compactly surrounded by highly aligned $\text{LiNi}_{0.841}\text{Co}_{0.077}\text{Mn}_{0.082}\text{O}_2$ in the shell region. The outermost layer is smartly designed with a lower Ni-content to dissipate the

internal strain induced by the H2-to-H3 phase transition during delithiation. The core- and shell-particles, therefore, undergo an unsynchronized lattice change due to the various Ni-contents.

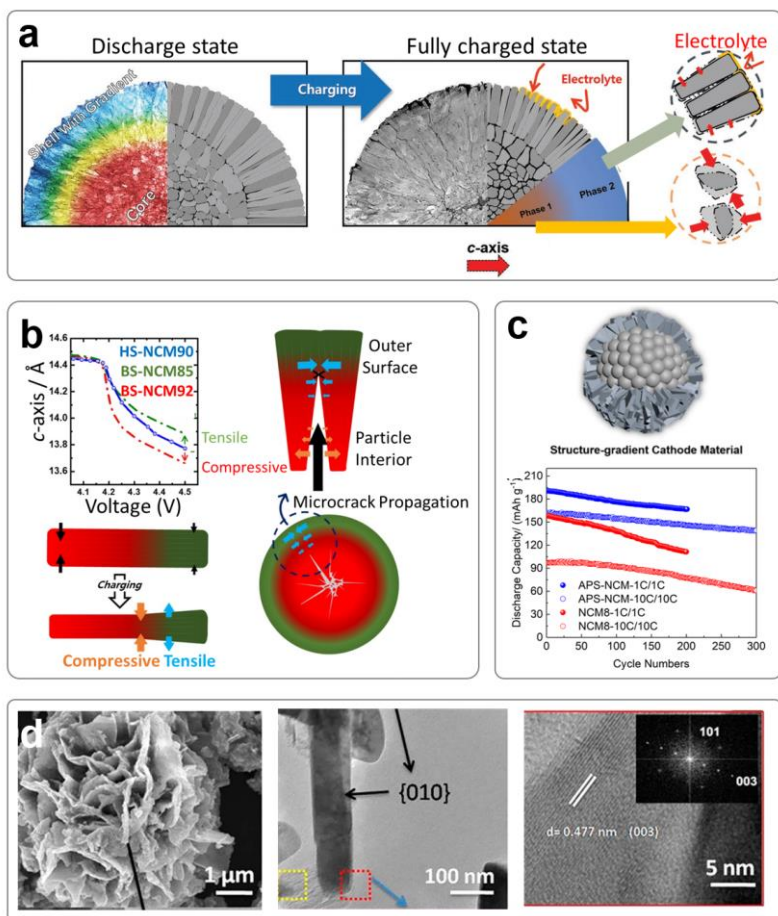


Figure 2.18 (a) Schematic representation of the discharge and charge state of a structurally modified NCM core-shell particle.^[88] (b) Evolution of lattice parameters during the H2-to-H3 phase transition in three different NCM cathode materials, illustrating the microcrack-resisting mechanism of HS-NCMA90.^[87] (c) Layout and electrochemical performance of active-plane exposing shell NCM811 (APS-NCM).^[89] (d) SEM and TEM images of NCM622 with hierarchical morphology.^[90]

As demonstrated in Figure 2.18a, the elongated primary particles in the outside layer are aligned along the a-direction and remain parallel to the radial direction, enabling the volume of the particles to change in the radial direction. As a result, the micro-scaled radial structure relieves the anisotropic strain. It constrains micro-crack propagation, enabling highly improved electrochemical properties and structural stability. Subsequently, Sun's group explained why microstructurally engineered Ni-rich cathodes are so stable against the micro-cracks formation, as visualized in Figure 2.18b.^[87] They investigated three different Ni-rich cathodes: bulk-structured $\text{LiNi}_{0.92}\text{Co}_{0.04}\text{Mn}_{0.03}\text{Al}_{0.01}\text{O}_2$ with higher Ni-content (BS-NCM92), bulk-structured $\text{LiNi}_{0.845}\text{Co}_{0.067}\text{Mn}_{0.078}\text{Al}_{0.01}\text{O}_2$ with lower Ni-content (BS-NCM85), and a hybrid-structured cathode (HS-NCMA90) with an interior BS-NCM92 core encapsulated by an exterior BS-NCM85 shell. *In situ* XRD measurements indicate the changes of the c-axis lattice parameters for the three cathodes during the H2-to-H3 phase transition during voltage variation. The degree of lattice contraction clearly depends on the Ni-content. Therefore, the core crystallites experienced compressive force while the shell-particles experienced tensile force during the delithiation process. This tensile stress in the outside layer clamps the wall of the micro-cracks and prevents it from propagation towards the particle surface.

Another way of producing hetero-structured Ni-rich cathode materials has been reported by Wu *et al.*^[89] The obtained NCM811 particles are composed of compacted cores and nanosheet-stacked shells (Figure 2.18c). By properly controlling the synthesis process, the primary particles in the outer region dominantly expose active (010) crystallographic facets, creating favorable Li^+ -ion transportation pathways. Furthermore, the highly-ordered microstructure enables enhanced Li-ion diffusion, exhibits excellent stability and rate capability.

Microstructural modification towards Ni-rich cathodes also includes studies on fabricating particles with other unique morphologies.^[91] For example, Wang *et al.* presented a 3D flower-like hierarchical NCM622 cathode material by

making use of a self-assembling synthesis process, as exemplified in Figure 2.18d.^[90] TEM measurements confirm that the side-wall of the primary particle is the active (010) plane, contributing to the faster ionic transport kinetics.

The main target of this microstructural modification strategy is to form a cathode particle with a well-designed and controlled structure, which can be beneficial in suppressing the continuous growth of micro-cracks and, hence, achieving improved electrochemical electrode properties. However, similar to the strategy of single-crystalline materials, it is not possible to avoid intragranular fracturing caused by crystal lattice mismatches. Also, in some cases, the particles with novel morphology may lead to a higher degree of transition-metal ion dissolution and lower tap density because of a higher specific surface area.^[91]

2.2.1.4 Doping

Incorporating various foreign ions into host materials is a well-known and frequently used method in material optimization. Elemental doping, including cation doping and anion doping, has been proven to significantly boost Ni-rich cathodes' structural and thermal stability.^[92] Elemental doping can facilitate the performance of Ni-rich cathodes as it inhibits the irreversible phase transitions during delithiation, especially under high-voltage operation conditions. The electrochemically inactive nature of dopants can explain this behavior in the cathode crystal lattice, which provides strong chemical bonds. Therefore, electrode degradation related to cation disorder, oxygen gas evolution, and intergranular cracking in a Ni-rich cathode can be suppressed. Up to now, numerous substitutional elements have been proposed, such as Mg, Zr, Ce, Mo, Ta, *etc.* as cation dopant and F, Br, *etc.* as anion dopant.^[93-95]

Some cation dopants can act as “pillar ions” in the Ni-rich cathode crystal lattice to strengthen the bulk structure, as depicted in Figure 2.19a.^[96] Pre-formed nanoscale cation disorder units are found in Ce⁴⁺ doped-NCM811 particles.

Because of the stabilizing “pillar effect” and stronger Ce-O bonds, ion migration and NiO phase formation are effectively constrained in doped materials compared to undoped materials. Other cation dopants with higher valence states (Ti^{4+} , W^{6+}) also show similar functions by firmly clamping the active lattice oxygen and stabilizing the crystal structure.^[99] It is noteworthy to remind that careful control of the doping ratio is critical for the cathode modification. Disproportionate dopant ratios cannot further improve the stability of the cathode. On the contrary, the capacity will be compromised because of blocking the active sites in the crystal lattice.

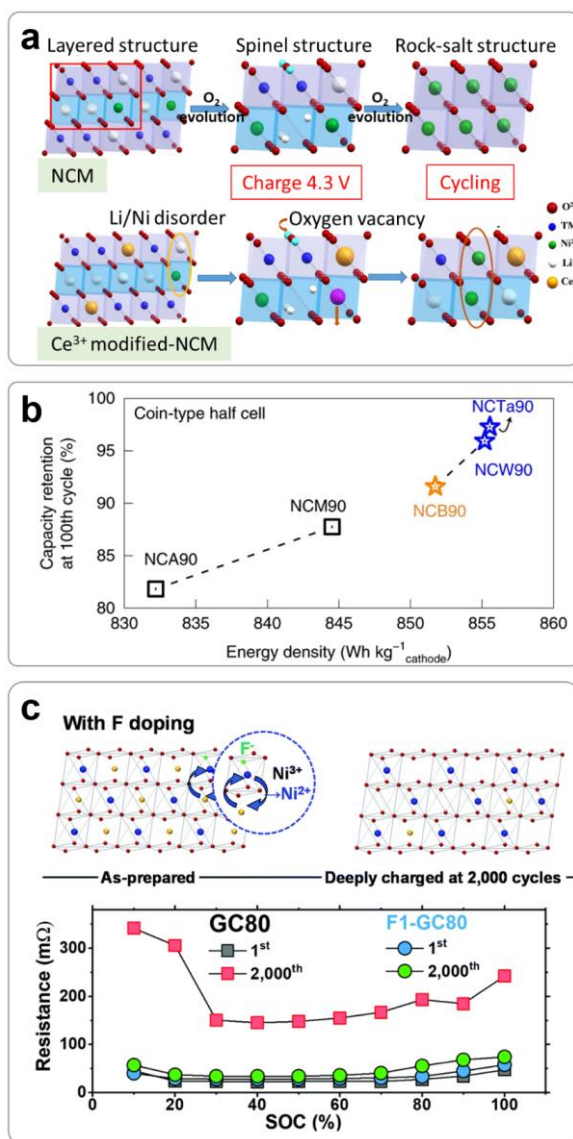


Figure 2.19 (a) Schematic illustration of suppressing intergranular cracks on Ce⁴⁺ doped-NCM811 particles and the phase transition mechanism.^[96] (b) Cathode-level energy density versus capacity retention for Ni-rich cathodes with different dopants.^[97] (c) Illustration of structural stability of F⁻ doped NCM and the evolution of resistance as a function of SOC after the first and 2000th cycles.^[98]

Conventional Ni-rich NCM and NCA materials originate from doping Co, Mn, and Al ions into the host lattice of LiNiO_2 to address structural instability. Another route for elemental doping is replacing the Mn and Al in Ni-rich NCMs and NCAs with other ions to form novel ternary cathodes. Sun *et al.* systematically studied five different substitutional cation dopants in $\text{LiNi}_{0.91}\text{Co}_{0.09}\text{O}_2$, including $\text{LiNi}_{0.90}\text{Co}_{0.05}\text{Mn}_{0.05}\text{O}_2$ (NCM90), $\text{LiNi}_{0.90}\text{Co}_{0.09}\text{Al}_{0.01}\text{O}_2$ (NCA90), $\text{LiNi}_{0.90}\text{Co}_{0.09}\text{W}_{0.01}\text{O}_2$ (NCW90), $\text{LiNi}_{0.895}\text{Co}_{0.09}\text{B}_{0.015}\text{O}_2$ (NCB90), and $\text{LiNi}_{0.90}\text{Co}_{0.09}\text{Ta}_{0.01}\text{O}_2$ (NCT90).^[97] NCT90 exhibits the highest stability among the different doped materials with capacity retention higher than 95% and energy density larger than 850 Wh kg^{-1} after 100 cycles (Figure 2.19b). The substitution of Ta enables the cathode to form a highly ordered structure when lithiation takes place at 730°C , demonstrating a decrease in inherent Li/Ni mixing compared with NCA90. Such cation ordering is also found in other cation doping cases. Furthermore, introducing foreign ions with larger ionic radii (Mo, Ta, Nb, *etc.*) increases the distance between the TM slabs, leading to the expansion of Li-ion diffusion channels and, consequently, improved electrochemical performance.

Anion doping is another kind of doping to stabilize the Ni-rich cathode structure by substituting O^{2-} with other anion dopants to form stronger chemical bonds with transition-metal ions. Among various choices, F^- doping is frequently adopted in many studies. It has been considered that the binding energy of the TM-F bond is higher than that of TM-O, which is attributed to the more electronegative value of F^- than O^{2-} .^[100] Most recently, Sun's group investigated the origin of the ultra-long cycle life of F^- -doped NCM cathode materials from an atomic point of view.^[98] This study reveals F^- -doped NCM materials will induce the formation of an ordered structure with $2a_{\text{hex}} * 2a_{\text{hex}} * c_{\text{hex}}$ superlattice. As shown in Figure 2.19c, Ni migration at the Li-sites occurs every two rows to form this superlattice structure. This ordered structure successfully survived 2000 cycles without revealing any lattice mismatches, which explains the long cycle life of the

F⁻-doped LiNi_{0.80}Co_{0.05}Mn_{0.15}O₂. This is accompanied by a minor evolution of the impedance after 2000 cycles.

In general, the elemental doping strategy appeared to be the most efficient method to solve this issue by constraining the growth of intragranular cracks in Ni-rich cathode materials. The introduced foreign ions can strengthen the crystal structure by directly forming stronger bonds with host ions and preventing the continuous propagation of lattice mismatches. However, as mentioned above, the optimal doping ratio needs to be used to achieve enhanced stability without compromising any intrinsic capacity since most of the dopants that have been proposed are electrochemically inactive.

2.2.1.5 Protective layer coatings

Although structural modification methods can mitigate defect formation in Ni-rich cathode materials, the degradation induced by surface side reactions, such as HF corrosion and CEI formation, remains unsolved. In response to these challenges, protective layer coatings emerged as the most sensible strategy to impede electrolyte decomposition and suppress the dissolution of transition-metal ions from the Ni-rich cathodes.^[101] Various coating techniques have been proposed, involving wet chemical coating, dry ball-milling, sputtering coating, chemical-vapor-deposition (CVD) coating, and atomic-layer-deposition (ALD) coating.^[102] Surface coating materials are also diverse and include metal oxides (Al₂O₃, TiO₂, MgO, *etc.*), metal fluorides (LiF, AlF₃, *etc.*), phosphates (MnPO₄, AlPO₄, Si₃(PO₄)₄, *etc.*), solid-state electrolytes (Li₃PO₄, LiNbO₃, Li₂ZrO₃, *etc.*), and conductive organic materials (polyimide, polyaniline, *etc.*).^[103-105]

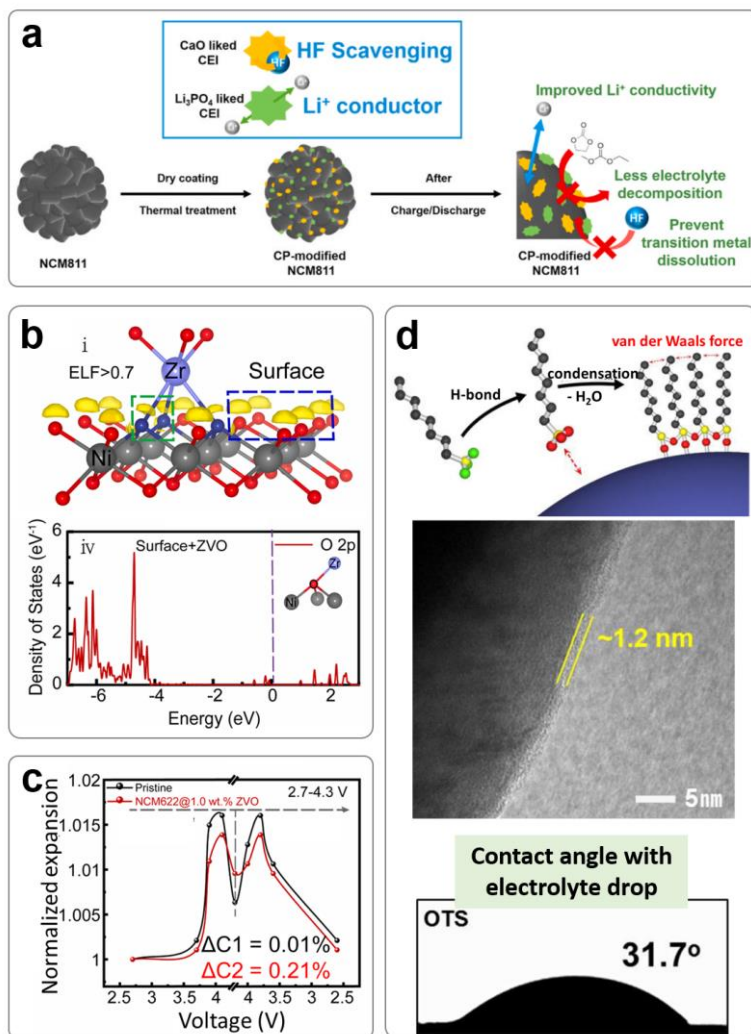


Figure 2.20 (a) Stability mechanism of surface-modified NCM811 cathode material.^[106] (b) Electron localization function (ELF) for the surface structure of LiNiO_2 with O-Ni-O termination reacted with ZrO_6 octahedron and DOS of O 2p orbitals of a Zr-modified NCM surface.^[107] (c) Crystal lattice parameter evolution as a function of the voltage for two NCM622 cathodes.^[107] (d) Illustration of the OTS coating process, SEM image, and contact angle result of OTS-coated NCM82.^[104]

Coating layers can be divided into non-conductive materials (metal oxides, fluorides, phosphates) with high stability and ionic conductive materials (solid-state electrolytes, conductive organic materials) with high Li-ion conductivity. As schematically shown in Figure 2.20a, Yim *et al.* fabricated a combined protective layer consisting of CaO and Li₃PO₄ at the NCM811 cathode surface via a dry coating technique.^[106] CaO was employed as HF scavenging material, preventing corrosion between the acid and cathode. Thus, the dissolution of TM ions by HF can be suppressed. ICP analyses of cycled Li-metal in modified NCM811 cells show a significantly smaller amount of TM components than that in unmodified NCM811. On the other hand, Li₃PO₄ provides favorable Li-ion transport pathways due to its high ionic conductivity. The combination of CaO and Li₃PO₄ shows the ability to alleviate electrolyte decomposition at the cathode surface, assuring the long-term cycling performance of protective-coated NCM811 cathodes.

Introducing negative thermal expansion (NTE) materials in electrodes is a novel design that emerged in recent studies. Such materials with extremely low expansion characteristics can be beneficial in stabilizing Ni-rich cathodes. Bai's group first applied a typical NTE material (ZrV₂O₇) to modify the surface of NCM622.^[107] The cycling performance of the cathode was improved sharply. It can be cycled up to 500 cycles with a capacity retention of 71.0%. DOS calculations of surficial O 2p orbits explain why the ZrV₂O₇ layer stabilizes the surface. By the influence of Zr, the DOSs of oxygen decreases below -4 eV and become inert, which has been attributed to Zr ions tailoring the local electron distribution around surficial oxygen (Figure 2.20b). In contrast, for an unmodified surface, the energy at 1.5 eV suggests labile oxygen existing at the surface, which is prone to react with the electrolyte. *In situ* XRD measurements further reveal a change of the lattice volume expansion upon (de)lithiation for ZrV₂O₇-coated NCM622 is only half of that of pristine NCM622, as shown in Figure 2.20c. The mechanism of surface stabilization presented above can help to understand the

functions of various electrochemically inert protective layers proposed in other studies.

Numerous organic materials have also been investigated to suppress electrolyte decomposition at the cathode electrode surface.^[73] Park *et al.* developed an OTS-coated (octyltrichlorosilane) $\text{LiNi}_{0.82}\text{Mn}_{0.09}\text{Co}_{0.09}\text{O}_2$ (NCM82) cathode with higher storage cyclability.^[104] The OTS molecules homogeneously self-assembled via van der Waals forces into a monolayer on the NCM82 surface, as depicted in Figure 2.20d. A uniform monolayer with a thickness of 1.2 nm has been observed by TEM. The modified surface reveals electrolyte-phobic characteristics, exhibiting a significantly larger contact angle of 31.7° with an electrolyte drop compared to a contact angle of 3.3° for a pristine cathode. The electrolyte-phobic surface increases the initial charge-transfer resistance (R_{ct}). However, after 70 cycles, OTS-NCM82 displays a smaller R_{ct} than the pristine NCM82, and its cyclability is also improved.

One major drawback of the protective layer coating strategy is that introducing a new interface will inevitably increase surface resistance and disturb ionic transport. Therefore, the layer thickness must be appropriately controlled, not hindering ionic transport through the surface.

2.2.1.6 Concentration gradient

Concentration gradient control is also an interesting strategy to improve the stability of the Ni-rich cathodes by attempting to increase the storage capacity simultaneously. Similar to the case of microstructural manipulation, a core-shell structure has been employed for this strategy. The Ni-rich component located in the central part of the cathode particles is expected to increase the capacity. In contrast, the Ni-deficient component located at the surface is expected to stabilize the particle structure during cycling.^[108] Based on this concept, three different configurations have been proposed so far, including core-shell concentration

gradients (CS), full concentration gradients (FCG), and two-slopes full concentration gradients (TSFCG).^[109] Figure 2.21a illustrates an NCM811 particle with a typical core-shell concentration gradient structure.^[110] Notably, the Ni concentration gradient is accompanied here by different phases. The Ni-deficient outer shell and Ni-rich inner core exist as spinel and layered phase, respectively. Between the two well-defined phases, a thin transitional layer can be observed. The tightly integrated structure with smooth phase transition enhances the binding between the bulk and surface in the particles.

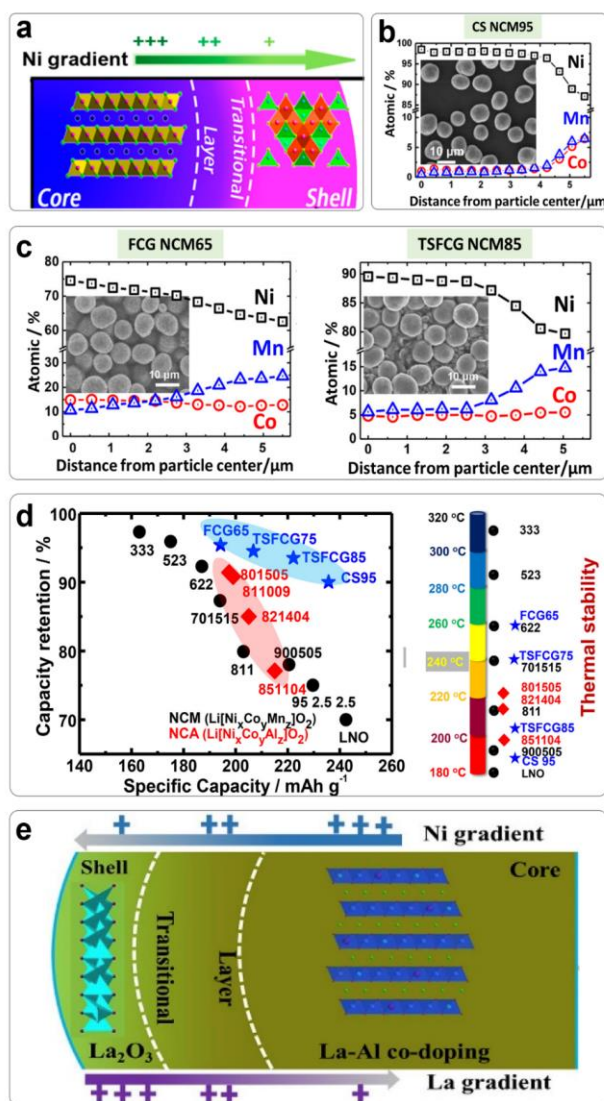


Figure 2.21 (a) Illustration of a concentration gradient particle.^[110] (b) Concentration gradient of various TM-contents in CS NCM95.^[111] (c) Concentration gradient of various TM in FCG NCM65 and TSFCG NCM85.^[109] (d) Specific capacity vs. cycling stability of various layered cathodes, including gradient-type NCMs and conventional NCAs and NCMs.^[109] (e) Illustration of a concentration gradient particle combined with surface coating.^[112]

Figure 2.21b presents an EDX line spectra of the cross-section of an NCM811@LiNiO₂ (CS NCM95) particle.^[111] It can be seen that for such CS particles, a distinct drop of Ni atomic ratio is found in the transitional region. The composition profiles of the cross-section of FCG NCM65 and TSFCG NCM85 primary particles are shown in Figure 2.21c. For both FCG and TSFCG particles, the Ni concentration gradually changes and does not show a noticeable drop in Ni concentration. Well visible concentration gradients of TM can be seen within the particles. FCG NCM65 demonstrates two linear concentration profiles. The concentration of Ni gradually declines from the core to the surface. In contrast, the concentration of Mn increases, and the concentration of Co remains stable. In contrast, for TSFCG NCM85 particles, the Ni and Mn concentration profiles show two linear regions with different slopes. The Ni concentration declines slowly at the core, and then the declining slope becomes larger near the surface. This design can maximize the Ni concentration at the core for a higher capacity delivery and maximize the Mn concentration near the surface for a more robust outer structure. Such a remarkable concentration profile was recently obtained by Sun *et al.* to strike a balance between the high capacity retention of FCG NCM65 and the high specific capacity of CS NCM95.^[109] Figure 2.21d presents a summary of the electrochemical and thermal stability of conventional and concentration-gradient-prepared cathodes. CS, FCG, and TSFCG-cathodes combine an overall superior capacity and electrode stability compared to their conventional counterparts with constant Ni-content. Especially among the three types of concentration-gradient cathodes, TSFCG-cathodes achieve a relatively high specific capacity without compromising cyclability and thermal stability.

Finally, concentration-gradient strategies combined with cation doping can also create modified epitaxial layers at the electrode particle surface. Incorporating electrochemically inert cations in the concentration gradient during the cathode synthesis process will lead to ultrathin coatings, enabling the cathode to resist electrolyte erosion by HF and H₂O. To date, La, Al, and B-modified

concentration-gradient cathodes have been reported.^[110, 113] A cathode material with a La and Ni gradient structure is depicted in Figure 2.21e. La-ion enrichment at the surface formed a layered olivine La_2O_3 structure, stabilizing the whole particle structure.^[112] However, despite the achievements described above, concentration-gradient strategies have limitations because electrode degradation induced by lattice mismatches and cation disorder cannot be avoided.

2.2.2 Anode

2.2.2.1 Graphite anode

The main strategies for achieving a favorable performance of graphite anodes are chemical treatment and coating. Chemical treatment aims to obtain an optimized graphite structure with expanded layer space. A major shortcoming of graphite is its narrow interlayer space of 0.335 nm, which restricts the number of Li^+ ions transported in the graphite interlayers and leads to exfoliation.^[114] A commonly used method for expanding the graphite interlayer distance is treating conventional graphite with acid or base solutions.^[115] As illustrated in Figure 2.22a, strong acid oxidation and base etching can convert pristine graphite into expanded graphite with porous voids. The higher specific surface area of the expanded graphite provides more active sites and facilitates the movement of Li^+ ions during the (de)intercalation process.

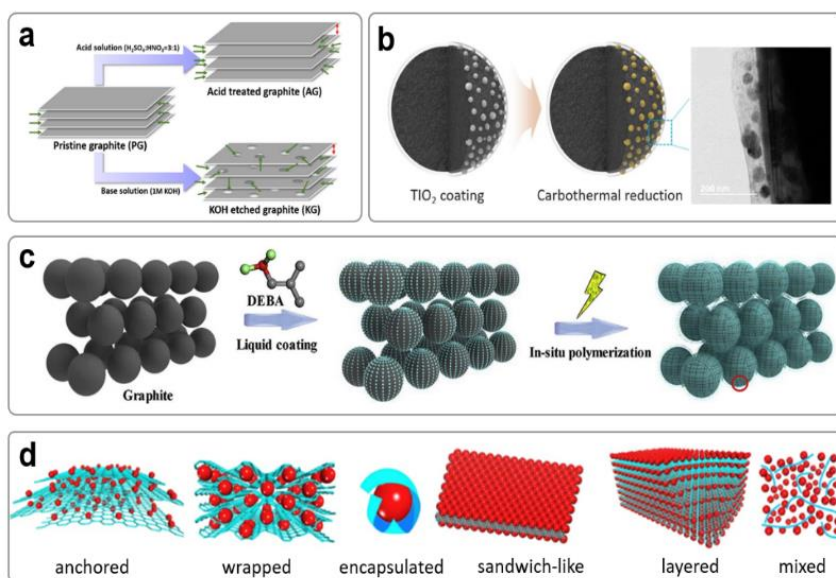


Figure 2.22 (a) Schematic illustration of the preparation of acid-treated graphite and KOH-etched graphite.^[115] (b) Illustration and TEM image of a TiO₂-coated graphite particle.^[116] (c) Schematic illustration of the preparation of DEBA-treated graphite.^[117] (d) Models of various graphene/metal oxide compositions.^[118]

Apart from the strategy of surface treatment without introducing foreign materials, coating graphite with a functional layer is a promising approach to mitigate the degradation of graphite anodes. Especially, the formation of the SEI layer can be reduced through the synergy between graphite and coating material. Metal oxides and polymers are popular components that have been widely used as coating materials for graphite anodes. For example, Park *et al.* plated TiO₂ nanoparticles at the surface of commercial graphite (Figure 2.22b).^[116] Their results demonstrate that SEI formation is suppressed at TiO₂-coated graphite, while the electrochemical performance and thermal stability are improved.

Though metal-oxide coatings have shown the ability to restrain the SEI layer growth, inorganic coating materials impose rigid structures. They are

incompatible with SEI components that mainly consist of organic species. Applying an organic artificial SEI layer as graphite coating is a smart strategy to form a continuous and more homogeneous artificial SEI layer before cycling. A robust and flexible artificial SEI layer composed of organic materials could subsequently guide a uniform SEI growth via chemical bonds and functional groups.

As indicated in Figure 2.22c, Zheng *et al.* synthesized a graphite anode with enhanced cycling stability by applying a functional 2,2-Dimethylethenylboronic acid (DEBA) layer as an SEI precursor at the graphite surface.^[117] *In situ* polymerization treatment produced a robust and flexible polymeric skeleton at the surface to control SEI formation. Strong chemical bonds are established between -COOH/-OH at graphite and the B-OH groups in DEBA, contributing to the enhanced mechanical strength of graphite anodes. Moreover, active intermediate species from electrolyte decomposition, such as PF_6^- , can be captured by electron-deficient B ions in DEBA.

A crucial improvement of graphite-based anodes emerged after graphene was discovered.^[119] Graphene is a novel product and was acquired from the micro(nano)layer-exfoliation of graphite. Some bottleneck problems in conventional graphite anodes, such as capacity, mechanical failures, and poor stability, are overcome in graphene-based anodes. However, due to the high cost and difficult extraction mechanism of graphene sheets, graphene-based materials have always been applied together with metal-oxide particles. Graphene sheets serve as a skeleton with a large specific surface area and high electronic conductivity.^[119] The various types of graphene/metal-oxides compositions have been comprehensively reviewed by Wu *et al.*, as summarized in Figure 2.22d, including anchored, wrapped, encapsulated, sandwiched, layered, and mixed models.^[118]

2.2.2.2 *Li-metal anode*

To meet expectations in the commercialization of Li metal anodes, three major challenges have to be overcome: (1) Nonuniform Li deposition, which accelerates the detrimental Li dendrite growth; (2) Considerable volume expansion that will result in a significant decrease of the coulombic efficiency; (3) Highly disordered SEI growth compared to other anode materials.^[120] According to literature, these strategies can be divided into three categories: (1) Fabrication of artificial protective layers (metal oxides, metal fluorides, metal nitrides, solid electrolyte, polymers, composite materials, *etc.*); (2) Construction of supporting scaffolds with electronic conductive materials (copper, nickel, carbon, *etc.*) to modulate Li plating; and (3) Tailoring the uniform Li nucleation sites for uniform Li deposition.

Creating an artificial protective layer at the Li-metal surface has been a topic of intensive research for decades. Many studies of various materials and techniques for the preparation of these layers are reported in the literature.^[125-127] Ideally, a protective layer should combine high mechanical strength with good flexibility and high ionic conductivity. It must be an electronically insulating material with a low dielectric constant and electrochemically and chemically stable. Mullins *et al.* recently comprehensively reviewed different kinds of protective layers for Li-metal electrodes.^[47] Single components of inorganic or organic layers were commonly examined in the early stage of research. However, although inorganic layers have sufficient mechanical strength, they are brittle and crack during Li volume expansion/contraction. On the contrary, organic layers are flexible enough to endure these volume changes, but they cannot suppress dendrite growth. Hence, more attention has been paid to developing combined-component layers to use the best properties of each component. For example, Huang's group constructed an organic-inorganic artificial layer with a high mechanical modulus, superior shape compliance, and high ionic conductivity.^[121] Rigid LiF particles are designed to anchor evenly on the soft poly(vinylidene-co-

hexafluoropropylene) (PVDF-HFP) film, as shown in Figure 2.23a. This hybrid artificial layer is obtained by the strengths of LiF and PVDF-HFP, enabling uniform Li^+ permeation and deposition.

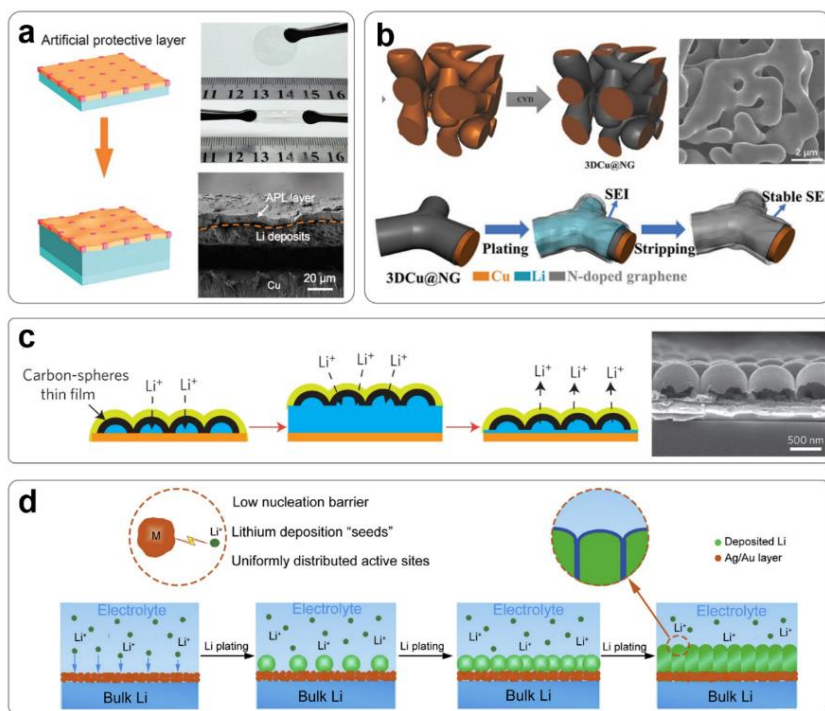


Figure 2.23 (a) Schematic illustration and SEM image of Li deposition with a protective PVDF-HFP layer.^[121] (b) Illustration and SEM image of Li deposition at a graphene-coated 3D copper substrate,^[122] and (c) at carbon-sphere modified copper substrate.^[123] (d) Illustration of uniform Li deposition on an Ag/Au coated copper substrate.^[124]

Another method to stabilize Li-metal anodes is applying scaffold materials with porous structures to achieve uniform Li deposition. Scaffold materials serve both as deposition substrates and current collectors. Copper foam, nickel foam, and carbon-based frameworks are the most frequently used current collectors in the studies because of their high electronic conductivity. Shi *et al.* prepared

graphene (nitrogen-doped)-coated porous copper substrates via CVD synthesis (Figure 2.23b).^[122] The 3D-modified current collector, on the one hand, provides a higher surface area for Li deposition. On the other hand, the strong binding between Li^+ in the electrolyte and graphene leads to a uniform Li^+ flux, thus contributing to a stable Li plating/stripping process without the formation of Li dendrites. Similarly, Cui *et al.* constructed hollow carbon nanospheres on copper foil to ensure a uniform Li deposition (Figure 2.23c).^[123] Interestingly, the composite carbon nanosphere layer can freely move up and down the copper foil, slightly adjusting the space with Li volume variation during cycling. The corresponding theoretical calculations and experimental explorations have revealed that the uniform Li deposition, achieved by porous substrates, is attributed to the even distribution of the electric field at the substrate surface, thereby enabling a uniform Li^+ permeation.

In principle, the growth of Li dendrites is a result of the self-amplifying behavior of Li deposition. Due to the inherent surface defects on Li foil, the nucleation initially started at defects because they are energetically more preferable for the Li reaction. Consequently, the nonuniformity of Li deposition will be gradually accelerated by the nonuniform nucleation during cycling, eventually leading to dendrite formation. Therefore, the uniformity of Li nucleation sites is also a vital factor for controllable Li deposition. Qian *et al.* proposed a heterogeneous metal layer at the Li-metal surface to form densely packed Li nucleation sites.^[124] As illustrated in Figure 2.23d, an Ag/Au layer evenly homogeneously coats the Li foil surface and provides uniformly distributed nuclei seeds for Li deposition. In this case, Li grows into a columnar-structured morphology instead of a dendrite structure observed in the case of untreated Li-metal.

2.2.3 Electrolyte

2.2.3.1 Multifunctional electrolyte additives

A variety of organic species originating from electrolyte solvent decomposition reactions comprise the majority of CEI and SEI films. Thus, using multifunctional electrolyte additives is considered a versatile strategy to stabilize CEI and SEI films in Ni-rich cathode-based LIBs.^[69] This stabilization mechanism is related to the higher HOMO energy level and lower LUMO energy level of the additives compared with conventional electrolyte solvents (*e.g.*, EC, DMC, DEC).^[128, 129] Hence, the electrolyte additives will oxidize at the cathode surface and reduce at the anode surface before the decomposition reactions of electrolyte solvents take place, resulting in the formation of homogeneous CEI and SEI films. Apart from the film-forming ability, multifunctional additives also possess a high affinity towards HF and PF₅ species, which could mitigate the HF-driven degradation, such as TM ions dissolution and gas formation. Recently, several kinds of multifunctional additives have been proposed in studies, aiming at the effective formation of protective films at both cathode and anode surfaces.^[130-132]

One typical example of a novel multifunctional additive applied in LiNi_{0.85}Co_{0.1}Mn_{0.05}O₂ (NCM851005)/graphite full cells is methoxytriethyleneoxypropyltrimethoxysilane (MTE-TMS), which belongs to the group of silane derivatives (Si-O) (Figure 2.24a).^[133] The reported cyclic voltammetry (CV) shows that a standard electrolyte with 1 wt% MTE-TMS reveals a couple of redox peaks at 3.75 V and 1.5 V (*vs.* Li/Li⁺) with a smaller potential interval (ΔV) compared with its additive-free counterpart. Further characterizations demonstrate that the MTE-TMS also stabilizes the formation of the CEI and SEI films at the electrodes and that the crack generation and TM dissolution is significantly reduced.

The interfacial engineering for both cathodes and anodes can also be achieved by the interaction between additive and electrolyte solvents. Choi *et al.* prepared ether-based electrolyte by 1,1,2,2-tetrafluoroethyl-2,2,3,3-tetrafluoropropyl ether (TTE) with 1 wt% fluoroethylene carbonate (FEC) as additive, and investigated its effect in NCM811/Li full cells.^[134] Figure 2.24b displays the HOMO-LUMO energy levels of various solvents (DME, EC, TTE) and additive (FEC) under their reduced states ($+1e^-$ reduction). It is known that neutral FEC has the lowest LUMO energy level among all components. Therefore, it will favorably initiate and control the SEI formation. The TTE solvent dominantly contributes to the subsequent SEI formation through further reduction on the anode because the LUMO energy level of the as-denoted reduced state $+1e^-$ -TTE after the first cycle of charging is much lower than $+1e^-$ -FEC. FEC also promotes the CEI formation at the cathode surface because the reduced state $+1e^-$ -FEC has a higher HOMO energy level than neutral DME. The NCM811/Li cells demonstrate superior cycling stability beyond 150 cycles with a capacity retention of 84.2%. An intact morphology without cracks is observed in NCM811 particles. More uniform SEI films with a more compact morphology are formed at Li-metal anode.

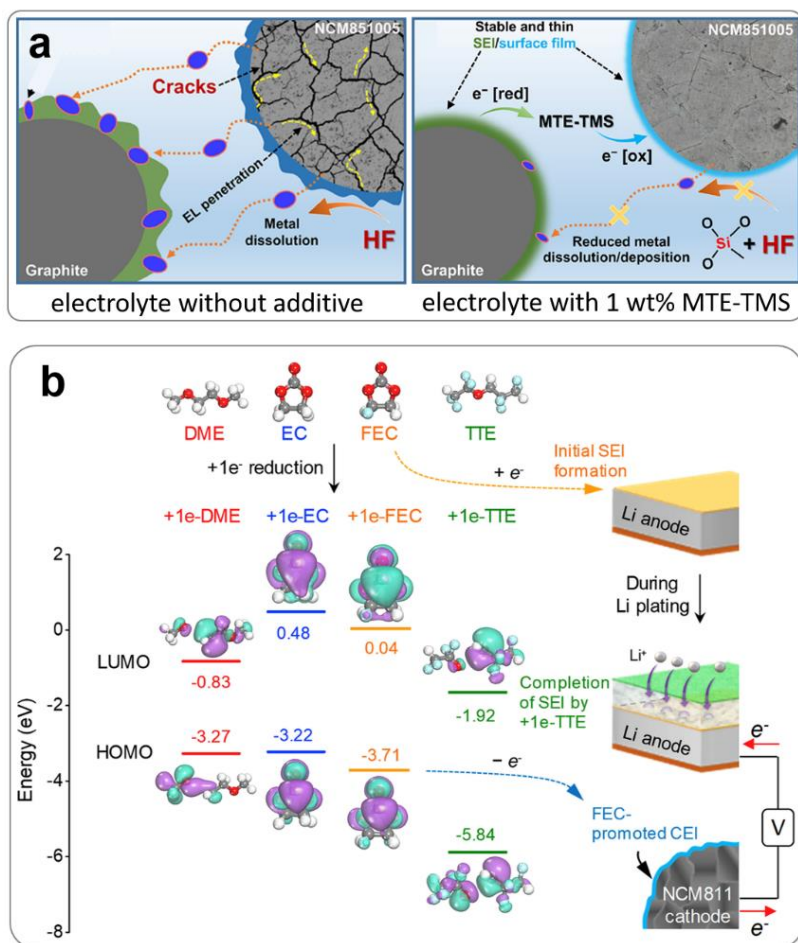


Figure 2.24 (a) Schematic representation of interfacial phenomena occurring in the NCM851005/graphite full-cells with and without electrolyte additive.^[133] (b) HOMO-LUMO energy levels of negatively charged electrolyte molecules, and schematic representation of the interface occurring in an NCM811/Li-metal full-cell.^[134]

2.3 Summary

The expanding production scale of electric vehicles during the last few years has been strongly dependent on the continuous improvement of LIBs. Among all sorts of cathode materials, Ni-rich cathodes have drawn massive

attention as near-term candidates for commercialization due to their high capacity, favorable rate capability, and reasonable cost.^[135] One can see significant successes in the EV market with Ni-rich cathode-based LIBs embedded in EVs, such as NCM811/graphite LIBs applied in the Nio ES6 with an energy density of 737 Wh l⁻¹, and NCA-graphite/silicon-oxide LIBs applied in Tesla Model 3 with an energy density of 866 Wh l⁻¹. Nevertheless, driven by the ambition for achieving even higher energy densities, more advanced battery materials are definitely needed to meet such goals. In addition, an in-depth understanding of electrochemical fatigue mechanisms is important for further optimization of the LIB chemistry.

This chapter thoroughly discussed the degradation upon cycling originating from the cathodes, electrolytes, and anodes in Ni-rich cathode-based LIBs. As an essential component in LIB, Ni-rich cathodes undergo the most destructive and complex degradation processes. These processes can be categorized into the negative reactions induced by RLCs, cation disorder (especially for Li/Ni mixing), surface reconstruction (from layered-to-spinel and rock-salt phase), gas generation, transition-metal dissolution, micro-cracks propagation (intragranular and intergranular), and the fragile thermal stability. The findings emphasize the importance of crystal structure stability with respect to the decreased strength of metal-oxygen bonding at high SOC and high temperatures. In response to these negative effects, various strategies have been proposed, including optimizing synthesis methods, fabricating single-crystal particles, optimizing microstructures, doping foreign ions, coating protective layers, and designing concentration gradients. All these strategies are designed to experimentally enhance the performance of Ni-rich cathodes. However, as discussed, one universal solution cannot be expected to solve all problems because each strategy has its clear limits.

Moving to the anode side, two typical anodes (graphite and Li-metal) that are commonly coupled with Ni-rich cathodes in the presented studies have been discussed. Graphite, as the most successful intercalation material, has been widely

applied in the battery industry. At the same time, the challenges of volume expansion, exfoliation, inferior SEI film formation, and nonuniform Li deposition still need to be handled carefully. Surface coating and chemical treatments help to stabilize the graphite anode. Additionally, the introduction of hybrid graphite-based anodes (graphite/silicon, graphite/silicon oxide, graphene/metal oxide, *etc.*) offers alternative directions for further developments in the anode design.

Regarding the Li-metal anode, it is undoubtedly the most promising anode that will enable the considerable growth of specific energy needed for the next generation of LIBs. However, the high (electro)chemical activity of Li-metal impedes the practical application of the Li-metal anode. Many approaches devoted to controlling the Li deposition are proposed, including applying artificial layers, introducing stable deposition skeletons and uniform nucleation sites at the electrode surface for Li deposition. These methods bring significant improvements in lab-scale demonstrations. Still, the challenge remains in large-scale manufacturing. Remarkably, the phenomenon of chemical crosstalk between cathodes and anodes has recently drawn rising attention. Some CEI/SEI film species have been found to dissolve in the electrolyte, penetrate through the separator, and react at the surface of the anode or cathode, leading to accelerated SEI and CEI formation. Thus, the chemical cross-over of components in full cells should be considered when modifications are adopted for both cathode and anode materials.

One more major problem of Ni-rich cathodes is the degradation related to the electrolyte. The decomposition of conventional electrolytes poses a risk to battery safety in terms of HF and gas generation. Also, the decomposition species are the major components of the CEI and SEI films, causing large lithium inventory losses. The use of multifunctional electrolyte additives with HF-scavenging ability is promising to stabilize the interfaces at both cathodes and anodes simultaneously.

The search for higher efficiencies and upscaling battery designs is under severe pressure of the exponential growth of the global EV market. More advanced materials and battery manufacturing methods are needed. With the growing efforts committed to improving Ni-rich cathode-based LIBs, it is to be expected that numerous exciting new opportunities will continuously arise shortly in the search for high-performance Li-ion batteries.

References

- 1 Y. Su, L. Li, G. Chen, L. Chen, N. Li, Y. Lu, L. Bao, S. Chen, F. Wu, *Chinese Journal of Chemistry* **39** (2020) 189.
- 2 D.-H. Cho, C.-H. Jo, W. Cho, Y.-J. Kim, H. Yashiro, Y.-K. Sun, S.-T. Myung, *Journal of The Electrochemical Society* **161** (2014) A920.
- 3 Y. Su, G. Chen, L. Chen, L. Li, C. Li, R. Ding, J. Liu, Z. Lv, Y. Lu, L. Bao, G. Tan, S. Chen, F. Wu, *Frontier in Chemistry* **8** (2020) 573.
- 4 H. S. Liu, Z. R. Zhang, Z. L. Gong, Y. Yang, *Electrochemical and Solid-State Letters* **7** (2004) A109.
- 5 J. H. Jo, C.-H. Jo, H. Yashiro, S.-J. Kim, S.-T. Myung, *Journal of Power Sources* **313** (2016) 1.
- 6 S. Xu, C. Du, X. Xu, G. Han, P. Zuo, X. Cheng, Y. Ma, G. Yin, *Electrochimica Acta* **248** (2017) 534.
- 7 J.-H. Park, B. Choi, Y.-S. Kang, S. Y. Park, D. J. Yun, I. Park, J. H. Shim, J.-H. Park, H. N. Han, K. Park, *Energy Technology* **6** (2018) 1361.
- 8 Z. Yu, X. Qu, T. Wan, A. Dou, Y. Zhou, X. Peng, M. Su, Y. Liu, D. Chu, *ACS Applied Materials & Interfaces* **12** (2020) 40393.
- 9 J. Zhao, W. Zhang, A. Huq, S. T. Misture, B. Zhang, S. Guo, L. Wu, Y. Zhu, Z. Chen, K. Amine, F. Pan, J. Bai, F. Wang, *Advanced Energy Materials* **7** (2017) 1601266.

- 10 S. Wang, W. Hua, A. Missyul, M. S. D. Darma, A. Tayal, S. Indris, H. Ehrenberg, L. Liu, M. Knapp, *Advanced Functional Materials* **31** (2021) 2009949.
- 11 X. Li, A. Gao, Z. Tang, F. Meng, T. Shang, S. Guo, J. Ding, Y. Luo, D. Xiao, X. Wang, D. Su, Q. Zhang, L. Gu, *Advanced Functional Materials* **31** (2021) 2010291.
- 12 A. Gao, X. Li, F. Meng, S. Guo, X. Lu, D. Su, X. Wang, Q. Zhang, L. Gu, *Small Methods* **5** (2020) 2000730.
- 13 Y.-S. Kang, S. Y. Park, K. Ito, Y. Kubo, Y. Shin, D. Y. Kim, D.-H. Seo, S. Kim, J.-H. Park, S.-G. Doo, M. Koh, J. A. Seo, K. Park, *Journal of Power Sources* **490** (2021) 229542.
- 14 S. S. Zhang, *Energy Storage Materials* **24** (2020) 247.
- 15 C. Xu, K. Marker, J. Lee, A. Mahadevegowda, P. J. Reeves, S. J. Day, M. F. Groh, S. P. Emge, C. Ducati, B. Layla Mehdi, C. C. Tang, C. P. Grey, *Nature Materials* **20** (2021) 84.
- 16 S. Li, Z. Yao, J. Zheng, M. Fu, J. Cen, S. Hwang, H. Jin, A. Orlov, L. Gu, S. Wang, Z. Chen, D. Su, *Angew Chem Int Ed Engl* **132** (2020) 22276.
- 17 C. Xu, P. J. Reeves, Q. Jacquet, C. P. Grey, *Advanced Energy Materials* **11** (2020) 2003404.
- 18 L. Zou, W. Zhao, H. Jia, J. Zheng, L. Li, D. P. Abraham, G. Chen, J. R. Croy, J.-G. Zhang, C. Wang, *Chemistry of Materials* **32** (2020) 2884.
- 19 J. Zhu, S. Sharifi-Asl, J. C. Garcia, H. H. Iddir, J. R. Croy, R. Shahbazian-Yassar, G. Chen, *ACS Applied Energy Materials* **3** (2020) 4799.
- 20 X. Tian, Y. Yi, B. Fang, P. Yang, T. Wang, P. Liu, L. Qu, M. Li, S. Zhang, *Chemistry of Materials* **32** (2020) 9821.
- 21 S. E. Renfrew, L. A. Kaufman, B. D. McCloskey, *ACS Applied Materials & Interfaces* **11** (2019) 34913.
- 22 S. E. Renfrew, B. D. McCloskey, *ACS Applied Energy Materials* **2** (2019) 3762.

- 23 D. Streich, C. Erk, A. Guéguen, P. Müller, F.-F. Chesneau, E. J. Berg, *The Journal of Physical Chemistry C* **121** (2017) 13481.
- 24 W. Li, *Journal of The Electrochemical Society* **167** (2020) 100510.
- 25 J. Kim, H. Ma, H. Cha, H. Lee, J. Sung, M. Seo, P. Oh, M. Park, J. Cho, *Energy & Environmental Science* **11** (2018) 1449.
- 26 D.-S. Ko, J.-H. Park, S. Park, Y. N. Ham, S. J. Ahn, J.-H. Park, H. N. Han, E. Lee, W. S. Jeon, C. Jung, *Nano Energy* **56** (2019) 434.
- 27 R. Jung, F. Linsenmann, R. Thomas, J. Wandt, S. Solchenbach, F. Maglia, C. Stinner, M. Tromp, H. A. Gasteiger, *Journal of The Electrochemical Society* **166** (2019) A378.
- 28 S. Yin, W. Deng, J. Chen, X. Gao, G. Zou, H. Hou, X. Ji, *Nano Energy* **83** (2021) 105854.
- 29 Q. Lin, W. Guan, J. Zhou, J. Meng, W. Huang, T. Chen, Q. Gao, X. Wei, Y. Zeng, J. Li, Z. Zhang, *Nano Energy* **76** (2020) 105021.
- 30 K. Min, E. Cho, *Phys Chem Chem Phys* **20** (2018) 9045.
- 31 G. W. Nam, N.-Y. Park, K.-J. Park, J. Yang, J. Liu, C. S. Yoon, Y.-K. Sun, *ACS Energy Letters* **4** (2019) 2995.
- 32 T. M. M. Heenan, A. Wade, C. Tan, J. E. Parker, D. Matras, A. S. Leach, J. B. Robinson, A. Llewellyn, A. Dimitrijevic, R. Jervis, P. D. Quinn, D. J. L. Brett, P. R. Shearing, *Advanced Energy Materials* **10** (2020) 1321.
- 33 H.-H. Ryu, K.-J. Park, C. S. Yoon, Y.-K. Sun, *Chemistry of Materials* **30** (2018) 1155.
- 34 J. Park, H. Zhao, S. D. Kang, K. Lim, C. C. Chen, Y. S. Yu, R. D. Braatz, D. A. Shapiro, J. Hong, M. F. Toney, M. Z. Bazant, W. C. Chueh, *Nature Materials* **20** (2021) 991.
- 35 H.-H. Ryu, B. Namkoong, J.-H. Kim, I. Belharouak, C. S. Yoon, Y.-K. Sun, *ACS Energy Letters* **6** (2021) 2726.
- 36 H. Wu, C. Qin, K. Wang, X. Han, M. Sui, P. Yan, *Journal of Power Sources* **503** (2021) 230066.

- 37 J. Duan, X. Tang, H. Dai, Y. Yang, W. Wu, X. Wei, Y. Huang, *Electrochemical Energy Reviews* **3** (2019) 1.
- 38 D. Hu, Q. Zhang, J. Tian, L. Chen, N. Li, Y. Su, L. Bao, Y. Lu, D. Cao, K. Yan, S. Chen, F. Wu, *ACS Applied Materials & Interfaces* **13** (2021) 6286.
- 39 M. Dixit, B. Markovsky, F. Schipper, D. Aurbach, D. T. Major, *The Journal of Physical Chemistry C* **121** (2017) 22628.
- 40 L. Geng, J. Liu, D. L. Wood, Y. Qin, W. Lu, C. J. Jafta, Y. Bai, I. Belharouak, *ACS Applied Energy Materials* **3** (2020) 7058.
- 41 X. Liu, G. L. Xu, L. Yin, I. Hwang, Y. Li, L. Lu, W. Xu, X. Zhang, Y. Chen, Y. Ren, C. J. Sun, Z. Chen, M. Ouyang, K. Amine, *J Am Chem Soc* **142** (2020) 19745.
- 42 E. Lee, S. Muhammad, T. Kim, H. Kim, W. Lee, W. S. Yoon, *Advanced Science (Weinh)* **7** (2020) 1902413.
- 43 J. U. Choi, N. Voronina, Y. K. Sun, S. T. Myung, *Advanced Energy Materials* **10** (2020) 2002027.
- 44 V. Gopalakrishnan, A. Sundararajan, P. Omprakash, D. Bhat Panemangalore, *Journal of The Electrochemical Society* **168** (2021) 040541.
- 45 J. Asenbauer, T. Eisenmann, M. Kuenzel, A. Kazzazi, Z. Chen, D. Bresser, *Sustainable Energy & Fuels* **4** (2020) 5387.
- 46 V. A. Sethuraman, L. J. Hardwick, V. Srinivasan, R. Kostecki, *Journal of Power Sources* **195** (2010) 3655.
- 47 M. L. Meyerson, P. E. Papa, A. Heller, C. B. Mullins, *ACS Nano* **15** (2021) 29.
- 48 N. Lin, Z. Jia, Z. Wang, H. Zhao, G. Ai, X. Song, Y. Bai, V. Battaglia, C. Sun, J. Qiao, K. Wu, G. Liu, *Journal of Power Sources* **365** (2017) 235.
- 49 S. Schweidler, L. de Biasi, A. Schiele, P. Hartmann, T. Brezesinski, J. Janek, *The Journal of Physical Chemistry C* **122** (2018) 8829.
- 50 A. Tornheim, R. Sahore, M. He, J. R. Croy, Z. Zhang, *Journal of The Electrochemical Society* **165** (2018) A3360.

- 51 W. Li, U. H. Kim, A. Dolocan, Y. K. Sun, A. Manthiram, *ACS Nano* **11** (2017) 5853.
- 52 S. Klein, P. Barmann, T. Beuse, K. Borzutzki, J. E. Frerichs, J. Kasnatscheew, M. Winter, T. Placke, *ChemSusChem* **14** (2021) 595.
- 53 L. Huang, G. Xu, X. Du, J. Li, B. Xie, H. Liu, P. Han, S. Dong, G. Cui, L. Chen, *Advanced Science (Weinh)* **8** (2021) e2100676.
- 54 M. K. Aslam, Y. Niu, T. Hussain, H. Tabassum, W. Tang, M. Xu, R. Ahuja, *Nano Energy* **86** (2021) 106142.
- 55 X. Fan, L. Chen, O. Borodin, X. Ji, J. Chen, S. Hou, T. Deng, J. Zheng, C. Yang, S. C. Liou, K. Amine, K. Xu, C. Wang, *Nature Nanotechnology* **13** (2018) 715.
- 56 D. Wang, W. Zhang, W. Zheng, X. Cui, T. Rojo, Q. Zhang, *Advanced Science (Weinh)* **4** (2017) 1600168.
- 57 B. Song, I. Dhiman, J. C. Carothers, G. M. Veith, J. Liu, H. Z. Bilheux, A. Huq, *ACS Energy Letters* **4** (2019) 2402.
- 58 S. H. Lee, J. Y. Hwang, J. Ming, Z. Cao, H. A. Nguyen, H. G. Jung, J. Kim, Y. K. Sun, *Advanced Energy Materials* **10** (2020) 2153.
- 59 S. J. Park, J. Y. Hwang, C. S. Yoon, H. G. Jung, Y. K. Sun, *ACS Appl Mater Interfaces* **10** (2018) 17985.
- 60 J. Langdon, A. Manthiram, *Advanced Functional Materials* **31** (2021) 2010267.
- 61 J. Fu, D. Mu, B. Wu, J. Bi, H. Cui, H. Yang, H. Wu, F. Wu, *ACS Applied Materials & Interfaces* **10** (2018) 19704.
- 62 D. Y. Kim, I. Park, Y. Shin, D.-H. Seo, Y.-S. Kang, S.-G. Doo, M. Koh, *Journal of Power Sources* **418** (2019) 74.
- 63 C. W. L. Xing, W. Li, M. Xu, X. Meng, S. Zhao, *Journal of Physical Chemistry B* **113** (2009) 5181.
- 64 J. Henschel, C. Peschel, S. Klein, F. Horsthemke, M. Winter, S. Nowak, *Angew Chem Int Ed Engl* **59** (2020) 6128.
- 65 Q. Wang, L. Jiang, Y. Yu, J. Sun, *Nano Energy* **55** (2019) 93.

- 66 I. Takahashi, H. Kiuchi, A. Ohma, T. Fukunaga, E. Matsubara, *The Journal of Physical Chemistry C* **124** (2020) 9243.
- 67 K. Kumai, H. Miyashiro, Y. Kobayashi, K. Takei, R. Ishikawa, *Journal of Power Sources* **81** (1999) 715.
- 68 Q. Li, Y. Wang, X. Wang, X. Sun, J. N. Zhang, X. Yu, H. Li, *ACS Applied Materials & Interfaces* **12** (2020) 2319.
- 69 M. Mao, B. Huang, Q. Li, C. Wang, Y.-B. He, F. Kang, *Nano Energy* **78** (2020) 105282.
- 70 W. Liu, P. Oh, X. Liu, M. J. Lee, W. Cho, S. Chae, Y. Kim, J. Cho, *Angew Chem Int Ed Engl* **54** (2015) 4440.
- 71 S. Fang, D. Jackson, M. L. Dreibelbis, T. F. Kuech, R. J. Hamers, *Journal of Power Sources* **373** (2018) 184.
- 72 H. Maleki Kheimeh Sari, X. Li, *Advanced Energy Materials* **9** (2019) 1970151.
- 73 J.-M. Kim, X. Zhang, J.-G. Zhang, A. Manthiram, Y. S. Meng, W. Xu, *Materials Today* (2021), DOI: 10.1016/j.mattod.2020.12.017.
- 74 X. B. Cheng, R. Zhang, C. Z. Zhao, Q. Zhang, *Chemical Reviews* **117** (2017) 10403.
- 75 J. Alvarado, M. A. Schroeder, T. P. Pollard, X. Wang, J. Z. Lee, M. Zhang, T. Wynn, M. Ding, O. Borodin, Y. S. Meng, K. Xu, *Energy & Environmental Science* **12** (2019) 780.
- 76 W. Zhao, J. Zheng, L. Zou, H. Jia, B. Liu, H. Wang, M. H. Engelhard, C. Wang, W. Xu, Y. Yang, J.-G. Zhang, *Advanced Energy Materials* **8** (2018) 2211.
- 77 M. Wood, J. Li, R. E. Ruther, Z. Du, E. C. Self, H. M. Meyer, C. Daniel, I. Belharouak, D. L. Wood, *Energy Storage Materials* **24** (2020) 188.
- 78 K. Yuan, N. Li, R. Ning, C. Shen, N. Hu, M. Bai, K. Zhang, Z. Tian, L. Shao, Z. Hu, X. Xu, T. Yu, K. Xie, *Nano Energy* **78** (2020) 105239.
- 79 Z. Tang, J. Bao, Q. Du, Y. Shao, M. Gao, B. Zou, C. Chen, *ACS Applied Materials & Interfaces* **8** (2016) 34879.

- 80 Y. Su, Q. Zhang, L. Chen, L. Bao, Y. Lu, Q. Shi, J. Wang, S. Chen, F. Wu, *ACS Applied Materials & Interfaces* **12** (2020) 37208.
- 81 Y. Shi, M. Zhang, C. Fang, Y. S. Meng, *Journal of Power Sources* **394** (2018) 114.
- 82 Y. Wang, E. Wang, X. Zhang, H. Yu, *Energy & Fuels* **35** (2021) 1918.
- 83 J. Leng, J. Wang, W. Peng, Z. Tang, S. Xu, Y. Liu, J. Wang, *Small* **17** (2021) e2006869.
- 84 X. Xu, H. Huo, J. Jian, L. Wang, H. Zhu, S. Xu, X. He, G. Yin, C. Du, X. Sun, *Advanced Energy Materials* **9** (2019) 1803963.
- 85 F. Zhang, S. Lou, S. Li, Z. Yu, Q. Liu, A. Dai, C. Cao, M. F. Toney, M. Ge, X. Xiao, W. K. Lee, Y. Yao, J. Deng, T. Liu, Y. Tang, G. Yin, J. Lu, D. Su, J. Wang, *Nature Communications* **11** (2020) 3050.
- 86 Y. Bi, J. Tao, Y. Wu, L. Li, Y. Xu, E. Hu, B. Wu, J. Hu, C. Wang, J.-G. Zhang, *Science* **370** (2020) 1313.
- 87 H.-H. Ryu, N.-Y. Park, T.-C. Noh, G.-C. Kang, F. Maglia, S.-J. Kim, C. S. Yoon, Y.-K. Sun, *ACS Energy Letters* **6** (2020) 216.
- 88 U. H. Kim, H. H. Ryu, J. H. Kim, R. Mücke, P. Kaghazchi, C. S. Yoon, Y. K. Sun, *Advanced Energy Materials* **9** (2019) 1970046.
- 89 Y. Su, G. Chen, L. Chen, Y. Lu, Q. Zhang, Z. Lv, C. Li, L. Li, N. Liu, G. Tan, L. Bao, S. Chen, F. Wu, *ACS Applied Materials & Interfaces* **11** (2019) 36697.
- 90 X. Ju, H. Huang, W. He, H. Zheng, P. Deng, S. Li, B. Qu, T. Wang, *ACS Sustainable Chemistry & Engineering* **6** (2018) 6312.
- 91 M. Jiang, Q. Zhang, X. Wu, Z. Chen, D. L. Danilov, R.-A. Eichel, P. H. L. Notten, *ACS Applied Energy Materials* **3** (2020) 6583.
- 92 H. Lv, C. Li, Z. Zhao, B. Wu, D. Mu, *Journal of Energy Chemistry* **60** (2021) 435.
- 93 Y. Su, Y. Yang, L. Chen, Y. Lu, L. Bao, G. Chen, Z. Yang, Q. Zhang, J. Wang, R. Chen, S. Chen, F. Wu, *Electrochimica Acta* **292** (2018) 217.

- 94 U. H. Kim, J. H. Park, A. Aishova, R. M. Ribas, R. S. Monteiro, K. J. Griffith, C. S. Yoon, Y. K. Sun, *Advanced Energy Materials* (2021) 2100884.
- 95 B. Chu, S. Liu, L. You, D. Liu, T. Huang, Y. Li, A. Yu, *ACS Sustainable Chemistry & Engineering* **8** (2020) 3082.
- 96 L. Wang, R. Wang, J. Wang, R. Xu, X. Wang, C. Zhan, *ACS Applied Materials & Interfaces* **13** (2021) 8324.
- 97 U.-H. Kim, G.-T. Park, B.-K. Son, G. W. Nam, J. Liu, L.-Y. Kuo, P. Kaghazchi, C. S. Yoon, Y.-K. Sun, *Nature Energy* **5** (2020) 860.
- 98 U.-H. Kim, G.-T. Park, P. Conlin, N. Ashburn, K. Cho, Y.-S. Yu, D. A. Shapiro, F. Maglia, S.-J. Kim, P. Lamp, C. S. Yoon, Y.-K. Sun, *Energy & Environmental Science* **14** (2021) 1573.
- 99 F. Wu, N. Liu, L. Chen, Y. Su, G. Tan, L. Bao, Q. Zhang, Y. Lu, J. Wang, S. Chen, J. Tan, *Nano Energy* **59** (2019) 50.
- 100 K. Li, D. Xue, *The Journal of Physical Chemistry A* **110** (2006) 11332.
- 101 S. H. Song, M. Cho, I. Park, J. G. Yoo, K. T. Ko, J. Hong, J. Kim, S. K. Jung, M. Avdeev, S. Ji, S. Lee, J. Bang, H. Kim, *Advanced Energy Materials* **10** (2020) 2000521.
- 102 S. Yang, Q. Fan, Z. Shi, L. Liu, J. Liu, X. Ke, J. Liu, C. Hong, Y. Yang, Z. Guo, *ACS Applied Materials & Interfaces* **11** (2019) 36742.
- 103 A. M. Wise, C. Ban, J. N. Weker, S. Misra, A. S. Cavanagh, Z. Wu, Z. Li, M. S. Whittingham, K. Xu, S. M. George, M. F. Toney, *Chemistry of Materials* **27** (2015) 6146.
- 104 S. Jeong, J. H. Park, S. Y. Park, J. Kim, K. T. Lee, Y. D. Park, J. Mun, *ACS Applied Materials & Interfaces* **13** (2021) 22475.
- 105 J. Kim, J. Lee, H. Ma, H. Y. Jeong, H. Cha, H. Lee, Y. Yoo, M. Park, J. Cho, *Advanced Materials* **30** (2018) 1704309.
- 106 H. J. Song, S. H. Oh, Y. Lee, J. Kim, T. Yim, *Journal of Power Sources* **483** (2021) 229218.
- 107 K. Du, A. Gao, L. Gao, S. Sun, X. Lu, C. Yu, S. Li, H. Zhao, Y. Bai, *Nano Energy* **83** (2021) 105775.

- 108 K. Wu, J. Wang, Q. Li, Y. Yang, X. Deng, R. Dang, M. Wu, Z. Wu, X. Xiao, X. Yu, *Nanoscale* **12** (2020) 11182.
- 109 C. S. Yoon, K.-J. Park, U.-H. Kim, K. H. Kang, H.-H. Ryu, Y.-K. Sun, *Chemistry of Materials* **29** (2017) 10436.
- 110 J. Zhang, Z. Yang, R. Gao, L. Gu, Z. Hu, X. Liu, *ACS Applied Materials & Interfaces* **9** (2017) 29794.
- 111 D.-W. Jun, C. S. Yoon, U.-H. Kim, Y.-K. Sun, *Chemistry of Materials* **29** (2017) 5048.
- 112 Y.-C. Li, W. Xiang, Y. Xiao, Z.-G. Wu, C.-L. Xu, W. Xu, Y.-D. Xu, C. Wu, Z.-G. Yang, X.-D. Guo, *Journal of Power Sources* **423** (2019) 144.
- 113 W. Yang, W. Xiang, Y. X. Chen, Z. G. Wu, W. B. Hua, L. Qiu, F. R. He, J. Zhang, B. H. Zhong, X. D. Guo, *ACS Applied Materials & Interfaces* **12** (2020) 10240.
- 114 K.-H. Chen, M. J. Namkoong, V. Goel, C. Yang, S. Kazemiabnavi, S. M. Mortuza, E. Kazyak, J. Mazumder, K. Thornton, J. Sakamoto, N. P. Dasgupta, *Journal of Power Sources* **471** (2020) 228475.
- 115 J. Kim, S. M. Nithya Jeghan, G. Lee, *Microporous and Mesoporous Materials* **305** (2020) 110325.
- 116 D. Y. Rhee, J. Kim, J. Moon, M.-S. Park, *Journal of Alloys and Compounds* **843** (2020) 156042.
- 117 S. Heng, X. Shan, W. Wang, Y. Wang, G. Zhu, Q. Qu, H. Zheng, *Carbon* **159** (2020) 390.
- 118 M. R. Al Hassan, A. Sen, T. Zaman, M. S. Mostari, *Materials Today Chemistry* **11** (2019) 225.
- 119 W. Jiang, H. Wang, Z. Xu, N. Li, C. Chen, C. Li, J. Li, H. Lv, L. Kuang, X. Tian, *Chemical Engineering Journal* **335** (2018) 954.
- 120 X. B. Cheng, R. Zhang, C. Z. Zhao, F. Wei, J. G. Zhang, Q. Zhang, *Advanced Science (Weinh)* **3** (2016) 1500213.
- 121 R. Xu, X.-Q. Zhang, X.-B. Cheng, H.-J. Peng, C.-Z. Zhao, C. Yan, J.-Q. Huang, *Advanced Functional Materials* **28** (2018) 1705838.

- 122 R. Zhang, S. Wen, N. Wang, K. Qin, E. Liu, C. Shi, N. Zhao, *Advanced Energy Materials* **8** (2018) 1800914.
- 123 G. Zheng, S. W. Lee, Z. Liang, H. W. Lee, K. Yan, H. Yao, H. Wang, W. Li, S. Chu, Y. Cui, *Nature Nanotechnology* **9** (2014) 618.
- 124 F. Guo, C. Wu, H. Chen, F. Zhong, X. Ai, H. Yang, J. Qian, *Energy Storage Materials* **24** (2020) 635.
- 125 K. Yan, H. W. Lee, T. Gao, G. Zheng, H. Yao, H. Wang, Z. Lu, Y. Zhou, Z. Liang, Z. Liu, S. Chu, Y. Cui, *Nano Letters* **14** (2014) 6016.
- 126 L. Wang, Q. Wang, W. Jia, S. Chen, P. Gao, J. Li, *Journal of Power Sources* **342** (2017) 175.
- 127 Y. Liu, D. Lin, P. Y. Yuen, K. Liu, J. Xie, R. H. Dauskardt, Y. Cui, *Advanced Materials* **29** (2017) 1605531.
- 128 A. Kazzazi, D. Bresser, M. Kuenzel, M. Hekmatfar, J. Schnaidt, Z. Jusys, T. Diemant, R. J. Behm, M. Copley, K. Maranski, J. Cookson, I. de Meatza, P. Axmann, M. Wohlfahrt-Mehrens, S. Passerini, *Journal of Power Sources* **482** (2021) 228975.
- 129 G. Lan, L. Xing, D. Bedrov, J. Chen, R. Guo, Y. Che, Z. Li, H. Zhou, W. Li, *Journal of Alloys and Compounds* **821** (2020) 153236.
- 130 T. Yang, S. Li, W. Wang, J. Lu, W. Fan, X. Zuo, J. Nan, *Journal of Power Sources* **505** (2021) 230055.
- 131 C. Wang, Q. Hu, J. Hao, X. Xu, L. Ouyang, W. Fan, J. Ye, J. Liu, J. Li, A. Mei, M. Zhu, *ACS Applied Energy Materials* **4** (2021) 2292.
- 132 G. Liu, N. Xu, Y. Zou, K. Zhou, X. Yang, T. Jiao, W. Yang, Y. Yang, J. Zheng, *ACS Applied Materials & Interfaces* **13** (2021) 12069.
- 133 H. Q. Pham, M. Mirolo, M. Tarik, M. El Kazzi, S. Trabesinger, *Energy Storage Materials* **33** (2020) 216.
- 134 Y. Lee, T. K. Lee, S. Kim, J. Lee, Y. Ahn, K. Kim, H. Ma, G. Park, S.-M. Lee, S. K. Kwak, N.-S. Choi, *Nano Energy* **67** (2020) 104309.
- 135 W. Li, E. M. Erickson, A. Manthiram, *Nature Energy* **5** (2020) 26.

Chapter 3

Experimental

Abstract

The research methods used in the experiments described further in the thesis are introduced in this chapter. The principles of material preparation and characterization techniques are briefly outlined. The electrode preparation process and cell configuration used in the electrochemical analysis are presented. Examples of detailed electrochemical measurements made with specific purposes are also included.

3.1 Materials Preparation Methods

3.1.1 Hydrothermal Synthesis

Hydrothermal synthesis is one of the most common methods to synthesize nanostructured inorganic materials, especially transition-metal oxides.^[1] Figure 3.1a shows an autoclave that was used in the experiments described in this thesis. Typically, one autoclave comprises a Teflon vessel as a container and an exterior cylinder made of stainless steel. Teflon is chemically inert and prevents corrosion at high temperatures. Other parts, such as springs and buffer discs, are made of stainless steel and are essential for sealing.

The crystal growth process in hydrothermal synthesis is schematically shown in Figure 3.1b. The reactants are well dispersed and mixed in aqueous solutions. Further, at high temperature and pressure, they crystallize into nanoparticles. The primary nanoparticles then gradually grow into rod and sheet morphologies. Eventually, the as-formed nanosheets self-assemble into spherical secondary particles. Many parameters can affect the morphology of the final substances, including the mass ratio of reactants, heating rate, temperature, pressure, setting time, *etc.* Hence, careful control of these parameters is vital for achieving optimal properties.

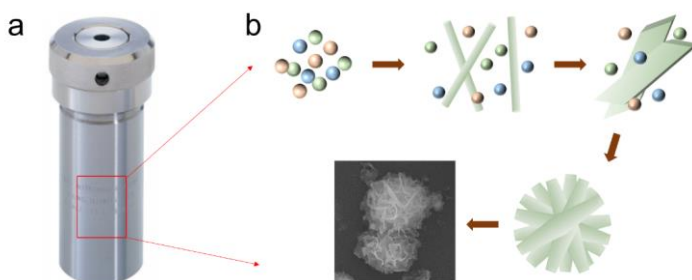


Figure 3.1 (a) Typical autoclave used in the hydrothermal synthesis. (b) Schematic illustration of the hydrothermal synthesis process.

The hydrothermal synthesis fundamentally relies on the high activity of reactants in solutions under extreme conditions. Water is the most widely used solution in numerous reactions. Its ion product constant (K_w) increases with the temperature and pressure, implying activity growth. The viscosity and surface tension of water significantly decreases at high temperatures and pressures. Therefore the activity of reactants in a water solution at a high temperature is also high, leading to higher solubility and a faster crystal growth process with enhanced dispersibility.^[2]

3.1.2 Sputter Deposition

The Physical-Vapor-Deposition (PVD) machine (Kurt J. Lesker, UK) was used to prepare the thin films investigated in this thesis. A PVD machine includes direct-current (DC) sputtering for the deposition of conductive materials and radio-frequency (RF) sputtering for the deposition of dielectric materials. Figure 3.2 illustrates the general process of sputter deposition. In a vacuum chamber, chemically inert argon served as a gas source, electrically excited into a gas plasma. The target side is energized as a cathode. The opposite part, where the deposition substrate is placed, serves as an anode.^[3] To obtain highly homogeneous films, the substrate holder keeps rotating at a fixed rate. The neutral atoms at the target surface are continuously bombarded by argon plasma, ejected from the target, and deposited on the substrate.^[4] Compact and flat films can be deposited in this way.

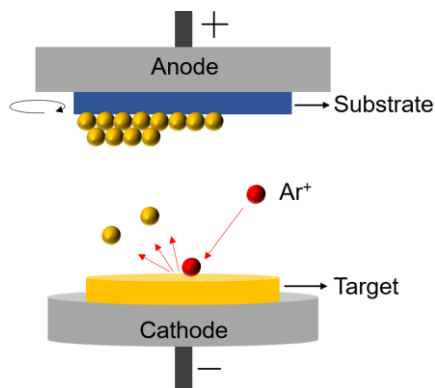


Figure 3.2 Schematic illustration of the sputtering deposition process.

The distance between target and substrate was fixed at 15 cm, and the rotation rate of the substrate holder was optimized as 20 rpm in all deposition processes. Other deposition parameters controlled in the experiments, including sputter power, chamber pressure, and deposition time, were selected material-wise. A stylus profilometer (Bruker, UK) was employed during the deposition process to determine thin-film thickness.

3.2 Characterization Techniques

3.2.1 X-ray Diffraction

X-ray diffraction (XRD) analysis is an analytical technique for the quantitative investigation of crystalline substances.^[5] The principle of XRD analysis is based on famous Bragg's law (Figure 3.3). According to this law, the ray diffracted on the surface of a periodical atomic structure will have peak intensity in the direction satisfying the following equation

$$2d\sin\theta = n\lambda \quad (3.1)$$

where d represents lattice distance in the crystalline sample, θ is the glancing angle, λ is the radiation wavelength, and n is the diffraction order. In the measurement, the sample is scanned by X-rays within a range of 2θ angle. Thus, a complete set of patterns with all diffraction directions in the lattice will be collected. By comparing the standard pattern of the substances with experimental results, the peak positions can be identified with unique d-spacing information. In this way, the corresponding crystallographic structure of the sample can be determined.

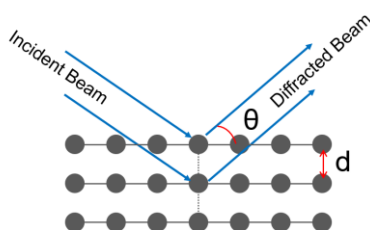


Figure 3.3 Schematic illustration of Bragg's law applied in XRD measurements.

XRD measurements in this thesis were performed over a 2θ range of 10° - 80° using $\text{Cu K}\alpha$ radiation at 40 kV and 40 mA via an EMPYREAN X-ray diffractometer (Panalytical, Netherlands). The collected XRD intensity data were analyzed by FullProf Suite analyzing software. Standard data of measured material and the "Profile Matching" configuration were applied to the analyses.

3.2.2 Scanning Electron Microscopy

Scanning electron microscopy (SEM) is a fundamental technique to examine sample morphologies. As illustrated in Figure 3.4, a beam of high-energy electrons is emitted and focused on the sample surface by several electromagnetic lenses. The incident electrons interact with atoms on the sample surface, creating secondary electrons, backscattered electrons, and X-rays. The detectors collect the produced primary particles and give the topography and elemental composition of

the sample. The energy-dispersive X-ray (EDX) system is generally combined with the SEM instrument. With EDX, the elemental mapping and spectra also can be obtained.

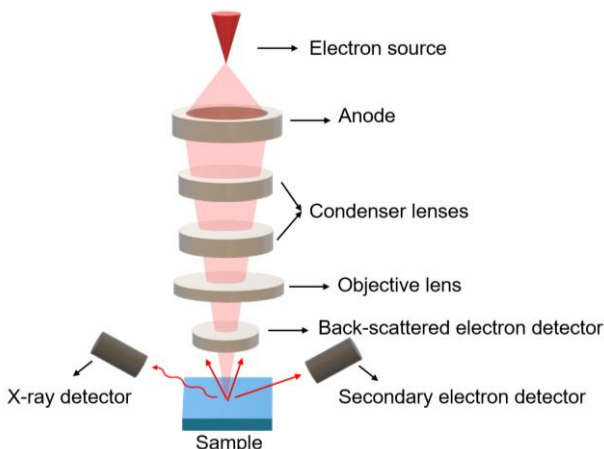


Figure 3.4 Schematic illustration of the SEM technique.

SEM images in this thesis were taken on a Quanta FEG 650 (FEI, USA) environmental scanning electron microscope operated at a voltage of 20 kV. A focused-ion-beam (FIB) milling system was also used to etch part of the sample particle and examine the internal morphology. The sample powder was carefully dispersed in the isopropanol, dropped on a clean silicon substrate, then thoroughly dried in the air for the SEM sample preparation. The distance between the sample holder and the objective lens was fixed at 10 mm. The elemental mapping and EDX spectra were collected as well.

3.2.3 Transmission Electron Microscopy

A transmission electron microscope (TEM) gives structural information by forming a magnified image of the diffraction pattern of the sample. An illustration of TEM measurement is shown in Figure 3.5. A beam of electrons emitted from

the electron gun passes through the condenser lenses and focuses on the sample. The sample for TEM measurement has to be ultrathin to allow the electron beam to penetrate the sample and create the 2D image on a fluorescent screen. The magnification of TEM can reach up to 50 million times and provide the sample details up to the atomic scale. The crystal structure can be investigated by high-resolution transmission electron microscopy (HRTEM). Also, the diffraction pattern of the crystal sample can be generated by selected-area electron diffraction (SAED) measurement.

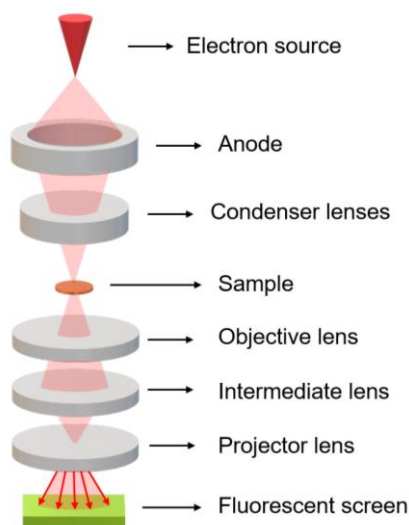


Figure 3.5 Schematic illustration of the TEM technique.

TEM, HRTEM images, and SAED patterns in this thesis were performed using a Tecnai F20 (FEI, USA) transmission electron microscope at an acceleration voltage of 200 kV. The sample preparation for TEM measurements is much more restrictive and complex than that for SEM measurements. The sample powder must be highly dispersed in an ethanol solution and then dropped onto a TEM carbon-coated copper grid. The agglomeration of sample particles

should be avoided to obtain high-quality images. Thus an ultrasonic dispersion process was used in all sample preparations.

3.2.4 X-ray Photoelectron Spectroscopy

X-ray photoelectron spectrometry (XPS) has been considered the most powerful technique for probing the chemical nature of the sample surface.^[6] The electron energy resolution in the XPS analyzer is significantly high (low to 0.1 eV), which allows an accurate probe for the chemical shift in the electron binding energies. Therefore, XPS is a surface-sensitive technique with a typical depth resolution of 2 nm. Figure 3.6 summarizes the basic process of XPS measurement. The atoms at the sample surface are excited by the monochromatic X-rays and emit photoelectrons with distinctive elemental characteristics. Based on the difference of binding energy and intensity of the photoelectron peak, the XPS spectra can provide detailed information on the chemical state of the sample. Besides, the ratio of peak area delivers quantitative information of the elemental composition.^[7]

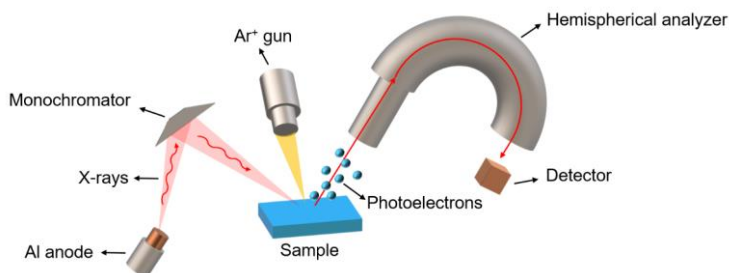


Figure 3.6 Schematic illustration of the XPS technique.

An argon ion gun is usually combined with XPS to perform depth-profiling analysis.^[8] The ion beam etches a thin layer on the sample surface before the XPS spectra acquisition, allowing the identification of the composition from the

sample's surface to hundreds of nanometers into the bulk. XPS depth-profiling analysis has been widely used in many works and is particularly suitable for thin-film samples.

XPS measurements, described in this thesis, were performed by a K-Alpha instrument (Thermo Scientific, USA) with a monochromatic X-ray source ($\text{Al K}\alpha$). Depth profiling was carried out by a 500 eV argon ion beam. The XPS sample preparation was similar to SEM sample preparation. The powder sample was dispersed and dried before being transferred into the XPS chamber. The collected experimental results were simulated by CasaXPS software.

3.2.5 Inductively Coupled Plasma-Mass Spectrometry

Inductively Coupled Plasma Source-Mass Spectrometry (ICP-MS) is a rapid technique to determine the relative content ratio of elements. Figure 3.7 shows the general process occurring during ICP-MS measurements. The ionized argon gas served as a plasma source during the measurements. Typically, the sample is ionized by an inductively coupled plasma and forming various ions. The flow of argon gas carries the sample ions into the attached mass spectrometry for further analysis. An ion signal proportional to the concentration can be detected based on its elemental presence.^[9]

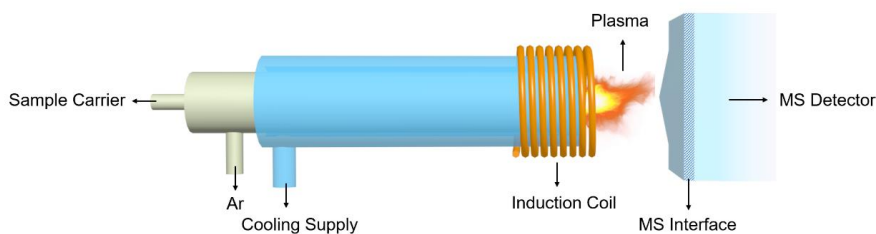


Figure 3.7 Schematic illustration of an ICP-MS set-up.

ICP-MS measurements were carried out by the Agilent 7900 ICP-MS (Agilent, USA). For the preparation, the samples were dissolved in an acidic solution (1 mL HNO₃, 0.5 mL H₂O₂), shaken, then made up to 10 mL solution with water.

3.3 Electrode Preparation

3.3.1 Electrode Slurry Preparation

The electrode slurry was a mixture of the active powder materials, carbon black (Super P, Alfa Aesar), and poly(vinylidene fluoride) binder (PVDF, Sigma-Aldrich) at the weight ratio of 8:1:1. The mixture was then dissolved in N-methyl pyrrolidone (NMP) solvent. An ARV-310 vacuum mixer (Thinky, Japan) was used for slurry mixing. Then, the slurry was coated uniformly by a semi-automatic film applicator ZAA 2300 (Zehntner, Switzerland) onto an aluminum foil. The as-prepared electrode sheet was placed in a vacuum oven (Binder, Germany) and dried overnight at 90 °C. Finally, an electric hot rolling press (MTI, USA) was used for densifying the electrode sheet. For the following electrochemical measurements, the electrode sheet was cut into discs of 12 mm diameter.

3.3.2 Cell Assembly

Two kinds of cells were involved in the electrochemical experiments. Swagelok cells with a two-electrode system were used for powder samples, as illustrated in Figure 3.8a. Both working electrode and lithium metal were cut into 12 mm diameter discs. In contrast, the separator (Whatman, UK) was cut into 13 mm discs. Metallic lithium metal (Alfa-Aesar, Germany) was used as both counter and reference electrodes. 1 M LiPF₆ in a 1:1 mixed solvent of ethylene carbonate (EC)/dimethyl carbonate (DMC) (LP30, BASF, USA) with a volume of 100 μL was used as electrolyte.

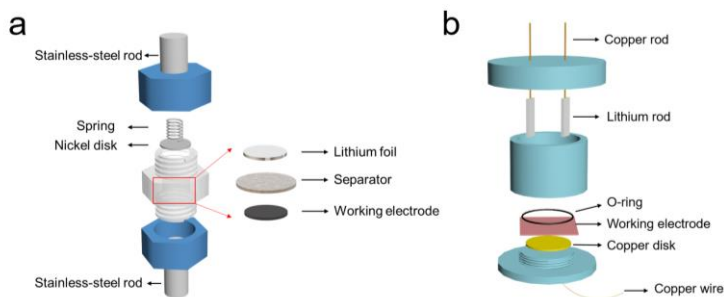


Figure 3.8 Schematic illustration of (a) a Swagelok cell and (b) a Teflon cell.

For the thin-film samples, a homemade Teflon cell was used for the electrochemical measurements. Figure 3.8b shows the configuration of the Teflon cell with a three-electrode system. The working electrode was cut into $3 \times 3 \text{ cm}^2$, and the contact area with electrolyte was fixed at 1.54 cm^2 . A copper disc welded to a copper wire served as conductive contact. Two metallic lithium rods were used as counter and reference electrodes. The electrolyte was the same as in the Swagelok cells, except that the volume was increased to approximately 10 mL. All the cell assemblies in this thesis were completed in an argon-filled glovebox.

3.4 Electrochemical Measurements

The electrochemical tests of the Swagelok cells were performed in an MKF120 climate chamber (Binder, Germany) by using a VMP3 potentiostat (BioLogic, France), and the data were collected by EC-Lab software. The electrochemical tests of Teflon cells were performed in an argon-filled glovebox using an M2300 galvanostat (Maccor, USA), and an Autolab PGSTAT 302 (Metrohm-Autolab B.V., The Netherlands).

For the measurements of the Swagelok cells to be described in Chapters 4 and 6, galvanostatic charge/discharge cycling was operated in the voltage range of 3.0–4.3 V *vs.* Li^+/Li ($\text{IC} = 200 \text{ mA g}^{-1}$). Cyclic voltammogram (CV) tests were

operated in a voltage window of 3.0–4.3 V vs. Li⁺/Li at a scan rate of 0.1 mV s⁻¹. Electrochemical impedance spectroscopy (EIS) tests were conducted with an amplitude of 10 mV in the frequency range of 200 kHz to 0.1 Hz. Galvanostatic intermittent titration (GITT) measurements were performed by using a small current of 0.05 C. The duration of each current pulse was 15 min and was followed by a 60 min resting period.

For the measurements of the Teflon cells to be described in Chapter 5, Galvanostatic charge/discharge cycling was operated in the voltage range of 3.0–4.1 V vs. Li⁺/Li (1C = 24 μA cm⁻²). EIS investigations were conducted with an amplitude of 5 mV in the frequency range from 100 kHz to 0.1 Hz.

References

- 1 A. Rabenau, *Angewandte Chemie International Edition in English* **24** (1985) 1026.
- 2 S. Sōmiya, R. Roy, *Bulletin of Materials Science* **23** (2000) 453.
- 3 E. Bertran, *Solid State Ionics* **165** (2003) 139.
- 4 C. J. Tavares, J. Vieira, L. Rebouta, G. Hungerford, P. Coutinho, V. Teixeira, J. O. Carneiro, A. J. Fernandes, *Materials Science and Engineering: B* **138** (2007) 139.
- 5 H. Stanjek, W. Häusler, *Hyperfine interactions* **154** (2004) 107.
- 6 C. J. Powell, A. Jablonski, *Nuclear Instruments and Methods in Physics Research Section A: Accelerators, Spectrometers, Detectors and Associated Equipment* **601** (2009) 54.
- 7 C. S. Fadley, *Journal of Electron Spectroscopy and Related Phenomena* **178** (2010) 2.
- 8 P. Niehoff, S. Passerini, M. Winter, *Langmuir* **29** (2013) 5806.
- 9 D. Beauchemin, *Analytical Chemistry* **80** (2008) 445.

Chapter 4

LiNi_{0.6}Co_{0.2}Mn_{0.2}O₂ Nanomaterials with Enhanced Li-ion Diffusion Pathways

Abstract

Ni-rich LiNi_{0.6}Co_{0.2}Mn_{0.2}O₂ nanomaterials with a high percentage of exposed {010} facets have been prepared by surfactant-assisted hydrothermal synthesis followed by solid-state reaction. Characterization by X-ray diffraction (XRD) and high-resolution transmission electron microscopy (HRTEM) confirms that the particles have enhanced the growth of nanocrystal planes in favor of Li-ion diffusion. Electrochemical tests show these cathode materials endow a large Li-ion diffusion coefficient, which leads to a superior rate capability and cyclability, suggesting these cathode materials are highly beneficial for practical application in Li-ion batteries.

4.1 Introduction

During the past decades, LIBs have been intensively studied as one of the most promising candidates for complementing fossil fuels in the energy storage field.^[1-3] Up to now, LIBs have successfully powered numerous electronic devices in practical applications, not only portable devices such as laptops, mobile phones, and cameras but also large-scale appliances such as electric vehicles.^[4, 5] Smart grid systems are also considered as a potential market for LIB, as these batteries can cater to the needs of load balancing, uninterrupted power supply, and peak leveling at low cost.

To be compatible with the ever-growing industrial applications, there exists a high demand to pursue batteries with larger storage capacity, extended cycling performance, and better safety for future generations of energy storage.^[6] Compared with the anode side, which can easily achieve a specific capacity of 4200 mAh g^{-1} (Si),^[7, 8] 994 mAh g^{-1} (Sn),^[9] or 782 mAh g^{-1} (SnO_2),^[10] optimization of the cathode side is always the bottleneck in LIB studies. Among the various cathode materials, Ni-rich layered transition-metal mixed-oxide $\text{LiNi}_x\text{Co}_y\text{Mn}_{1-x-y}\text{O}_2$ (NCM $x > 0.5$) has drawn intense attention in investigating high-energy-density, low-cost, and reduced-Co-content cathode materials.^[11, 12] Within the class of Ni-rich cathode materials, $\text{LiNi}_{0.6}\text{Co}_{0.2}\text{Mn}_{0.2}\text{O}_2$ displays a better Li-ion diffusion behavior with negligible temperature dependence, as well as an optimal balance between high energy density and cost-efficiency.^[13-15] However, despite the above merits, as member of Ni-rich NCM cathodes, $\text{LiNi}_{0.6}\text{Co}_{0.2}\text{Mn}_{0.2}\text{O}_2$ is still suffering from several drawbacks. Further improvements and optimization are therefore necessary to utilize its full potential as next generation of cathode materials in LIBs.

It has been established that cation disorder and volume expansion during Li-ion (de)intercalation are mainly responsible for the intrinsically poor rate capacity and moderate cycling stability of Ni-rich NCM cathodes.^[16,17]

Conventional NCM materials have a morphology with a micro-sized, sphere-like structure, in which crystal facets are randomly oriented and densely aggregated. Due to this disordered orientation, the inter-grain stress that mainly occurs at the grain boundaries will be deteriorated upon volume expansion. That may provoke the development of cracks and eventually lead to inferior electrochemical performance.^[18] Several strategies have been employed to overcome these problems, such as cation doping,^[19, 20] surface coating,^[21-23] and structure modification.^[24] However, cation doping and surface coating are always at the expense of energy density, as the introduced compounds are typically electrochemically inactive.^[25] As the NCM material properties are strongly dependent on the microstructure, it has been identified that architecture control is crucial for promoting Li-ion transport within the electrodes, thereby improving the electrode performance without compromising the energy density of NCM cathodes.

Ni-rich NCM cathode materials have a layered hexagonal structure with $R\bar{3}m$ space group. The Li-ion diffusion channels are oriented two-dimensionally, parallel to the Li layers along the a and b axes. Hence in the hexagonal crystal, Li-ion diffusion-active facets are denoted by $\{010\}$, consisting of (010) , $(0\bar{1}0)$, (100) , (110) , $(1\bar{1}0)$ and $(\bar{1}00)$ facets. The (001) and $(00\bar{1})$ facets, perpendicular to the c axis, are closely packed by MO_6 ($M=\text{Ni, Co, Mn}$) octahedra, which hinder Li-ion transport and can therefore be considered as inactive Li-ion diffusion facets.^[26-29] Based on the understanding of the NCM crystal structure, the efforts of structure modification are generally aiming at the fabrication of high-ratio $\{010\}$ facets-exposed materials. However, this is difficult to achieve as the NCM nanomaterials are dominated by $\{001\}$ facets. This phenomenon is related to the much lower surface energy of $\{001\}$ facets. In contrast, the $\{010\}$ facets easily vanish during the synthesis process. Although various surfactants, such as polyvinylpyrrolidone (PVP)^[30, 31] and sodium dodecyl sulfate (SDS)^[32] have been applied to synthesize

favorable NCM crystals,^[33] it remains a challenge to structurally and morphologically control the growth conditions.

In this chapter, we demonstrate the synthesis of Ni-rich $\text{LiNi}_{0.6}\text{Co}_{0.2}\text{Mn}_{0.2}\text{O}_2$ nanomaterials with a unique nanobrick NCM morphology (NB-NCM), which endows a significantly exposed ratio of high-energy {010} facets. A facile hydrothermal method was used in the synthesis. A new type of surface-active agent, cetyltrimethylammonium bromide (CTAB), was introduced to control particle growth. TEM measurements showed that the lateral surfaces of NB-NCM are active {010} facets. These highly exposed {010} facets accordingly resulted in favorable Li-ion diffusion coefficients. Consequently, the NB-NCM electrode materials demonstrated an enhanced rate capability and higher cycling stability than commercial NCM cathode materials. In addition, ordered structural orientation in NB-NCM microparticles displayed crack-free surfaces even after long-term cycling due to the moderate inner-grain stress induced by volume expansion.

4.2 Materials Preparation

Synthesis of transition-metal (TM) hydroxide precursor: the precursor was prepared by a hydrothermal method. Typically, 0.1 M TM-acetate (molar ratio of $\text{Ni}(\text{CH}_3\text{COO})_2 \cdot 4\text{H}_2\text{O}$, $\text{Mn}(\text{CH}_3\text{COO})_2 \cdot 4\text{H}_2\text{O}$ and $\text{Co}(\text{CH}_3\text{COO})_2$ is 6:2:2), 0.2 M urea, and 0.1 M CTAB were evenly stirred in a mixed solution of deionized water and ethanol (volume ratio 1:1). After vigorously stirring, the reactant solution was transferred into the Teflon-lined stainless-steel autoclave. The autoclave was sealed and maintained in an oven at 150 °C for 5 h. After the reaction had been completed, the precipitate was washed and centrifuged three times by deionized water and dried overnight in an oven at 80 °C.

Synthesis of NB-NCM material: the as-prepared TM hydroxide precursor was thoroughly mixed with $\text{LiOH} \cdot \text{H}_2\text{O}$ in an agate mortar, calcinated at 500 °C

for 4h and at 750 °C for 10 h in air. Commercial $\text{LiNi}_{0.6}\text{Co}_{0.2}\text{Mn}_{0.2}$ (C-NCM), used as reference material, was obtained from Tianjin B&M Science and Technology Co., Ltd., China.

4.3 Results and Discussion

4.3.1 Characterization Analysis

The TM hydroxide precursor and NB-NCM material are schematically shown in Figure 4.1a. The precursor with nanoplate morphology serves as a skeleton in the subsequent calcination process. The porous three-dimensional morphology widely opens pathways, promoting Li-ion (de)intercalation during the high-temperature solid-state reaction. The final NB-NCM product with exposed {010} facets maintained the original crystal structure for the Ni-rich cathode, as indicated in Figure 4.1a. The morphology of the TM hydroxide precursor and NB-NCM are shown in the SEM images of Figure 4.1b, c, and Figure 4.2. Due to the adsorbate-directed reaction nature of the cationic surfactant CTAB, the precursors adopted the nanoplate architecture with an average diameter of around 1 μm and assembled randomly into a sphere-like morphology.^[34]

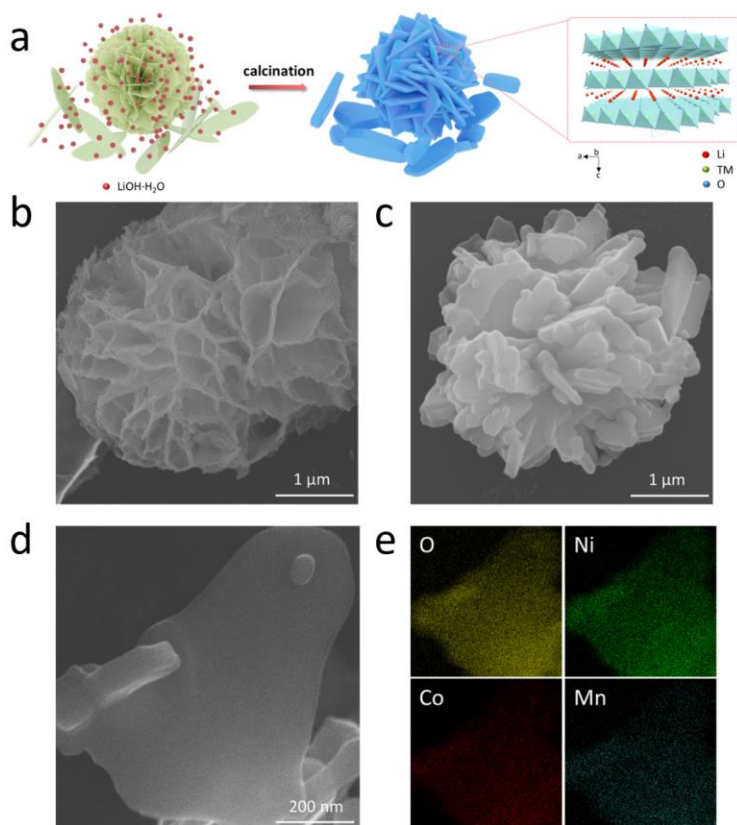


Figure 4.1 (a) Schematic representation of the TM hydroxide precursor and NB-NCM after calcination. SEM images of (b) the TM hydroxide precursor, (c) the NB-NCM product, (d) SEM image of a single NCM-nanobrick, (e) EDS element mapping of a single nanobrick.

The CTAB molecules can effectively stabilize the surface energy of high-energy facets and guarantee the exposure of a significantly increased number of $\{010\}$ facets. After the lithiation reaction, the final NB-NCM product maintained a nanoplate architecture similar to that of the precursor. The as-grown nanobricks possess smooth surfaces and enhanced sidewalls. The thickness of these nanobricks is about 100 nm, which provides a high number of exposed $\{010\}$

facets in contrast to C-NCM materials with irregularly oriented particles (Figure 4.3). Comparing Figure 4.1b and c it is worth noting that the thickness of the final product had increased significantly after the calcination process, which might be due to multilayer plate merging during the high-temperature reaction. The optimized structure not only provides fast Li-ion transfer pathways during the (dis)charging process but also effective electrolyte penetration into the porous electrodes and, in addition, reduces the grain stress between the electrode particles during the (de)lithiation process. Figures 4.1d and e show an example of element mapping results within a single NB-NCM particle. It is found that the Ni, Co, Mn atoms are uniformly distributed. EDX reveals that the ratio of the metal atoms is 42.6: 12.7: 12.3, which is close to the designed metal precursor proportions (Figure 4.4).

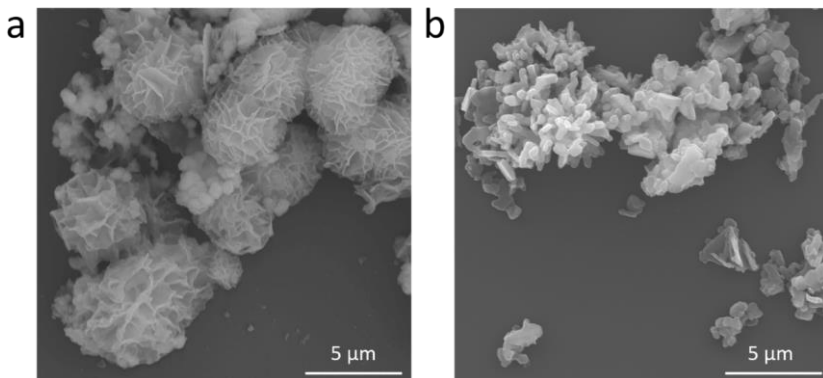


Figure 4.2 SEM images at high resolution of (a) the TM-precursor and (b) the calcinated NB-NCM electrode material.

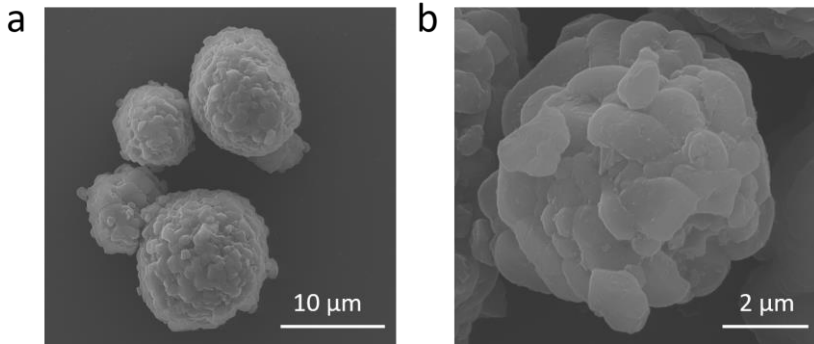


Figure 4.3 SEM images of C-NCM at different magnification.

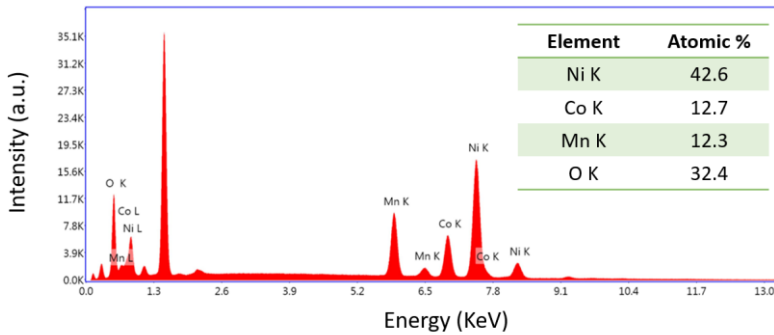


Figure 4.4 EDX spectrum of NB-NCM.

Structural characterization of the TM hydroxide precursor and NB-NCM has been carried out by XRD and is shown in Figure 4.5a and Figure 4.6a, respectively. The peaks in the XRD patterns for the TM hydroxide precursor can be assigned to typical $\text{M}(\text{OH})_2$ compounds where M refers to Ni, Co, or Mn. Figure 4.6a confirms the high crystallinity of NB-NCM as it does not reveal any impurities. All diffraction peaks can be precisely indexed with an $\alpha\text{-NaFeO}_2$ layered structure with R-3m space group. The distinctly separated peaks (003)/(104) and (110)/(018) indicate their well-crystallized layered structure.

According to the calculated results, the intensity ratio of (003)/(104) of NB-NCM from the refined pattern is about 1.74, which is higher than that of the commercial C-NCM material (1.53 in Figure 4.5b), implying negligible cation mixing disorder.^[16] Additionally, NB-NCM shows a slightly higher intensity ratio of 1.12 for (110)/(018) than C-NCM. These results exhibit the enhanced growth of {010} facets in NB-NCM, which must be attributed to the surfactant-assisted synthesis. The lattice parameters of NB-NCM and C-NCM as obtained from the Rietveld refinements are listed in Table 4.1. The similar parameter values suggest that synthetic optimization has little effect on the material's lattice structure. The real difference is related to the material's morphology.

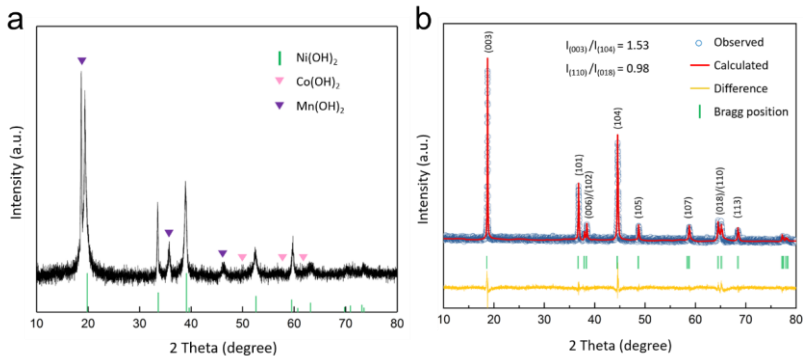


Figure 4.5 (a) XRD pattern of TM hydroxide precursor, (b) Refined XRD pattern of C-NCM.

To elucidate more detailed crystalline information of NB-NCM, TEM, HRTEM, and SAED studies were carried out of an individual nanosheet (Figure 4.6b). Figures 4.6c and d represent the HRTEM images of a lateral and front panel of a nanosheet, respectively. The observed apparent lattice fringes with interplanar spacings of 4.76 and 2.46 Å can be assigned to the (003) and (010) planes, respectively, suggesting that the nanosheets were growing along the *c*-axis. Combined with the SAED patterns, shown in Figures 4.6e and f, it can be

concluded that the obtained NB-NCM nanosheets consisted of a (001) front panel and a (010) plane exposed on the lateral panel. Conclusively, these layered-structured cathode materials reveal two-dimensional Li-ion diffusion pathways perpendicular to the (010) plane. That might favorably enhance the rate capability and power density of NB-NCM cathodes.^[28, 30, 31, 33, 35]

Table 4.1 Lattice parameters, ratio of c/a , and χ^2 for both samples refined from XRD.

Sample	Cell parameters				
	a/Å	c/Å	c/a	Unit volume/ Å ³	χ^2
NB-NCM	2.86255	14.18299	4.9547	100.648	8.48
C-NCM	2.85834	14.16897	4.9571	100.253	6.34

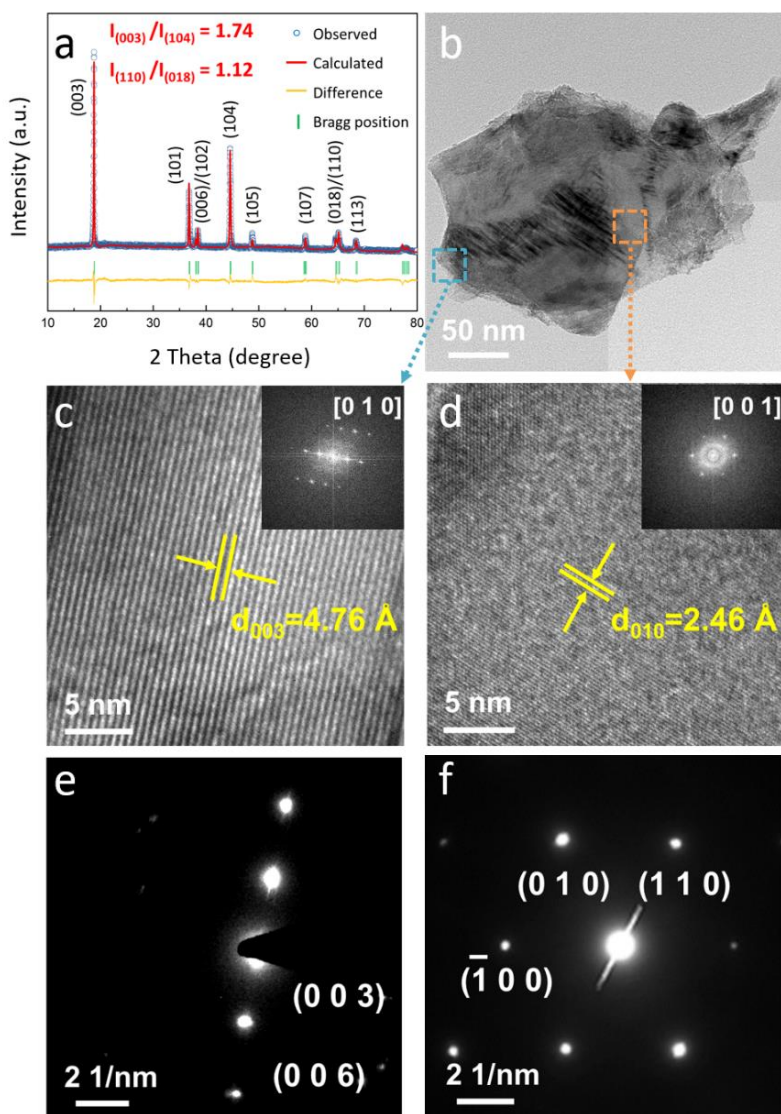


Figure 4.6 (a) Refined XRD patterns of NB-NCM, (b) TEM image of a single NB-NCM nanosheet, (c) HRTEM image of a lateral panel, (d) HRTEM image of a front panel, (e) SAED pattern of the lateral panel, (f) SAED pattern of the front panel.

XPS has been performed on both NB-NCM and C-NCM to analyze the chemical elements' oxidation states at the nanosheets' surface. Figure 4.7a shows that Ni presents a mixture of two valence states for Ni²⁺ and Ni³⁺. The peaks at 854.3 and 860.8 eV can be attributed to Ni²⁺ (2p_{3/2}) and Ni²⁺ (2p_{1/2}), respectively, while that located at 855.9 eV relates to Ni³⁺ (2p_{3/2}).^[36] Interestingly, NB-NCM shows a relatively higher Ni²⁺ ratio in comparison with the C-NCM sample. According to previous studies, NCM cathode materials tend to be structurally more stable with higher Ni²⁺ content at the surface.^[37] Figure 4.7b reveals the XPS spectra of Co 2p, where the peaks at 780.2 and 795.4 eV correspond to Co³⁺ (2p_{3/2}) and Co³⁺ (2p_{1/2}), respectively, implying that the most dominant cobalt oxidation state is Co³⁺.^[38] Additionally, the Mn 2p spectra indicate a mixture of Mn³⁺ and Mn⁴⁺ in both NB-NCM and C-NCM (Figure 4.7c).^[39] In conclusion, these XPS results show almost identical valence states for NB-NCM and C-NCM, except for the Ni spectra: NB-NCM shows that the surface is enriched with Ni²⁺, which might contribute to better electrode stability, as will be shown below.

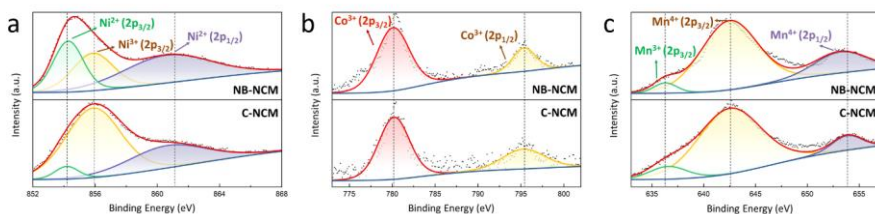


Figure 4.7 XPS spectra of (a) Ni 2p, (b) Co 2p, (c) Mn 2p in as-prepared NB-NCM (upper curves) and C-NCM (lower curves).

4.3.2 Electrochemical Analysis

The electrochemical performance of both the NB-NCM and C-NCM material has been investigated to evaluate the structural advantages of NB-NCM to be applied as cathode material in LIB. Figure 4.8a shows the cycling stability of NB-NCM and C-NCM electrodes in the voltage range of 3.0 - 4.3 V at 1C rate

($1\text{C} = 200\text{ mA g}^{-1}$). Both samples were charged with a constant current up to 4.3 V followed by a constant voltage period of 30 min. The discharge was performed with a constant current. The mass loading for both samples was the same, around 0.002 g. A sharp capacity drop occurs for both electrodes during the first cycle due to the activation process, resulting from the LiOH residue formed during the synthesis. After activation, the NB-NCM electrode combines a high initial capacity of 161 mAh g^{-1} with a high capacity retention of 86.9% after 100 cycles (141 mAh g^{-1}). The Coulombic efficiency maintains close to 100%. The C-NCM electrode delivers a comparable initial storage capacity of 156 mAh g^{-1} , but the capacity degrades much faster. This distinct contrast between the two electrodes indicates that the cathode with an ordered-oriented architecture is more stable upon cycling.

The rate capability is another limiting factor highly relevant for practical use in LIB. Figure 4.8b shows the influence of the current (0.1, 0.2, 0.5, 1, 2, 5 and 10 C) on the electrode storage capacity. The initial storage capacity of 180.6 mAh g^{-1} for the NB-NCM electrode at 0.1 C is reduced to 98.6 mAh g^{-1} at 10 C-rate. Still, it can almost be fully recovered to 175.5 mAh g^{-1} at 0.1 C after 50 cycles, which shows a significantly better rate capability than C-NCM.

These electrochemical results demonstrate that the as-prepared NB-NCM material is intrinsically superior in cycling stability and rate capability, especially at high rates. On the one hand, the nanobrick electrode morphology will endure moderate stress during long-term cycling, thus improving stability. On the other hand, the structure with a high percentage of exposed $\{010\}$ facets offers more Li-ion diffusion channels, which is beneficial for the fast (dis)charge performance.

EIS has been performed with both electrodes to investigate the charge-transfer resistance in pristine and cycled electrodes (Figure 4.8c). Measurements are applied every ten cycles for each battery. As shown in Figure 4.9, it is evident that NB-NCM reveals an approximately four times lower charge-transfer

resistance than C-NCM during cycling. For instance, R_{ct} of NB-NCM is around 35Ω after 100 cycles, while that of C-NCM is 137Ω . The excellent charge-transfer kinetics of NB-NCM results from the modification of the surface chemistry, as demonstrated by XPS, and the ability to keep the structural stability upon electrochemical cycling.

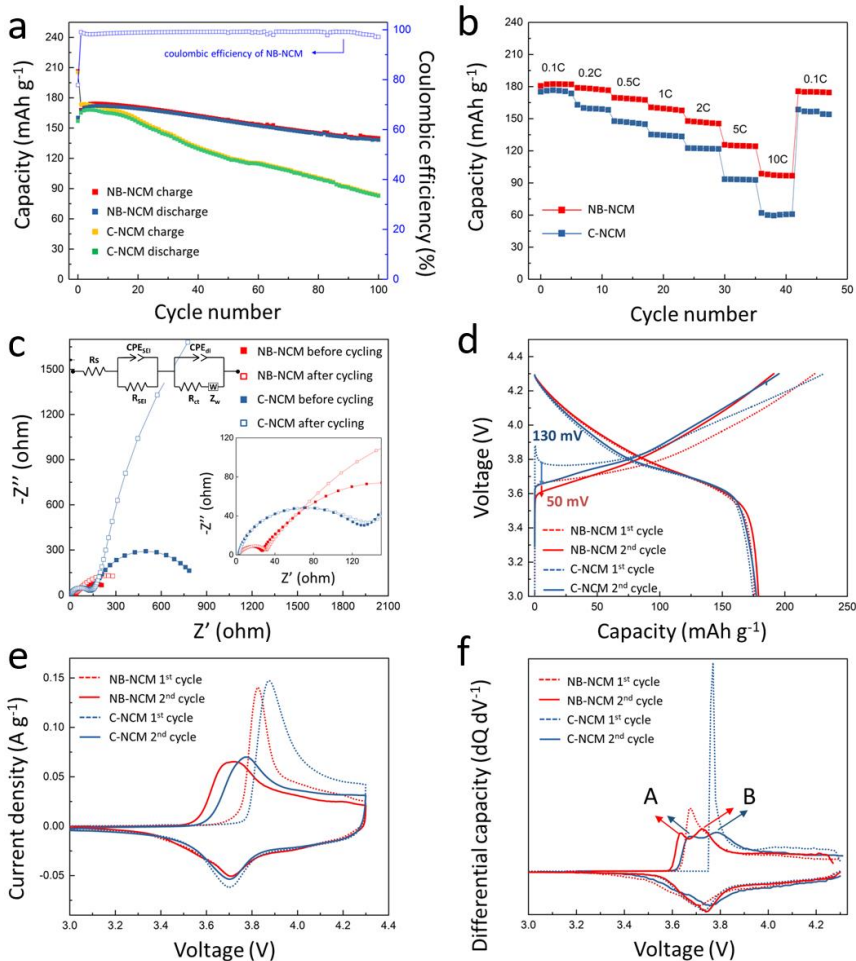


Figure 4.8 (a) Cycling performance of NB-NCM and C-NCM electrodes at 1 C rate, (b) Rate capability at various indicated C-rates, (c) EIS plots of both fresh and cycled electrodes (inset are zoom-in plots in the high-frequency region and analyzed

equivalent circuit), (d) Constant-current voltage (dis)charge curves in the first and second cycle, (e) CV curves of the first and second cycle at a scan rate of 0.1 mV s^{-1} , (f) Differential capacity curves of electrodes in the first and second cycles.

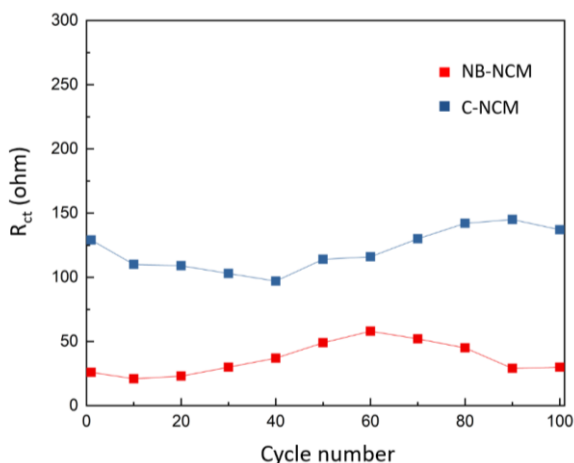


Figure 4.9 Charge-transfer resistance (R_{ct}) of an NB-NCM and C-NCM electrode as a function of cycle number.

To further explore the electrochemical behavior of both electrodes, the first two voltage charge-discharge curves are shown in Figure 4.8d at 0.1 C in the voltage range of 3.0 to 4.3 V . Both NB-NCM and C-NCM deliver a comparable discharge capacity of 178.9 mAh g^{-1} and 177.3 mAh g^{-1} , respectively. C-NCM presents a sharp peak during the initial stages of the first charge cycle, which is related to Li_2CO_3 and LiOH residues at the Ni-rich electrode surface.^[32] At the beginning of the first and second charge curves, the NB-NCM cathode displays significantly lower voltages of around 50 mV than those of the C-NCM electrode (130 mV). This observation indicates that the deintercalation of Li-ions from the NB-NCM electrode is indeed more facile.

CV has also been carried out to study the oxidation and reduction peaks of the electrode materials. As indicated in Figure 4.8e, both samples have oxidation and reduction peaks, representing the delithiation and lithiation processes, respectively. Notably, the separation between the oxidation and reduction peak in the second cycle is around 18 mV for the NB-NCM cathode. In contrast, the value for C-NCM is 55 mV. The substantially reduced voltage separation for NB-NCM demonstrates a decreased electrochemical polarization in contrast to the C-NCM cathode.^[40] Corresponding differential capacity *versus* voltage (dQ/dV) curves obtained from Figure 4.8d are also provided in Figure 4.8f. The dQ/dV curves are in good agreement with the measured CV curves, except that the oxidation peak splits into two peaks, revealing the actual phase transitions of cathodes. During the first cycle, both electrodes exhibit a sharp oxidation peak related to the activation process. After activation, two secondary oxidation peaks appear during the deintercalation process, denoted as peaks A and B. According to previous studies, peaks A and B have been identified as a phase transition from hexagonal (H1) to monoclinic (M) and monoclinic (M) to hexagonal (H2).^[41] In the CV curves of the second cycle, lower oxidation peaks and smaller voltage separation between the oxidation and reduction peaks are observed for the NB-NCM electrode.

GITT is a reliable method to evaluate the lithium-ion diffusion coefficient (D_{Li^+}) inside electrode materials. Figure 4.10a displays typical GITT curves for both electrodes as a function of time with an applied current of 0.02 C in the voltage range of 2.0 to 4.3 V. The D_{Li^+} values can be calculated according to Eq. (1), which has been derived from Fick's second law^[42-44]

$$D_{Li^+} = \frac{4}{\pi} \left(\frac{V_M}{FS} \right)^2 \left[\frac{I \left(\frac{dE}{d\delta} \right)}{\left(\frac{dE}{d\sqrt{\tau}} \right)} \right]^2 \tau \ll \frac{L^2}{D_{Li^+}}, \quad (4.1)$$

where V_M [cm³ mol⁻¹] is the molar volume of the electrode material, F [C mol⁻¹] the Faraday constant, S [cm²] the area of the electrode-electrolyte interface, I [A] the applied current during the titration process, L [cm] the electrode thickness, E [V] the equilibrium voltage and δ is the stoichiometric index in Li _{δ} MO₂. In Eq. (1), two differential factors $dE/d\delta$ and $dE/d\sqrt{\tau}$ are the most crucial values in the calculations. Both derivatives are estimated by finite differences, *e.g.* $\frac{dE}{d\delta} \approx \frac{\Delta E}{\Delta\delta}$ where ΔE is the decrement of the equilibrium voltage during the titration period, and $\Delta\delta$ is the change of the electrode stoichiometry caused by coulometric titration. ΔE can be found from the voltages observed at the end of the relaxation periods after every two subsequent titrations. $\Delta\delta$ obeys

$$\Delta\delta = \frac{I\tau M_B}{zm_B F}, \quad (4.2)$$

where τ [s] is the time interval of the current titration, M_B [g mol⁻¹] the atomic weight of the electrode material, z [-] the valence number of Li ions, and m_B [g] is the mass loading of active material in the electrode. Similarly, $\frac{dE}{d\sqrt{\tau}} \approx \frac{\Delta E}{\Delta\sqrt{\tau}}$ where $\Delta\sqrt{\tau}$ is the increment of the square root of the current titration time. Both differential factors during the discharging process are shown in Figure 4.10b as the function of SOC for the two electrodes. The calculated values for D_{Li+} are summarized in Figure 4.10c as a function of SOC. The NB-NCM electrode reveals D_{Li+} values in the range of $3.0 \cdot 10^{-13}$ to $6.45 \cdot 10^{-11}$ cm² s⁻¹, while those of C-NCM are significantly lower in the range of $6.74 \cdot 10^{-15}$ to $3.96 \cdot 10^{-11}$ cm² s⁻¹. It can be concluded that the NB-NCM electrode clearly shows higher D_{Li+} values compared to those of the C-NCM electrode.

The higher Li-ion diffusion coefficient is also favorable for the fast-charging performance of the NB-NCM electrode. As shown in Figure 4.10d, an ultrahigh charging current of 20 C and a relatively low discharging current (0.2 C) are applied to both electrodes to evaluate their fast-charging storage capacity. The charging time is estimated at around 2.5 min. The inset of Figure 4.10d shows a

sharp distinction in extracted capacity between NB-NCM and C-NCM. NB-NCM still maintains 93.3% capacity after 20 cycles. At the same time, the performance of C-NCM deteriorates severely, and only 68.5% capacity remains after cycling. Another possible conclusion is that these results in terms of high D_{Li^+} and excellent fast-charging ability of NB-NCM illustrate that a well-designed structure with the same orientation and high exposure of active $\{010\}$ facets contribute to the enhanced electrochemical performance. Such an architecture promotes the Li^+ diffusion and withstands the Li^+ intercalation and deintercalation even at high current densities.

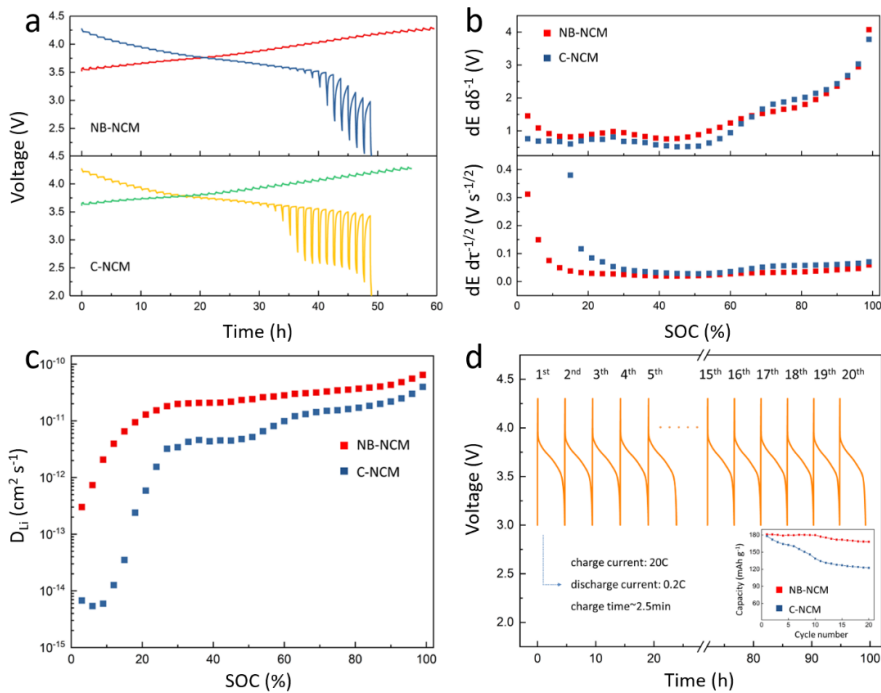


Figure 4.10 (a) GITT curves for both electrodes as a function of time, (b) $dE/d\delta^{-1}$ and $dE/d\tau^{-1/2}$ plots as a function of SOC, (c) Calculated D_{Li^+} values as a function of SOC, (d) The fast-charging capability of the NB-NCM electrode (inset shows fast-charging stability of both electrodes at 20 C-rate).

4.3.3 Post-Mortem Analysis

The electrodes after long-term cycling are disassembled and characterized by cross-sectional SEM. It has been reported that crack formation occurring inside the particles leads to capacity decay during cycling. Figures 4.11a and b show the morphology of post-cycled C-NCM and NB-NCM particles. The small residues attached at the particle surface are carbon black, used during the cathode slurry preparation. As emphasized by the arrows, the cycled C-NCM has extensive cracks throughout the surface, suggesting anisotropic volume expansion inside the particles during Li^+ insertion and extraction. On the other hand, the structure of the cycled NB-NCM particle remains intact and is crack-free at the surface.

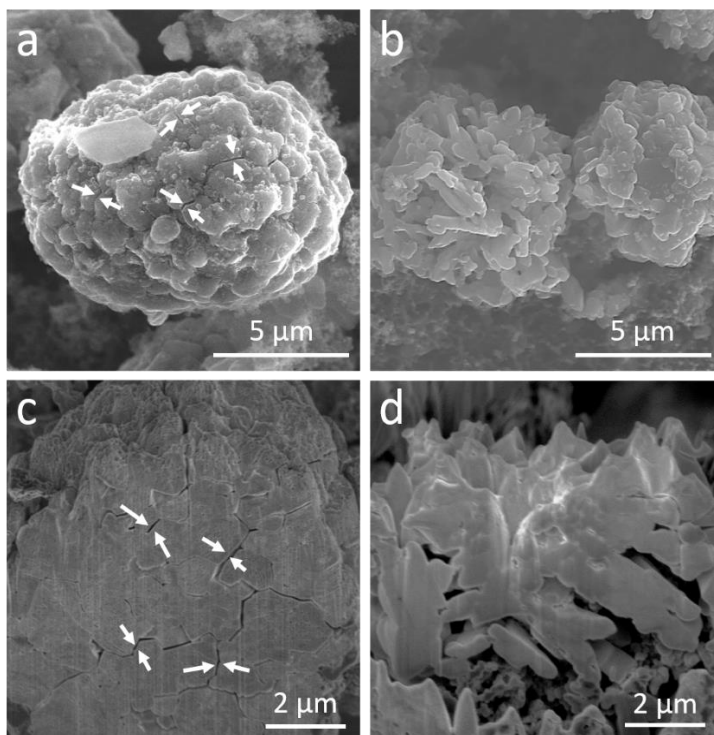


Figure 4.11 SEM images of (a) a C-NCM particle and (b) NB-NCM particle after cycling. SEM images of the cross-section of (c) a C-NCM particle and (d) an NB-NCM particle.

To study structural changes inside the particles after long-term cycling, randomly selected particles were selected and subjected to focused-ion-beam (FIB) processing. Figure 4.11c shows further fracturing inside the C-NCM particle. Cracks inside the C-NCM particles result from internal grain stress induced by the anisotropic volume change during (dis)charging. The as-formed cracks then block the electronic connection between the particles and consequently sacrifice the active material parts. The electrolyte will also penetrate through the cracks and accelerate the formation of contaminating layers, such as Li_xCO_3 and LiOH , resulting in the observed capacity losses.^[45] On the contrary, the NB-NCM electrode reveals a well-preserved intrinsic architecture over the same cycling period (Figure 4.11d), owing to the ordered morphological orientation and accordant volume change of each primary nanobrick. Besides, the unique structure with improved Li-ion diffusion coefficient favors the homogeneous formation of inevitable contaminating layers and contributes to the alleviated capacity decay during cycling.

4.4 Conclusions

Ni-rich $\text{LiNi}_{0.6}\text{Co}_{0.2}\text{Mn}_{0.2}\text{O}_2$ cathode materials with a well-structured nanobrick morphology have been developed, using a facile surfactant-assisted hydrothermal method followed by solid-state reaction. HRTEM and corresponding SAED analyses validate the crystal facet orientation of the nanobrick $\text{LiNi}_{0.6}\text{Co}_{0.2}\text{Mn}_{0.2}\text{O}_2$ cathode material and show the exposed active $\{010\}$ facets in the particles which can facilitate the presence of Li-ion diffusion tunnels and improve the Li-ion diffusivity. Benefitting from this structural advantage, the nanobrick $\text{LiNi}_{0.6}\text{Co}_{0.2}\text{Mn}_{0.2}\text{O}_2$ cathode demonstrates a more favorable Li-ion (de)intercalation reaction kinetics, promising discharge rate capability, and stable cycling performances compared with commercial samples. Additionally, faster reaction kinetics also endowed the NB-NCM material the ability of the fast-charging property, showing the high potential for practical

applications in Li-ion batteries. However, it is noteworthy that the tap density for this nanostructured material has not been improved due to its porous structure. A more suitable pathway must be found to enhance the tap density further and maintain the exposure of high-energy facets. One possible way would be to apply a modified coprecipitation method, carefully control the precipitant concentration, and/or introduce new reagents and surfactants into the synthesis process.^[27, 40] In this way, the agglomeration of small secondary particles will be facilitated, and the compactness of the material will improve.

References

- 1 Q. Cui, Y. Zhong, L. Pan, H. Zhang, Y. Yang, D. Liu, F. Teng, Y. Bando, J. Yao, X. Wang, *Advanced Science (Weinh)* **5** (2018) 1700902.
- 2 S. N. S. Hapuarachchi, Z. Sun, C. Yan, *Advanced Sustainable Systems* **2** (2018) 1700182.
- 3 R. Schmich, R. Wagner, G. Hörpel, T. Placke, M. Winter, *Nature Energy* **3** (2018) 267.
- 4 T. H. Kim, J. S. Park, S. K. Chang, S. Choi, J. H. Ryu, H. K. Song, *Advanced Energy Materials* **2** (2012) 860.
- 5 J. B. Goodenough, *Nature Electronics* **1** (2018) 204.
- 6 S. Natarajan, V. Aravindan, *Advanced Energy Materials* **8** (2018) 1802303.
- 7 J. Z. Xiuxia Zuoa, Peter Müller-Buschbaum, Ya-Jun Cheng, *Nano Energy* **31** (2017) 113.
- 8 Q. W. Xin Su , Juchuan Li , Xingcheng Xiao , Amber Lott , Wenquan Lu , Brian W. Sheldon , Ji Wu, *Advanced Energy Materials* **4** (2014) 1802303.
- 9 W. J. Zhang, *Journal of Power Sources* **196** (2011) 13.
- 10 U. Kasavajjula, C. Wang, A. J. Appleby, *Journal of Power Sources* **163** (2007) 1003.
- 11 F. Schipper, E. M. Erickson, C. Erk, J.-Y. Shin, F. F. Chesneau, D. Aurbach, *Journal of The Electrochemical Society* **164** (2016) A6220.

- 12 A. Manthiram, B. Song, W. Li, *Energy Storage Materials* **6** (2017) 125.
- 13 S. Cui, Y. Wei, T. Liu, W. Deng, Z. Hu, Y. Su, H. Li, M. Li, H. Guo, Y. Duan, W. Wang, M. Rao, J. Zheng, X. Wang, F. Pan, *Advanced Energy Materials* **6** (2016) 1501309.
- 14 Z. Chen, G.-T. Kim, Y. Guang, D. Bresser, T. Diemant, Y. Huang, M. Copley, R. J. Behm, S. Passerini, Z. Shen, *Journal of Power Sources* **402** (2018) 263.
- 15 W. Liu, X. Li, D. Xiong, Y. Hao, J. Li, H. Kou, B. Yan, D. Li, S. Lu, A. Koo, K. Adair, X. Sun, *Nano Energy* **44** (2018) 111.
- 16 J. Zhao, W. Zhang, A. Huq, S. T. Misture, B. Zhang, S. Guo, L. Wu, Y. Zhu, Z. Chen, K. Amine, F. Pan, J. Bai, F. Wang, *Advanced Energy Materials* **7** (2017) 1601266.
- 17 H. H. Ryu, K. J. Park, C. S. Yoon, Y. K. Sun, *Chemistry of Materials* **30** (2018) 1155.
- 18 H. H. Sun, A. Manthiram, *Chemistry of Materials* **29** (2017) 8486.
- 19 S. Gao, X. Zhan, Y. T. Cheng, *Journal of Power Sources* **410** (2019) 45.
- 20 Q. Ran, H. Zhao, X. Shu, Y. Hu, S. Hao, Q. Shen, W. Liu, J. Liu, M. Zhang, H. Li, X. Liu, *ACS Applied Energy Materials* **2** (2019) 3120.
- 21 C.-H. Jo, D.-H. Cho, H.-J. Noh, H. Yashiro, Y.-K. Sun, S. T. Myung, *Nano Research* **8** (2014) 1464.
- 22 C. H. Jo, D. H. Cho, J. W. Lee, Y. Hitoshi, S. T. Myung, *Journal of Power Sources* **282** (2015) 511.
- 23 H. Kim, M. G. Kim, H. Y. Jeong, H. Nam, J. Cho, *Nano Letter* **15** (2015) 2111.
- 24 Y. Chen, P. Li, Y. Li, Q. Su, L. Xue, Q. Han, G. Cao, J. Li, *Journal of Materials Science* **53** (2017) 2115.
- 25 Z. F. Tang, R. Wu, P. F. Huang, Q. S. Wang, C. H. Chen, *Journal of Alloys and Compounds* **693** (2017) 1157.
- 26 G. Z. Wei, X. Lu, F. S. Ke, L. Huang, J. T. Li, Z. X. Wang, Z. Y. Zhou, S. G. Sun, *Advanced Materials* **22** (2010) 4364.

- 27 L. Zhang, N. Li, B. Wu, H. Xu, L. Wang, X. Q. Yang, F. Wu, *Nano Letter* **15** (2015) 656.
- 28 M. Xu, L. Fei, W. Zhang, T. Li, W. Lu, N. Zhang, Y. Lai, Z. Zhang, J. Fang, K. Zhang, J. Li, H. Huang, *Nano Letter* **17** (2017) 1670.
- 29 Y. Cho, P. Oh, J. Cho, *Nano Letter* **13** (2013) 1145.
- 30 F. Fu, G. L. Xu, Q. Wang, Y. P. Deng, X. Li, J. T. Li, L. Huang, S. G. Sun, *Journal of Materials Chemistry A* **1** (2013) 3860.
- 31 J. Tian, Y. Su, F. Wu, S. Xu, F. Chen, R. Chen, Q. Li, J. Li, F. Sun, S. Chen, *ACS Applied Materials & Interfaces* **8** (2016) 582.
- 32 X. Ju, H. Huang, W. He, H. Zheng, P. Deng, S. Li, B. Qu, T. Wang, *ACS Sustainable Chemistry & Engineering* **6** (2018) 6312.
- 33 W. Xiang, W. Y. Liu, J. Zhang, S. Wang, T. T. Zhang, K. Yin, X. Peng, Y. C. Jiang, K. H. Liu, X. D. Guo, *Journal of Alloys and Compounds* **775** (2019) 72.
- 34 Y. Ma, C. Zhang, C. Hou, H. Zhang, H. Zhang, Q. Zhang, Z. Guo, *Polymer* **117** (2017) 30.
- 35 L. Chen, Y. Su, S. Chen, N. Li, L. Bao, W. Li, Z. Wang, M. Wang, F. Wu, *Advanced Materials* **26** (2014) 6756.
- 36 J. Fu, D. Mu, B. Wu, J. Bi, H. Cui, H. Yang, H. Wu, F. Wu, *ACS Applied Materials & Interfaces* **10** (2018) 19704.
- 37 Y. Zhang, Z. B. Wang, F. D. Yu, L. F. Que, M. J. Wang, Y. F. Xia, Y. Xue, J. Wu, *Journal of Power Sources* **358** (2017) 1.
- 38 Q. Ran, H. Zhao, Q. Wang, X. Shu, Y. Hu, S. Hao, M. Wang, J. Liu, M. Zhang, H. Li, N. Liu, X. Liu, *Electrochimica Acta* **299** (2019) 971.
- 39 Y. Shi, M. Zhang, C. Fang, Y. S. Meng, *Journal of Power Sources* **394** (2018) 114.
- 40 X. Xu, H. Huo, J. Jian, L. Wang, H. Zhu, S. Xu, X. He, G. Yin, C. Du, X. Sun, *Advanced Energy Materials* **9** (2019) 1803963.
- 41 S.-U. Woo, C. S. Yoon, K. Amine, I. Belharouak, Y.-K. Sun, *Journal of The Electrochemical Society* **154** (2007) A1005.

- 42 Z. Shen, L. Cao, C. D. Rahn, C. Y. Wang, *Journal of The Electrochemical Society* **160** (2013) A1842.
- 43 R. Yu, X. Wang, D. Wang, L. Ge, H. Shu, X. Yang, *Journal of Materials Chemistry A* **3** (2015) 3120.
- 44 W. Weppner, R. A. Huggins, *Journal of The Electrochemical Society* **124** (1977) 1569.
- 45 W. Liu, P. Oh, X. Liu, M. J. Lee, W. Cho, S. Chae, Y. Kim, J. Cho, *Angewandte Chemie International Edition* **54** (2015) 4440.

Chapter 5

Interfacial Characterization of

LiNi_{0.6}Co_{0.2}Mn_{0.2}O₂ Thin Film Cathodes

Abstract

Ni-rich LiNi_{0.6}Co_{0.2}Mn_{0.2}O₂ and LiNbO₃-protected LiNi_{0.6}Co_{0.2}Mn_{0.2}O₂ thin-film cathodes have been prepared by radio-frequency (RF) magnetron sputtering. Electrochemical investigations show enhanced stability of LiNbO₃-protected cathodes compared with bare LiNi_{0.6}Co_{0.2}Mn_{0.2}O₂. The interfacial interaction of LiNbO₃ and LiNi_{0.6}Co_{0.2}Mn_{0.2}O₂ layers has been investigated by XPS depth profiling and demonstrates different cathode-electrolyte-interface (CEI) film formation processes at the electrodes. The results elaborate on the interaction between LiNbO₃ and LiNi_{0.6}Co_{0.2}Mn_{0.2}O₂, emphasizing the role of the LiNbO₃ layer in improving the cycling performance of Ni-rich cathodes.

5.1 Introduction

Rechargeable LIBs have undoubtedly become one of the most powerful energy storage devices upon intensive studies for decades. They have been successfully applied in various fields, such as portable devices, electric vehicles, and large-scale energy systems.^[1] Over the last decades, wide-ranging research has been pursuing battery systems with higher energy density, higher safety, and lower cost for meeting the increasing demands of LIBs.^[2, 3] Cathode materials are considered the bottleneck for further improving the battery performance to the next level. Among all sorts of cathode materials, Ni-rich layered transition-metal oxide $\text{LiNi}_x\text{Co}_y\text{Mn}_z\text{O}_2$ ($x > 0.5$) has shown the largest commercial interest as an alternative to LiCoO_2 , owing to its demonstrated high capacity of up to $\sim 200\text{mAh g}^{-1}$. Despite a promising high energy density, Ni-rich cathodes are not yet very stable compared with other conventional cathodes (LiCoO_2 , LiMnO_2 , LiFePO_4).^[4, 5] Ni-rich cathodes suffer from several deficiencies, including transition-metal dissolution, surface phase transformation from layered to inactive rock-salt structure, and residuals adhered on the electrode caused by electrolyte decomposition.^[6, 7] All side products comprise a CEI film on the electrode/electrolyte interface, which dramatically increases the system impedance and can be detrimental to battery performance and lifetime.^[8]

Many candidates have been introduced as protective layers to stabilize the CEI film on Ni-rich cathodes. One can mention metal oxides (Al_2O_3 , TiO_2 , MgO , *etc.*),^[9-11] metal fluorides (AlF_3 , LiF , *etc.*),^[12, 13] solid-state electrolytes (Li_3PO_4 , Li_2ZrO_3 , *etc.*),^[14-16] carbon (*e.g.* graphene, carbon-nanotube (CNT)) and polymers.^[17-20] However, most materials are Li-ion insulators with extremely low Li-ion diffusion coefficients, leading to low initial discharge capacities. Good Li-ion conductors, such as the solid-state electrolytes, can efficiently alleviate electrode degradation by suppressing the CEI film formation and providing facile Li-ion transportation across the interface. Lithium niobate (LiNbO_3), a solid-state electrolyte with high ionic conductivity and a relatively wide electrochemical

stability window, has been applied as a coating layer on other cathode materials (LiCoO_2 , LiMn_2O_4 , $\text{LiNi}_{0.5}\text{Mn}_{1.5}\text{O}_4$).^[21-23] However, the combination of LiNbO_3 and a Ni-rich cathode is rarely reported in the literature. The mechanism behind the improved performance of a LiNbO_3 -coated Ni-rich cathode remains unclear, and the interaction between layers was neither studied.

Additionally, existing research has recognized that additives used in conventional powder electrodes, such as conductive carbon and PVDF binder, also play a critical role in CEI and SEI film formation at cathodes and anodes, respectively.^[24, 25] The contributions from these additives are likely to obscure reactions between the electrodes and electrolytes, making it essential to fabricate a simplified system to study the electrode degradation mechanisms fundamentally. Thin-film electrodes can provide a simple electrode configuration to study interfacial phenomena by isolating the additives from the electrodes and electrolytes. Another feature of the thin-film electrodes is the highly homogeneous morphology, which offers a clean and identical sample surface for analyses. Recently, several reports described thin-film electrodes for interfacial investigations. Still, the study of the LiNbO_3 /Ni-rich cathode thin-film electrode system has not been reported before.^[26-29]

In this work, we fabricated $\text{LiNi}_{0.6}\text{Co}_{0.2}\text{Mn}_{0.2}\text{O}_2$ cathodes (bare-NCM) and LiNbO_3 -coated $\text{LiNi}_{0.6}\text{Co}_{0.2}\text{Mn}_{0.2}\text{O}_2$ cathodes (LiNbO_3 @NCM) by RF magnetron sputtering. Clearly enhanced electrochemical performance was obtained with LiNbO_3 -protected electrodes. The interaction between NCM and LiNbO_3 and the CEI film formation mechanism between the electrodes and electrolyte are also illustrated.

5.2 Materials Preparation

All sputter deposition targets were obtained from Advanced Engineering Materials Co., Ltd., China. Silicon wafers and quartz wafers with 3' diameters

were used as substrates. The current collector was deposited by direct-current magnetron sputtering of Pt onto the Si substrates. Thin-film electrodes were prepared by radio-frequency magnetron sputtering (Lesker, UK), combined with post-annealing. The sputtering process was performed in an Ar atmosphere under the chamber pressure of 5 mTorr and the sputtering power of 70 W. After deposition, the thin-film samples were annealed in air at either 300, 400, or 500 °C.

5.3 Results and Discussion

5.3.1 Characterization Analysis

Ni-rich $\text{LiNi}_{0.6}\text{Co}_{0.2}\text{Mn}_{0.2}\text{O}_2$ thin-films were deposited using a $\text{Li}_{1.1}\text{Ni}_{0.6}\text{Co}_{0.2}\text{Mn}_{0.2}\text{O}_2$ ceramic target. Excess of Li was used to compensate for Li losses during sputtering and subsequent annealing. SEM images and corresponding EDX elemental mapping analyses of the annealed- $\text{LiNi}_{0.6}\text{Co}_{0.2}\text{Mn}_{0.2}\text{O}_2$ thin-film samples deposited on Si substrate are shown in Figure 5.1. Compared with the as-deposited NCM films (Figure 5.2), the thin film surface after high-temperature annealing presents a relatively rough morphology, with small sphere-like aggregated particles (Figure 5.1a).

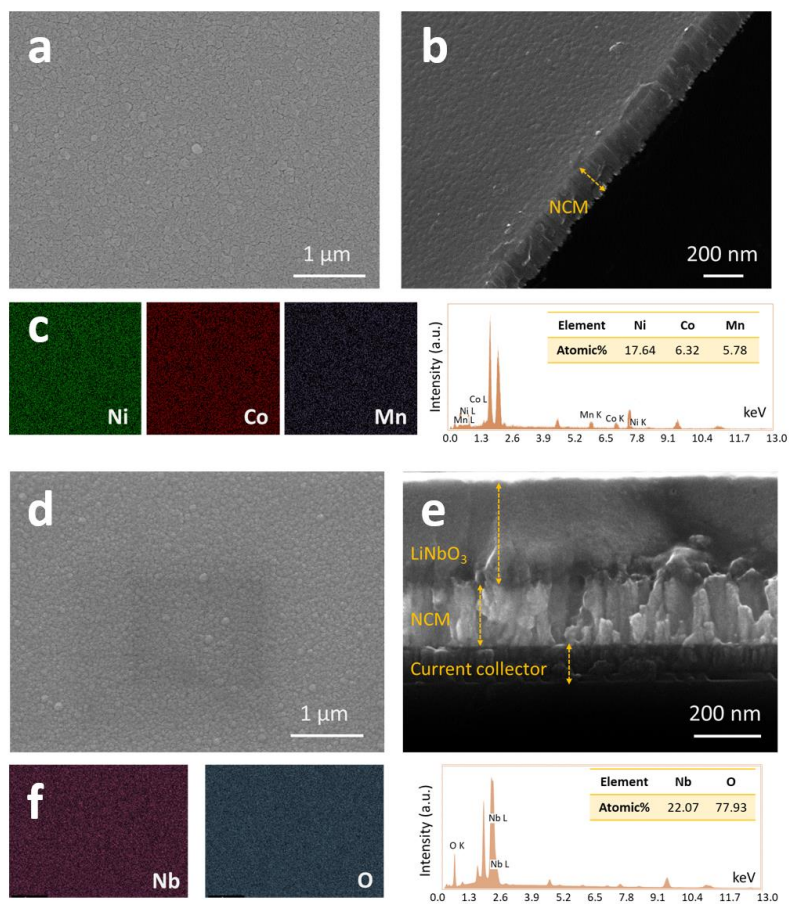


Figure 5.1 SEM image of (a) bare-NCM thin-film, and (d) LiNbO_3 @NCM thin-film. Cross-sectional SEM image of (b) bare-NCM thin-film, and (e) LiNbO_3 @NCM thin-film. EDX elemental analysis of (c) bare-NCM thin-film, and (f) LiNbO_3 @NCM thin-film.

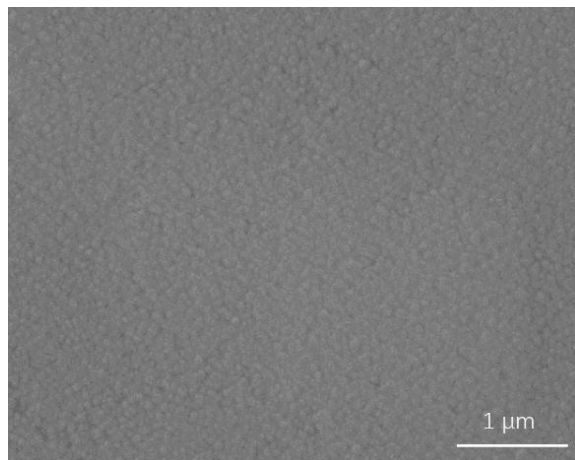


Figure 5.2 SEM image of an as-deposited bare-NCM thin-film.

The EDX elemental analysis shows a uniform elemental distribution for the crystallized NCM film (Figure 5.1c). It reveals that the Ni:Co:Mn atomic ratio is 17.64:6.32:5.78, consistent with the NCM sputtering target's elemental ratio. Similar to the pure NCM film, the surface of LiNbO_3 @NCM film shows nano-sized crystalline grains (Figure 5.1d). A cross-sectional view of the film is given in Figure 5.1e. The thickness of NCM and LiNbO_3 layers are 200 and 300 nm, respectively. The interfacial contact between the layers is found to be compact. The elemental distribution of Nb and O in the LiNbO_3 @NCM thin film has also been examined by EDX measurements (Figure 5.1f). The atomic ratio between Nb and O (22.07:77.93) is similar to that of the LiNbO_3 target. Note that EDX of active electrode materials often shows some unlabeled peaks related to the elements in the substrate, the adhesive layer, barrier layer, and current collector. In the present study, the irrelevant elements are excluded, and a precise elemental ratio of active material is obtained.

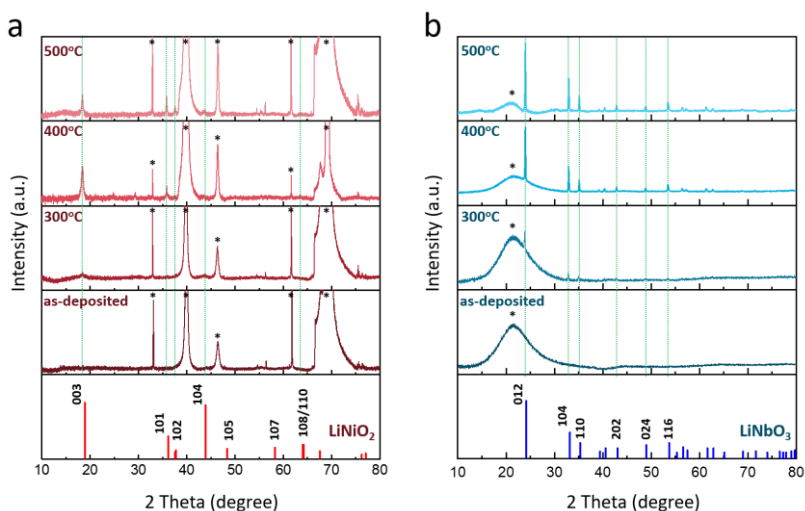


Figure 5.3 XRD patterns of (a) NCM thin film and (b) LiNbO_3 thin film under different annealing conditions. The peaks marked with black asterisks are related to the substrates. Silicon and quartz wafers were used as substrates for the XRD measurements of NCM and LiNbO_3 thin films, respectively. The broad peak of the quartz wafers will overlap with the characterized (003) reflection of NCM thin film because the silicon wafer was used for the XRD measurements of NCM thin films.

XRD is employed to compare the crystal structure of the as-prepared films at various annealing temperatures to determine the most optimized crystallization conditions. The diffraction patterns of the as-deposited NCM film and samples post-annealed at 300, 400, and 500 °C (Figure 5.3a) indicate a structural transformation from the amorphous phase to a crystalline structure with the sharpest peaks at the highest temperature. Compared to the standard LiNiO_2 hexagonal layered structure (R-3m space group), the samples annealed at 400 and 500 °C are in good agreement with the reference material. Notably, the film annealed at 500 °C displays more distinct (101) and (104) reflections than the 400 °C annealed film. It has been proven that Li-ion transportation takes place along

the (101) and (104) planes, while it is impeded along the (003) plane.^[29] Therefore, post-annealing NCM thin films at 500 °C were further applied in all experiments. In addition, LiNbO_3 thin-films prepared at various annealing temperatures have been XRD analyzed in detail. As shown in Figure 5.3b, the as-deposited LiNbO_3 presents an amorphous structure. However, with increasing annealing temperature, the crystallinity of the thin film is significantly enhanced. The characteristic peaks of the 400 and 500 °C annealed films correspond nicely to the standard hexagonal LiNbO_3 structure (R3cH space group). Considering that the NCM layer was annealed at 500 °C, the heating process for the LiNbO_3 layer applied at 400 °C will not influence the crystallinity of NCM.

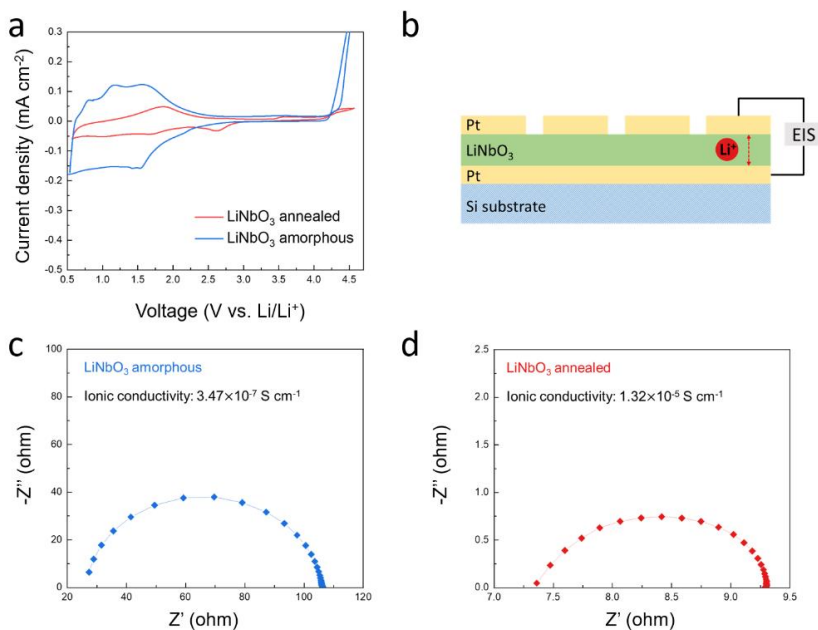


Figure 5.4 (a) CV curves of a LiNbO_3 thin-film electrode. (b) Schematic diagram of Pt/ LiNbO_3 /Pt sandwich electrode. (c) and (d) Ionic conductivity measurements of amorphous and crystalline LiNbO_3 thin films, respectively.

Electrochemical examinations are carried out on LiNbO_3 thin-film electrodes to probe its feasibility as a solid-state electrolyte. The stability window of the annealed LiNbO_3 film is investigated (the liquid electrolyte used in the measurement is 1M LiPF_6 , EC/DMC 1:1), and one reversible redox couple is found at 2.6 and 3.7 V in the CV of Figure 5.4a. In contrast to the amorphous LiNbO_3 film, the annealed sample is more stable with a stability window ranging from approximately 2.0 to 4.2 V, comparable with what has been reported in literature.^[30,31] Impedance measurements are made with a sandwich-structured Pt/ LiNbO_3 /Pt electrode to investigate the ionic conductivity (Figure 5.4b). The area and thickness of each micro-electrode are $1 \times 1 \text{ cm}^2$ and 300 nm, respectively. The result reflects that the annealed films reveal a higher Li-ion conductivity ($1.32 \cdot 10^{-5} \text{ S cm}^{-1}$) at room temperature, compared to the amorphous films ($3.47 \cdot 10^{-7} \text{ S cm}^{-1}$ in Figures 5.4c and 5.4d).

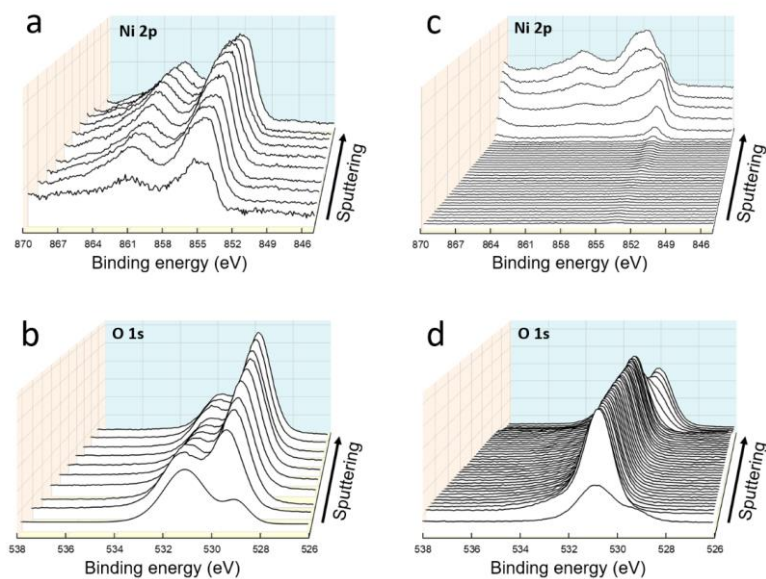


Figure 5.5 XPS depth profiling of a pristine bare-NCM thin-film for (a) Ni 2p, (b) O 1s, and a pristine LiNbO_3 @NCM thin-film for (c) Ni 2p, (d) O 1s spectra.

The effect of the LiNbO_3 layer coating on NCM cathodes is further investigated by a XPS depth-profiling analysis. Multiple signals are collected after sputtering with an Ar500+ cluster ion source for 80 s for each collection. The evolution of the Ni 2p, Co 2p, Mn 2p, Nb 3d, and O 1s reflections for a bare-NCM film and a LiNbO_3 @NCM electrode are shown in Figures 5.5 and 5.6, respectively. In the Ni 2p spectra (Figure 5.5a), two characteristic peaks located at 855.8 and 862.5 eV are corresponding with the binding energy of $\text{Ni}^{3+} 2p_{3/2}$ and $\text{Ni}^{2+} 2p_{1/2}$, respectively. The elemental valence of Ni in the bare-NCM film remains consistent along with the increasing sputtering depth. In Figure 5.5b, two peaks of O 1s spectra are assigned to the bonding energy in M-O (M=Ni, Co, Mn; 529.1 eV) and Li_2CO_3 (or LiOH; 532.2 eV). The existence of Li_2CO_3 (or LiOH) results from the chemically adsorbed species. This phenomenon has been commonly observed in the XPS spectra of Ni-rich cathode materials.^[12] The sample is prepared in the open air. Thus a higher content of adsorbed species is found at the sample surface, leading to a higher intensity of the Li_2CO_3 (or LiOH) peak on the first sputtering layer.^[32]

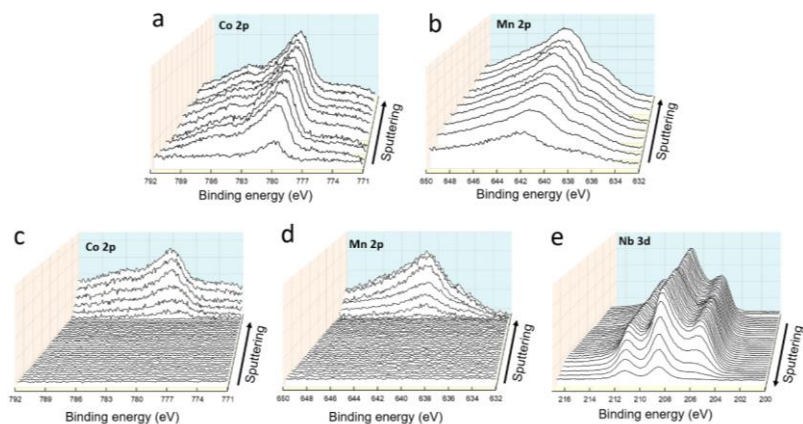


Figure 5.6 XPS depth profiling analysis of the pristine bare-NCM thin-film for (a) Co 2p, (b) Mn 2p, and pristine LiNbO_3 @NCM thin-film for (c) Co 2p, (d) Mn 2p, (e) Nb 3d spectra.

The XPS depth profiles obtained with a LiNbO_3 @NCM thin film lead to interesting observations of the NCM/ LiNbO_3 interface. In Figure 5.5c, the evolution of Ni 2p spectra reveals a gradual valence change at the NCM/ LiNbO_3 interface. The O spectra of LiNbO_3 @NCM thin-film also present the transition from the LiNbO_3 layer (single peak located at 530.8 eV) to the NCM layer (two peaks) (Figure 5.5d). In addition, the Nb 3d spectra extracted from LiNbO_3 @NCM thin-film display the valence evolution as well (Figure 5.6e). However, for Co and Mn, both thin films show identical elemental valences. Apparently, no valence state changes can be found at the interface. In Figures 5.6a and 5.6c, the dominant valence of Co is Co^{3+} and is represented by the strong peak at 779.5 eV. For the Mn spectra, the binding energy of 641.9 eV indicates that the Mn ions mainly exist as tetravalent in as-prepared NCM film (Figures 5.6b and 5.6d). The results obtained on NCM films match well with the NCM samples

prepared by other synthesis methods.^[33] The corresponding Ni 2p, Nb 3d, and O 1s spectra at the NCM/LiNbO₃ interface are summarized in Figure 5.7.

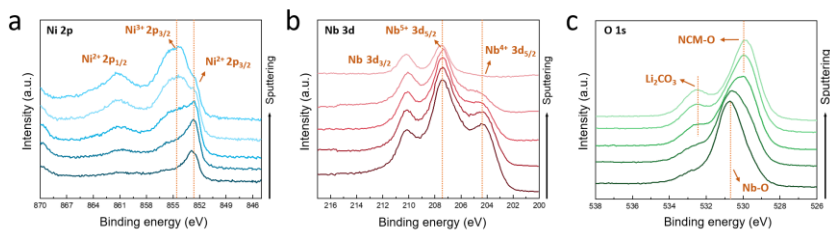


Figure 5.7 XPS spectra of (a) Ni 2p, (b) Nb 3d, and (c) O 1s XPS spectra extracted from the LiNbO₃/NCM interface.

As displayed in Figure 5.7, the spectra of Ni 2p, Nb 3d, and O 1s along the depth direction from the LiNbO₃ top layer towards the underlying NCM layer are extracted. Figure 5.7a shows that Ni exists in the interlayer as Ni²⁺ ions. The intensity of the Ni²⁺ 2p_{3/2} peak (853.6 eV) increases while the etching process approaching the NCM layer, and the dominant valence state of Ni ion gradually transfers into Ni³⁺ (855.8 eV), consistent with the chemical environment in pure NCM material. Accordingly, the spectra of Nb 3d presents Nb⁵⁺ 3d_{5/2} (207.1 eV) on the LiNbO₃ surface, while the co-existence of Nb⁵⁺ 3d_{5/2} and Nb⁴⁺ 3d_{5/2} peaks (204.2 eV) in the bulk of the LiNbO₃ layer (Figure 5.8). This phenomenon can be explained by insufficient oxygen exposure to LiNbO₃ during the heat treatment; the structure of the as-deposited layer is highly compact. The Nb⁴⁺ peak intensity decreases in the interface layer and eventually becomes undetectable along with an increasing sputtering depth (Figure 5.7b).

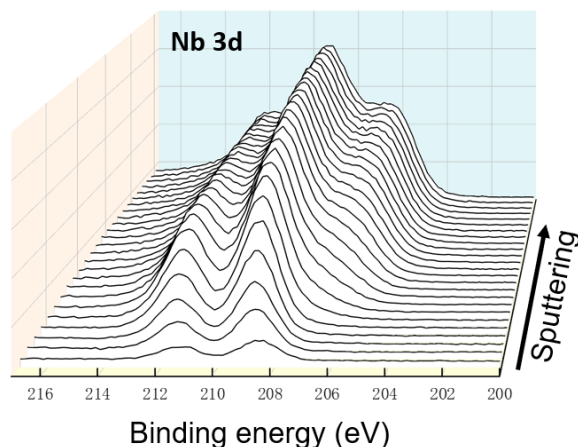


Figure 5.8 Nb 3d XPS depth profiling spectra of LiNbO_3 layer on LiNbO_3 @NCM thin-film.

The decreasing intensity of Nb^{4+} peak when approaching the NCM layer is related to the escalating influence of Ni ions on Nb species. Ni reveals a much stronger electronegativity than Nb.^[34] Thus, the electronic cloud of Nb^{4+} was polarized toward Ni ions, resulting in the raised valence state of Nb^{4+} . The lattice oxygen released from the NCM surface may also oxidize Nb^{4+} into Nb^{5+} in the interface area. In addition, the O 1s spectra at the interface show a transformation at the interface (Figure 5.7c). The single sharp peak located at 530.8 eV demonstrates that the O element at the interface is mainly from Nb-O. With increasing depth, the O 1s spectra become gradually dominated by O species from the NCM material (M-O, M=Ni, Co, Mn). As discussed before, a small peak observed at 532.2 eV is attributed to chemically adsorbed oxygenic species (Li_2CO_3 or LiOH), displaying an identical characteristic peak as the O spectra obtained for pure NCM films. In short, the interface between NCM and LiNbO_3 layers formed during the heat treatment in the preparation process is associated with Ni ion diffusion and interaction with the LiNbO_3 films. Moreover, based on

the XPS depth profiling analyses, the intrinsic thickness of the interface is analyzed at approximately 30 nm.

5.3.2 Electrochemical Analysis

The electrochemical properties of the as-obtained thin-film electrodes are shown in Figure 5.9 within a voltage range of 3.0 to 4.1 V (*vs.* Li/Li^+). As a reference, the performance of a commercial $\text{LiNi}_{0.6}\text{Co}_{0.2}\text{Mn}_{0.2}\text{O}_2$ powder electrode is also included in Figures 5.9a and 5.9b. The characteristic sloping voltage regions for thin-film electrodes can be found in the (dis)charge curves and are comparable to that for an NCM powder electrode. Obviously, the discharge specific capacity of the thin-film electrodes is somewhat lower than that of the commercial powder electrode. A probable explanation is that the thin-film electrode configuration is restricted by its contact area with the electrolyte. Consequently, the electrochemical reaction of active material is somewhat hampered during operation. A similar phenomenon has been reported in other work.^[25] Nevertheless, the LiNbO_3 -coated sample demonstrates an improved specific discharge capacity (161.4 mAh g^{-1}) in comparison to the bare NCM thin-film (157.5 mAh g^{-1}) (Figure 5.9a). Figure 5.9b shows the differential capacity (dQ/dV) plot of all electrodes shown in Figure 5.9a. Two oxidation peaks appeared during the deintercalation process, revealing the identical phase transition for all electrodes. According to previous research, these two peaks can be identified as phase transformation from hexagonal (H1) to monoclinic (M) and monoclinic to hexagonal (H2) in Ni-rich cathodes.^[35, 36] These results indicate that the thin films underwent the same phase transformation process as powder electrodes.

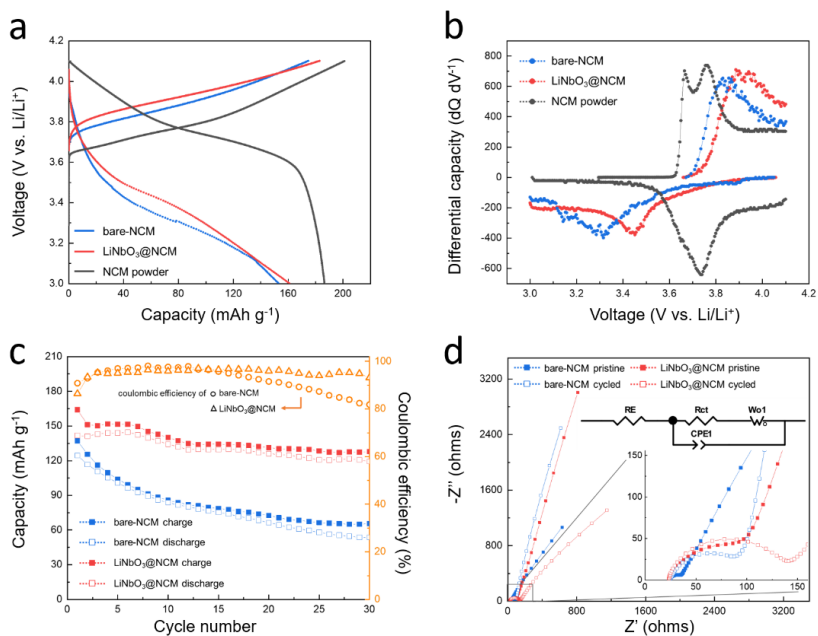


Figure 5.9 (a) Constant-current (dis)charge voltage curves of thin-film and powder electrodes at 0.2 C-rate, (b) Differential capacity curves of the constant-current curves of (a), (c) Cycling performance of thin-film electrodes at 0.5 C, (d) EIS plots of pristine and cycled electrodes.

The cycling stability of thin-film electrodes during the first 30 cycles is shown in Figure 5.9c. For the LiNbO_3 -protected NCM thin-film, it can be seen that the initial discharge capacity and coulombic efficiencies are higher than those of the bare-NCM thin-film electrode. The discharge capacity of both films is declining upon cycling, whereas the bare-NCM film exhibits a faster fading rate. Its capacity drops 51.8% and can only deliver approximately 58.1 mAh g^{-1} after 30 cycles. On the other hand, the specific capacity of LiNbO_3 @NCM film retains 84.1% and reveals 119.2 mAh g^{-1} at the end of cycling. Furthermore, the LiNbO_3 @NCM film demonstrates an enhanced and steady coulombic efficiency

above 90% compared to bare NCM film of around 80%. The continuous decay of coulombic efficiency for the bare-NCM film suggests degradation of its reversible specific capacity during operation.

The electrochemical impedance of both thin-film electrodes before and after cycling is shown in Figure 5.9d. The Nyquist plots show a semicircle in the high-frequency range and a straight line at low frequencies, representing the charge-transfer resistance (R_{ct}) and Li-ion diffusion, respectively. The fitting parameters of ohmic resistance (R_E) and R_{ct} for electrodes are presented in Table 5.1. For the pristine samples, the bare-NCM reveals a low R_{ct} value of 11.4 Ω , while the R_{ct} of the $\text{LiNbO}_3@\text{NCM}$ sample shows an impedance of 93.5 Ω owing to the increased layer thickness. However, after cycling, the initial resistance of bare-NCM shows a significant increase and rise to 77.1 Ω . In contrast, the $\text{LiNbO}_3@\text{NCM}$ shows only a modest rise in R_{ct} to 115.1 Ω . Such behavior implies that the electrochemical kinetics of the bare-NCM sample is significantly hindered over time, suggesting that some inactive species might agglomerate at the electrode surface.

Table 5.1. Fitting parameters of EIS results of pristine and cycled cathodes.

	bare-NCM pristine	bare-NCM cycled	$\text{LiNbO}_3@\text{NCM}$ pristine	$\text{LiNbO}_3@\text{NCM}$ cycled
R_E (Ω)	23.6	24.4	23.1	23.2
R_{ct} (Ω)	11.4	77.1	93.5	115.1

5.3.3 Post-Mortem Analysis

To further investigate the electrode properties after cycling, SEM and EDX are applied to explore the electrode surface morphological and elemental evolution. In Figure 5.10, the bare-NCM film surface exhibits a destructive morphology with several cracks. This is considered to be induced by volume

changes upon cycling the Ni-rich cathode. The electrolyte could penetrate through the cracks during cycling and give rise to renewed CEI-formation of freshly exposed material. The existence of CEI is generally seen as a factor strongly related to the capacity deterioration of Ni-rich cathodes. In comparison, the morphology of cycled $\text{LiNbO}_3@\text{NCM}$ thin-film electrode presents a relatively intact structure. The LiNbO_3 layer tends to protect the underlying NCM layer from structural collapse. The EDX results detect P and F-residuals at the surface, resulting from the CEI-formation. $\text{LiNbO}_3@\text{NCM}$ films demonstrate a reduced P and F amount compared to bare-NCM thin films, suggesting a lower content of residuals formed at the electrode surface.

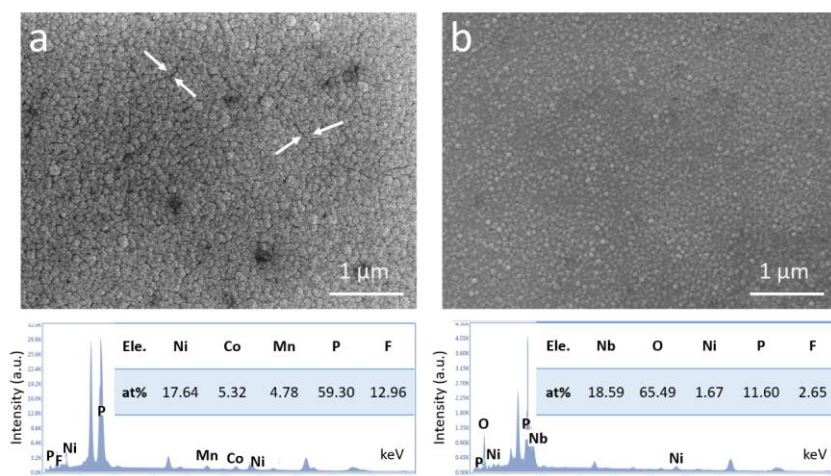


Figure 5.10 SEM images and EDX elemental analysis of (a) cycled bare-NCM and (b) cycled $\text{LiNbO}_3@\text{NCM}$ thin-film electrodes.

Most importantly, for Ni-rich cathode materials, a relatively intact structure helps to survive HF attack from the electrolyte. HF arises from the reaction between LiPF_6 salt and H_2O traces in the electrolyte, as described by reaction (5.1)^[32, 37]



where the production of reaction (5.2) not only contains LiPOF_2 , with a various reacting ratio between POF_3 and Li^+ , the compound thus can be denoted as $\text{Li}_x\text{PO}_y\text{F}_z$.

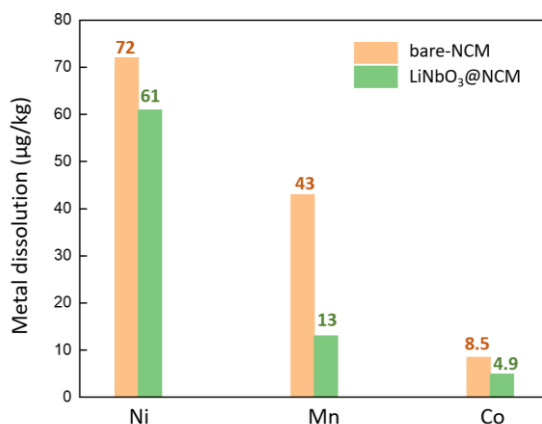


Figure 5.11 ICP measurement of electrolyte in cycled electrodes.

HF is highly toxic to most electrodes because HF tends to react with active materials, which leads to structural fatigue and transition-metal dissolution. Regarding metal dissolution, it has been reported that nickel dissolution is one of the strongest degradation mechanisms of Ni-rich cathodes.^[38] An ICP test of the electrolyte after cycling is presented in Figure 5.11 to evaluate the transition-metal dissolution status for both electrodes. The result indicates that the LiNbO_3 @NCM sample has a lower amount of metal ions than bare-NCM, showing the capability of the LiNbO_3 layer to inhibit the transition-metal dissolution caused by HF.

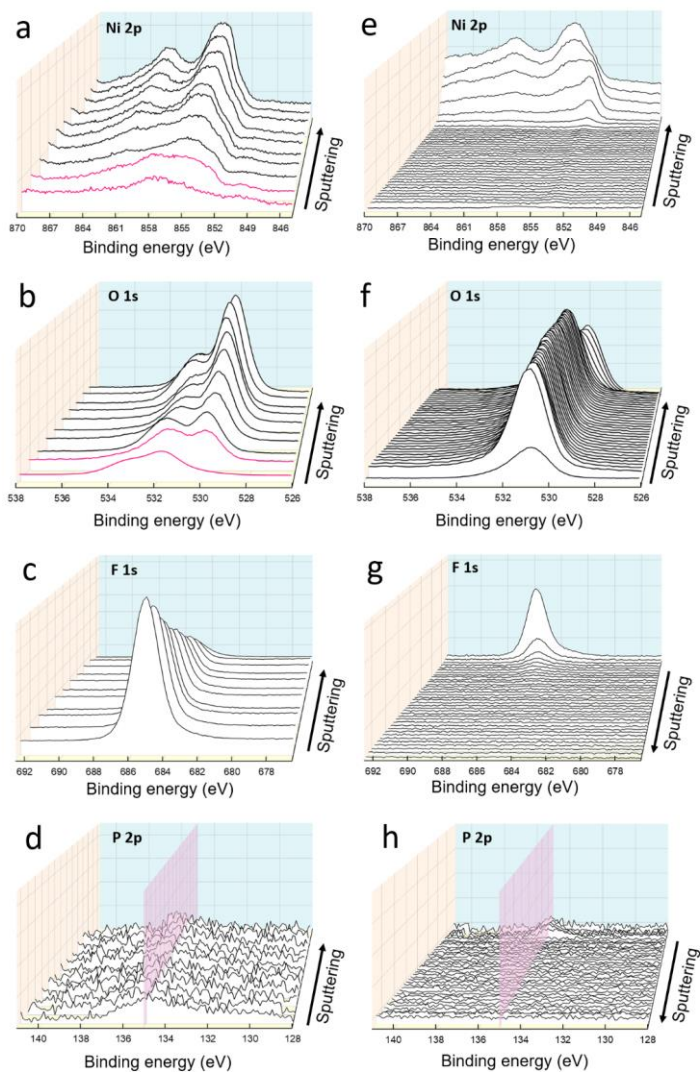


Figure 5.12 XPS depth profiles of a cycled bare-NCM thin-film electrode for (a) Ni 2p, (b) O 1s, (c) F 1s (d) P 2p spectra, and cycled LiNbO_3 @NCM thin-film electrode for (e) Ni 2p, (f) O 1s, (g) F 1s (h) P 2p spectra. The pink curves in (a) and (b) represent the existence of NiO-type rock-salt layer; the pink planes in (d) and (h) indicate the P 2p peak position.

XPS depth profiling is again employed to get more in-depth information of the chemical evolution of components in both thin films after cycling. For the bare-NCM electrode, shown in the Ni 2p spectra of Figure 5.12a, the peaks of the first two layers are significantly different from those of the pristine NCM film, indicating the formation of Ni-species at the electrode surface. For the Co and Mn spectra, no such striking transformation can be observed in depth (Figures 5.13a and 5.13b). In the O 1s spectra (Figure 5.12b), the peak development further reveals the complexity of the chemical environment at the electrode surface. Moreover, P and F-contained residuals are detected that are generated in the relatively deeper layers inside the NCM film (Figures 5.12c and 5.12d). The F 1s peak located at 685.1 eV is assigned to LiF, and the P 2p peak located at 135.0 eV is assigned to $\text{Li}_x\text{PO}_y\text{F}_z$. Both LiF and $\text{Li}_x\text{PO}_y\text{F}_z$ are decomposition products of LiPF_6 (reaction 5.2) and have been confirmed to be unfavorable to Li-ion transportation due to the high impedance.^[37, 39] Therefore, this finding suggests that the cracks in the cycled NCM film accelerate electrolyte penetration and the formation of undesirable reaction products.

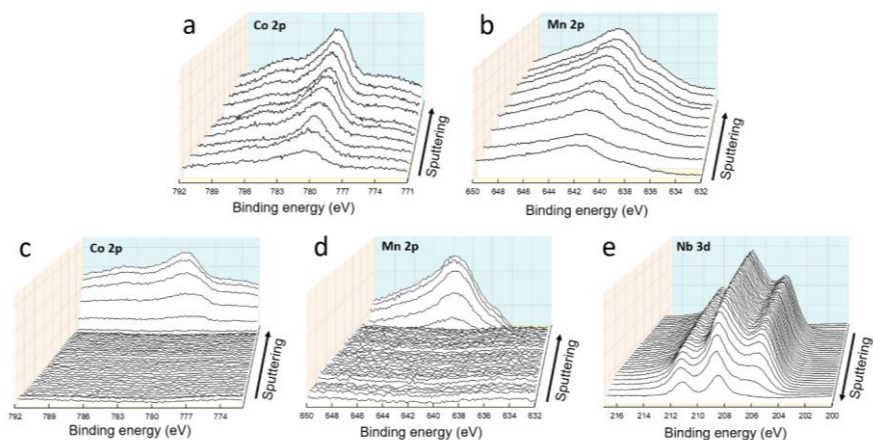


Figure 5.13 XPS depth-profiling analysis of a cycled bare-NCM thin-film electrode for (a) Co 2p, (b) Mn 2p, and cycled LiNbO_3 @NCM thin-film electrode for (c) Co 2p, (d) Mn 2p, (e) Nb 3d spectra.

XPS depth profiling of elements in a LiNbO_3 @NCM thin film is also demonstrated in Figures 5.12 and 5.13. No noticeable evolution can be seen in the Ni 2p (Figure 5.12e) and Nb 3d spectra (Figure 5.13e) peaks compared with those of the pristine sample, suggesting the stability of the NCM/ LiNbO_3 interface during the (dis)charge process. The valence state of O also displays a neglectable change after cycling (Figure 5.12f). Similarly, Co 2p and Mn 2p spectra retain the consistent valence states after cycling (Figures 5.13c and 5.13d). In particular, according to the depth profiles of F 1s and P 2p, residuals of P, F-species can only be found in the first few layers, implying the intact structure of LiNbO_3 @NCM thin film (Figures 5.12g and 5.12h). The lower content of LiF and $\text{Li}_x\text{PO}_y\text{F}_z$ at the electrode surface is associated with the fact that the LiNbO_3 layer significantly suppresses the decomposition of LiPF_6 . Hence, one can conclude that the underlying NCM material is protected from electrolyte corrosion. Its

electrochemical performance is less declined than the bare-NCM thin-film electrode.

A more-detailed analysis of the composition of the CEI film generated on the electrode/electrolyte interface can be made. Figures 5.14 and 5.15 analyze corresponding XPS spectra obtained from the surface of both thin-film electrodes. For the bare-NCM film, the Ni 2p spectra show a rather complex development. As indicated in Figure 5.14a, the initial Ni ion existed as Ni^{2+} (854.5 eV) and Ni^{3+} (855.2 eV) in the pristine electrode. While after cycling, three new Ni-containing phases are found at the surface. The peak located at 861.2 eV is ascribed to NiO, resulting from the side reaction in the Ni-rich cathode, such as cation disorder during (dis)charging.^[40] In addition, the peak at 857.2 eV can be attributed to the binding energy of the Ni-F bond in NiF_2 , which may be induced by the reaction between dissolved Ni^{2+} ions and the decomposition products of LiPF_6 : POF_3 and HF .^[41] Moreover, a peak representing Ni^0 is also identified at 850.1 eV. A possible explanation of this is that the dissolved Ni-ions in the electrolyte reduce at the anode surface and form metallic Ni species. Then, the metallic Ni species partially transport from the anode side to the cathode surface during cycling. Recently, several reports have reported the chemical crossing of CEI/SEI components between the cathode and anode. These results indicate that the CEI is not only formed by electrolyte decomposition at the cathode surface but also by the transportation of anodic components.^[43] This phenomenon has also been found in other studies.^[42-44]

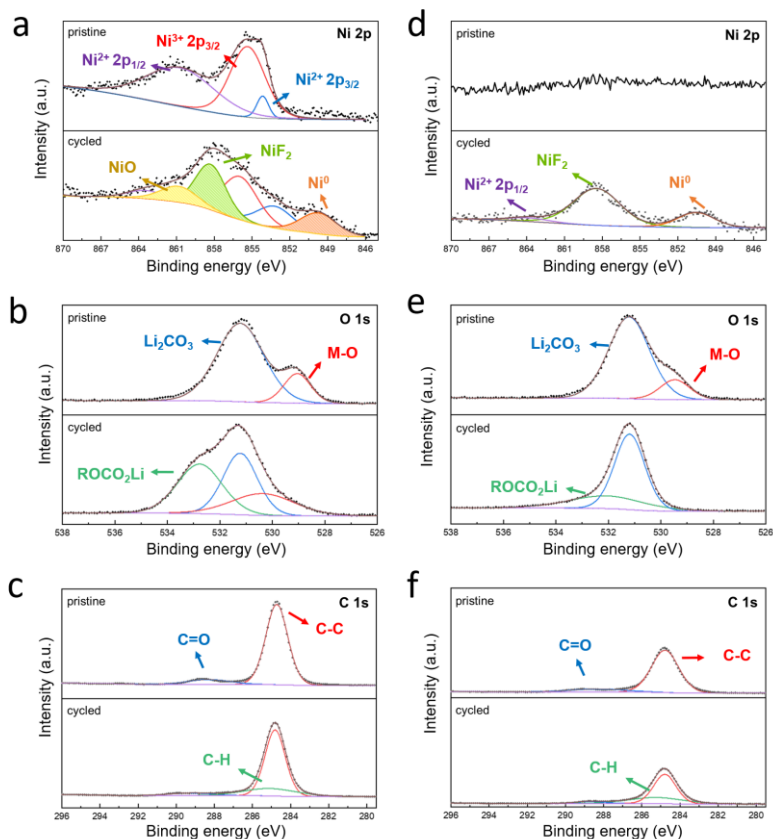


Figure 5.14 XPS surface analysis of a pristine and cycled bare-NCM thin-film electrode for (a) Ni 2p, (b) O 1s, (c) C 1s spectra, and pristine and cycled $\text{LiNbO}_3@$ NCM electrode for (d) Ni 2p, (e) O 1s, (f) C 1s spectra.

Figures 5.15a and 5.15b display the Co and Mn spectra collected from the cycled bare-NCM electrode surface. With no new peaks found in both spectra, Co and Mn elements show a relatively stable behavior during cycling. In particular, the Mn 2p spectrum has two major peaks located at 641.3 eV (representing $\text{Mn}^{3+} 2p_{3/2}$) and 642.4 eV (representing $\text{Mn}^{4+} 2p_{3/2}$). The content of $\text{Mn}^{3+} 2p_{3/2}$ increases slightly for the cycled electrode. The higher amount of Mn^{3+} results from the

oxygen loss in the Ni-rich cathode when the surface structure transforms from layered to the rock-salt phase. As-formed Mn^{3+} tends to partially reduce into Mn^{2+} and dissolve into the electrolyte, consequently declining the electrode capacity to some extent.^[45]

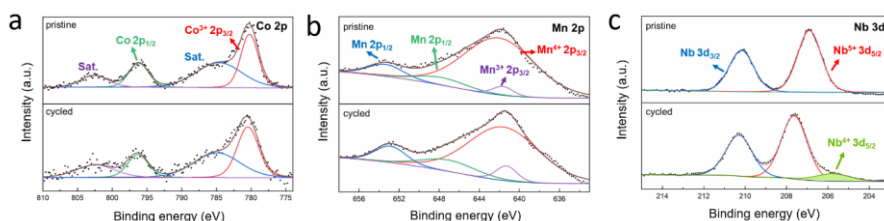
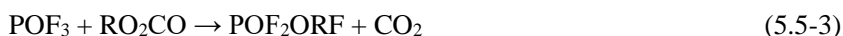


Figure 5.15 XPS surface analysis of a pristine and cycled bare-NCM thin-film electrode for (a) Co 2p, (b) Mn 2p, and pristine and cycled $\text{LiNbO}_3@$ NCM electrode for (c) Nb 3d spectra.

The O 1s and C 1s spectra also provide information about the CEI components formed at the electrode surface. For the bare-NCM electrode before cycling (Figure 5.14b), the dominant peaks are located at 529.0 and 531.1 eV. They can be associated with the M-O bond (M=metal) in NCM and the C-O bond in Li_2CO_3 , respectively. While after cycling, a relatively strong peak emerges at 533.7 eV, which can be ascribed to lithium alkyl carbonates (ROCO_2Li).^[32, 37] Accordingly, in the C 1s spectra (Figure 5.14c), two peaks can be detected for the pristine electrode. The peak at 584.8 eV is related to the C-C bond in the carbon contamination. It has been confirmed that most samples that have been exposed to the atmosphere will have a detectable quantity of carbon at the surface.^[37] The peak at 288.5 eV is the binding energy of O-C=O and should be attributed to Li_2CO_3 . In cycled bare-NCM, a new peak located at 285.1 eV is identified, corresponding to the chemical state C-O-C in ROCO_2Li . Although the generation

mechanism of ROCO₂Li remains unclear, several different reaction routes have been proposed^[46-49]



On the other hand, for the LiNbO₃@NCM thin film electrode, the surface component development after cycling displays a different trend. In Figure 5.14d, the Ni spectra exhibit two peaks at 850.1 and 861.2 eV, attributing to Ni⁰ 2p_{3/2} and the Ni-F bond in NiF₂, respectively. According to Figure 5.14a, ions generated from dissolved Ni during cycling, NiF₂, and metallic Ni products are also detected at the LiNbO₃@NCM electrode surface, similar to the bare-NCM electrode. Figure 5.15c shows the XPS spectra of the Nb element, where a new peak located at 205.8 eV for the cycled electrode can be assigned to Nb⁴⁺ 3d_{5/2}. Accordingly, the presence of Nb⁴⁺ might be induced by the reduction effect of metallic Ni. Likewise, regarding the O 1s and C 1s spectra (Figures 5.14e and 5.14f, respectively), the characteristic peaks of Li₂CO₃ and ROCO₂Li are also found at the surface. However, compared with bare-NCM, the LiNbO₃@NCM electrode displays a weaker peak intensity, especially for the ROCO₂Li component. This comparison suggests that the LiNbO₃ layer can suppress the electrolyte decomposition and residuals formation at the electrode surface.

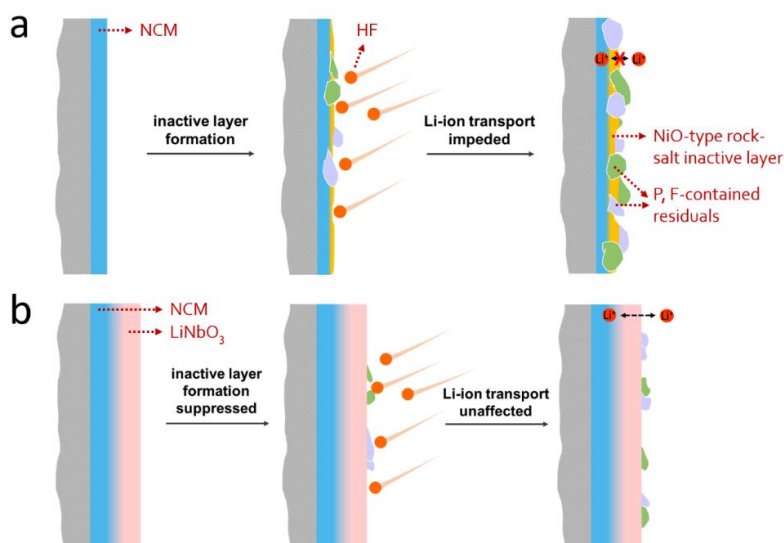


Figure 5.16 Schematic diagram of the CEI film formation at bare-NCM (a) and LiNbO_3 @NCM thin-film electrodes (b).

Based on XPS depth-profiling and surface analysis, the chemical evolution of the CEI film at the electrode surface is illustrated in Figure 5.16. For the bare-NCM electrode (Figure 5.16a), an inactive NiO-like rock-phase layer is formed at the electrode surface during cycles, initiated by cation-mixing and structural transition. Meanwhile, the electrolyte component decomposes and reacts at the electrode surface, creating various residuals, such as LiF , $\text{Li}_x\text{PO}_y\text{F}_z$, ROCO_2Li , *etc.*^[50-52] On the other hand, the diffusing Ni-ions react with decomposition substances and form NiF_2 . Notably, traces of P and F-containing residuals can be detected deeper inside the electrode, suggesting that the CEI formation not only occurs at the electrode surface. This phenomenon is mainly related to the growth of cracks and structural deterioration of the electrode, leading to a severe electrolyte penetration during cycling. As reported, most species formed inside CEI films (LiF , NiF_2 , ROCO_2Li) are bad Li-ion conductors.^[32] The relatively high

impedance will hinder Li-ion transport, leading to fading of the electrochemical performance.

In contrast, the $\text{LiNbO}_3@\text{NCM}$ electrode demonstrates the absence of a NiO-like layer at the NCM/ LiNbO_3 interface. It contains fewer inactive products in the CEI film (Figure 5.16b). The inactive products only exist on the first few electrode layers, showing that the LiNbO_3 layer successfully protects the underlying NCM material from electrolyte penetration and HF attack. The presented analyses indicate that the stability of the NCM/ LiNbO_3 interface during cycling and the existence of the LiNbO_3 layer can effectively inhibit HF corrosion, suppress electrolyte decomposition, and eventually mitigate the CEI film growth.

5.4 Conclusions

$\text{LiNi}_{0.6}\text{Co}_{0.2}\text{Mn}_{0.2}\text{O}_2$ and LiNbO_3 -coated $\text{LiNi}_{0.6}\text{Co}_{0.2}\text{Mn}_{0.2}\text{O}_2$ thin-film electrodes have been fabricated via sputtering deposition on silicon substrates. Chemical and structural characterizations reveal that the obtained films were of the desired crystallinity. XPS depth profiling has been intensely applied to collect information from the $\text{LiNbO}_3/\text{LiNi}_{0.6}\text{Co}_{0.2}\text{Mn}_{0.2}\text{O}_2$ interface and CEI film formation at the electrodes. An interface with a thickness around 30 nm is identified between $\text{LiNi}_{0.6}\text{Co}_{0.2}\text{Mn}_{0.2}\text{O}_2$ and LiNbO_3 layers, caused by Ni^{2+} ions diffusion from $\text{LiNi}_{0.6}\text{Co}_{0.2}\text{Mn}_{0.2}\text{O}_2$ in the LiNbO_3 layer. The electrochemical tests show that $\text{LiNbO}_3/\text{LiNi}_{0.6}\text{Co}_{0.2}\text{Mn}_{0.2}\text{O}_2$ electrode shows enhanced electrode stability and mitigates the impedance increase upon cycling compared to bare $\text{LiNi}_{0.6}\text{Co}_{0.2}\text{Mn}_{0.2}\text{O}_2$ electrodes.

Post-mortem analyses reveal the stability of the $\text{LiNbO}_3/\text{LiNi}_{0.6}\text{Co}_{0.2}\text{Mn}_{0.2}\text{O}_2$ interface and show the elemental distribution in the CEI film of both thin-film electrodes. The LiNbO_3 layer maintains a compact morphology and effectively suppresses cation-mixing, resisting HF attack and restraining electrolyte decomposition, which leads to an alleviated CEI film

growth. Residuals unfavorable to Li-ion transport have been detected in lower amounts at the surface of $\text{LiNbO}_3/\text{LiNi}_{0.6}\text{Co}_{0.2}\text{Mn}_{0.2}\text{O}_2$ electrodes.

This work presents a simple solution to isolate active material from carbon additives and binders. The interaction between Ni-rich $\text{LiNi}_{0.6}\text{Co}_{0.2}\text{Mn}_{0.2}\text{O}_2$ cathodes and LiNbO_3 , and the CEI film formation between the electrodes and electrolyte, has been demonstrated. More information on the interface formation during cycling can be obtained by applying more advanced characterization methods, such as *in situ* atomic-scale techniques. Considering LiNbO_3 is a promising solid-state electrolyte with high ionic conductivity and a wide stability window, the present work also contributes to developing electrochemically stable all-solid-state Li-ion batteries.

References

- 1 R. Schmich, R. Wagner, G. Hörpel, T. Placke, M. Winter, *Nature Energy* **3** (2018) 267.
- 2 S. Natarajan, V. Aravindan, *Advanced Energy Materials* **8** (2018) 1802303.
- 3 P. Teichert, G. G. Eshetu, H. Jahnke, E. Figgemeier, *Batteries* **6** (2020) 8.
- 4 L. Liang, W. Zhang, F. Zhao, D. K. Denis, F. u. Zaman, L. Hou, C. Yuan, *Advanced Materials Interfaces* **7** (2019) 1901749.
- 5 X. Wang, Y. L. Ding, Y. P. Deng, Z. Chen, *Advanced Energy Materials* **10** (2020)
- 6 J. Kim, H. Cha, H. Lee, P. Oh, J. Cho, *Batteries & Supercaps* **3** (2020) 309.
- 7 M. Jiang, Q. Zhang, X. Wu, Z. Chen, D. L. Danilov, R.-A. Eichel, P. H. L. Notten, *ACS Applied Energy Materials* **3** (2020) 6583.
- 8 I. Hamam, N. Zhang, A. Liu, M. B. Johnson, J. R. Dahn, *Journal of The Electrochemical Society* **167** (2020) 130521.
- 9 W. Liu, X. Li, D. Xiong, Y. Hao, J. Li, H. Kou, B. Yan, D. Li, S. Lu, A. Koo, K. Adair, X. Sun, *Nano Energy* **44** (2018) 111.

- 10 Y. Li, X. Liu, D. Ren, H. Hsu, G.-L. Xu, J. Hou, L. Wang, X. Feng, L. Lu, W. Xu, Y. Ren, R. Li, X. He, K. Amine, M. Ouyang, *Nano Energy* **71** (2020) 104643.
- 11 D. Hu, Y. Su, L. Chen, N. Li, L. Bao, Y. Lu, Q. Zhang, J. Wang, S. Chen, F. Wu, *Journal of Energy Chemistry* **58** (2020) 1.
- 12 K. Liu, Q. Zhang, S. Dai, W. Li, X. Liu, F. Ding, J. Zhang, *ACS Applied Materials & Interfaces* **10** (2018) 34153.
- 13 H. H. Sun, J. Y. Hwang, C. S. Yoon, A. Heller, C. B. Mullins, *ACS Nano* **12** (2018) 12912.
- 14 Q. Gan, N. Qin, Z. Wang, Z. Li, Y. Zhu, Y. Li, S. Gu, H. Yuan, W. Luo, L. Lu, Z. Xu, Z. Lu, *ACS Applied Energy Materials* **3** (2020) 7445.
- 15 B. Song, W. Li, S. M. Oh, A. Manthiram, *ACS Applied Materials & Interfaces* **9** (2017) 9718.
- 16 Y.-J. Kim, R. Rajagopal, S. Kang, K.-S. Ryu, *Chemical Engineering Journal* **386** (2020) 123975.
- 17 Q. Fan, S. Yang, J. Liu, H. Liu, K. Lin, R. Liu, C. Hong, L. Liu, Y. Chen, K. An, P. Liu, Z. Shi, Y. Yang, *Journal of Power Sources* **421** (2019) 91.
- 18 Q. Ran, H. Zhao, X. Shu, Y. Hu, S. Hao, Q. Shen, W. Liu, J. Liu, M. Zhang, H. Li, X. Liu, *ACS Applied Energy Materials* **2** (2019) 3120.
- 19 S. Yang, Q. Fan, Z. Shi, L. Liu, J. Liu, X. Ke, J. Liu, C. Hong, Y. Yang, Z. Guo, *ACS Applied Materials & Interfaces* **11** (2019) 36742.
- 20 S. Chen, T. He, Y. Su, Y. Lu, L. Bao, L. Chen, Q. Zhang, J. Wang, R. Chen, F. Wu, *ACS Applied Materials & Interfaces* **9** (2017) 29732.
- 21 T. Teranishi, M. Inohara, J. Kano, H. Hayashi, A. Kishimoto, K. Yoda, H. Motobayashi, Y. Tasaki, *Solid State Ionics* **314** (2018) 57.
- 22 M. Gellert, K. I. Gries, J. Sann, E. Pfeifer, K. Volz, B. Roling, *Solid State Ionics* **287** (2016) 8.
- 23 Z. J. Zhang, S. L. Chou, Q. F. Gu, H. K. Liu, H. J. Li, K. Ozawa, J. Z. Wang, *ACS Applied Materials & Interfaces* **6** (2014) 22155.

- 24 J. Syzdek, M. Marcinek, R. Kostecki, *Journal of Power Sources* **245** (2014) 739.
- 25 N. D. Phillip, R. E. Ruther, X. Sang, Y. Wang, R. R. Unocic, A. S. Westover, C. Daniel, G. M. Veith, *ACS Applied Energy Materials* **2** (2019) 1405.
- 26 S. Lobe, C. Dellen, M. Finsterbusch, H. G. Gehrke, D. Sebold, C. L. Tsai, S. Uhlenbruck, O. Guillon, *Journal of Power Sources* **307** (2016) 684.
- 27 Z. P. W. Shraavan Suresh, Stephen F. Bartolucci, Swastik Basu, Rahul Mukherjee, Tushar Gupta, Prateek Hundekar, Yunfeng Shi, Toh-Ming Lu, and Nikhil Koratkar, *ACS Nano* **11** (2017) 5051.
- 28 Z. Yu, H. Xu, G. Zhu, D. L. Yan, A. Yu, *Energy Technology* **4** (2016) 798.
- 29 G. Tan, F. Wu, J. Lu, R. Chen, L. Li, K. Amine, *Nanoscale* **6** (2014) 10611.
- 30 S. Moitzheim, B. Put, P. M. Vereecken, *Advanced Materials Interfaces* **6** (2019) 1900805.
- 31 Y. Zhu, X. He, Y. Mo, *Journal of Materials Chemistry A* **4** (2016) 3253.
- 32 J. Fu, D. Mu, B. Wu, J. Bi, H. Cui, H. Yang, H. Wu, F. Wu, *ACS Applied Materials & Interfaces* **10** (2018) 19704.
- 33 X. Ju, H. Huang, W. He, H. Zheng, P. Deng, S. Li, B. Qu, T. Wang, *ACS Sustainable Chemistry & Engineering* **6** (2018) 6312.
- 34 K. Li, D. Xue, *The Journal of Physical Chemistry A* **110** (2006) 11332.
- 35 J. Zhao, W. Zhang, A. Huq, S. T. Misture, B. Zhang, S. Guo, L. Wu, Y. Zhu, Z. Chen, K. Amine, F. Pan, J. Bai, F. Wang, *Advanced Energy Materials* **7** (2017) 1601266.
- 36 W. Li, J. N. Reimers, J.R. Dahn, *Solid State Ionics* **67** (1993) 123.
- 37 W. Zhao, G. Zheng, M. Lin, W. Zhao, D. Li, X. Guan, Y. Ji, G. F. Ortiz, Y. Yang, *Journal of Power Sources* **380** (2018) 149.
- 38 J. Kim, H. Ma, H. Cha, H. Lee, J. Sung, M. Seo, P. Oh, M. Park, J. Cho, *Energy & Environmental Science* **11** (2018) 1449.
- 39 H. Chen, L. Xiao, H. Chen, Y. Zhu, K. Xiang, H. Liao, *Electrochimica Acta* **344** (2020) 136142.

- 40 Y. Zhang, Z.-B. Wang, F.-D. Yu, L.-F. Que, M.-J. Wang, Y.-F. Xia, Y. Xue, J. Wu, *Journal of Power Sources* **358** (2017) 1.
- 41 J. Kim, J. Lee, H. Ma, H. Y. Jeong, H. Cha, H. Lee, Y. Yoo, M. Park, J. Cho, *Advanced Materials* **30** (2018) 17043091.
- 42 X. Xiong, D. Ding, Y. Bu, Z. Wang, B. Huang, H. Guo, X. Li, *Journal of Materials Chemistry A* **2** (2014) 11691.
- 43 C. M. Julien, A. Mauger, *AIMS Materials Science* **6** (2019) 406.
- 44 J. M. Lim, N. S. Luu, K. Y. Park, M. T. Z. Tan, S. Kim, J. R. Downing, K. He, V. P. Dravid, M. C. Hersam, *Journal of Vacuum Science & Technology A* **38** (2020) 0632101.
- 45 Y. Shi, M. Zhang, C. Fang, Y. S. Meng, *Journal of Power Sources* **394** (2018) 114.
- 46 K. Kumai, H. Miyashiro, Y. Kobayashi, K. Takei, R. Ishikawa, *Journal of Power Sources* **81** (1999) 715.
- 47 B. Ravdel, K. M. Abraham, R. Gitzendanner, J. DiCarlo, B. Lucht, C. Campion, *Journal of Power Sources* **119-121** (2003) 805.
- 48 C. L. Campion, W. Li, B. L. Lucht, *Journal of The Electrochemical Society* **152** (2005) A2327.
- 49 W. Li, B. L. Lucht, *Journal of The Electrochemical Society* **153** (2006) A1617.
- 50 P. Niehoff, M. Winter, *Langmuir* **29** (2013) 15813.
- 51 Q. Li, Y. Wang, X. Wang, X. Sun, J. N. Zhang, X. Yu, H. Li, *ACS Applied Materials & Interfaces* **12** (2020) 2319.
- 52 G. Liu, N. Xu, Y. Zou, K. Zhou, X. Yang, T. Jiao, W. Yang, Y. Yang, J. Zheng, *ACS Applied Materials & Interfaces* **13** (2021) 12069.

Chapter 6

Stabilized Li-metal Anodes for

LiNi_{0.6}Co_{0.2}Mn_{0.2}O₂/Li Batteries

Abstract

The stability of solid-electrolyte interphase (SEI) surface films at Li-metal anodes is crucial for the safe and durable operation of lithium-metal batteries (LMBs). Combining Li-metal anodes with high-performance Ni-rich transition-metal-oxide cathodes, LMBs can meet the goal of a high specific energy density of more than 500 Wh kg⁻¹. However, Li-metal anodes suffer from serious problems, especially the nonuniform lithium deposition and uncontrollable SEI formation. In this chapter, a robust Li-metal anode with a LiNbO₃ protective layer is proposed. Full-cells composed of protected Li-metal anodes and LiNi_{0.6}Co_{0.2}Mn_{0.2}O₂ cathodes are examined electrochemically and by physical characterization methods. Post-mortem analyses of pristine and prolonged cycled Li-metal anodes are performed. The results reveal the formation of more stable SEI films at the protected Li-metal anodes than unprotected electrodes. Consequently, the LiNbO₃ layers improve the cycle-life performance of Li-metal anodes in LMBs. Furthermore, XPS analyses show that the reduction of metallic ions stemming from Ni-rich cathodes is also inhibited by the protective LiNbO₃ layers, thereby further controlling the degradation of Li-metal anodes.

6.1 Introduction

LIBs are commercially successful and have been studied over several decades, thanks to the growing number of energy storage applications, including portable devices and (hybrid) electric vehicles.^[1-3] Nevertheless, the development of conventional LIBs, which are based on the intercalation chemistry of both electrodes, is gradually approaching the capacity limit of about 300 Wh kg^{-1} .^[4] The demand for rechargeable batteries with higher energy density is therefore of crucial importance for future applications.

Considering Li-metal offers a very high theoretical specific capacity as an anode of 3860 mAh g^{-1} at the lowest redox potential of $0 \text{ V vs. Li}^+/\text{Li}$, lithium-metal secondary batteries (LMBs) are likely to be the most promising alternative for the next generation of LIBs.^[5, 6] In this regard, Li-metal electrodes are considered the ultimate goal as anode material in rechargeable batteries. In combination with high-performance Ni-rich nickel-cobalt-manganese layered oxides (NCM), such a new battery system is expected to deliver a capacity of more than 500 Wh kg^{-1} .^[7] Despite these advantages, the remaining challenges associated with serious safety concerns severely constrain further commercialization of Li-metal anodes in LIBs.^[8-10]

On the one hand, Li, by nature, has an extremely high reactivity towards organic electrolytes. Multiple side reactions spontaneously occur at metallic lithium electrodes in contact with the electrolyte, leading to numerous by-products at the anode surface. During battery operating, these side reactions will be accelerated, resulting in an even increased electrolyte consumption and, consequently, severe battery degradation.^[11] Furthermore, uneven Li-metal deposition will lead to unfavorable dendrite formation, generating serious safety issues, such as internal short-circuiting and thermal runaway.^[12] Therefore, unlike graphite anodes that form a relatively stable SEI film, the SEI formation at Li-

metal anodes is rather uncontrolled and accompanied by the growth of a high-porosity surface morphology.^[13]

Many approaches have been adopted to tailor the surface of Li-metal anodes by controlling both the SEI formation and Li-metal deposition morphology.^[14-17] Most studies only focused on symmetric metallic Li cells or Li/Cu cells where Cu is used as current collector.^[18-20] However, the influence of cathode materials on the electrochemistry of Li-metal anodes is rarely discussed. Notably, it has been identified that the surface reactions at the anode show a strong correlation with the cathode material.^[21, 22] It was found that applying various cathode materials leads to different SEI surface layers at the anodes. Up to now, several reports have presented this so-called crossover effect between the cathode and anode in LIB chemistries, such LiCoO_2/Li ,^[23] $\text{LiFePO}_4/\text{Li}$,^[24] and $\text{LiNi}_{0.5}\text{Co}_{0.3}\text{Mn}_{0.2}\text{O}_2/\text{graphite}$,^[21] cells while a detailed analysis of Ni-rich NCM/Li batteries is still lacking.

A single report discussed the influence of three different cathode materials ($\text{LiNi}_{0.5}\text{Mn}_{1.5}\text{O}_4$, $\text{LiNi}_{0.6}\text{Co}_{0.2}\text{Mn}_{0.2}\text{O}_2$, and LiFePO_4) on the morphology of Li-metal deposition. Still, the investigation of the SEI formation was rather limited.^[25] Another report recently presented results of cathode-anode crossover, occurring in $\text{LiNi}_{0.9}\text{Co}_{0.05}\text{Mn}_{0.05}\text{O}_2/\text{Li}$ and $\text{LiNi}_{0.9}\text{Co}_{0.05}\text{Mn}_{0.05}\text{O}_2/\text{graphite}$ cells.^[26] However, this work only explored the SEI formation for the cells (dis)charged up to 50 cycles, which is unrepresentative for long-life batteries as some effects induced by the cathode, such as the dissolution of transition-metal ions, can only be appropriately detected during prolonged cycling. Given the importance of improving the Li-metal anode, it is vital to understand the SEI evolution at metallic Li anodes.

In this chapter, LiNbO_3 , a solid-state electrolyte with a high ionic conductivity, is proposed as protective layer for Li-metal anodes. After protection, the Li-metal anodes show an enhanced stripping/plating stability in symmetric

cells, indicating that the surface reactions are well controlled by the presence of these LiNbO_3 layers. Subsequently, $\text{LiNi}_{0.6}\text{Co}_{0.2}\text{Mn}_{0.2}\text{O}_2/\text{Li}$ cells were assembled and investigated. The electrochemical performance of cells using bare-Li anodes and LiNbO_3 -coated Li anodes are compared comprehensively. Particular attention is drawn to the differences of the SEI surface film evolution and Li-metal deposition morphology on both types of anodes during initial and prolonged cycling. The distinct responses of Li-anodes towards crossover induced by the cathode have been investigated, and the insights regarding the optimization role of LiNbO_3 protective layers in achieving the suppressed SEI formation are revealed.

6.2 Materials Preparation

LiNbO_3 -coated Li-metal electrodes: Li-metal foil with 0.75 mm thickness was purchased from Alfa Aesar (USA), commercial Ni-rich $\text{LiNi}_{0.6}\text{Co}_{0.2}\text{Mn}_{0.2}\text{O}_2$ powders (NCM) was obtained from Tianjin B&M Science and Technology (China), and LiNbO_3 sputtering targets were obtained from Lesker (UK). The whole process was operated in a glove box, avoiding any exposure to air. LiNbO_3 thin films were deposited on Li foil by radio-frequency magnetron sputtering (Lesker, UK). The distance between substrate and target was fixed at 15 cm. The substrates kept rotating at a speed of 20 rpm to guarantee homogeneous deposition. The sputtering process was performed in an Ar atmosphere at a chamber pressure of 5 mTorr, and 60 W sputtering power. The thickness of the obtained LiNbO_3 layers was determined to be 30 nm at a deposition rate of approximately 2 \AA min^{-1} .

6.3 Results and Discussion

6.3.1 Characterization Analysis

Figure 6.1 shows the SEM results of the surface morphology of bare Li-metal (a) and LiNbO_3 -protected Li-metal (b). The surface of bare-Li demonstrates an overall smooth surface morphology with several intrinsic micro-scratches. After deposition of LiNbO_3 , it can be seen that the layer has been homogeneously and conformally coated onto the Li-metal. This layer compactly covers the micro-scratches at the Li-metal surface. Note that the LiNbO_3 layer prepared via sputtering at room temperature is amorphous. No diffraction peaks can be identified in the XRD pattern (Figure 6.2). The EDX spectrum of obtained LiNbO_3 -Li sample shows a strong Nb signal. The mapping analysis reveals a uniform elemental distribution of the LiNbO_3 layer (Figure 6.1c).

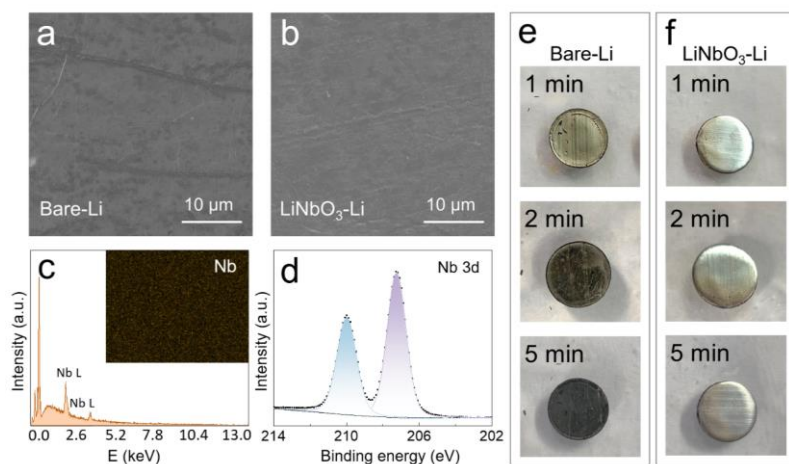


Figure 6.1 SEM images of (a) pristine bare Li-metal, and (b) pristine LiNbO_3 -coated Li-metal electrode. (c) EDX spectrum and elemental Nb-mapping of the LiNbO_3 protective layer. (d) XPS spectrum of the as-deposited amorphous LiNbO_3 layer. Optical images of the Li-corrosion process under ambient atmospheric conditions of (e) bare Li-metal and (f) LiNbO_3 -coated Li-metal.

The elemental valence state of Nb in the amorphous LiNbO_3 layer has also been analyzed by XPS. The Nb 3d spectrum shown in Figure 6.1d implies that Nb ions exist in the amorphous LiNbO_3 layer on Li-metal as Nb^{5+} , the peaks located at 207.2 and 210.5 eV are attributed to $\text{Nb}^{5+} 3d_{5/2}$ and $\text{Nb}^{5+} 3d_{3/2}$, respectively. In addition, to evaluate the compactness of the coating, both protected and unprotected metal samples are placed under ambient atmospheric conditions at 25°C for 5 min. It is well known that Li-metal is highly reactive with oxygen, nitrogen, and water in the air. Thus, after exposure, the surface of the bare-Li sample rapidly turns into tarnish within a few minutes to become ultimately black after 5 min (Figure 6.1e). The color change is associated with multiple compounds formed at the Li-metal surface, including Li_2CO_3 , Li_2O , LiOH , Li_3N , *etc.*^[9]

In contrast, the surface of LiNbO_3 -protected Li-metal remains stable. It nearly maintains its original metallic shining state after 5 min exposure to air (Figure 6.1f). This observation indicates that a homogeneous coating of LiNbO_3 might be effective as a protective layer at metallic Li electrodes.

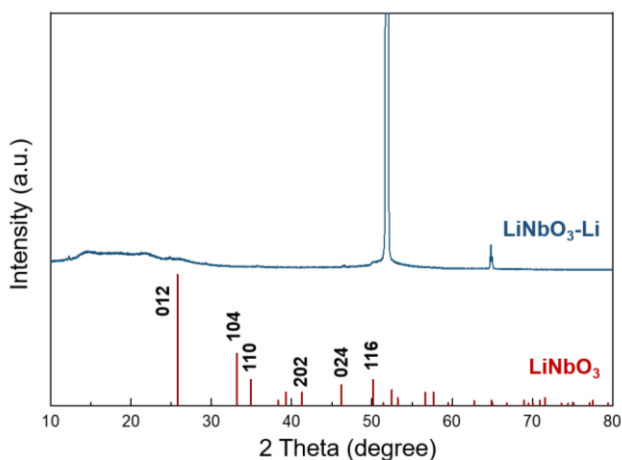


Figure 6.2 XRD pattern of as-deposited LiNbO_3 layer.

6.3.2 Electrochemical Analysis

Lithium stripping and plating have been performed in symmetric Li-Li cells to investigate the interfacial stability of Li-metal electrodes. Figure 6.3 shows the evolution of the cell impedance with storage time, keeping the cells under open-circuit conditions. The impedance of the bare Li-cell (a) increases significantly over time. This is due to the spontaneous reaction of metallic Li with the electrolyte, leading to the continuous growth of the passive layer. However, the impedance of the symmetric $\text{LiNbO}_3\text{-Li}$ cell (Figure 6.3b) shows that the charge-transfer resistance reached a highly stable state after approximately 20 h storage. That can be attributed to the effective isolation properties of the LiNbO_3 coating, which suppresses parasitic reactions at the Li-metal surface. Notably, the pristine $\text{LiNbO}_3\text{-Li}$ symmetric cell (b) shows a larger initial resistance, owing to the additional ionic conductivity of the protective coating. It has been extensively reported that Li-metal is thermodynamically unstable in organic solvents.^[13] Thus, protecting Li-metal electrodes from side reactions with the electrolyte is essential to stabilize the anodes of LMBs.

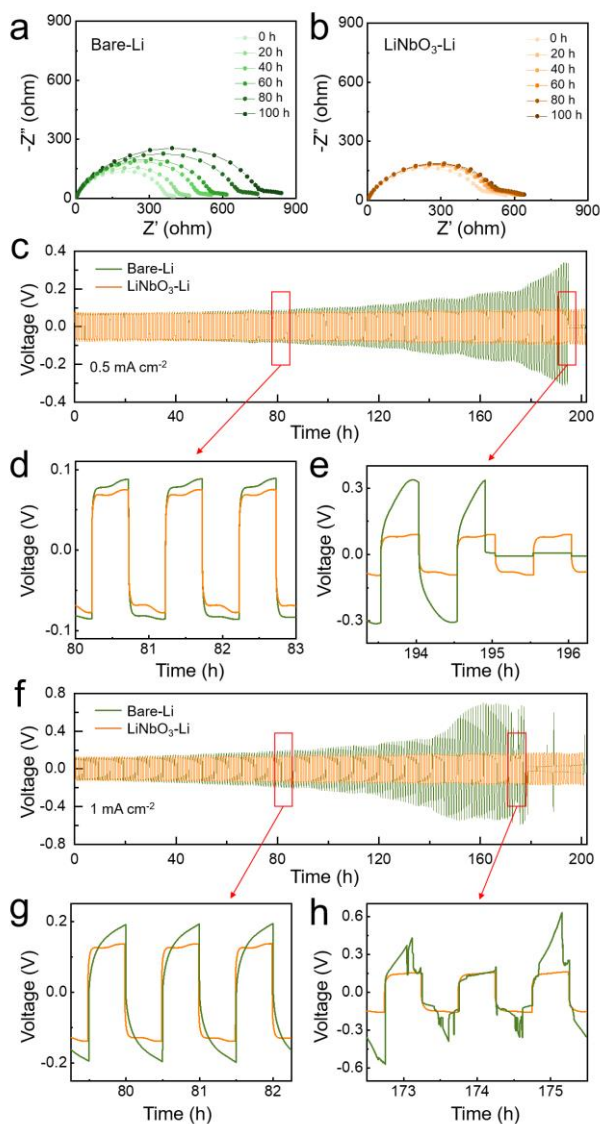


Figure 6.3 EIS spectra of symmetric Li cells with (a) bare Li and (b) LiNbO₃-protected Li during storage at room temperature. (c) Overview of galvanostatic cycling experiments of symmetric Li cells at 0.5 mA cm⁻² and at a higher magnification after (d) 80 hours cycling and after (e) 195 hours cycling. (f) Overview of galvanostatic profiles of symmetric Li cells cycled at 1 mA cm⁻² and in more detail after (d) 80 hours cycling, and after (e) 175 hours cycling.

The stability of the Li stripping/plating process has been further investigated in symmetric cells. Figure 6.3c shows the voltage profiles of bare-Li (green) and $\text{LiNbO}_3\text{-Li}$ (orange) symmetric cells cycled in a commercial electrolyte (1 M LiPF_6 in 1:1 EC/DMC) at a current density of 0.5 mA cm^{-1} during 0.5 h for each step. It can be seen that the bare-Li symmetric cell revealed significantly enlarged overpotentials with increasing cycling time. As shown in Figure 6.3d, the stripping/plating overpotentials after about 80 hours are very similar for both symmetric cells (160 mV vs. Li^+/Li). However, the overpotential of the bare-Li cell continuously increases up to 600 mV at the end of cycling and encounters a sudden voltage drop after 195 h (green curve in Figure 6.3e), implying a detrimental cell failure caused by short-circuits. The unstable voltage is attributed to the nonuniform Li-metal nucleation and SEI formation during cycling. The end of life is clearly related to the formation of detrimental short-circuits. In contrast, the performance of the $\text{LiNbO}_3\text{-Li}$ symmetric cell (orange curve) demonstrates improved stability with no sign of any short-circuits even after 200 h of cycling.

Remarkably, at a higher current density of 1 mA cm^{-2} , the $\text{LiNbO}_3\text{-Li}$ symmetric cell still demonstrates highly stable behavior with negligible overpotential changes. The overview of Figure 6.3f shows a sharp contrast between the two voltage profiles. The summation of the overpotentials, occurring during charging and discharging the bare-Li symmetric cell, increase from 400 mV after 80 hours (Figure 6.3g) to around 900 mV after 175 hours (Figure 6.3h). Also, the significant increase of overpotential is followed by considerable noisy fluctuations at 173 h (Figure 2h). Cell failure can be observed after 180 h, whereas for the $\text{LiNbO}_3\text{-protected Li}$ cell, the voltage profile at higher current density shows similar behavior to that of 0.5 mA cm^{-2} . In this case, the overpotentials only slightly increase from 220 mV to 250 mV at the end of cycling. The much longer cycle life and improved stability of the $\text{LiNbO}_3\text{-Li}$ symmetric cells show that the LiNbO_3 protective layer facilitates unobstructed Li-ion transport, leading to

homogeneous Li deposits and only moderate volume expansion during the stripping and plating process.

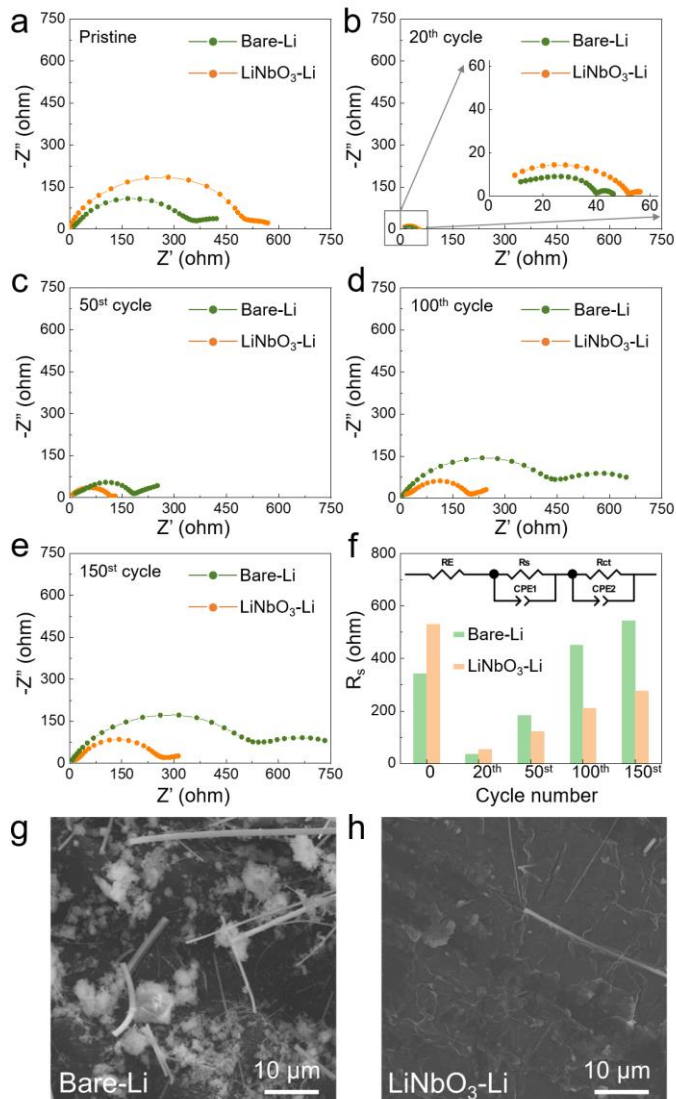


Figure 6.4 EIS spectra of symmetric Li cells at (a) pristine state, (b) 20th cycle, (c) 50st cycle, (d) 100th cycle, (e) 150st cycle, (f) Equivalent circuit, and R_s evolution during cycling. SEM images of cycled (g) bare Li, and (h) LiNbO₃-protected Li.

EIS measurements have been conducted with both symmetric cells after various cycles (Figure 6.4a-e). The adopted equivalent circuit and the surface film resistance obtained by spectra fitting are shown in Figure 6.4f. The bare-Li and LiNbO_3 -coated Li have shown surface film resistance of 341 and 529 Ω for the pristine cells, respectively (Figure 6.4a). The larger resistance of pristine LiNbO_3 -Li must be attributed to the deposited LiNbO_3 layer, which acts as a barrier for Li^+ -ion transport, in contrast to the bare-Li case. Figure 6.4b shows that after the initial cycles of stripping and plating, both symmetric cells experience a significant reduction of R_s to 35 and 53 Ω . Subsequently, R_s of the LiNbO_3 -Li cell increases from 122 Ω after 50 cycles to 276 Ω after 150 cycles. While for the bare-Li symmetric cell, a much larger increase of R_s is observed. The impedance of bare-Li cell gradually rises from 183 (50st cycle) to 543 Ω (150st cycle), displaying approximately a two times higher resistance than for LiNbO_3 -Li cell after long-term cycling.

The electrode morphologies have been further examined by SEM after 200 hours of stripping and plating. The intensively cycled bare-Li cell reveals a notably rough and porous surface morphology (Figure 6.4g) with Li dendrites and a needle-like structured Li surface layer. The Li structures on the bare-Li surface have been considered as "dead Li", losing electronic contact with the bulk Li-foil, and are associated with the sharp impedance increase during cycling. Contrastingly, the surface of the cycled LiNbO_3 -protected Li cell maintains a relatively flat and compact structure (Figure 6.4h). It is also found that the surface of the LiNbO_3 -Li electrode adopts a slightly convex shape after cycling compared to its pristine state. This observation suggests the presence of internal stress induced by the Li volume expansion underneath the LiNbO_3 layer. These results, therefore, demonstrate that the LiNbO_3 -coating with intrinsic high ionic conductivity effectively provides smooth Li transportation through the LiNbO_3/Li interface. That leads to a homogeneous Li stripping/plating process with relatively uniform Li deposition.

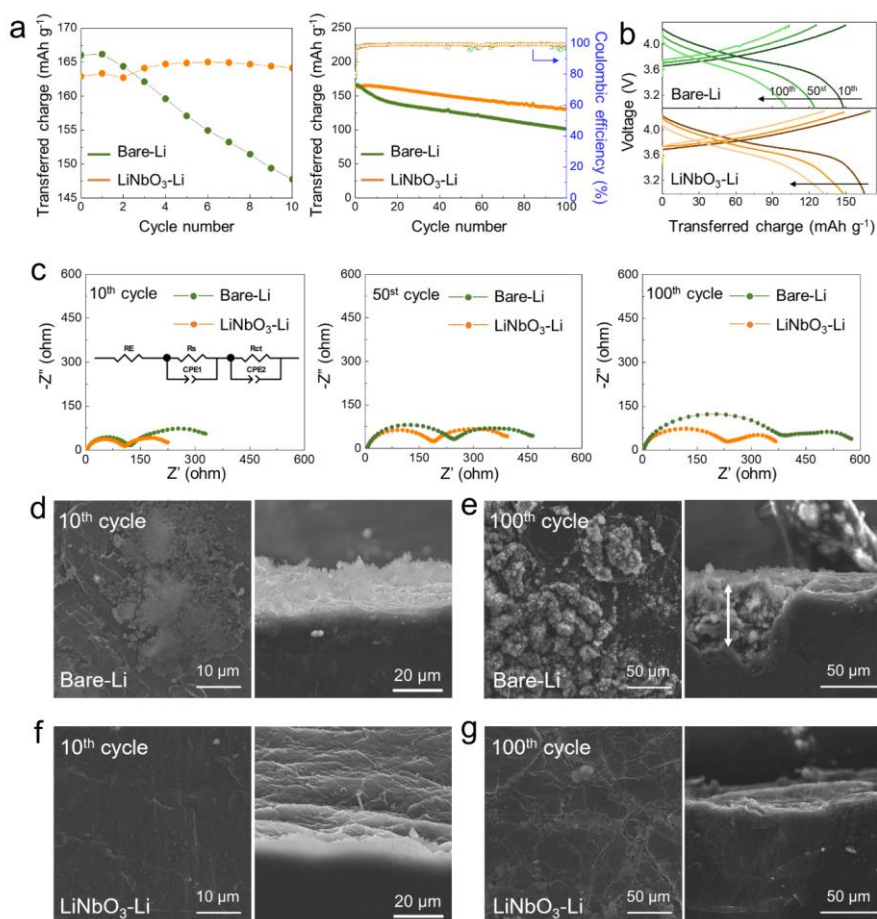


Figure 6.5 (a) Galvanostatic (1 C) cycling of the initial 10 and 100 cycles, and (b) voltage profiles of NCM/Li cells at various cycles. (c) EIS spectra of the Li anodes after cycling. Top view and cross-section view of SEM images of bare-Li anode after (d) 10 cycles, and (e) 100 cycles. Top view and cross-section view of SEM images of LiNbO₃-Li anode after (f) 10 cycles, and (g) 100 cycles.

The electrochemical performance and corresponding materials characterization of full cells with commercial Ni-rich NCM cathodes and Li-metal anodes have been investigated for the potential practicability of LiNbO₃-protected

Li anodes. Figure 6.5a demonstrates the cycling performance of the two NCM/Li cells cycled at 1 C-rate within the voltage range of 3.0-4.3 V vs. Li^+/Li . The cycling profiles of the first 10 cycles highlight the rapid degradation of the NCM/Li cell with bare-Li anode (green symbols). Initially, the cells with bare-Li and LiNbO_3 -Li anode deliver similar specific capacities of 166 and 164 mAh g^{-1} , respectively. After 100 cycles, the bare-Li cell shows a higher degradation rate with 60% capacity retention leading to a capacity of 101.3 mAh g^{-1} . In contrast, an improved cycling performance is achieved in the cell with the LiNbO_3 -protected Li anode. The cell exhibits a discharge capacity of 131.6 mAh g^{-1} after 100 cycles (capacity retention of 80%).

The voltage profiles of both cells at the 10th, 50st, and 100th cycle are shown in Figure 6.5b, revealing a smaller transferred charge upon cycling and a higher voltage decay of the cell with the bare-Li anode than for the LiNbO_3 -Li cell. The interphase characteristics of the electrodes upon cycling have also been studied by EIS (Figure 6.5c). Note that the cycled NCM cathode has been replaced here by fresh Li foils. In addition, the electrolyte and separator have also been refreshed before the EIS measurements. Two semicircles can be identified in the Nyquist plots, one at high frequencies related to the SEI surface film resistance and another semicircle at low frequencies, which can be attributed to the electrode charge-transfer resistance^[27]. For the bare-Li anode cell, the fitted values for the SEI resistance significantly increase from 123 (10th cycle) to 405 Ω (100th cycle).

On the other hand, the SEI resistance for the LiNbO_3 -Li cell increases from 109 (10th cycle) to 234 Ω after 100 cycles. It can be concluded from these results that the SEI formation predominantly occurs at the initial stages of cycling and proceeds with a more moderate rate during prolonged cycling. Furthermore, the impedance comparison shows that the modified-Li anode cell reveals a more moderate SEI resistance increase, thus slowing down the SEI formation during cycling.

6.3.3 Post-Mortem Analysis

The NCM/Li cells were disassembled after cycling for further characterization to investigate the origin of degradation of both Li anodes. Figure 6.5d shows the surface morphology of the bare-Li anode after 10 and 100 cycles. Mossy-Li with small particles can initially be observed at the bare-Li surface after 10 cycles, and the underlying Li-metal displays a much rougher morphology compared to the pristine Li-metal (Figure 6.1a). The cross-section (Figure 6.5d) also reveals that microstructures are formed at the bare-Li anode. After 100 cycles, the SEM top-view shows the growth of a highly porous Li-surface morphology at the bare-Li anode (Figure 6.5e). The inhomogeneous Li deposition during cycling resulted in highly loose and irregular surface structures.

In the case of the LiNbO_3 -Li anode (Figure 6.5f and g), the morphology remains virtually unchanged after 10 cycles compared to its pristine state (Figure 6.1b), no mossy-Li is observed at the surface. The corresponding cross-section SEM image in Figure 6.5f also confirms the compact coating of the LiNbO_3 layer at the Li-metal. A relatively flat surface is found at the LiNbO_3 -Li anode after 100 cycles, not revealing an open lithium morphology (Figure 6.5g). The appearing microcracks provide evidence of mechanical stress originating from the anode volume expansion during Li deposition, which negatively influence the LiNbO_3 -interfacial stability. Moreover, from the cross-section SEM image (Figure 6.5g), it can be concluded that the SEI film at the modified-Li anode is remarkably thin. These results show that the LiNbO_3 -protected Li-anodes facilitate a more uniform and compact Li deposition during cycling with negligible open Li structures. The thin-film protective LiNbO_3 -coating can effectively limit the growth of SEI film.

The dissolution of transition-metal ions from the Ni-rich cathode material during cycling is a widely known phenomenon.^[28-30] The dissolved metal ions are transported through the separator and transformed into the reduced state at the anode surface. Subsequently, these reduced species also participate in the SEI formation process. They may catalyze the various side reactions.^[31-33] The

introduced LiNbO₃ protective layer is a poor electronic conductor, inhibiting the metallic ion reduction at the anode. XPS measurements are therefore carried out to investigate whether the bare-Li and LiNbO₃-Li anodes might undergo different SEI evolutions during cycling. The results of these XPS measurements, including detailed valence state analyses, are listed in Table 6.1.

Table 6.1 Summary of XPS results for bare Li and LiNbO₃-protected electrodes.

<i>Binding energy (eV)</i>		<i>Peak assignment</i>	<i>Reference</i>
C 1s	~ 283.9	C-Li (RLi, lithium alkyl)	[24]
	~ 287.3	C-C, C-H	[24]
	~ 289.6	C-O (ROLi, lithium alkoxide)	[24]
	~ 289.5	C=O	[24]
	~291.8	C-F	[34]
O 1s	~ 527.3	Li ₂ O	[26]
	~ 528.7	Li ₂ CO ₃ /O=C-O (ROCO ₂ Li, lithium alkyl carbonates)	[26]
	~ 531.1	C-O	[26]
F 1s	~ 685.3	LiF	[35]
	~ 686.1	Li _x PF _y /Li _x PO _y F _z	[36]
	~ 687.5	C-F	[35]
P 2p	~ 133.1	Li _x PO _y F _z	[37]
	~ 136.2	Li _x PF _y	[37]
Ni 2p	~ 850.1	Ni	[33]
	~ 857.8	NiF ₂	[33]

Figure 6.6 shows the C 1s, O 1s, F 1s, P 2p, and Ni 2p spectra for both anodes after 10 cycles. In the C 1s spectra (Figure 6.6a), peaks located at 283.9, 287.3, 289.6, and 289.5 eV correspond to C-Li, C-C/C-H, C-O, and C=O (Li₂CO₃), respectively. The C-Li, C-C/C-H, and C-O bonds are attributed to organic components originating from the electrolyte solvent decomposition and

polymerization, such as RLi and ROLi .^[38] $\text{C}=\text{O}$ (Li_2CO_3) might result from electrolyte decomposition and the reaction between metallic Li and the gaseous by-product CO_2 formed in the cell. Both electrodes show similar peaks in the C 1s spectra, except that significantly decreased peak intensities are found for the LiNbO_3 -protected Li-anode. The O 1s spectra are shown in Figure 6.6b. The peaks are related to Li_2O (527.3 eV), Li_2CO_3 , or $\text{O}=\text{C}-\text{O}$ bond originated from ROCO_2Li (528.7 eV). The C-O bond at 531.1 eV originating from RLi , is visible at the bare-Li surface. The small amount of Li_2O at 527.3 eV can be associated with reactions induced by traces of oxygen and water present in the cell. In contrast, the absence of the Li_2O peak, along with the reduced intensity of the Li_2CO_3 (or $\text{O}=\text{C}-\text{O}$) and C-O peaks, is found for the LiNbO_3 -Li anode.

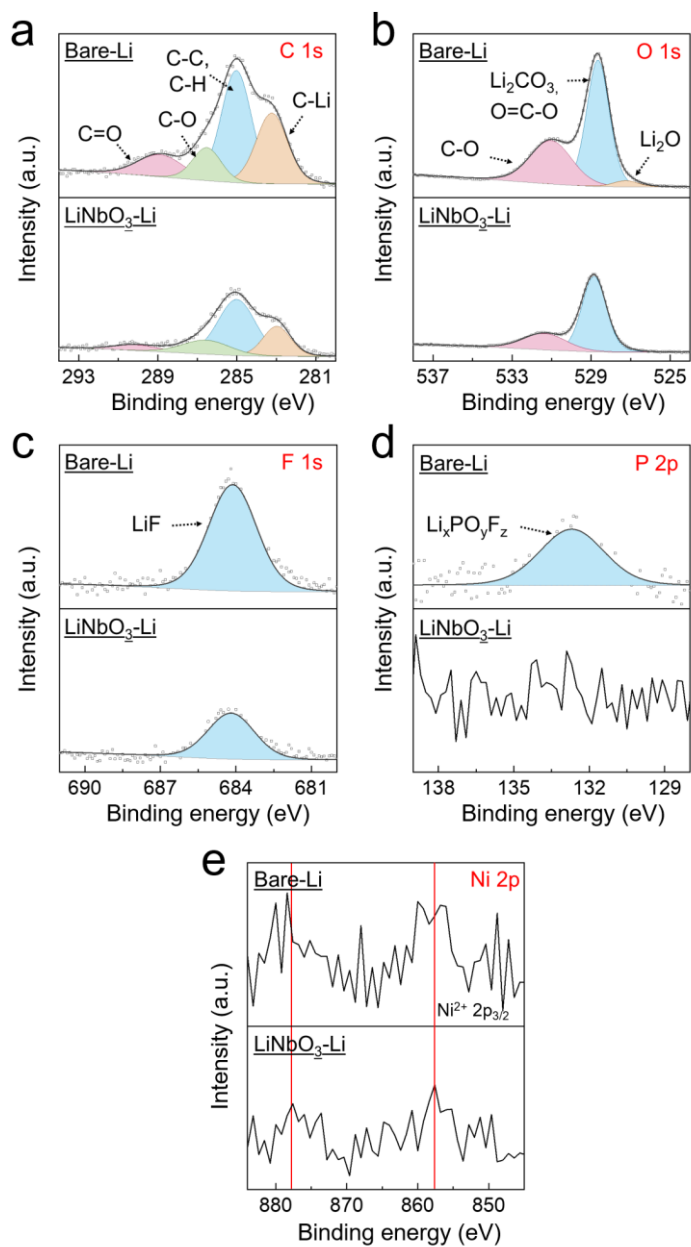


Figure 6.6 XPS spectra of (a) C 1s, (b) O 1s, (c) F 1s, (d) P 2p, and (e) Ni 2p obtained from both Li anodes after 10 cycles.

Additionally, peaks at 685.3 eV in the F 1s spectra (Figures 6.6c) and at 133.1 eV in the P 2p spectra (Figures 6.6d) can be assigned to LiF and $\text{Li}_x\text{PO}_y\text{F}_z$, respectively, which results from the decomposition of lithium salt in the electrolyte. Compared to the bare-Li anode, a much smaller amount of LiF and no $\text{Li}_x\text{PO}_y\text{F}_z$ is observed at the $\text{LiNbO}_3\text{-Li}$ anode surface after 10 cycles. Furthermore, the signals of the Ni 2p spectra of both anodes only reveal a relatively low resolution (Figure 6.6e), suggesting that the dissolution and transport of transition-metal ions occurred to some extent during the initial cycles. However, based on the quantitative analyses of the XPS survey scan shown in Figure 6.8c, the surface of bare-Li anode exhibits a higher atomic ratio of Ni element after 10 cycles (0.22%) than that at the $\text{LiNbO}_3\text{-Li}$ anode (0.09%). XPS surface analyses of both anodes after 10 cycles show that the reduction rate of metal ions is limited during the initial cycles. Moreover, the initial SEI film predominantly consists of inorganic components, including LiF , Li_2CO_3 , Li_2O , and $\text{Li}_x\text{PO}_y\text{F}_z$, accompanied by the generation of a few organic components, such as lithium alkyl (RLi) and lithium alkoxide (ROLi) species.

Furthermore, the surface components of both anodes after long-term cycling have been investigated by XPS. Figure 6.7 shows the spectra of the corresponding elements after 100 cycles. In the C 1s spectra (Figure 6.7a), a new peak located at 291.8 eV is found at the bare-Li anode, which can be assigned to the C-F bond. A significantly growing C-Li content originating from lithium alkyl is detected at the $\text{LiNbO}_3\text{-Li}$ anode. Accordingly, the O 1s spectrum of the bare-Li anode after 100 cycles (Figure 6.7b) is very consistent with the results obtained after 10 cycles. The peak corresponding to C-O has become more intense for the $\text{LiNbO}_3\text{-Li}$ anode after prolonged cycling. The F 1s and P 2p spectra indicate the complexity of phosphorous and fluorine-containing components formed at both long-term cycled anodes. In the F 1s spectrum (Figure 6.7c), two new peaks emerged at the surface of the bare-Li anode. The peaks at 686.1 and 687.5 eV correspond to Li_xPF_y (or $\text{Li}_x\text{PO}_y\text{F}_z$) and the C-F bond, originating from electrolyte degradation and PVDF migration from the cathode.

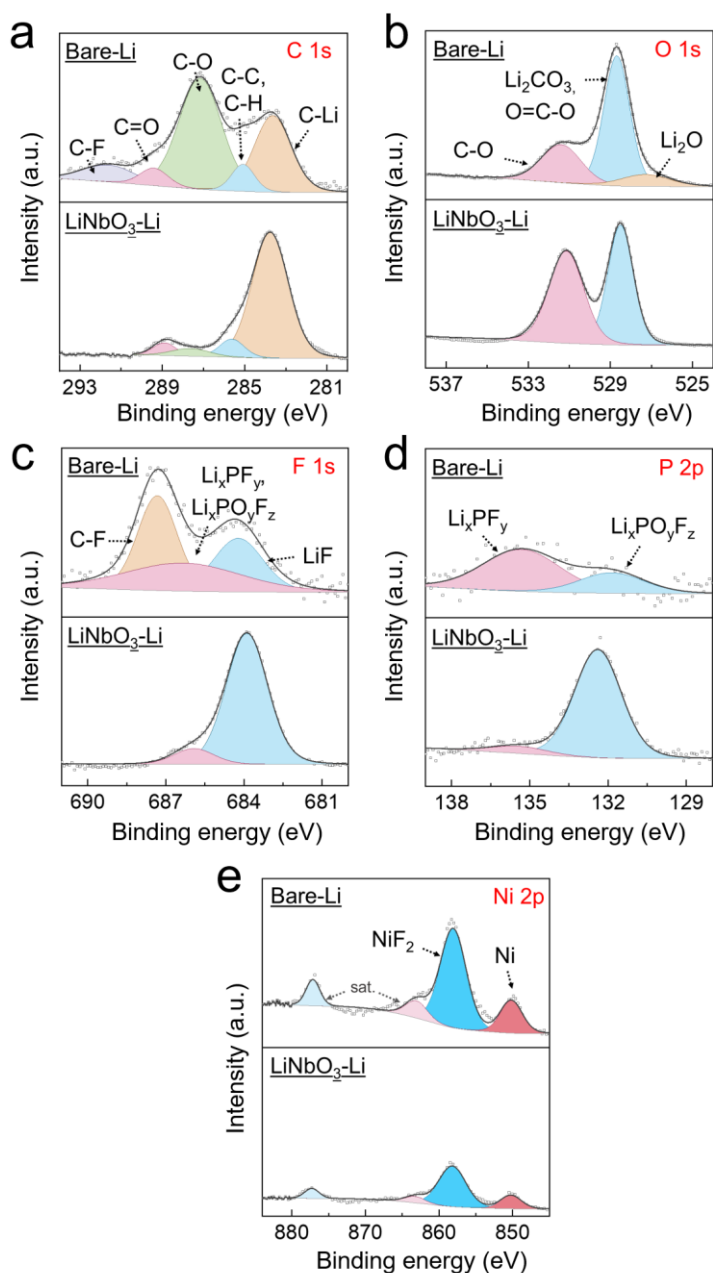


Figure 6.7 XPS spectra of (a) C 1s, (b) O 1s, (c) F 1s, (d) P 2p, and (e) Ni 2p obtained from the bare-Li and $\text{LiNbO}_3\text{-Li}$ anode after 100 cycles.

Regarding the F 1s spectra of $\text{LiNbO}_3\text{-Li}$ anode, no C-F species can be found, and the signal of LiF is significantly higher than that of the Li_xPF_y (or $\text{Li}_x\text{PO}_y\text{F}_z$) peaks. Additionally, the P 2p spectra in Figure 6.7d demonstrate that the phosphorous components at the surfaces are dominated by Li_xPF_y for a bare-Li anode and by $\text{Li}_x\text{PO}_y\text{F}_z$ for the $\text{LiNbO}_3\text{-Li}$ anode. It is also worth noting that Ni is identified in both Ni 2p spectra after long-term cycling (Figure 6.7e): two pairs of peaks can be assigned to metallic Ni at 850.1 eV and NiF_2 at 857.8 eV, which are the reduction states of dissolved Ni ions at the anode surface. Interestingly, according to the semi-quantitative XPS analyses in Figure 6.8c, the atomic ratio of Ni at the $\text{LiNbO}_3\text{-protected}$ Li-anode remained virtually unchanged from 10 cycles (0.09%) to 100 cycles (0.10%). In contrast, the detectable Ni-content at the bare-Li anode unravels a considerable increase from 0.22% at 10 cycles to 1.05% after 100 cycles. This increase shows that Ni is continuously reduced at the bare-Li anode.

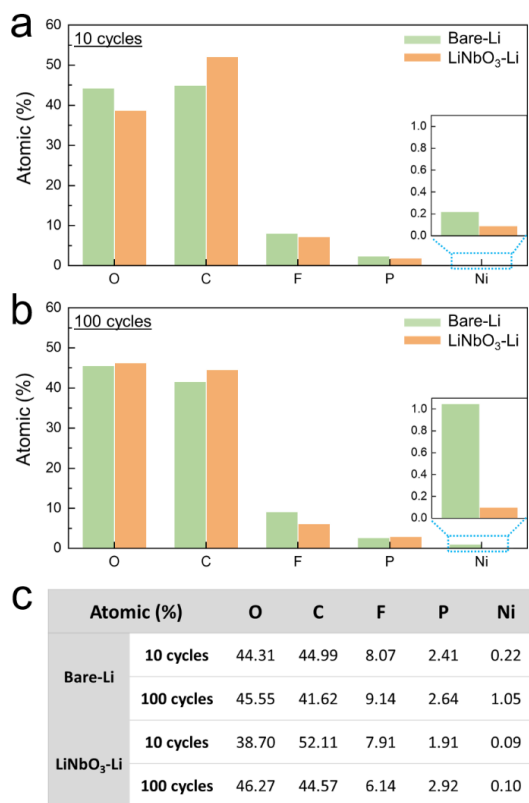


Figure 6.8 The atomic ratio obtained from the surface of bare-Li (green) and $\text{LiNbO}_3\text{-Li}$ (orange) anodes after (a) 10 and (b) 100 cycles. (c) Corresponding summary of the XPS analyses.

From the above XPS analyses, general information about the chemistry of the SEI formation upon anode cycling is provided. For the bare-Li anode, apart from the components that have been presented after initial cycling in Figure 6.6, new species arise upon long-term cycling. These species can be assigned to organic components (lithium alkyl carbonates (ROCO_2Li) and PVDF) and inorganic components (Li_xPF_y and NiF_2). PVDF can be attributed to the migration

of the binder material from the cathode, while NiF_2 is due to the reaction of metal ions crossing the electrolyte.

For the $\text{LiNbO}_3\text{-Li}$ anode, much more restrained growth of SEI film can be observed. New components show up after extensive cycling, including ROCO_2Li , $\text{Li}_x\text{PO}_y\text{F}_z$, and NiF_2 . Also, the absence of PVDF and the barely growing Ni-content at the $\text{LiNbO}_3\text{-Li}$ anode demonstrate that the LiNbO_3 protective layer appropriately suppresses the chemical crossing from the cathode.

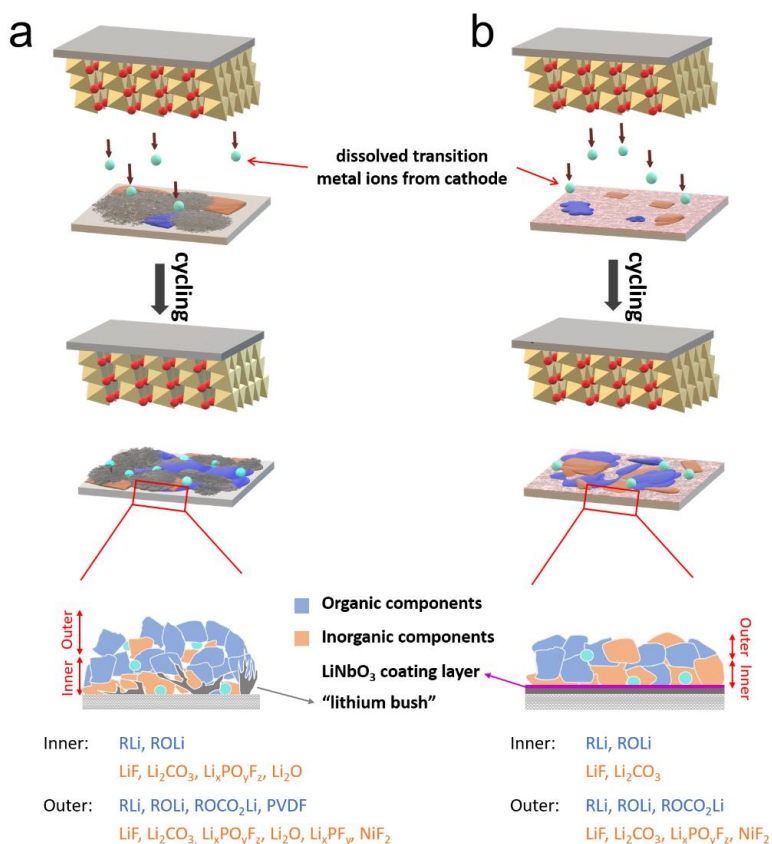


Figure 6.9 Schematic representation of the SEI film growth at the (a) bare-Li and (b) $\text{LiNbO}_3\text{-Li}$ anode.

Figure 6.9 schematically shows the development of the SEI layers at the bare-Li (a) and protected-Li anode (b). A loose and fragile SEI film, composed of inorganic-rich components, is formed at the bare-Li anode at the beginning of cycling, accompanied by uneven lithium deposition and mossy-Li growth. The initially deposited mossy-Li eventually develops into a highly porous structure during cycling due to repeated deposition and stripping of Li. In conclusion, the evolution of the SEI surface layer is a complex process in which many components are formed during cycling in both the inner and outer SEI-layers.^[39] Notably, the presence of PVDF species and the increase of Ni are observed at the bare-Li anode surface, indicating the increased impact of the cathode on the performance of the Li-anode during cycling.

In contrast, the evolution of the SEI film on the LiNbO_3 -protected Li-anode is a more straightforward process (Figure 6.9b). Firstly, no porous lithium is formed at the anode surface, implying smooth and uniform lithium deposition and stripping. Secondly, the lack of PVDF species and the limited amount of Ni formed inside the SEI layer during cycling confirm the stabilizing role of the LiNbO_3 protective layer at the Li-anode surface. It suppresses the reduction of Ni-ions, stemming from the cathode dissolution, at the anode surface.

Although the different evolutions of SEI films on two Li-metal anodes have been discussed above, the detailed underlying mechanisms for SEI growth remain not fully understood. According to previous studies, the catalytic effect of metallic Ni may play a key role in accelerating the SEI growth.^[33, 40, 41] Metallic nanoparticles formed at the anode surface may potentially act as nucleation sites for multiple side reactions due to their high electronic conductivity and surface energy. When a bare-Li anode is coupled with a Ni-rich cathode in a complete Li/NMC cell, Ni ions will dissolve into the electrolyte and move through the separator to the anode, where the ions are randomly deposited and embedded into the open SEI film. To make things worse, Li-metal itself is already highly reactive towards the electrolyte, as concluded in the storage tests of Figure 6.3a. Thus, the mossy and open Li-structure that emerges upon cycling provides a large specific

surface area for these side reactions. Given the additional electronic pathways provided by Ni contamination, exacerbated surface passivation can indeed be expected for bare-Li anodes.

On the other hand, in LiNbO_3 -protected Li anodes, the following aspects explain the observed improvements: (1) LiNbO_3 layers efficiently isolate Li-metal from direct interaction with the electrolyte, inhibiting side reactions; (2) the growth of Li-structures is suppressed by the LiNbO_3 layer, while its intrinsically high ionic conductivity guarantees a smooth transfer of Li ions as well as a more uniform Li deposition; (3) the rate of Ni-ions reduction is effectively declined due to the electronically non-conductive LiNbO_3 layer, though the dissolution of transition-metal ions accelerates with cycling, the amount of Ni-contamination on the LiNbO_3 -Li anode is kept relatively stable; (4) the growth of the SEI film is limited at LiNbO_3 -protected Li-anodes, resulting in a moderate and more compact SEI formation. More detailed investigations from a computational perspective, such as density functional theory calculations, are necessary to understand SEI evolution in more detail.

6.4 Conclusions

Amorphous LiNbO_3 thin films deposited by RF sputtering onto Li metal were used as a protective coating on a Li-metal anode. Compared with unprotected bare-Li anodes, LiNbO_3 -protected Li-metal anodes demonstrate an enhanced electrochemical stripping and plating performance in symmetrical cells, with prolonged cycling life and lower polarization. Full cells composed of Ni-rich NCM cathodes and various Li-metal anodes have been assembled to explore the influence of the crossover effect induced by the cathode on the SEI formation process. Electrochemical measurements show significantly improved cycling stability of NCM/ LiNbO_3 -Li cells with a capacity retention of 80% after 100 cycles, which is considerably higher than that of NCM/bare-Li cells.

In addition, post-mortem XPS characterization reveals differences in SEI evolution of LiNbO_3 -protected Li-anodes upon cycling. For bare-Li anodes, the surface shows a highly loose morphology with various Li-structures. In contrast, a more compact and flat structure is observed at a LiNbO_3 -protected Li anode surface upon cycling, implying uniform Li deposition and more moderate SEI-film formation. Furthermore, the chemical composition of the SEI layer during cycling is investigated by XPS. In particular, the migrated PVDF species from the cathode side and reduced Ni states (NiF_2 and Ni) are found in large concentrations at bare-Li anodes, indicating that Ni dissolution from the cathode plays a dominant role.

On the other hand, for LiNbO_3 -protected Li-anodes, no PVDF species have been detected, as well as a virtually unchanged low amount of Ni-content after cycling. Considering a catalytic role of reduced metal ions, it is expected that LiNbO_3 layers are preventing the deposition of Ni-species inside the SEI layer at metallic Li, thereby favorably influencing the SEI film morphology and, consequently, improving the overall cell performance. Additionally, artificial layers deposited on the cathode, novel electrolyte additives, separator with enhanced selectivity, and protective coatings for Li-metal with higher flexibility could further mitigate the reactivity of Li-metal anodes and promote the long-term stability for the next-generation LMBs.

References

- 1 A. Manthiram, *Nature Communication* **11** (2020) 1550.
- 2 G. L. Zhu, C. Z. Zhao, J. Q. Huang, C. He, J. Zhang, S. Chen, L. Xu, H. Yuan, Q. Zhang, *Small* **15** (2019) 1805389.
- 3 L. Wen, J. Liang, J. Chen, Z. Y. Chu, H. M. Cheng, F. Li, *Small Methods* **3** (2019) 1900323.

- 4 X. Fan, L. Chen, O. Borodin, X. Ji, J. Chen, S. Hou, T. Deng, J. Zheng, C. Yang, S. C. Liou, K. Amine, K. Xu, C. Wang, *Nature Nanotechnology* **13** (2018) 715.
- 5 W. Xu, J. Wang, F. Ding, X. Chen, E. Nasybulin, Y. Zhang, J. G. Zhang, *Energy & Environmental Science* **7** (2014) 513.
- 6 S. J. Park, J. Y. Hwang, C. S. Yoon, H. G. Jung, Y. K. Sun, *ACS Applied Materials & Interfaces* **10** (2018) 17985.
- 7 J. W. Choi, D. Aurbach, *Nature Reviews Materials* **1** (2016) 16013.
- 8 N. W. Li, Y. X. Yin, C. P. Yang, Y. G. Guo, *Advanced Materials* **28** (2016) 1853.
- 9 L. Wang, Q. Wang, W. Jia, S. Chen, P. Gao, J. Li, *Journal of Power Sources* **342** (2017) 175.
- 10 R. Xu, X. Q. Zhang, X. B. Cheng, H. J. Peng, C. Z. Zhao, C. Yan, J. Q. Huang, *Advanced Functional Materials* **28** (2018) 1705838.
- 11 X. B. Cheng, R. Zhang, C. Z. Zhao, Q. Zhang, *Chemical Reviews* **117** (2017) 10403.
- 12 D. Wang, W. Zhang, W. Zheng, X. Cui, T. Rojo, Q. Zhang, *Advanced Science* **4** (2017) 1600168.
- 13 X. B. Cheng, R. Zhang, C. Z. Zhao, F. Wei, J. G. Zhang, Q. Zhang, *Advanced Science* **3** (2016) 1500213.
- 14 Y. Sun, Y. Zhao, J. Wang, J. Liang, C. Wang, Q. Sun, X. Lin, K. R. Adair, J. Luo, D. Wang, R. Li, M. Cai, T. K. Sham, X. Sun, *Advanced Materials* **31** (2019) e1806541.
- 15 E. Cha, M. D. Patel, J. Park, J. Hwang, V. Prasad, K. Cho, W. Choi, *Nat Nanotechnol* **13** (2018) 337.
- 16 Y. Liu, D. Lin, P. Y. Yuen, K. Liu, J. Xie, R. H. Dauskardt, Y. Cui, *Advanced Materials* **29** (2017) 1605531.
- 17 H. Ye, Z. J. Zheng, H. R. Yao, S. C. Liu, T. T. Zuo, X. W. Wu, Y. X. Yin, N. W. Li, J. J. Gu, F. F. Cao, Y. G. Guo, *Angewandte Chemie* **58** (2019) 1094.

- 18 Z. Huang, G. Zhou, W. Lv, Y. Deng, Y. Zhang, C. Zhang, F. Kang, Q. H. Yang, *Nano Energy* **61** (2019) 47.
- 19 K. Liu, A. Pei, H. R. Lee, B. Kong, N. Liu, D. Lin, Y. Liu, C. Liu, P. C. Hsu, Z. Bao, Y. Cui, *Journal of the American Chemical Society* **139** (2017) 4815.
- 20 E. Kazyak, K. N. Wood, N. P. Dasgupta, *Chemistry of Materials* **27** (2015) 6457.
- 21 S. Fang, D. Jackson, M. L. Dreibelbis, T. F. Kuech, R. J. Hamers, *Journal of Power Sources* **373** (2018) 184.
- 22 C. Mao, R. E. Ruther, L. Geng, Z. Li, D. N. Leonard, H. M. Meyer, R. L. Sacci, D. L. Wood, *ACS Applied Materials & Interfaces* **11** (2019) 43235.
- 23 J. N. Zhang, Q. Li, Y. Wang, J. Zheng, X. Yu, H. Li, *Energy Storage Materials* **14** (2018) 1.
- 24 H. Lee, H. S. Lim, X. Ren, L. Yu, M. H. Engelhard, K. S. Han, J. Lee, H. T. Kim, J. Xiao, J. Liu, W. Xu, J. G. Zhang, *ACS Energy Letters* **3** (2018) 2921.
- 25 J. Betz, J. P. Brinkmann, R. Nölle, C. Lürenbaum, M. Kolek, M. C. Stan, M. Winter, T. Placke, *Advanced Energy Materials* **9** (2019) 1900574.
- 26 J. Langdon, A. Manthiram, *Advanced Functional Materials* **31** (2021) 2010267.
- 27 S. J. An, J. Li, C. Daniel, H. M. Meyer, S. E. Trask, B. J. Polzin, D. L. Wood, *ACS Applied Materials & Interfaces* **9** (2017) 18799.
- 28 D. S. Ko, J. H. Park, S. Park, Y. N. Ham, S. J. Ahn, J. H. Park, H. N. Han, E. Lee, W. S. Jeon, C. Jung, *Nano Energy* **56** (2019) 434.
- 29 T. Kim, L. K. Ono, N. Fleck, S. R. Raga, Y. Qi, *Journal of Materials Chemistry A* **6** (2018) 14449.
- 30 S. S. Zhang, *Energy Storage Materials* **24** (2020) 247.
- 31 W. Li, *Journal of The Electrochemical Society* **167** (2020) 090514.
- 32 R. Jung, F. Linsenmann, R. Thomas, J. Wandt, S. Solchenbach, F. Maglia, C. Stinner, M. Tromp, H. A. Gasteiger, *Journal of The Electrochemical Society* **166** (2019) A378.

- 33 J. Kim, H. Ma, H. Cha, H. Lee, J. Sung, M. Seo, P. Oh, M. Park, J. Cho, *Energy & Environmental Science* **11** (2018) 1449.
- 34 W. Liu, J. Li, W. Li, H. Xu, C. Zhang, X. Qiu, *Nature Communication* **11** (2020) 3629.
- 35 P. Niehoff, M. Winter, *Langmuir* **29** (2013) 15813.
- 36 W. Li, B. L. Lucht, *Journal of The Electrochemical Society* **153** (2006) 15813.
- 37 Q. Li, Y. Wang, X. Wang, X. Sun, J. N. Zhang, X. Yu, H. Li, *ACS Applied Materials & Interfaces* **12** (2020) 2319.
- 38 Q. Wang, L. Jiang, Y. Yu, J. Sun, *Nano Energy* **55** (2019) 93.
- 39 D. Li, D. Danilov, Z. Zhang, H. Chen, Y. Yang, P. H. L. Notten, *Journal of The Electrochemical Society* **162** (2015) A858.
- 40 W. Li, U. H. Kim, A. Dolocan, Y. K. Sun, A. Manthiram, *ACS Nano* **11** (2017) 5853.
- 41 W. Li, A. Dolocan, P. Oh, H. Celio, S. Park, J. Cho, A. Manthiram, *Nature Communication* **8** (2017) 14589.

Chapter 7

Summary and Outlook

Nowadays, a global consensus on the impending global warming crisis and the urgent need to replace fossil fuels with renewable energy has been reached. The majority of countries worldwide have pledged to realize carbon-neutrality before 2050 by restraining the CO₂ emission and expanding the proportion of renewable energy sources. Therefore, expectations on such a scheme stimulate intensive research and development efforts on various energy storage solutions. Among all renewable energy strategies, rechargeable battery systems play a predominant role in the application of sophisticated portable devices. It also has been widely recognized as the most promising candidate for replacing fossil fuels in automobiles. As one of the most mature battery systems, the Li-ion batteries (LIBs) have received tremendous attention from industry and academia. There is no doubt that the rapid increase of the electric vehicle market in recent years relies heavily on the successful commercialization of LIBs. Still, challenges on developing next-generation LIBs with higher energy density, prolonged cycle life, and enhanced safety remain due to the performance limitations of currently used electrode materials.

The bottleneck of further increasing the energy density of LIBs is mainly related to the cathode material. The energy density of almost all emerging cathodes do not match with those of the anodes. Moreover, for cathode materials, the balance between three essential battery properties - energy density, cyclability, safety - is challenging to reach due to their complex compounds and fragile structures. Layered Ni-rich transition-metal oxides have a relatively high energy

density but are suffering from a poor cycling stability. The instability of Ni-rich cathode-based LIBs is associated with various passive reactions occurring inside batteries. Material optimization strategies can be adopted to mitigate these detriments. This thesis is mainly focusing on the electrode material design and degradation mechanism studies of Ni-rich cathode-based batteries. Ni-rich NCM cathodes and Li-metal anodes with superior battery performance are achieved through these novel optimization strategies. The corresponding degradation phenomena are investigated, and detailed mechanisms are identified.

In **Chapter 1**, the basics of LIBs and the state-of-art electrode materials are introduced. A comprehensive comparison among the cathode materials exhibits the considerable potential of Ni-rich-based cathodes as the candidate for the next-generation LIBs with boosted energy density. However, the phase transformation of Ni-rich cathodes is prone to occur irreversibly during battery cycling, which significantly hinders their practical applications. Fundamentals of Ni-rich cathodes presented in Chapter 1, including crystal structure and electrochemical properties, offer a glimpse of the fragile feature of Ni-rich cathodes and are in favor of in-depth understanding of underlying decay mechanisms.

Sound knowledge of degradation phenomena is of importance for optimal material design. In **Chapter 2**, a variety of passivation reactions occurring in Ni-rich cathode-based LIBs is thoroughly discussed. The performance decay of a battery can be attributed to cathode, anode, and electrolyte. For Ni-rich cathodes, the currently existing challenges involve: 1) residual lithium compounds at the surface; 2) cation disorder in the crystal structure; 3) structural reconstruction leading to inactive NiO layer formation; 4) gas releasing introducing safety hazards; 5) transition-metal dissolution; 6) intragranular and intergranular cracks formation; and 7) thermal instability. Regarding the anode side, degradation of graphite and Li-metal are discussed as they are most commonly coupled with Ni-rich cathodes. Volume expansion, graphite layer exfoliation, and Li dendrite growth are of specific concern. Noteworthy, crossover between the cathode and

anode has been drawing growing attention recently. It is found that decomposed species from one electrode can accelerate the passive reactions at the other electrode surface. Moreover, electrolyte decomposition and solid-electrolyte-interphase formation at the electrode surface will significantly consume mobile Li-ions, causing Li inventory loss and capacity decline.

Different remedying strategies are systematically discussed based on the understanding of degradation mechanisms for Ni-rich cathode-based LIBs, targeting the optimizations of the cathode, anode, and electrolyte. Though considerable progress has been achieved by implementing novel strategies, the obstacles in batteries cannot be overcome by one single method. A hybrid design is foreseen to guide the further development of LIBs based on Ni-rich cathodes.

Chapter 3 presents the experimental methods applied in this thesis, including the synthesis principles, characterization techniques, electrode preparations, and electrochemical measurements. The listed methods are essential for material optimization and performance assessment, providing solid evidence of improvements proposed in the following chapters.

The random crystal orientation of Ni-rich particles holds great responsibility for the capacity decline. The nonuniform volume change will result in the formation of intragranular cracks. **Chapter 4** reports a method of structural optimization for NCM cathodes. Hydrothermal synthesis assisted by the surfactant CTAB is employed to improve the stability and Li-ion transportation kinetics of Ni-rich $\text{LiNi}_{0.6}\text{Co}_{0.2}\text{Mn}_{0.2}\text{O}_2$ cathodes. The obtained $\text{LiNi}_{0.6}\text{Co}_{0.2}\text{Mn}_{0.2}\text{O}_2$ particles possess a unique nanobrick morphology with enlarged specific surface area. HRTEM images and SAED patterns clearly reveal the exposed active {010} facets on the lateral panel in the particles, which will provide extra Li-ion diffusion pathways and facilitate Li-ion (de)intercalating during operation. The electrochemical measurements confirm the significantly enhanced stability of nanobrick $\text{LiNi}_{0.6}\text{Co}_{0.2}\text{Mn}_{0.2}\text{O}_2$ materials with a capacity

retention of 85% after 100 cycles, compared to that of the commercial counterpart with only 60% capacity retention. The rate capability has also been boosted, and the charge-transfer resistance of nanobrick $\text{LiNi}_{0.6}\text{Co}_{0.2}\text{Mn}_{0.2}\text{O}_2$ cathodes is reduced. Calculations of the Li-ion diffusion coefficient claim a much higher value for nanobrick $\text{LiNi}_{0.6}\text{Co}_{0.2}\text{Mn}_{0.2}\text{O}_2$, thus, enabling fast-charging capability and mitigated microcracks propagation during cycling.

Structural optimization of $\text{LiNi}_{0.6}\text{Co}_{0.2}\text{Mn}_{0.2}\text{O}_2$ described in Chapter 4 has substantiated the alternative strategy for cathode improvement. It consists in preventing the HF corrosion effect and constraining CEI formation. Following this strategy in **Chapter 5**, the fabrication of a LiNbO_3 -coated $\text{LiNi}_{0.6}\text{Co}_{0.2}\text{Mn}_{0.2}\text{O}_2$ cathode has been proposed. The thin-film system has been used to provide a simple object for investigating the evolution of the CEI film and excluding the contributions from electrode additives (PVDF binder and conductive carbon). $\text{LiNi}_{0.6}\text{Co}_{0.2}\text{Mn}_{0.2}\text{O}_2$ and LiNbO_3 -coated $\text{LiNi}_{0.6}\text{Co}_{0.2}\text{Mn}_{0.2}\text{O}_2$ thin films are successfully obtained via sputtering deposition, achieving highly homogeneous surfaces for further analyses. The XPS depth-profiling technique is intensively applied for surface and interface detections. An intrinsic interlayer with a thickness of around 30 nm has been identified between LiNbO_3 and LiNbO_3 -coated $\text{LiNi}_{0.6}\text{Co}_{0.2}\text{Mn}_{0.2}\text{O}_2$ films, induced by the diffusion of Ni^{2+} ions.

The results show that the LiNbO_3 -coated cathode demonstrates a stabilized electrochemical cycling behavior and moderate increase of charge-transfer resistance. Post-mortem analysis reveals the function of the LiNbO_3 layer. Much fewer transition-metal ions can be detected in the electrolyte with the LiNbO_3 -coated sample as cathode, and SEM image finds no microcracks at the LiNbO_3 surface. XPS depth profiles of both cycled thin films affirm the stability of the $\text{LiNbO}_3/\text{LiNi}_{0.6}\text{Co}_{0.2}\text{Mn}_{0.2}\text{O}_2$ interface and portray differences in CEI evolutions. The LiNbO_3 -coated cathode inhibits CEI formation and reduces the amount of residuals from electrolyte decomposition. The surface reconstruction layer, an inactive NiO phase, is also absent at the LiNbO_3 -coated $\text{LiNi}_{0.6}\text{Co}_{0.2}\text{Mn}_{0.2}\text{O}_2$

cathode. Thus, as presented in Chapter 5, a better understanding of the LiNbO_3 functional layer, CEI formation in Ni-rich cathode, and the interaction between $\text{LiNi}_{0.6}\text{Co}_{0.2}\text{Mn}_{0.2}\text{O}_2$ and LiNbO_3 is realized.

Aiming to address the chemical cross-over problem in $\text{LiNi}_{0.6}\text{Co}_{0.2}\text{Mn}_{0.2}\text{O}_2/\text{Li}$ cells and improve the performance from a full-cell prospect, the surface modification of Li-metal anodes is described in **Chapter 6**. LiNbO_3 , as a solid-state electrolyte with intrinsic high ionic conductivity, is again proposed as protective layer for Li-metal anodes. Prolonged stripping/plating measurements in symmetric Li cells demonstrate the robustness of the LiNbO_3 layer. The results show that LiNbO_3 -coated Li-metal anodes preserve compact morphology with cycling up to 200 h by effectively suppressing the Li dendrite growth and providing uniform Li deposition. The enhanced stability of LiNbO_3 -coated Li-metal is further demonstrated in $\text{LiNi}_{0.6}\text{Co}_{0.2}\text{Mn}_{0.2}\text{O}_2/\text{Li}$ cells. The SEI film formed on the LiNbO_3 -coated Li-metal is dense and flat. No lithium-deposited structures can be observed. Subsequently, the analysis of chemical components in SEI films of both anodes confirms the constrained growth of SEI film on LiNbO_3 -coated Li-metal. Notably, the residuals cross-over from the cathode side are also found in decreased amounts, including PVDF species and reduced Ni ions. The results presented in Chapter 6 establish a new approach to improve LIBs with a Ni-rich-based cathode and bring more potential to the commercialization of Li-metal anodes.

In summary, this thesis built up a comprehensive knowledge of Ni-rich cathodes, providing new insights on future developments towards Ni-rich cathode-based LIBs with superior performances. Systematical studies on material optimizations and degradation mechanism investigations are carried out. The results presented here contribute to a deep understanding of LIBs and inspire future strategies for continuous improvements and the eventual application of next-generation LIBs. Summarizing the knowledge described in this thesis, it can be concluded that more advanced materials and battery manufacturing methods

are still needed. Several research directions for the near future can therefore be envisioned: 1) the development of Ni-rich/Co-free layered cathode materials; 2) in-depth investigations on the degradation mechanisms of newly proposed materials are of utmost necessity; 3) the combined synergetic effect of several strategies could offer additional performance benefits to new Ni-rich cathode materials, and 4) further progress of anode-free LIBs will lead to new methods for the modification of uniform Li deposition. This will eventually lead to a new generation of high-performance Li-ion batterie.

List of Abbreviations

ALD	atomic layer deposition
ASSBs	all-solid-state batteries
<i>ccp</i>	cubic-close-packed lattice
CEI	cathode-electrolyte interphase
C-NCM	commercial NCM
CS	core-shell concentration gradient
CNT	carbon-nanotube
CTAB	cetyltrimethylammonium bromide
CV	cyclic voltammogram
CVD	chemical vapor deposition
DC	direct current
DEC	diethyl carbonate
DEMS	differential electrochemical mass spectrometry
DFT	density functional theory
DMC	dimethyl carbonate
EC	ethylene carbonate
EDX	energy dispersive X-ray
EIS	electrochemical impedance spectroscopy
EMC	ethyl-methyl carbonates
EMS	electrochemical mass spectroscopy
EVs	electric vehicles
FCG	full concentration gradient
FIB	focused ion beam
GITT	galvanostatic intermittent titration
H	hexagonal phase
HAADF-STEM	high-angle annular dark-field STEM

HE-NCM	lithium-rich metal oxides
HOMO	the highest occupied molecular orbital
HRPD	high-resolution powder diffraction
HRTEM	high-resolution transmission electron microscopy
HTSRD	high-temperature synchrotron radiation diffraction
ICP-MS	inductively coupled plasma source-mass spectrometry
LCO	LiCoO_2
LFP	LiFePO_4
LIBs	lithium-ion batteries
Li-ion	lithium-ion
LMBs	lithium-metal batteries
LNMO	$\text{LiNi}_{0.5}\text{Mn}_{1.5}\text{O}_4$
LTO	$\text{Li}_4\text{Ti}_5\text{O}_{12}$
LUMO	the lowest unoccupied molecular orbital
M	monoclinic phase
NB-NCM	nanobrick NCM
NCA	$\text{LiNi}_x\text{Co}_y\text{Al}_{1-x-y}\text{O}_2$
NCM	$\text{LiNi}_x\text{Co}_y\text{Mn}_{1-x-y}\text{O}_2$
NCM111	$\text{LiNi}_{1/3}\text{Co}_{1/3}\text{Mn}_{1/3}\text{O}_2$
NCM622	$\text{LiNi}_{0.6}\text{Co}_{0.2}\text{Mn}_{0.2}\text{O}_2$
NCM811	$\text{LiNi}_{0.8}\text{Co}_{0.1}\text{Mn}_{0.1}\text{O}_2$
NCM900505	$\text{LiNi}_{0.90}\text{Co}_{0.05}\text{Mn}_{0.05}\text{O}_2$
NMP	N-methylpyrrolidone
NTE	negative thermal expansion
P3m1	trigonal layered structure
PC	propylene carbonate
PVDF	poly (vinylidene fluoride)
RF	radio frequency

RLCs	residual lithium compounds
RLi	lithium alkyl
ROLi	lithium alkoxide
ROCO ₂ Li	lithium alkyl carbonates
SAED	selected area electron diffraction
SEI	solid-electrolyte-interphase
SEM	scanning electron microscopy
SOC	state of charge
SRL	surface reconstruction layer
SR-PXRD	synchrotron-radiation powder X-ray diffraction
STEM	scanning transmission electron microscopy
TEM	transmission electron microscope
TM	transition-metal
ToF-SIMS	time-of-flight secondary ion mass spectrometry
TSFCG	two-slopes full concentration gradient
UPD	underpotential deposition
XANES	X-ray absorption near edge structure
XAS	X-ray absorption spectroscopy
XPS	X-ray photoelectron spectroscopy
XRD	X-ray diffraction

List of Symbols

d	[Å]	lattice space
D_{Li^+}	[cm ² s ⁻¹]	diffusion coefficient
E_{cell}	[Wh g ⁻¹]	specific energy density
E	[V]	equilibrium voltage
F	[C mol ⁻¹]	Faraday constant
I	[A]	applied current
L	[cm]	electrode thickness
M_B	[g mol ⁻¹]	atomic weight of the electrode material
m_B	[g]	mass loading of active material in the electrode
n	[-]	diffraction order
Q_{cell}	[mAh g ⁻¹]	charge capacity
R_{ct}	[Ω]	charge transfer resistance
S	[cm ²]	area of the electrode-electrolyte interface
V_{cell}	[V]	cell voltage
V_M	[cm ³ mol ⁻¹]	molar volume of the electrode material
W	[-]	Warburg element
z	[-]	valence number of Li ions
δ	[-]	stoichiometric index in Li _δ MO ₂
τ	[s]	time interval of the current titration
θ	[°]	glancing angle
λ	[m]	wavelength of radiation
σ	[S cm ⁻¹]	ionic conductivity
$\mu_{cathode}^{Li}$	[J mol ⁻¹]	chemical potential of Li in the cathode
μ_{anode}^{Li}	[J mol ⁻¹]	chemical potential of Li in the anode

List of Publications

Journal Publications

1. **Ming Jiang**, Dmitri L. Danilov, Rüdiger-A. Eichel and Peter H. L. Notten, A review of degradation mechanisms and recent achievements for Ni-rich cathode-based Li-ion batteries, *Advanced Energy Materials* **11** (2021) 2103005.
2. **Ming Jiang**, Qian Zhang, Dmitri L. Danilov, Rüdiger-A. Eichel and Peter H. L. Notten, Formation of a Stable Solid-Electrolyte Interphase at Metallic Lithium Anodes Induced by LiNbO₃ Protective Layers, *ACS Applied Energy Materials* **4** (2021) 10333.
3. **Ming Jiang**, Xiaochao Wu, Qian Zhang, Dmitri L. Danilov, Rüdiger-A. Eichel and Peter H. L. Notten, Fabrication of Ni-rich thin-film cathodes and interfacial characterizations for stable Li-ion batteries, *Electrochimica Acta* **398** (2021) 139316.
4. **Ming Jiang**, Qian Zhang, Xiaochao Wu, Zhiqiang Chen, Dmitri L. Danilov, Rüdiger-A. Eichel, and Peter H. L. Notten, Synthesis of Ni-Rich Layered-Oxide Nanomaterials with Enhanced Li-Ion Diffusion Pathways as High-Rate Cathodes for Li-Ion Batteries, *ACS Applied Energy Materials* **3** (2020) 6583.
5. Chunguang Chen, **Ming Jiang**, Tao Zhou, Luc Raijmakers, Egor Vezhlev, Baolin Wu, Tobias, U. Schüllli, Dmitri L. Danilov, Yujie Wei, Rüdiger-A. Eichel and Peter H. L. Notten, Interface aspects in all-solid-state Li-based batteries reviewed, *Advanced Energy Materials* **11** (2021) 2003939.
6. Kudakwashe Chayambuka, **Ming Jiang**, Grietus Mulder, Dmitri L. Danilov and Peter H. L. Notten, Physics-based Modeling of Sodium-ion Batteries Part I: Experimental parameter determination, Under review (2021).
7. Dmitri L. Danilov, Chunguang Chen, **Ming Jiang**, Rüdiger-A. Eichel and

Peter H. L. Notten, On the conversion of NDP energy spectra into depth concentration profiles for thin-films all-solid-state batteries, *Radiation effects and defects in solids* **175** (2020) 367.

8. Lei Zhou, Hao Li, Yue Zhang, **Ming Jiang**, Dmitri L. Danilov, Rüdiger-A. Eichel and Peter H. L. Notten, Enhanced sulfur utilization in lithium-sulfur batteries by hybrid modified separators, *Materials Today Communications* **26** (2021) 102133.
9. Zhiqiang Chen, Dmitri L. Danilov, Kudakwashe Chayambuka, Lei Zhou, **Ming Jiang**, Luc H.J. Raijmakers, Jiang Zhou, Rüdiger-A. Eichel and Peter H. L. Notten, Overpotential analysis of Graphite-based Li-ion batteries, seen from a porous electrode modeling perspective, *Journal of Power Sources* **509** (2021) 230345.

Conference Contribution

1. **Ming Jiang**, Dmitri L. Danilov, Rüdiger-A. Eichel, and Peter H. L. Notten, Ni-rich cathode nanomaterials with enhanced exposed Li-ion diffusion pathways for Li-ion batteries, Advanced Battery Power Conference (2021), Essen, Germany.

Curriculum Vitae

Ming Jiang was born on 25th June 1992 in Tianjin City, China. She received a BSc degree in Applied Chemistry from Beijing University of Chemical Technology (BUCT) in 2014. Then she started her postgraduate study in State Key Laboratory of Chemical Resource Engineering, College of Science, BUCT, under the supervision of Prof. dr. Xiaoming Sun. In 2017 she graduated on the research topic of “nanoarray electrodes and their application in electrocatalysis” and received an MSc degree in Chemistry. After that, she continued with doctoral research under the supervision of Prof. dr. Peter H. L. Notten and Prof. dr. Rüdiger-A. Eichel at the Eindhoven University of Technology (TU/e, the Netherlands). Her topic focused on the material design and degradation mechanistic studies of Ni-rich cathode-based Li-ion batteries.

Acknowledgements

At the endpoint of the doctoral period, the intense emotions filled my heart with lots of gratitude and happiness. First of all, I would like to express my great appreciation to my first supervisor: Prof. P.H.L. Notten, who kindly offered me this valuable opportunity to join the group in TU/e and carry out my research in IEK-9. Peter, you are always so nice and being solid supportive on whatever I'm interested in. I appreciate all the insights and guidance you provided from the bottom of my heart. It's always a great pleasure to talk with you, and I learned a lot from all our discussions. I put this quote on the front page – 'Wisdom comes out of dialogue. You have to develop a capacity to expose your own ignorance so that they may discover their own wisdom.' – is not only because it comes from the John B. Goodenough's Noble Lecture, but also the most important thing that I've learned from you. During our first meeting, I remember I was extremely unwilling to express my unknown on some topics because I thought that would make me seem ignorant. But you told me that it's okay to say I don't know and encouraged me to raise any questions that I wanted to ask. Though it seems a trifle, it keeps fresh in my memory and always gives me the courage to expose my ignorance in the research. All in all, your continuous curiosity, dedication, and preciseness in science will always be what I shall look up to in my future career.

I would also like to thank my second supervisor, Prof. R.-A. Eichel, for supporting my experiments in IEK-9. It would be impossible to finish my research without your generous assistance. I sincerely thank Prof. H.J. Bergveld, Prof. M. Huijben, Prof. F. Hausen, and Prof. P.M.J. Van den Hof for agreeing to be the committee members of my defense and spending time and effort on reviewing my thesis. I would also like to thank Prof. P. de With for being the chairman of my defense ceremony. The financial support from China Scholarship Council is highly appreciated as well.

Many thanks for the solid support and guidance from my co-promoter: Dr. D.L. Danilov. You have shown me consistent patience with my questions and helped me resolve the puzzles I encountered in the research. I valued every meeting we had in the past four years and will always remember what I learned from you.

I would like to thank all the colleagues in TU/e and IEK-9. Thanks to Achim Weber for the instruction and assistance on the sputtering machine and other experimental devices; thanks to Dr. Chunguang Chen for the instruction and help on the equipment operation and advice in the experiments; thanks to Dr. Lei Zhou for actively arranging the equipment training and laboratory access; thanks to Dr. Xiaochao Wu for generous assistance in my doctoral period; thanks to Dr. Dongjiang Li for the help and discussion on battery modeling; thanks to Dr. Luc Raijmakers for the help on Maccor/Autolab measurement and the revision of Dutch abstract; thanks to Christian Hellenbrandt for the help on the design of electrochemical cell; thanks to Dr. Peter Jakes for the kindhearted help on any problems occurred in the lab. Furthermore, I would like to thank other colleagues in the group and friends in Forschungszentrum: Zhiqiang Chen, Baolin Wu, Zhenya Wang, Dr. Ruoheng Sun, Dr. Kudakwashe Chayambuka for all the support, you made my work and life more colorful in Germany.

In the end, I want to express my greatest gratitude to my family for their selfless support and endless love. I will never be able to be here without you. Many thanks to my best friend, Xin Chen, who has been being a friend with me since we were only kids, always embracing me with care and encouragement whenever I felt low. Special thanks to my boyfriend, Qian Zhang; thank you not only for the support in the laboratory work but most importantly, for the warm companionship over six years. Finally, I want to thank myself for persisting in the path I chose. The occasional frustration is inevitable; however, it can always turn into a priceless lesson and experience.

